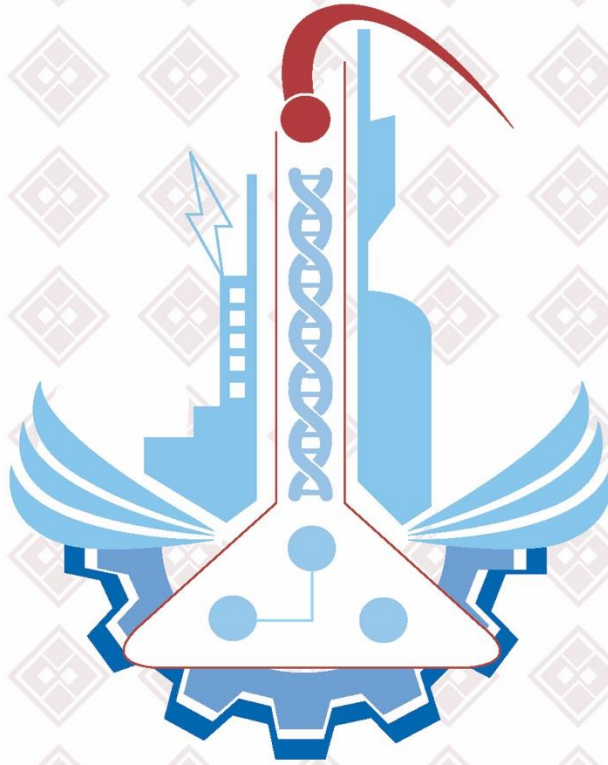


PRINTED ISSN: 1308-9080 / OLINE ISSN: 1308-9099

Volume: 16 / Number: 1 / Year: 2021

TURKISH JOURNAL OF SCIENCE & TECHNOLOGY



TURKISH JOURNAL OF SCIENCE AND TECHNOLOGY (TJST)

Year: 2021 Vol: 16 Number: 1

Address:

Fırat Üniversitesi
Fen Bilimleri Enstitüsü
23119, Elazığ - TURKEY

Tel: 0 424 212 27 07

Fax: 0 424 236 99 55

e-mail: fenbilim@firat.edu.tr

New ISSN

Online: 1308-9099

Printed: 1308-9080

Old ISSN

Online: 1306 – 8555

Printed: 1306 – 8547

Refereed journal. Published twice a year

<https://dergipark.org.tr/tr/pub/tjst>

TURKISH JOURNAL OF SCIENCE & TECHNOLOGY (TJST)
Published by Firat University

Owner

Prof Dr. Fahrettin GÖKTAŞ
Rector of Firat University

Editor in Chef

Assoc. Prof. Dr. Fatih ÖZKAYNAK
Firat University, Faculty of Technology
Department of Software Engineering

Responsible Director

Assoc. Prof. Dr. Kürşat Esat ALYAMAÇ
Firat University, Faculty of Engineering
Department of Civil Engineering

Editor

Assoc. Prof. Dr. Emrah YILMAZ
Firat University, Faculty of Science
Department of Mathematic

ADVISORY BOARD

Eyüp BAĞCI

Firat University, Department of Biology,
Elazig-Turkey

Eres SOYLEMEZ

Middle East Technical University,
Department of Engineering Science,
Ankara-Turkey

Coskun BAYRAK

UALR Donaghey Collage of Eng. and
Information Tech. Dept. of Computer
Science, Little Rock, AR, USA

Hikmet GECKIL

Inonu University, Department of Biology,
Malatya-Turkey

Metin CALTA

Firat University, Fisheries Faculty,
Elazig-Turkey

Ertan GOKALP

Karadeniz Technical University,
Department of Geodesy and
Photogrametry Engineering, Trabzon-
Turkey

Abdulkadir ŞENGÜR

Firat University, Department of
Electronics and Computer Education,
Elazig-Turkey

Hasan EFEOGLU

Ataturk University, Department of
Electrical-Electronics Engineering,
Erzurum-Turkey

Yanhui GUO

St. Thomas University, School of Science
and Technology, Miami, FL, USA

İbrahim TURKMEN

Bahkesir University, Department of
Geology Engineering, Bahkesir-Turkey

Deniz UNER

Middle East Technical University,
Department of Chemical Engineering,
Ankara-Turkey

M.Polat SAKA

Bahreyn University, Department of Civil
Engineering, Bahrain

Siqing XIA

Tongji Univ, State Key Lab Pollut Control
& Resource Reuse, Coll Environm Sci &
Engn, Shanghai 200092, R China

Zihni DEMIRBAG

Karadeniz Technical University,
Department of Biology, Trabzon-Turkey

Hanifi GULDEMİR

Firat University, Department of Electronics
and Computer Education, Elazig-Turkey

Nilgun GULEC

Middle East Technical University,
Department of Geology Engineering,
Ankara-Turkey

Erdogan GUNEL

West Virginia University, Department of
Statistics, Morgontown, USA

Sedigheh GHOFRANI

Islamic Azad University, Electrical
Engineering Department, Tehran South
Branch, Iran

Wang XIBAO

Tianjin University, The School of
Materials Science and Engineering, China

Brain WOERNER

West Virginia University, Department of
Computer Sciences & Electrical
Engineering, Morgontown, WV, USA

A. Kadri CETIN

Firat University, Department of Biology,
Elazig-Turkey

Yusuf Kağan KADIOĞLU

Ankara University, Department of Geology
Engineering, Ankara-Turkey

Sezgin BAKIRDERE

Yıldız Technical University, Department of
Chemistry, Ankara-Turkey.

Tuncay OREN

Ottawa Univ, Fac Eng, Inform Technol.
McLeod Inst Sim.t Sci, Ottawa, ON KIN
6N5 Canada

Halil ONDER

Middle East Technical University,
Department of Civil Engineering, Ankara-
Turkey

Nazmi POLAT

Ondokuz Mayıs University, Department of
Biology, Samsun-Turkey

Mustafa DORUCU

Firat University, Fisheries Faculty,
Elazig-Turkey

Binod Chandra TRIPATHY

Mathematical Sciences Division, Institute
of Advanced Study Science and Tech.
Paschim Boragaon; Guwahati, India

Eoin CASEY

University College Dublin, Chemical and
Bioprocess Engineering, Dublin, Ireland

Farid El-TANTAWY

Suez Canal University, Faculty of
Science, Department of Physics, Ismailia,
Egypt

Saleem HASHMI

International College of Technology,
Dublin, Ireland

Sakir ERDOĞDU

Karadeniz Technical University,
Department of Civil Engineering, Trabzon-
Turkey

Serdar SALMAN

Marmara University, Metallurgical and
Materials Engineering, İstanbul-Turkey

Firat University Turkish Journal of Science & Technology (TJST)
16-1, 2021

CONTENTS / İÇİNDEKİLER

1. **A methodology for implementation of the mechanistic-empirical rigid pavement design in Turkey**
Türkiye'de mekanistik-ampirik rijit üstyapı tasarımının uygulanması için bir metodoloji
Mohammad Razeq SHAKHAN, Ali TOPAL, Burak SENGOZ..... 1-10
2. **Modelling a Static VAR Compensator consist of TCR and TSC**
TCR ve TSC'den Oluşan Bir Statik VAR Kompansatör Modellemesi
Onur TURAN, Yavuz SARI, Rasit KOKER 11-21
3. **4×4 Knight's Graph Analysis by Modularity: A Knight Graph Application**
Modülerlik ile 4×4 At Graf Analizi: At Graf Uygulaması
Serkan GÜLDAL..... 23-30
4. **The Change of The Magnitude of The Electric Field Vector (Ey/E0) in The Ionosphere in The Magnetic Equator Through**
Manyetik Ekvator Bölgesinde İyonosferde Elektrik Alan Vektörünün (Ey/E0) Büyüklüğünün Değişimi
Ali YEŞİL, Osman ÖZCAN, Mustafa İNÇ, Selçuk SAĞIR, Kadri KURT, Luba TSAMALASHVILI, Tamas KALADZE, David Tamas KALADZE 31-38
5. **Correlation Based Regression Imputation (CBRI) Method for Missing Data Imputation**
Eksik Veriler için Korelasyona Dayalı Regresyon Yöntemi İle Değer Atama
Uğur ÜRESİN..... 39-46
6. **Enhancing The Data Security by using Audio Steganography with Taylor Series Cryptosystem**
Taylor Serisi Kriptosistem ile Ses Steganografisi Kullanılarak Veri Güvenliğinin Artırılması
Muharrem Tuncay GENÇOĞLU, Mehmet VURAL..... 47-64
7. **Performance Analysis of Various Classification Algorithms for Computer-Aided Breast Cancer Diagnosis System Using Thermal Medical Images**
Fotovoltaik Sistemler için YSA Tabanlı MPPT Algoritması
Muhammet BAYKARA..... 65-84
8. **Energy and Exergy Analysis of Drying Behavior for a Fish**
Bir Balık için Kuruma Davranışının Enerji ve Ekserji Analizi
Murat ERDEM, Fethi KAMISLI, Yasin VAROL, Hakan Fehmi OZTOP..... 85-95
9. **Quantum Cryptography, Quantum Communication and Quantum Computing Problems and Solutions**
Kuantum Kriptografi, Kuantum İletişim ve Kuantum Hesaplama Problem ve Çözümler
Muharrem Tuncay GENÇOĞLU 97-101
10. **Classification of 40 Different Human Movements with CNN Architectures and Comparison of Their Performance**
Agrega Boyutu ve Kür Şartlarının Betonun Mühendislik Özelliklerine Etkisi
Muhammed YILDIRIM, Ahmet ÇINAR. 103-112

11. The Helix and Slant Helices Generated by non-Degenerate Curves in $M_3(\delta_0) \subset E^4$ <i>$M_3(\delta_0) \subset E^4$ 3-Uzayında non-Dejenere Eğriler Tarafından Elde Edilen Helis ve Slant Helisler</i> Fatma ALMAZ, Mihriban ALYAMAÇ KÜLAHÇI.....	113-117
12. Poisonous Mushroom Detection using YOLOV5 <i>YOLOV5 Kullanarak Zehirli Mantar Tespiti</i> Emine CENGİL, Ahmet ÇINAR	119-127
13. Smart Arms Detection System Using YOLO Algorithm and OpenCV Libraries <i>YOLO Algoritmasını ve Açık Kütüphanelerini Kullanan Akıllı Silah Algılama Sistemi</i> Rayan KHALAF, Yaman AKBULUT.....	129-136
14. Classification of Brain Tumor Images using Deep Learning Methods <i>Derin Öğrenme Yöntemleri Kullanılarak Beyin Tümörü Görüntülerinin Sınıflandırılması</i> Harun BINGOL, Bilal ALATAS.....	137-143
15. Performance of Chaotic Mapping Multi-Objective Optimization Algorithms <i>Kaotik Haritalı Çok Amaçlı Optimizasyon Algoritmalarının Performansı</i> Eyup EROZ, Erkan TANYILDIZI.....	145-153
16. One-dimensional Center Symmetric Local Binary Pattern Based Epilepsy Detection Method <i>Tek Boyutlu Merkez Simetrik Yerel İkili Desen Tabanlı Epilepsi Tespit Yöntemi</i> Serkan METİN.....	155-162
17. Novel Fuzzy Kernels Based Local Binary Pattern And Local Graph Structure Methods <i>Yeni Bulanık Çekirdeklere Dayalı Yerel İkili Desen ve Yerel Grafik Yapısı Yöntemleri</i> Serkan METİN, Şengül DOĞAN	163-177
18. Industrial Automation and Edge Computing: SCADA, PLC, PAC, IO-LINK <i>Endüstriyel Otomasyon ve Uç Bilişim: SCADA, PLC, PAC, IO-LİNK</i> Fatih TOPALOĞLU.....	179-185

A methodology for implementation of the mechanistic-empirical rigid pavement design in Turkey

Mohammad Razeq SHAKHAN^{1*}, Ali TOPAL², Burak SENGOZ²

¹ The Graduate School of Natural and Applied Science, Dokuz Eylul University, Izmir, Turkey

² Department of Civil Engineering, Engineering Faculty, Dokuz Eylul University, Izmir, Turkey

*¹raziqshakhan@yahoo.com, ²ali.topal@deu.edu.tr, ²burak.sengoz@deu.edu.tr

(Geliş/Received: 19/02/2020;

Kabul/Accepted: 21/10/2020)

Abstract: The Mechanistic-Empirical Pavement Design Guide (MEPDG) was emerged and calibrated based on the North American conditions for analysis and designing of flexible and rigid pavements. Implementing this guide in elsewhere needs evaluation using local data, if need be, the local calibration should be conducted to improve the accuracy of the pavement distress prediction models. The state agencies in United States of America (USA) and some developing countries have followed different implementation methodologies to apply the method. In this study, a detailed methodology was developed for the implementation of the ME Rigid Pavement Design Guide in Turkey. This methodology can serve as a guide for local calibration of the MEPDG in Turkey as well as the other countries.

Key words: Data collection, local calibration, mechanistic-empirical pavement design guide (MEPDG), rigid pavement

Türkiye'de mekanistik-ampirik rijit üstyapı tasarımının uygulanması için bir metodoloji

Öz: Mekanistik-Ampirik Üstyapı Tasarım Rehberi (MEPDG), esnek ve rijit üstyapıları analiz etmek ve tasarlamak için Kuzey Amerika koşullarına göre geliştirilmiş ve kalibre edilmiştir. Bu rehberin farklı koşullar altında gerçekleştirilmesi amacıyla, üstyapı yüzey bozuklukları tahmin modellerinin değerlendirilmesi ve kalibrasyonuna ihtiyaç duyulmaktadır. Amerika'daki eyaletler ve bazı gelişmekte olan ülkeler, MEPDG'yi uygulamak için farklı metodolojiler kullanmışlardır. Bu çalışmada, Türkiye'de ME Rijit Üstyapı Tasarım Rehberi uygulanması için ayrıntılı metodoloji geliştirilmiştir. Bu metodoloji, Türkiye'de ve diğer ülkelerde MEPDG'nin yerel kalibrasyonu için bir kılavuz olarak kullanılabilecektir.

Anahtar kelimeler: Veri toplanması, yerel kalibrasyon, mekanistik-ampirik üstyapı tasarım rehberi, rijit üstyapı

1. Introduction

The MEPDG is an attempt to overcome various shortages and disadvantages of the empirical pavement design methods as well as to design both rigid and flexible pavements. It is a sophisticated pavement design method that analyses and designs Jointed Plain Concrete Pavement (JPCP) and Continuously Reinforced Concrete Pavement (CRCP) using the Finite Element Method. The MEPDG calculates pavement performance (stress and deflection) under the combination of traffic loading and environmental effects, computes incremental damages, and predicts pavement distresses such as joint faulting and transverse cracking (bottom-up and top-down cracking) in JPCP and Punch-out in CRCP as well as International Roughness Index (IRI) using various design parameters (material properties, traffic characteristics, and hourly climate data) [1, 2]. The MEPDG was developed and calibrated only for the North American conditions. To implement in other parts of the world, the MEPDG should be evaluated for local conditions to determine the accuracy level of pavement distress prediction models, and the local calibration should be conducted if it is needed. State agencies in the USA and some developing countries have made efforts to implement this guide. The implementation methodology which was persuaded by state agencies in the USA and other countries is different but has some similar activities (e.g., local data preparation, sensitivity analysis, establishing of design threshold values and reliability levels, evaluation, local calibration, validation, preparing design manual, and staff training) [3-7]. In the Ohio state, the MEPDG for JPCP was calibrated for local conditions. It was found that predicted distresses are close to the field observed distresses [8]. Won collected the data from 27 roadway segments in Texas USA to evaluate the MEPDG rigid pavement. He found that the MEPDG using nationally calibrated transfer functions highly over-estimates the amount of pavement distress (punch-out) [9]. In order to implement the MEPDG in Italy, the local data like vehicle classification, truck distribution factors, and truck axle load distribution, materials properties, and climate data were collected and prepared [10]. In Iran the fatigue cracking (alligator and longitudinal) model was calibrated for the local conditions. Forensic investigation

* Corresponding author: raziqshakhan@yahoo.com. ORCID: 0000-0002-9756-7331¹, 0000-0002-2601-1926², 0000-0003-0684-4880²

was done to confirm the obtained data from Tehran municipality. The Tehran Climate data were obtained from Meteorological Organizations in their original formats and then converted to Enhanced Integrated Climatic Model (EICM) format to be used in the MEPDG software. The default traffic data were used. The local calibration results shown that default calibrated transfer functions extensively overestimate the fatigue cracking [11]. To conduct the local calibration of the MEPDG in New Mexico, the local data (e.g., traffic, climate, pavement structure, materials, and pavement distresses) were prepared. The local calibration successfully reduced the MEPDG prediction model error [12]. The Egyptian climate data were collected and converted to the MEPDG format and the environmental effects on flexible pavement performances was evaluated [13]. In the State of Qatar, the sensitivity analysis was done using local data (material properties which were extracted from the Qatar Highway Design Manual (QHDM)) and default data (equivalent climate data from Needles Airport in California and traffic data [14]). In China, the local calibration of the MEPDG were done for local material properties with using some default (Level Three) design inputs such as axle load distribution factors and climate data [15]. In India, material properties, traffic data and three years hourly climate data were prepared to conduct the local calibration of the MEPDG [16]. The local design data such as material properties, traffic data (vehicle class, vehicle class distribution factors, vehicle growth factors, axle load distribution, monthly adjustment factors, hourly distribution, axle per truck, axle configuration, and lateral traffic wander), climate data, and pavement performance were collected, analyzed and converted to the MEPDG format to be used in local calibration of MEPDG in Saudi Arabia [17]. The traffic data (e.g., vehicle classification, growth rate, and truck distribution factors) was collected and the sensitivity analysis was done for various climate condition in Lebanon [18]. Before conducting the evaluation and local calibration of the MEPDG, developing a procedure for local data preparation, evaluation, local calibration, and validation of the MEPDG are needed. It can assist to precisely carry out the data preparation, evaluation, local calibration, and evaluation efforts, improve the pavement distresses prediction models, and ultimately lead to the successful implementation of the MEPDG for local conditions. The objective of this study is to develop a methodology and procedure for local data collection, evaluation, local calibration, and validation of the ME Rigid Pavement Design in Turkey to be used as preliminary foundation for whoever wants to implement the MEPDG for local conditions.

2. Development of Methodology

To adopt the MEPDG for the local conditions, the evaluation and local calibration efforts are highly required. The local calibration can be carried out by following a realistic implementation methodology. In other words, developing a reliable and applicable methodology for data collection and preparation, evaluation, local calibration, and validation can lead to enhance the accuracy of the pavement distresses prediction models and finally successfully adopt the MEPDG for local conditions. Considering local material specifications, pavement structure, traffic characteristics, climate conditions, construction methodology as well as follow up the AASHTO guide for local calibration of the MEPDG [19], a methodology for the implementation of the MEPDG-Rigid Pavement for Turkey is developed. The implementation methodology consists of seven main stages and several sub-sections which are explained as follows. Also, for a better understanding, the methodology is illustrated in a flow chart as shown in Figure 1.

2.1. Select input level

The MEPDG requires design inputs in three levels which are based on availability of local data and capability of highway agencies. The Level 1 design inputs are provided through actual laboratory tests while the Level 3 is mostly default values, and design data in Level 2 is estimated based on previous laboratory works. To select the input level, a comprehensive sensitivity analysis should be done to find out the sensitivity level of local design inputs (materials, traffic, and climate). Highly sensitive inputs can be selected as Level 1 and low sensitive inputs can be selected in Level 3.

2.2. Select pavement segments

In this stage, the existing pavement segments with three conditions survey in 10 years are selected.

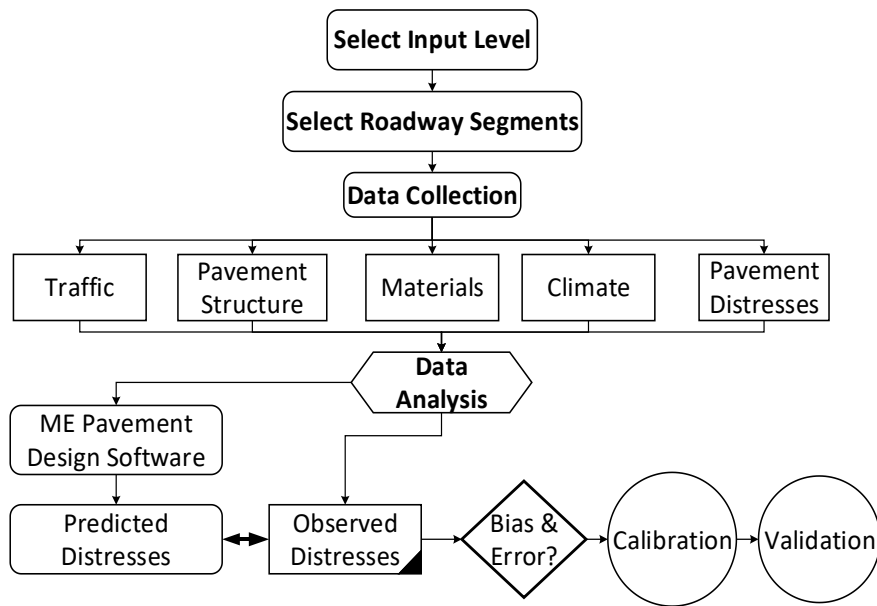


Figure 1. Methodology for local data collection and calibration of the MEPDG in Turkey

2.2.1. Data Collection

From the selected pavement segments, the local design parameters should be collected to start the evaluation and local calibration efforts. The local data which is required to be collected will be explained as follows.

2.2.2. Pavement structure

In this step, the rigid pavement type (JPCP or CRCP), pavement thickness, and the base thickness if any should be selected.

2.2.3. Pavement distresses

In this stage, the pavement distresses (Transvers cracking, Joint faulting, and International Roughness Index) should be collected. The pavement distress can be collected by two methods: 1). Distresses can be extracted from Turkish Directorate General of Highways database, if any. 2). Establishing the Pavement Management System (PMS) to complete distress survey in accordance with the MEPDG requirements.

2.2.4. Materials properties

Various and detailed material properties for Plain Cement Concrete PCC, base and subgrade should be collected such as joint spacing, dowel diameter, steel percentage, PCC unit weight, PCC Elastic modulus, modulus of rupture, indirect tensile strength in 7, 14, 28, and 90 days, PCC pozzolan's ratio, Air content, Coefficient of thermal expansion, water cement ratio, cement type, base and subgrade resilient modulus, and groundwater depth.

2.2.5. Traffic characteristics

The following traffic data should be collected for local calibration and sensitivity analysis efforts.

2.2.5.1. Base Year Traffic Information

- Design Life
- Opening Date
- Initial Two Way Annual Average Daily Truck Traffic (AADTT)

- Number of Lanes in Design Direction
- Percent Trucks in Design Direction
- Percent Trucks in Design Lane
- Operational Speed

2.2.5.2. Traffic Volume Adjustment Factors

- Monthly Adjustment Factors
- Vehicle Class Distribution
- Hourly Distribution
- Traffic Growth Factors

2.2.5.3. Axle Load Distribution Factors

The axle load distribution factors are required to be collected in four separate groups based on axle type and truck classification, such as single axle load distribution, tandem axle load distribution factors, tridem axle load distribution factors as well as quad axle load distribution factors if any.

2.2.5.4. General Traffic Inputs

- Lateral Traffic Wander
- Number of Axles per Truck
- Axle Configuration

2.2.6. Climate data

Climate data such as hourly temperature, wind speed, sunshine, precipitation, and relative humidity are required to be collected. It is recommended that the climate data should exist for the whole pavement design life. In Turkey, the hourly climate data can be obtained from Turkish State Meteorological Service (TC Meteoroloji Genel Müdürlüğü, MGM).

2.3. Data analysis

Some of the local data are not suitable to be used directly as design inputs in the MEPDG software; therefore, data analysis is required to be made to improve the local data and convert them to a suitable format. Right now, in Turkey, vehicles are classified in five groups as per vehicle types such as Cars, Medium Goods Vehicles, Bus, Trucks, and Trailers while, in the MEPDG the vehicles are classified based on axle types, number, and spacing as well as vehicle types in ten groups. Therefore, a comprehensive study is required to classify the observed vehicles in Turkey as per the MEPDG standard. The observed vehicles in Turkey which are shown in Figure 2 are classified based on axle type (single, tandem, and tridem axles), axle number (two, three, four, five and six), and tire configurations (single and dual). For example: “1” represents single axle and single tire, “2” represents single axle and dual tire, “11” shows single tire and tandem axle, “111” represent super-single tire and tridem axle as well as “222” represents dual tire and tridem axle. Another important design parameter that should be considered is the axle load distribution factors. In Turkey, the axle load distribution is collected in interval of 1000 Kg using weighbridge measurement system which is shown in Table 1. But the MEPDG requires different axle load intervals as follows [1, 20-21].

- Single Axle Load Distribution Factors (1000 kg to 20000 kg) at interval of 500 kg.
- Tandem Axle Load Distribution Factors (2000 kg to 40000 kg) at interval of 1000 kg.
- Tridam and Quad Axle Load Distribution Factors (4500 kg to 49500 kg) at interval of 1500 kg.

Therefore, the local axle load distribution should be converted as per the MEPDG standard that can be used as design inputs in the MEPDG software. The bus axle load is not measured in Turkey. Thus, the default bus axle load distribution factors can be used until further measurement.

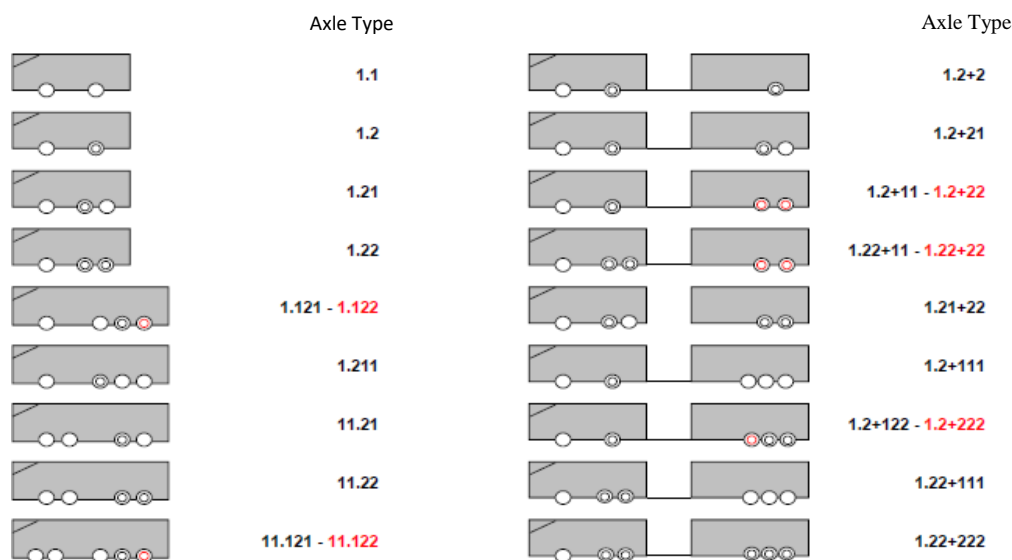


Figure 2. Measured axle load distribution [9]

Table 1. Measured axle load distribution [9]

Load class (ton)	Single axle		Tandem axle		Tridem axle	
	Axle Number	%	Axle Number	%	Axle Number	%
0-1	200	0.203273	9	0.032619	6	0.016634
1-2	3155	3.206627	11	0.039868	8	0.022178
2-3	6748	6.858421	74	0.268203	155	0.429708
3-4	10353	10.52241	522	1.891921	386	1.070112
4-5	16137	16.40106	1156	4.189772	2088	5.788584
5-6	20190	20.52038	1838	6.661593	3221	8.929611
6-7	17104	17.38388	2773	10.05038	1974	5.47254
7-8	8250	8.384998	2528	9.162408	1828	5.067783
8-9	3614	3.673138	2233	8.093219	1587	4.399656
9-10	3360	3.414981	1849	6.701461	1162	3.221424
10-11,5	5539	5.629637	2350	8.51727	1293	3.584597
11,5-12	1264	1.284683	781	2.830633	363	1.006349
12-13	1598	1.624149	1633	5.918597	793	2.198442
13-14	640	0.650473	1557	5.643145	806	2.234482
14-15	158	0.160585	1410	5.110362	797	2.209531
15-16	46	0.046753	1085	3.932442	899	2.492307
16-17	13	0.013213	1040	3.769345	1009	2.797261
17-18	11	0.01118	955	3.461274	1114	3.088354
18-19	6	0.006098	950	3.443152	1374	3.809154
19-20	4	0.004065	875	3.171324	1586	4.396884
20-21			669	2.424704	1876	5.200854
21-22			369	1.337393	2268	6.287599
22-23			288	1.043819	2355	6.52879
23-24			192	0.695879	2081	5.769177
24-25			140	0.507412	1621	4.493915

25-26			82	0.297198	1067	2.958055
26-27			48	0.17397	830	2.301017
27-28			35	0.126853	535	1.483186
28-29			31	0.112355	311	0.862188
29-30			17	0.061614	191	0.529511
30-31			27	0.097858	127	0.352083
31-32			19	0.068863	87	0.241191
32-33			17	0.061614	60	0.166339
33-34			7	0.025371	49	0.135843
34-35			11	0.039868	39	0.10812
35-36			7	0.025371	22	0.060991
36-37			3	0.010873	13	0.03604
37-38					16	0.044357
38-39					11	0.030495
39-40					6	0.016634
40-41					12	0.033268
41-42					6	0.016634
42-43					7	0.019406
43-44					10	0.027723
>44					22	0.060991
Total	98390	100	27591	100	36071	100

The MGM measures the cloud cover in the 8-Okta unit but sunshine is used in the MEPDG in percent. In okta measurement unit the sky is divided in eight parts (0-8), which 0 shows a sunny day and 8 represents 100% cloud cover [17]. Therefore, the okta unit should be converted into percent and the cloud percentage cover should be changed to sunshine percentage. And finally, the collected local climate data should be converted to the MEPDG format (text file in “.hcd” extension) because the climate data has not been yet developed in the MEPDG format for all parts of Turkey [22]. Each climatic file consists of date (YYYY/mm/dd/hr), air temperature (°C), precipitation (mm), wind speed (m/hr), cloud cover (%), and humidity (%) which is shown in Figure. 3. Due to several reasons (maintenance, extreme weather or malfunction) the weather stations are not able to record continuously; therefore, the missed data should be completed using interpolation method or adoption from another stations [13][23].

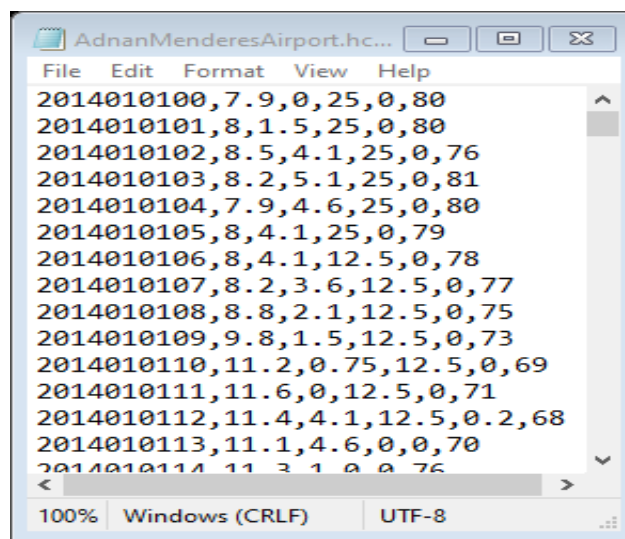


Figure 3. Climate data in MEPDG required format

2.4. Evaluation

In this step the prepared local design data are used as design inputs in the MEPDG software and the pavement distresses (transvers cracking, joint faulting, punch-outs, and IRI) are predicted for each selected pavement segments. The predicted and observed pavement distresses are compared together to verify the accuracy level of pavement distress prediction models. If significant bias and standard error exist between predicted and observed distresses, the local calibration step is required to be carried out. In this purpose, the Null hypothesis which is shown by Equation. 1 is used.

$$H^0: \sum_{i=1}^n (Y_{\text{measured}} - X_{\text{predicted}}) = 0 \quad (1)$$

Where;

Y_{measured} = Measured value and $X_{\text{Predicted}}$ = Predicted value

2.5. Local calibration

In the case of the existence of significant bias and standard error between measured and predicted pavement distresses, the local calibration is conducted to remove the bias and decrease the standard error to an acceptable level. In this stage, the local calibration factors should be adjusted to eliminate the bias and reduce the standard error. The following activity can be done.

2.5.1. Local calibration of transvers cracking

To remove the bias and decrease the standard error from the cracking model the calibration factors (C_1, C_2, C_3, C_4, C_5) in Equation 2 and Equation 4 should be adjusted.

$$CRK = \frac{100}{1 + C_4 (DI_F)^{C_5}} \quad (2)$$

Where;

CRK = predicted amount of bottom-up or top-down cracking;

DI_F = fatigue damage calculated using the equation 3.

C_4 and C_5 = calibration coefficients

$$DI_F = \sum \frac{n_{i,j,k,l,m,n,o}}{N_{i,j,k,l,m,n,o}} \quad (3)$$

Where;

$n_{i,j,k,l,m,n,o}$ = applied number of load applications at condition i, j, k, l, m, n, o .

$N_{i,j,k,l,m,n,o}$ = allowable number of load applications at condition i, j, k, l, m, n, o .

$$\text{Log} (N_{i,j,k,l,m,n,o}) = C_1 \left(\frac{MR_i}{\sigma_{i,j,k,l,m,n,o}} \right)^{C_2} \quad (4)$$

Where;

$N_{i,j,k,l,m,n,o}$ = allowable number of load applications at condition i, j, k, l, m, n, o .

MR_i = PCC modulus of rupture at age i , Mpa,

$\sigma_{i,j,k,l,m,n,o}$ = applied stress at condition i, j, k, l, m, n, o .

C_1 and C_2 = calibration factors

2.5.2. Local calibration of joint faulting

The local calibration coefficients ($C_1, C_2, C_3, C_4, C_5, C_6, C_7$, and C_8) from joint faulting predicted model (Equation 5 and 6) should be adjusted to eliminate the bias and reduce the standard error.

$$Fault_m = \sum_{i=1}^m \Delta Fault_i \quad (5)$$

Where;

$Fault_m$ = mean joint faulting at the end of month m ;

$\Delta fault_i$ = incremental change in mean transverse joint faulting during month, i .

$$\Delta Fault_i = C_{34} * (FAULTMAX_{i-1} - Fault_{i-1})^2 * DE_i \quad (6)$$

$$FAULTMAX_i = FAULTMAX_0 + C_7 * \sum_{j=1}^m DE_j * \text{Log} \left(1 + C_5 * 5.0^{EROD} \right)^{C_6} \quad (7)$$

And,

$$FAULTMAX_0 = C_{12} * \delta_{curling} * \left[\sum_{i=1}^m \text{Log} \left(1 + C_5 * 5.0^{EROD} \right) * \text{Log} \left(\frac{P_{200} * WetDays}{P_s} \right) \right]^{C_6} \quad (8)$$

Where;

$FAULTMAX_i$ = maximum mean transverse joint faulting for month i , m.,

$FAULTMAX_0$ = initial maximum mean transverse joint faulting, m.,

$EROD$ = base and subbase erodibility coefficients

DE_i = differential density of energy of subgrade deformation accumulated during month, i .

$\delta_{curling}$ = maximum mean monthly slab corner upward deflection PCC due to temperature curling and moisture warping,

PS = overburden on subgrade, kg,

P_{200} = percent subgrade material passing #200 sieve,

$WetDays$ = average annual number of wet days

$C_1, C_2, C_3, C_4, C_5, C_6, C_7$, and C_8 are calibration constants.

$$C_{12} = C_1 + C_2 * FR^{0.25} \quad (9)$$

$$C_{34} = C_3 + C_4 * FR^{0.25} \quad (10)$$

Where;

FR = base freezing index defined as percentage of time the top base temperature is below 0°C temperature.

2.5.3. Local calibration of smoothness

In order to conduct the local calibration for the International Roughness Index (IRI) prediction model, the C_1, C_2, C_3, C_4 factors should be adjusted to eliminate the bias and reduce the standard error from the model which are shown in Equation. 11.

$$IRI = IRI_1 + C_1 * CRK + C_2 * SPALL + C_3 * TFAULT + C_4 * SF \quad (11)$$

Where:

IRI = Predicted IRI, in./mi,

IRI_1 = Initial smoothness measured as IRI, in./mi,

CRK = Percent slabs with transverse cracks (all severities),

SPALL = Percentage of joints with spalling (medium and high severities),
TFAULT = Total joint faulting cumulated per mi, in., and
SF = Site factor

2.6. Validation

In this step the prepared local design data are used as design inputs in the MEPDG software and the pavement distresses (transvers cracking, joint faulting, punch-outs, and IRI) are predicted for each selected pavement segments. The predicted and observed pavement distresses are compared together to verify the accuracy level of pavement distress prediction models. If significant bias and standard error exist between predicted and observed distresses, the local calibration step is required to be carried out. In this purpose, the Null hypothesis (Equation 1) is used.

2.7. Conclusion and summary

The MEPDG was developed and calibrated based on the USA conditions. Therefore, to implement it in countries, the MEPDG has to be evaluated for local conditions and the local calibration and validation should be conducted if required. The local calibration is done to improve the accuracy level of the MEPDG distress prediction models. Developing a methodology is required to carry out such efforts. The summary of local calibration efforts and local data collection are summarized as follows.

- State agencies and countries followed different methodologies for data collection and local calibration. But they still have some similar activities (e.g., data collection, sensitivity analysis, evaluation, local calibration, and validation).
- Some of the collected data may not be directly used as design input in the MEPDG. Therefore, they should be analysed and converted to the suitable format that is required by the MEPDG.
- In Turkey, vehicles are classified based on their types in five groups (e.g., cars, medium goods vehicles, buses, trucks, and trailers) which is different from truck classification in the MEPDG. Therefore, a new vehicle classification is required to be developed.
- In Turkey, vehicles axles load (single, tandem, and tridem) are measured in the interval of 1000kg using weighbridge system, which is not based on the MEPDG standard. The measured axle load should be analysed and converted to the MEPDG required format.
- The extracted hourly climate data from automatic weather stations may have missing data and gaps (hours, days, months, and years), which can be provided and completed using data from the closest weather stations or by using interpolation. Climate data (temperature, wind speed, sunshine, precipitation, and humidity) should be converted to the text file format with “.hcd” extension.
- The cloud cover is measured in 8-Okta units in Turkey, while the sunshine is used by MEPDG in percentage. Therefore, the 8-Okta unit should be converted to percent and then the cloud cover percentage should be changed to sunshine percentage.

Acknowledgment

The authors would like to express their profound gratitude to the Department of Scientific and Research Project, Dokuz Eylul University, Izmir, Turkey for their financial support (Project Number: 2019.KB.FEN.038). Also, thank and appreciate the Graduate School of Natural and Applied Sciences, Dokuz Eylul University for their valuable supports.

References

- [1] American Association of State Highway and Transportation Officials. Washington, D.C., USA: Mechanistic Empirical Pavement Design Guide. American Association of State Highway and Transportation Officials (AASHTO), 2008.
- [2] National Cooperative Highway Research Program. Guide for Mechanistic-Empirical Design of New and Rehabilitated Pavement Structures. Washington, D.C., USA: National Cooperative Highway Research Program, 2004.
- [3] Shakhan MR, Topal A, Şengöz B, Almusawi A. Review of the implementation of the mechanistic-empirical pavement design guide. 3rd International Students Science Congress; 3-4 May 2019; Izmir, Turkey. pp. 138–153.

- [4] Geary GM. User Review of the AASHTO ‘Guide for the Local Calibration of the Mechanistic-Empirical Pavement Design Guide’. Stockbridge, Georgia, USA: Transportation Research Board of the National Academies of Sciences, Engineering, and Medicine, 2018.
- [5] Pierce LM, Ginger M. Implementation of the AASHTO Mechanistic-Empirical Pavement Design Guide and Software. Washington D.C., USA: National Cooperative Highway Research Program, 2014.
- [6] Xiao D, Wang KCP, Qiu Y. Mechanistic-empirical pavement design guide (MEPDG): A bird’s-eye view. *J. Mod. Transp.* 2011; 19(2):114–133.
- [7] Robbins MM, Rondezno C, Tran N, Timm DH. Pavement Me Design – A Summary of Local Calibration Efforts for Flexible Pavements. Auburn, Alabama, USA: National Center for Asphalt Technology, 2017.
- [8] Mallela J, Glover LT, Darter MI, Harold VQ, Gotlif A, Stanley M, Sandasivam S. Guidelines for Implementing NCHRP 1-37A M-E Design Procedures in Ohio: Volume 1— Summary of Findings, Implementation Plan, and Next Steps Ohia, USA: Ohio Department of Transportation, 2009.
- [9] Won M. Evaluation of MEPDG with TxDOT Rigid Pavement Database. Texas, USA: Texas Department of Transportation; 2009.
- [10] Caliendo C. Local calibration and implementation of the mechanistic-empirical pavement design guide for flexible pavement design. *J Transp Eng.* 2012; 138(3):348–60.
- [11] Azadi M, Nasimifar SM, Pouranian MR. Determination of local fatigue model calibration used in MEPDG for Iran’s dry-no freeze region. *Arab J Sci Eng.* 2013; 38(5):1031–1039.
- [12] Tarefder R, Rodriguez-Ruiz JI. Local Calibration of MEPDG for Flexible Pavements in New Mexico. *J Transp Eng.* 2013; 139(10):981–91.
- [13] A. Elshaeb M, M. El-Badawy S, A. Shawaly E-S. Development and Impact of the Egyptian Climatic Conditions on Flexible Pavement Performance. *Am J Civ Eng Archit [Internet].* 2014; 2(3):115–21.
- [14] Sadek HA, Masad EA, Sirin O, Al-Khalid H, Sadeq MA, Little D. Implementation of mechanistic-empirical pavement analysis in the State of Qatar. *Int J Pavement Eng.* 2014; 15(6):495–511.
- [15] Ma H, Wang D, Zhou C, Feng D. Calibration on MEPDG Low Temperature Cracking Model and Recommendation on Asphalt Pavement Structures in Seasonal Frozen Region of China. *Adv Mater Sci Eng.* 2015; 2015(3):1–11.
- [16] Ghosh, A., Padmarekha, A., Krishnan, J. M. Implementation and proof-checking of mechanistic-empirical pavement design for Indian highways using AASHTOWARE Pavement ME Design Software, *Procedia - 2nd Conference of Transportation Research Group of India;* 2013; India. pp. 119–128.
- [17] Alqaili AH, Alsoliman HA. Preparing Data for Calibration of Mechanistic-Empirical Pavement Design Guide in Central Saudi Arabia. *World Acad Sci Eng Technol Int J Urban Civ Eng.* 2017; 11(2):248–55.
- [18] Chhade RH, Mrad R, Houssami L, Chehab G, Asce AM. Formulation of Traffic Inputs Required for the Implementation of the M-E PDG Formulation of Traffic Inputs Required for the Implementation of the M-E PDG in Data-Scarce Regions: Lebanon Case Study. *J Mater Civ Eng, © ASCE.* 2018; 30(9): 04018198
- [19] American Association of State Highway and Transportation Officials. Guide for the local calibration of the Mechanistic-Empirical Pavement Design Guide. Washington, D.C.: American Association of State Highway and Transportation Officials (AASHTO), 2010.
- [20] Karayolları Genel Müdürlüğü. Karayolları Esnek Üstyapılar Projelendirme Rehberi. Ankara, Turkey: Karayolları Genel Müdürlüğü, 2008.
- [21] Karayolları Genel Müdürlüğü. Karayollarında Ağır Taşıt Trafığının ve Yük Taşımacılığının Özellikleri ve Eğilimleri. Ankara, Turkey: Trafik Güvenliği Dairesi Başkanlığı, 2016.
- [22] Öztürk HI, Tan EB, Şengün E, and. Yaman İÖ. Farklı trafik, zemin, malzeme ve iklim koşulları için mekanistik-ampirik (M-E) yöntemle tasarlanan derzli donatısız rijit üstyapı sistemlerinin karşılaştırılması. *Gazi Üniversitesi Mühendislik-Mimarlık Fakültesi Derg.*, 2019; 34(2):771–784.
- [23] Shakhan MR, Topal A, Şengöz B. Data Collection for Implementation of the Mechanistic-Empirical Pavement Design Guide (MEPDG) in Izmir, Turkey, *Tek. Dergi [Internet].* 2021; 32(6), doi: 10.18400/tekderg.651399.

Modelling a Static VAR Compensator consist of TCR and TSC

Onur TURAN^{1*}, Yavuz SARI², Rasit KOKER³

¹Electrical Engineering, Faculty of Electrical & Electronics, Yildiz Technical University, Istanbul, Turkey

²Electronics Technology, Hendek Vocational School, Sakarya University of Applied Sciences, Sakarya, Turkey

³Electrical and Electronic Engineering, Faculty of Technology, Sakarya University of Applied Sciences, Sakarya, Turkey

*f4920029@std.yildiz.edu.tr, ²sari@subu.edu.tr, ³rkoker@subu.edu.tr

(Geliş/Received: 27/02/2020;

Kabul/Accepted: 06/10/2020)

Abstract: As an alternative to traditional solutions, systems that flexible alternating current transmission systems (FACTS) have been developed in order to make electrical energy systems more efficient, to improve stability and power quality, and these systems have been used in different parts of the world including our country. In general, FACTS can be described as systems providing voltage, impedance and phase angle control in AC systems. With the recent studies, the use of modern technology devices such as static VAR compensator and static synchronous compensator is becoming more common in order to ensure the energy quality in power systems. Furthermore, due to the developments in semiconductor technology, static VAR compensation systems have been started to be applied on medium and high voltage side. The most important feature of these systems is that they can compensate without needing reactive power from the grid. In this study, necessary reactive power required by the system provided by using a static VAR compensator consisting of thyristor-controlled reactor and thyristor switched capacitor structures. In the simulation studies, the reactive energy is supplied through the static compensator instead of the voltage source. In this way, unnecessary capacity utilization in the system was prevented. It is recommended to use static VAR compensators especially where there is unbalanced load and instant reactive power is required.

Key words: Svc, Tcr, Tsc, Facts, Power System Stability

TCR ve TSC'den Oluşan Bir Statik VAR Kompansatör Modellemesi

Öz: Geleneksel çözümlere alternatif olarak, elektrik enerjisi sistemlerini daha verimli hale getirmek, kararlılık ve güç kalitesini artırmak için esnek alternatif akım iletim sistemleri (FACTS) geliştirilmiştir ve bu sistemler ülkemizin de içinde bulunduğu dünyanın farklı yerlerinde kullanılmaktadır. Genel olarak, FACTS, AC sistemlerde voltaj, empedans ve faz açısı kontrolü sağlayan sistemler olarak tanımlanabilir. Son yıllarda yapılan çalışmalar ile, statik VAR kompanzator ve statik senkron kompanzator gibi modern teknoloji cihazlarının kullanımı güç sistemlerinde enerji kalitesini sağlamak için daha yaygın hale gelmektedir. Ayrıca, yarıiletken teknolojisindeki gelişmeler sonucunda orta ve yüksek gerilimlerde statik VAR kompanzasyon sistemlerinin uygulanmasına başlanmıştır. Bu sistemlerin en önemli özelliği şebekeden reaktif güce ihtiyaç duymadan kompanzasyon yapabilmeleridir. Bu çalışmada, sistemin ihtiyaç duyduğu reaktif güç tristör anahtarlamalı kapasitör ve tristör kontrollü reaktör yapılarından oluşan bir static Var kompanzatoru kullanılarak sağlanmaktadır. Simülasyon çalışmalarında, reaktif enerji, voltaj kaynağı yerine statik kompanzator yoluyla sağlanır. Böylelikle sistemde gereksiz kapasite kullanımı önlenmiş olmaktadır. Özellikle dengesiz yüklerde ve anlık reaktif gücün gerekli olduğu durumlarda statik VAR kompanzatorlarının kullanılması tavsiye edilir.

Anahtar kelimeler: Svc, Tcr, Tsc, Facts, Güç Sistem Kararlılığı

1. Introduction

In recent years, due to high switching speeds, power electronics components have been used in electrical power systems compensation applications. Thus, it is foreseen that voltage collapses can be prevented and stability can be increased. The developments in the elements of power electronics system have made a revolutionary impact on the electric power systems all over the world. The use of thyristors in power systems for control and switching operations has resulted in new generation thyristor-based rapid operating devices. These new devices, based on power electronics, enable the controllable, stable and power transfer capability of alternating current transmission systems, called flexible alternating current transmission systems (FACTS). FACTS devices are installed to improve power system stability. Power system stability is the major part of electrical engineering work. Basically, it depends on the minimum amount of loss by the generation of electricity and the transmission from the sending end to the receiving end according to the consumer need. The power at the end of the consumer is usually subject to changes due to changes in the load or disturbances along the transmission line. Therefore, the term power system

* Corresponding author: f4920029@std.yildiz.edu.tr. ORCID Number of authors: ¹0000-0001-6523-3428, ²0000-0002-5212-4246, ³0000-0002-3811-2310

stability is extremely important and is used to describe the ability of the system to stabilize the operation as soon as possible after some kind of temporary disturbance [1-2].

The correction of the power factor of fast-acting and unbalanced loads with traditional electro-mechanical compensation mechanisms is problematic in order to ensure power system stability. One reason for this is that conventional compensation systems (with reactive power control relay and contactor) cannot respond immediately to the load of the reactive power demand and that the required capacitive reactive power cannot be compensated from the compensation system. On the other hand, in the case of unbalanced loading, there is no possibility of three-phase systems to respond to the needs of each phase. With static VAr compensation systems, instant compensation of unstable loads can be made quickly, such as spot welding machine, arc furnaces, port cranes used in sectors such as automotive, glass, cement, iron and steel, where power factor can show frequent and large changes [3-4].

2. Basic Principles of Static VAr Compensator Systems

SVC is one of the FACTS devices, which are connected in parallel to the power system, which generate or absorb reactive power from the system to control power system parameters such as voltage. They are safe and operationally flexible, capable of producing or consuming continuous reactive power, operating at an unlimited range, with high response times [5]. SVCs are mainly used in power systems to improve voltage control and system stability. In recent years, many researchers have proposed the technique of improving stability with SVC to extinguish electromechanical fluctuations in power systems [6-7-8]. Generally the SVC structure consists of a combination of thyristor controlled reactor (TCR) and / or thyristor switched capacitor (TSC) structures. Figure 1 shows general schematic block diagram of SVC control systems. In this study, a static VAr compensator formed by TCR and TSC structures is modeled.

The problem of voltage fluctuations caused by arc furnaces during steel production has always been serious concern about power quality all over the world. SVC systems are widely used today, especially in facilities such as arc furnaces and rolling mills where fast-changing loads has. The reactive power consumption of the arc furnaces becomes quite dynamic due to the random variation of the arc length during the melting of the scrap. Besides the use of SVC improves the transient stability of the transmission line and thesis where it use [9-10].

On the other hand, static VAr compensator systems are also used in wind power plants where improve the voltage stability and prevent the wind power plant from being disabled in the case of voltage drops caused by the transmission lines [11].

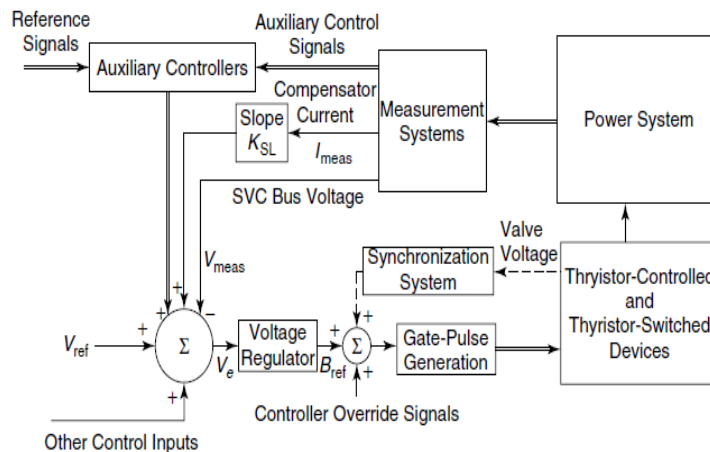


Figure 1. General schematic block diagram of SVC control systems [2-4].

In voltage control cycles, the SVC can effectively switch off power system surges and improve the stability of power systems. An ideal SVC is defined as a controller that does not have an active and reactive power loss, the voltage is equal to the reference voltage, it cannot be changed and can respond very quickly.

2.1. V-I Characteristic of the SVC

The variation of SVC bus voltage and SVC current or reactive power is defined by the steady state and dynamic properties of SVC. Figure 2 shows the voltage–current characteristic of the SVC.

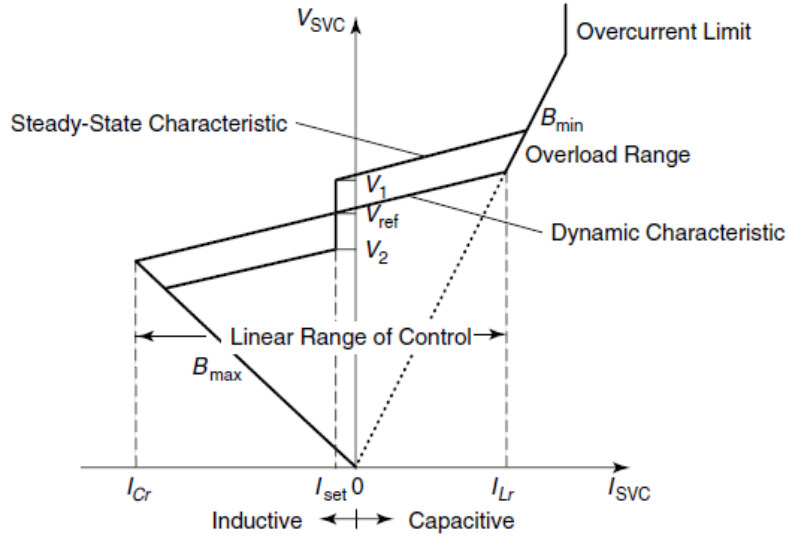


Figure 2. The voltage–current characteristic of the SVC [4].

At the reference voltage V_{ref} , the voltage is regulated while the SVC susceptance (B) continues among the maximum and minimum susceptance values enforced by the total reactive power of capacitor banks (B_{cmax}) and reactor banks (B_{lmax}) [12].

SVC V-I curve can be described following three equations (1-3).

$$V = V_{ref} + X_S \cdot I \quad -B_{cmax} < B < B_{lmax} \quad (1)$$

$$V = -\frac{I}{B_{cmax}} \quad \text{SVC capacitive } B = B_{cmax} \quad (2)$$

$$V = \frac{I}{B_{lmax}} \quad \text{SVC inductive } B = B_{lmax} \quad (3)$$

3. TCR and TSC Structures

3.1. TCR Structure

One of the most significant blocks of thyristor-based SVCs is TCR. Although it can be used alone, to provide quick and continuous control of reactive power across the selected lagging-to-leading range, it is more often used with fixed or thyristor switched capacitors [4].

As denoted in Figure 3, a fundamental single phase TCR contains a pair of thyristor valves anti-parallel connected in series with a linear air-core reactor as T_1 and T_2 . The attitude of the anti-parallel-connected thyristor pair is similar with a bidirectional switch. In positive half-cycles the thyristor valve T_1 conducts and in negative half-cycles of the supply voltage the thyristor valve T_2 conducts. The measurement of the firing angle of the thyristors can be implemented from the zero crossing voltage seen across its terminals [2-4-13].

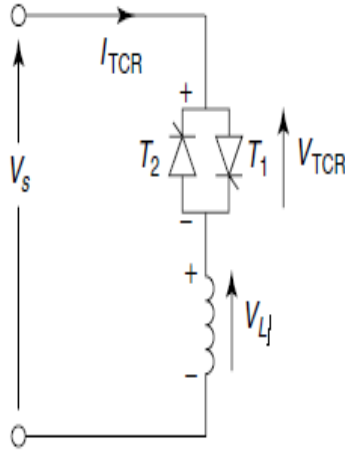


Figure 3. Basic structure of a TCR [4]

In the thyristors inside the systems which generally constitute the static VAr control system, it is very important to know which intervals to trigger. In the first half of the alternance, ie in the triggers to be performed below 90° , the inverted thyristor groups generate DC current, so that the thyristors connected to each other symmetrically are disrupted. Also, a change in the trigger angle after a thyristor has been transmitted can only take place at the next period. This is called the dead time of the thyristor [4].

There is a relationship between the trigger angle α and the transmission angle σ as follows.

$$\alpha + \frac{\sigma}{2} = \pi \quad (4)$$

TCR current can be expressed as equation 5.

$$i(t) = \frac{1}{L} \int V_s(t) dt + C \quad (5)$$

Boundary condition $i(\omega t = \alpha) = 0$;

If we solve Equation 5 according to boundary condition and then do fourier analysis we get;

$$I_1(\alpha) = \frac{V}{\omega L} \left(1 - \frac{2\alpha}{\pi} - \frac{1}{\pi} \sin 2\alpha \right) \quad (6)$$

Equation 6 can also be written as;

$$I_1(\alpha) = V B_{TCR}(\alpha) \quad (7)$$

Where;

$$B_{TCR}(\alpha) = B_{MAX} \left(1 - \frac{2\alpha}{\pi} - \frac{1}{\pi} \sin 2\alpha \right) \quad (8)$$

$$B_{MAX} = \frac{1}{\omega L} \quad (9)$$

Substituting Equation 4 in Equation 6 gives the alternative expression of the fundamental component of the TCR current:

$$I_1(\sigma) = V B_{MAX} \left(\frac{\sigma - \sin \sigma}{\pi} \right) \quad (10)$$

$$I_1(\sigma) = V B_{TCR}(\sigma) \quad (11)$$

As a result, the TCR susceptance value; using the Equations 10 and 11 is expressed as in Equation 12.

$$B_{TCR}(\sigma) = B_{MAX} \left(\frac{\sigma - \sin \sigma}{\pi} \right) \quad (12)$$

Control characteristics of the TCR susceptance, B_{TCR} is shown in Figure 4.

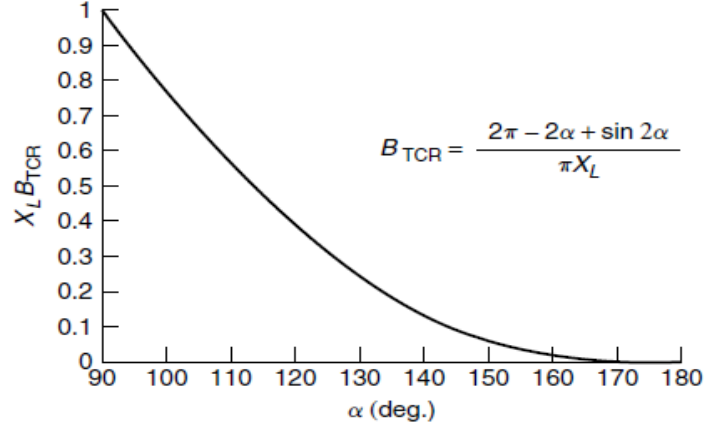


Figure 4. Control characteristics of the TCR susceptance, B_{TCR} [2-4]

3.2. TSC Structure

Thyristor switched capacitors (TSC) are generally used instead of constant capacity thyristor controlled reactor (FC-TCR). TSC is also a subset of SVC, where thyristor-based ac switches are used to turn on and off the shunt capacitor units (without firing angle control), unlike shunt reactors, to provide the necessary step change in the reactive power supplied to the system. The shunt capacitors cannot be changed continuously with variable firing angle control. Basic structure of a TSC is shown in Figure 5.

Generally single or more than one TSC structure is connected to the same load bus in parallel (the reactive power values of TCS are chosen approximately equal to each other). As the demand for reactive power increases, the thyristors are triggered and the required number of TSCs are activated. We can say that TSCs are commissioned in sequence step by step.

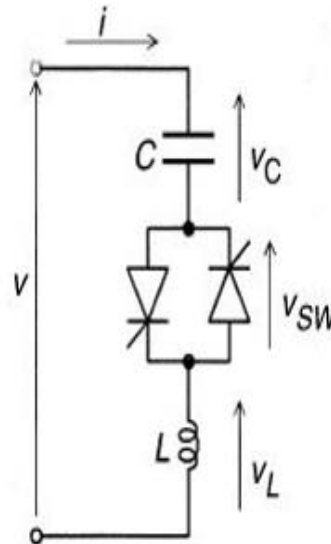


Figure 5. Basic structure of a TSC [4]

The operating logic of the TSC is done by switching on and off the capacitor, which is pre-charged to the peak value of the source voltage [14]. Under steady-state conditions, when the TSC branch is connected to a

sinusoidal AC voltage source $V(t) = V\sin\omega t$ and the thyristor valve is closed, the current in the branch is given by (13);

$$i(\omega t) = V \frac{n^2}{n^2-1} \omega C \cos \omega t \quad (13)$$

$$n = \sqrt{\frac{X_C}{X_L}} \quad (14)$$

$$V_c = V \frac{n^2}{n^2-1} \quad (15)$$

4. Simulation Studies

In this paper, in order to analyze a static VAr compensator behavior which consist of a TCR and 3 TSC Matlab/Simulink program used. Modeled SVC system single line diagram is shown in Figure 6.

The SVC connected to 154 KV, 50 Hz, 6000 MVA short circuit level transmission line with a 154KV/15.8 KV, 85 MVA coupling transformer. SVC consist of a 100 Mvar TCR bank and three 80 Mvar TSC banks (TSC_1 , TSC_2 , TSC_3) connected on the secondary side of the transformer.

Here, with the SVC, 3 TSCs are controlled 240 MVar (each of them has 80 MVar capacity) capacitive reactive power and a TCR 100 MVar inductive reactive power. This means that the control field of the SVC is 100MVar inductive and 240 MVar capacitive. Therefore the working area of the system is between +240 MVar / -100 MVar. As seen from the single-line diagram, the SVC system was installed on the secondary side of the transformer.

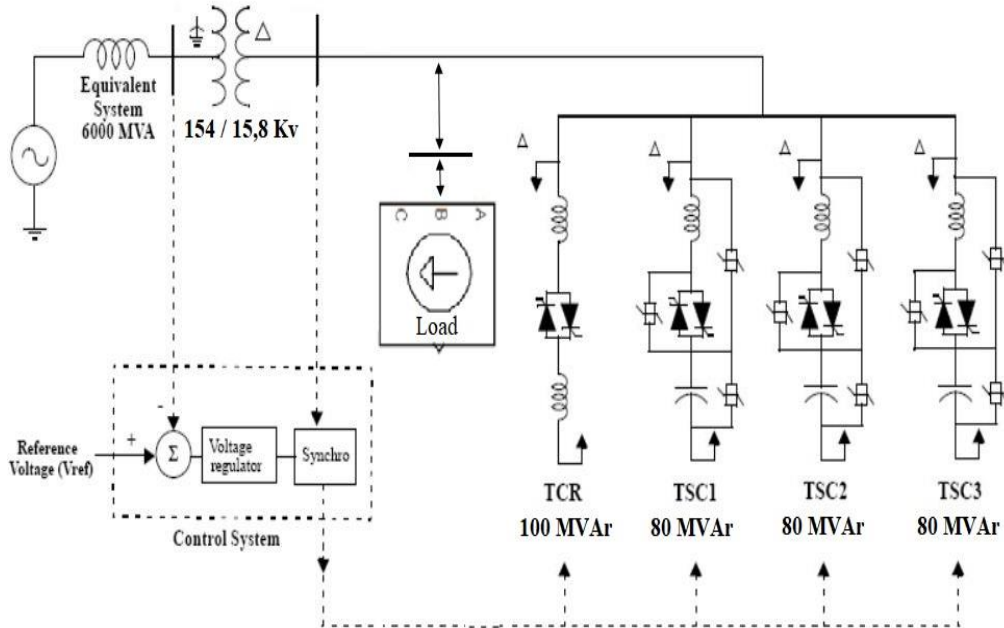


Figure 6. Modeled SVC system single line diagram.

When the thyristor controlled reactor is activated, it is ensured that the triggering angle of TCR is above 90° . In this way, the formation of DC current is prevented from the connections of the thyristors which connected opposite to each other. On-off controls of TSCs have been made compatible with the TCR. In this way, synchronous operation of the system is provided.

Besides in this paper, a dynamic load which has 55-40MW active power and 6-10 MVar reactive power capacity used in order to see SVC behavior under the dynamic load condition. Modeled dynamic load swings as its stated Figure 7 and Simulink model of designed system is shown in Figure 8.

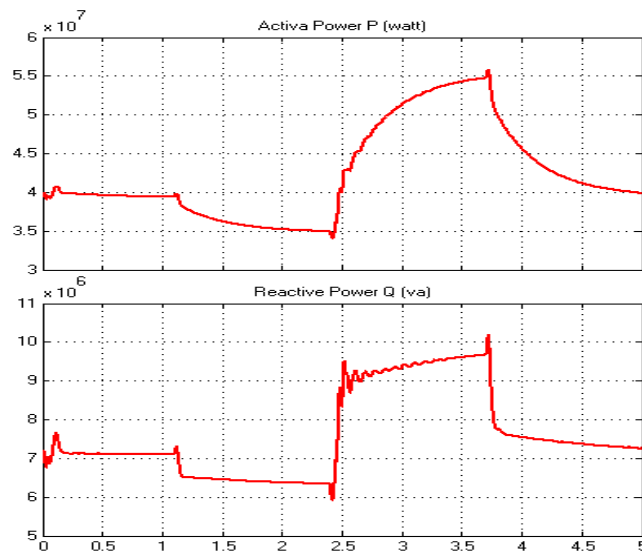


Figure 7. Dynamic load active and reactive capacity swings.

In the designed model, SVC controller block monitors the primary voltage and sends appropriate pulses to the all thyristors bank in order to obtain the susceptance required by the voltage regulator. For one phase TCR and TSC thyristors banks are shown in the Figure 9 a. and 9 b. respectively and designed SVC system controlling unit is shown in Figure 10.

Total 24 thyristors are controlled in the modeled system. There are 6 thyristors in each phase and the thyristors are activated with the appropriate firing pulses in order to produce the required susceptance value in the voltage regulator section.

Measurement system: measures the voltage of the primary side of transformer. This system calculates the fundamental voltage value using a discrete fourier transform in a single-count window to calculate the fundamental voltage value. This unit is controlled by PLL (phase locked loop) to take into account the changes in system frequency.

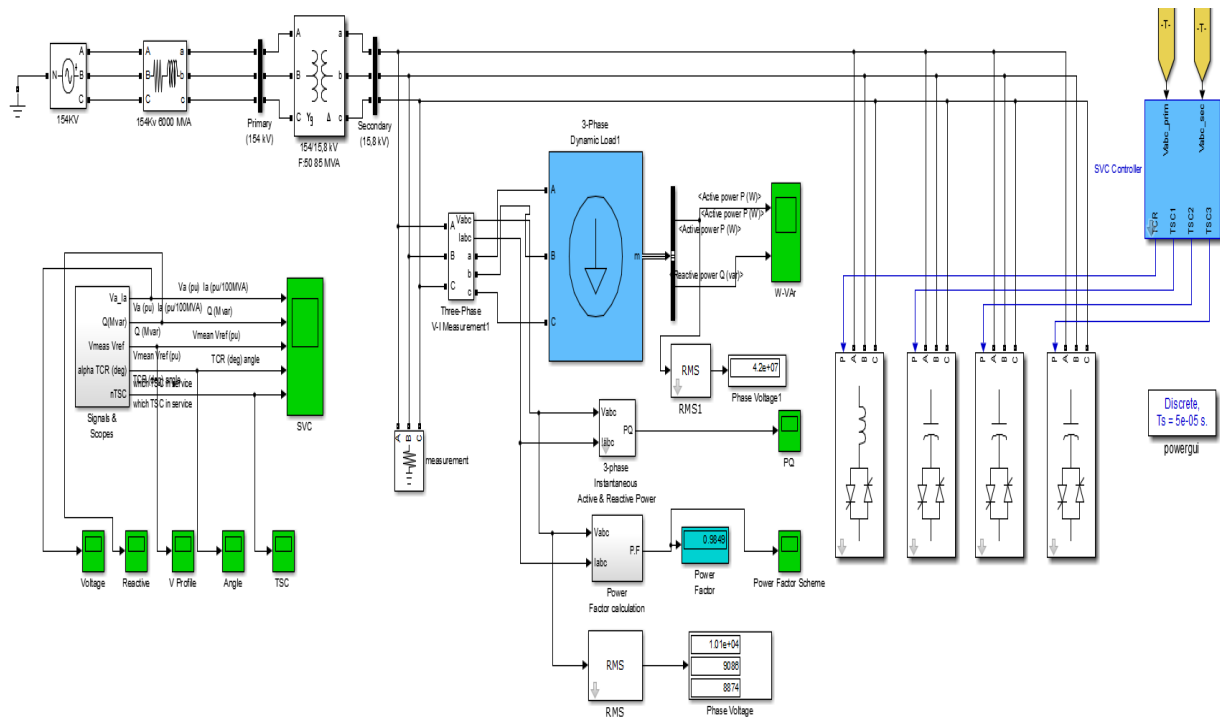


Figure 8. Simulink model of designed system

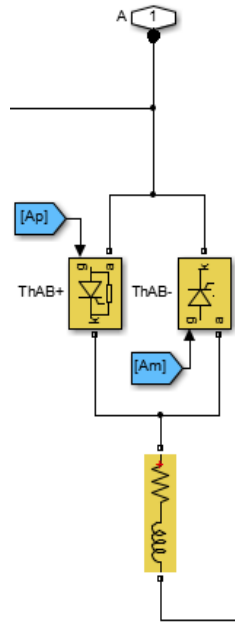


Figure 9 a. TCR bank

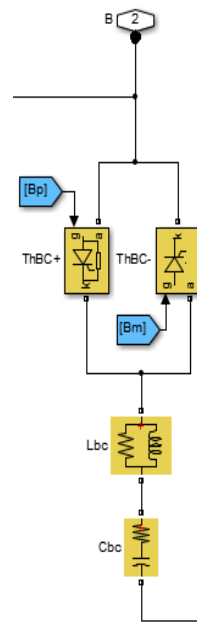


Figure 9 b. TSC bank

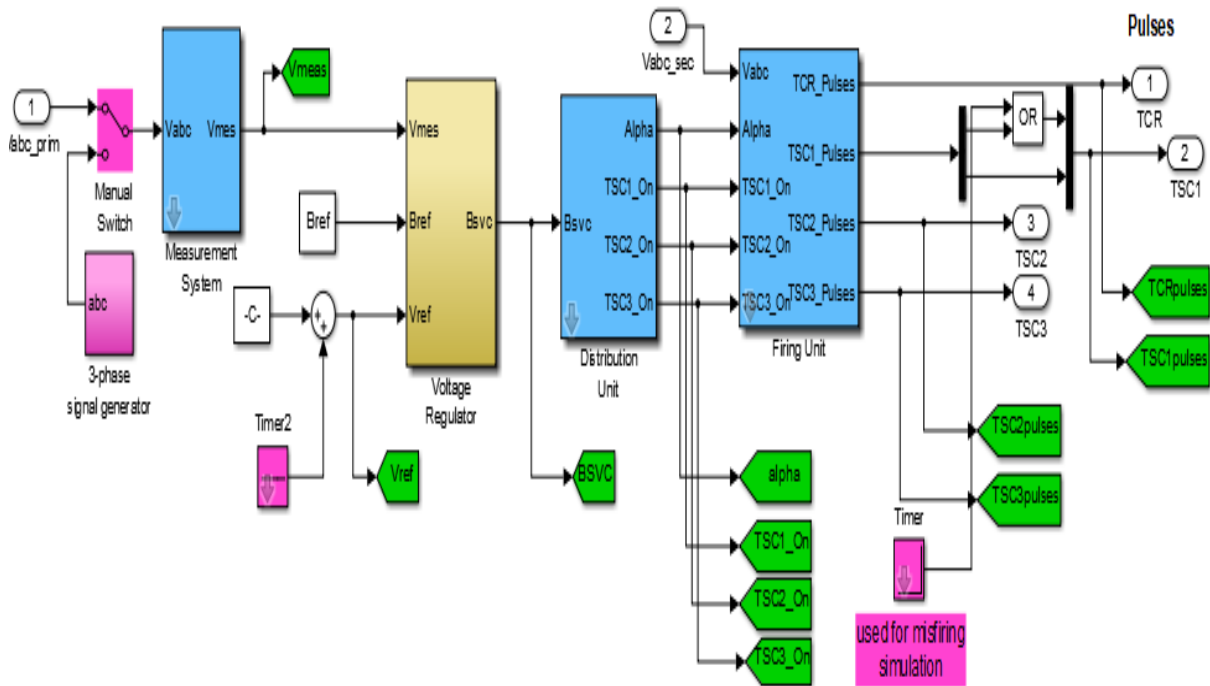


Figure 10. Designed SVC system controlling unit [15].

Voltage regulator: This unit regulates primary side voltage regulation through PI regulator.

Distribution Unit: Uses B_{svc} , the susceptance that calculated by the voltage regulator to determine the triggering angle α and the three TSC's on-off status.

Firing Unit: This unit consists of three independent subsystems, which are AB, BC and CA where one for each phase. Each subsystem consists of a pulse generator for each of the TCR and TSC branches and a PLL synchronized to line-line secondary voltage. Pulse generators generate pulses by using the triggering angle α and

the TSC on / off information which coming from the distribution unit. Designed SVC system firing unit is shown in Figure 11.

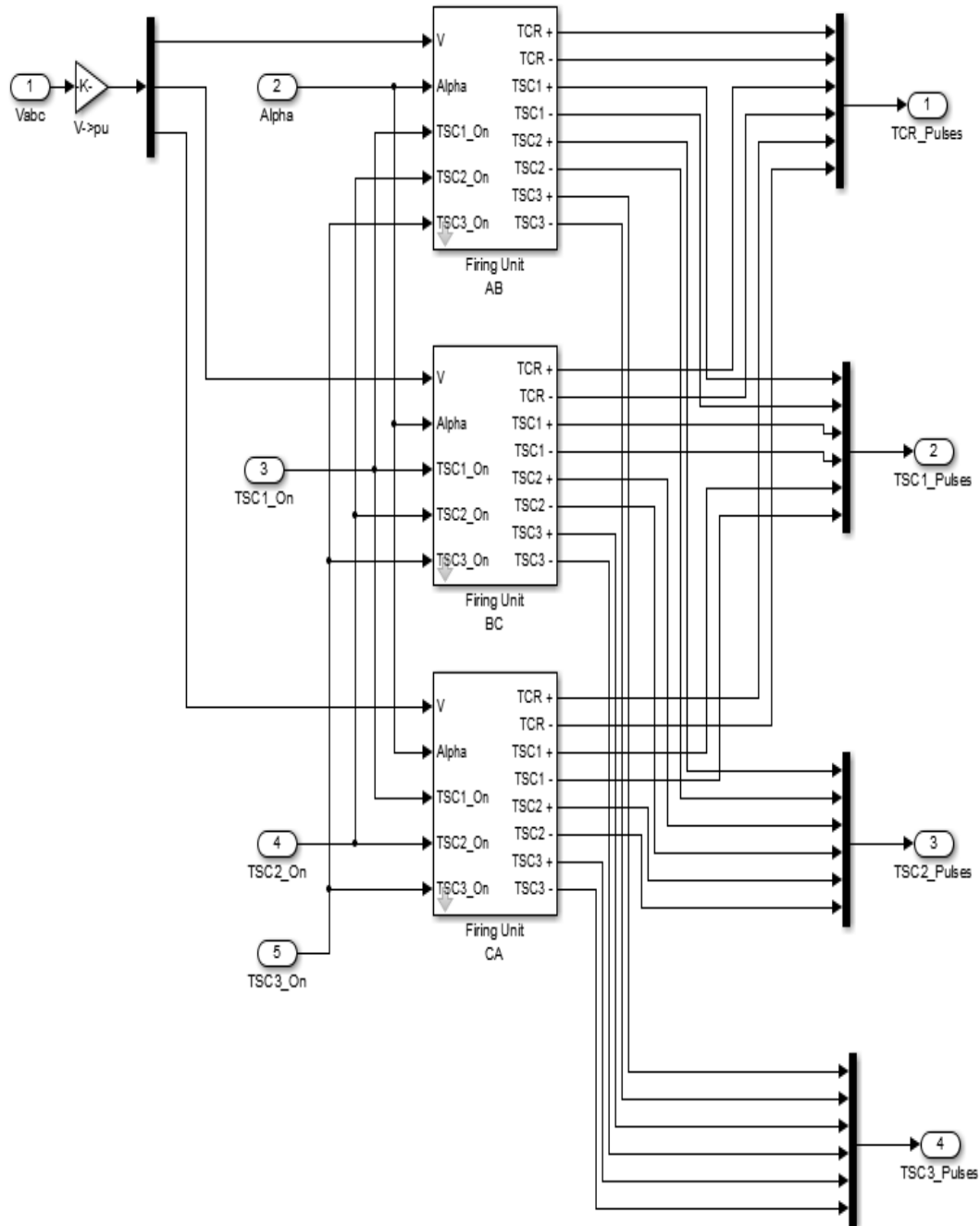


Figure 11. Designed SVC system firing unit [15].

5. Simulation Results

In this study, the simulation time set to 5 seconds. In addition, the adjustable voltage source is arranged according to the values in Table 1. Simulation results are shown in Figure 12 a, b, c, d, e.

Table 1. Programmable voltage source parameter values

Disturbance moment (s)	0	1.1	2.4	3.7	5
Corresponding voltage (p.u.)	1,0	1,06	0,93	0,98	1,0

Modelling a Static VAr Compensator consist of TCR and TSC

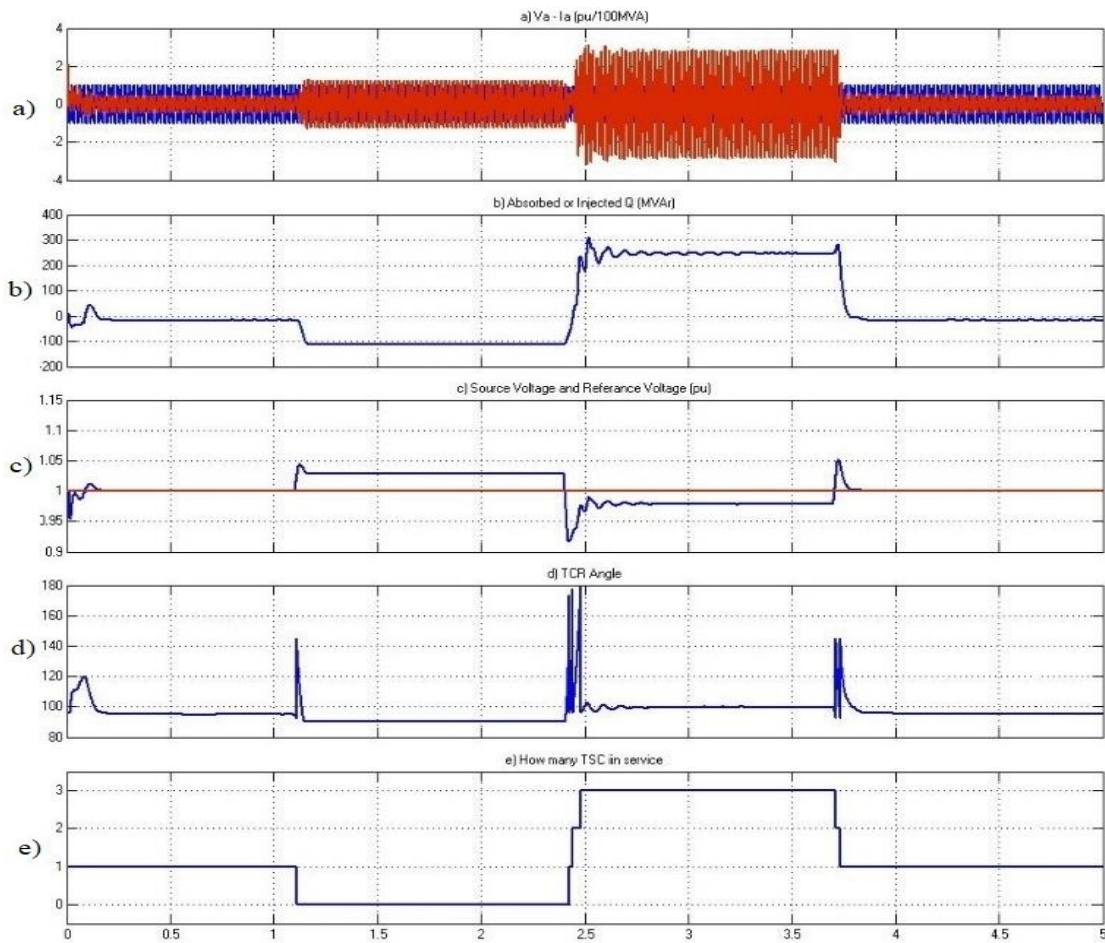


Figure 12. Simulation results a) Transformer primary side voltage and current b) SVC reactive power response c) Reference and source voltage condition d) Firing angle of TCR e) Number of TCS conduction condition

When the results of the simulation are examined at 1,1. seconds; the source voltage suddenly increases to 1.05 Pu. At this point it is seen that the Static VAr compensator compensates the voltage to the value of 1,03 pu by switching on the TCR with absorbing 90 Mvar reactive power. At this point all TCS are out off service.

The source voltage is suddenly decreases to 0.93 pu at 2.4. seconds. The SVC generates approximately 300 MVar reactive power, increasing the voltage to 0.98 pu. At this point, all TSCs are activated gradually within 0.1 seconds. The TCR absorbs approximately 40% of the nominal reactive power ($\alpha = 100$ degrees).

Figure 12. d and e show how TSCs are opened and closed in sequence. Each time a TSC is switched on. The TCR angle α , changes from 90 degrees (full conduction) to 180 degrees (no conduction).

Finally, as shown in Figure 12 c., the voltage is increased to 1.0 pu and the SVC reactive power is reduced to zero at 3,7. seconds.

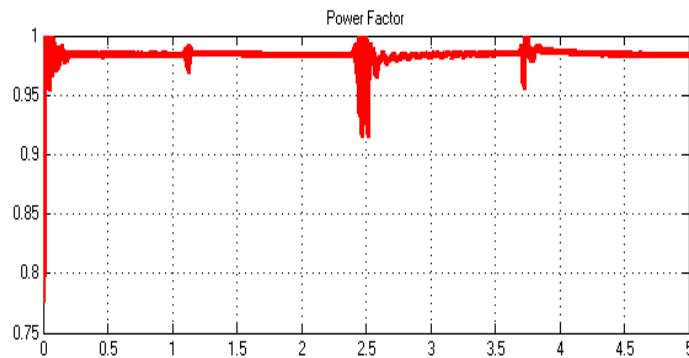


Figure 13. Measured system power factor

As it seen that Figure 13 with SVC system average power factor (φ) has increased to 0,99. This an important improvement for the secondary side voltage of transformer [16].

With these simulation results, we prove that static VAR compensation systems can solve many problems such as power factor correction, active-reactive power problems in power systems.

6. Conclusion

For the control of the parameters of the power transmission system in conventional power systems the methods used are sometimes insufficient in dynamic system conditions. Therefore, it is necessary to ensure that the system is adapted to the new conditions by intervening rapidly and effectively in the power system under dynamic conditions.

Static VAR compensator systems compensates the reactive power in the system by using modern power electronics and control systems where reactive power is needed or where reactive power is required. By using static VAR compensation systems, quality and reliability are increased in power networks, and in an inductive and capacitive region, an effective compensation process is performed in a shorter time than classical compensation systems.

In this study, modeling system with Matlab/Simulink environment simulations revealed that static VAR compensator provides voltage regulation, corrects the power factor and prevents the need for reactive power supply from the grid and prevents unnecessary capacity increase and consequently additional costs.

References

- [1] Tukur. A, "Simulation and Analysis of Static Var Compensator with Matlab," The International Journal of Engineering and Science, Volume 4, Issue 12, PP -07-11, 2015.
- [2] Hingorani N.G and Gyugyi, L., "Understanding FACTS: concepts and technology of flexible AC transmission systems," IEEE Press, New York, 2000.
- [3] Kıyan. M, "Implementation of a low voltage thyristor controlled reactor based var compensator," Msc Thesis, Hacettepe University, 2010.
- [4] Mathur. R, and Varma. R. K, "Thyristor-Based FACTS Controllers for Electrical Transmission Systems," Wiley-IEEE Press, USA, 2002.
- [5] Çitci. A, "Voltage stability analysis based energy function of electrical power systems incorporating facts devices," Phd Thesis, Sakarya University, 2015.
- [6] Esfahani. M. T, Vahidi. B, "Electric arc furnace power quality improvement by applying a new digital and predicted-based TSC control," Turkish Journal Elec Eng & Comp Science, 2016.
- [7] M. A. Rahman and M. S. Islam, "Voltage Control and Dynamic Performance of Power Transmission Using Static VAR Compensator," International Journal of Interdisciplinary and Multidisciplinary Studies, Vol 1, No.4, 141-151, 2014.
- [8] A. Garg and S. K. Agarwal, "Modeling and Simulation of Static Var Compensator for Improvement of Voltage Stability in Power System," International Journal of Electronics Communication and Computer Engineering, Volume 2, Issue 2, 2011.
- [9] M. H. Shwehdi and A. H. Mantawy, "Investigation of Electrical Load Disturbances Influences on Steel Factory Production Lines," International Journal of Education and Research Vol. 7 No. 1 January 2019
- [10] C. S. Chen, H. J. Chuang, T. Hsu and S. M. Tseng, "Mitigation of Voltage Fluctuation for an Industrial Customer with Arc Furnace," Power Engineering Society Summer Meeting, Conference Proceedings, 2001.
- [11] M. G. Hemeida, H. R. Hussien and M. A. Abdel Wahab, "Stabilization of a Wind Farm Using Static VAR Compensators Based Fuzzy Logic Controller," Advances in Energy and Power 3(2): 61-74, 2015.
- [12] Vishwakarma. A.K., Dhaneshwari Sahu. D., "Efficient Voltage Regulation in Three Phase A.C. Transmission Lines Using Static VAR Compensator", International Journal of Advanced Research in Electrical, Electronics and Instrumentation Engineering Vol. 2, Issue 5, May 2013.
- [13] Kundur. P, "Power system stability and control," Mc Graw-Hill Inc, Toronto, 1994.
- [14] Gelen. A, and T. Yalçınöz, " The behavior of thyristor switched capacitor installed in an infinite bus system," The IEEE Region 8 Eurocon Conference, pp. 629-632, Saint-Petersburg, Russia, 2009.
- [15] <https://www.mathworks.com/help/physmod/sps/ug/svc-detailed-model.html> (5.10.2020)
- [16] Turan. O, "Investigation of the effect of flexible alternative current transmission system devices on stability in symmetric and asymmetric failure," Msc Thesis, Sakarya University, 2019.

4×4 Knight's Graph Analysis by Modularity: A Knight Graph Application

Serkan GÜLDAL^{1*}

¹ Department of Physics, Faculty of Arts and Sciences, Adiyaman University, Adiyaman, Turkey
*sguldal@adiyaman.edu.tr

(Geliş/Received: 27/03/2020;

Kabul/Accepted: 21/10/2021)

Abstract: Modularity is a well-known technic to analyze datasets that are in the form of graphs. The modularity divides the network into clusters concerning the connections between nodes. The clusters present the existence of shared properties between the nodes in the same clusters. In the present study, we analyze the 4×4 knight's graph by modularity to seek the relation with Knight Covering Problem solutions (for the specified problem a.k.a. 4-KCP). Our investigation is completed for resolutions from 0.2 to 3.2. The maximum modularity score is 0.417 which is found for the resolution = 0.6, 0.8, 1, and 1.4. Moreover, resolution 1.4 is the optimum resolution to find some solutions of 4-KCP. Also, the analyses show that resolution 0.2 is the best resolution to find all solutions of 4-KCP since it approximates the permutation algorithm.

Keywords: Knight's graph; modularity, 4-KCP

Modülerlik ile 4×4 At Graf Analizi: At Graf Uygulaması

Öz: Modülerlik graf biçimli verilerin analizinde iyi bilinen bir tekniktir. Modülerlik düğümler arasındaki bağları göz önünde bulundurarak anlamlı gruplara ayırır. Gruplar aynı gruptaki düğümler arasındaki ortak özelliklerin varlığını tanımlar. Bu çalışmada At Kaplama Problem çözümleri ile 4×4 at grafını (bu çalışmada tanımlan problem için kısaca 4-KCP) modülerlik analizi arasındaki ilişkiyi araştırıyoruz. Araştırmamız çözünürlüğün 0.2 ile 3.2 olduğu aralık için tamamlandı. Maksimum modülerlik puanı 0.417'dir ve bu modülerlik puanı 0.6, 0.8, 1, ve 1.4 çözünürlükleri için hesaplanmıştır. Buna ek olarak 1.4 4-AKP'nin bazı çözümlerini bulmak için ideal çözünürlüktür. Ayrıca, analizler 0.2 çözünürlüğünün permutasyon metoduna yakınsadığından dolayı 4-AKP'nin tüm çözümleri bulmak için en iyi çözünürlük olduğunu gösterdi.

Anahtar kelimeler: At grafi; modülerlik, 4-AKP

1. Introduction

The moves of a knight on the chess introduces surprise attacks against to opponent beyond the regular moves such as jumping over pieces. The generated problems by knights movements on the board have been subject to the many types of research, for instance, the knight's tour problem is investigated to obtain a solution [1-3]. The moves are used for encryption images [4-6]. Additionally, to position a certain number of knights on a board based on the movements which are the various versions of the Knight Covering Problem (KCP) [7-14]. There are methods are developed to solve by the means of the knight graph to find solutions for knight covering problems such as the independent set [15, 16] and the Girvan-Newman clustering algorithm [17].

The network analyses are intensively utilized to extract information in data networks such as social networks [18-20], computational networks [21-23], word networks [24-26], biological networks [27-29], infection networks [30, 31]. There are plenty of analysis methods such as statistical analysis, power graph analysis, visual analysis, and clustering. Clustering divides the whole network to clusters of the nodes. The clusters present the common properties of nodes in the same cluster. The clustering method is one of the first attempts to understand the considered graph since it generates intuitive results in a computationally efficient manner. There are various clustering algorithms based on the properties of the network. For example, the Girvan-Newman algorithm uses edge betweenness, Highly Connected Clusters uses graph connectivity, k-means clustering uses the mean value, and Modularity uses the strength of division of a network into modules (a.k.a. clusters). The modularity algorithm has flexibility based on the resolution for different graphs. Higher resolutions divide the network to greater clusters and lower resolutions are otherwise. The optimum resolution changes respect to the network and the intent. We intend to understand the response for various resolutions in the search of 4-KCP solutions. Thus, we have investigated a range of resolutions to obtain the resolution which is computationally most efficient and extracts all solutions of 4-KCP.

In the present study, the knight graph illustration of 4-KCP is investigated by the modularity of the graph. 4-KCP has 16 cells to be occupied by the knights (See **Figure 1**). The cells on the corners can attack 2 cells. The cells

* Corresponding author: sguldal@adiyaman.edu.tr. ORCID Number of authors: 1 0000-0002-4247-0786

on the edges can attack 3 cells, and the cells in the middle can attack 4 cells. Additional to cells which knight attacks, an extra cell is occupied by the particular knight.

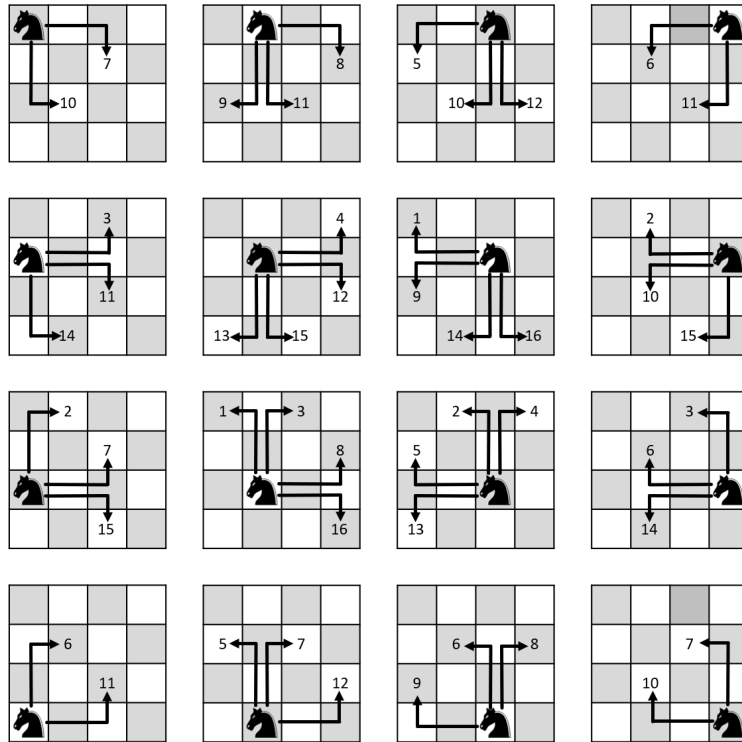
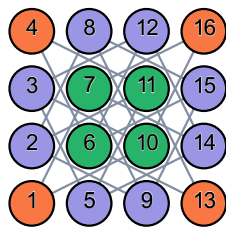


Figure 1. 4-KCP has 16 cells to place the knight

4-KCP board is indexed and presented color-coded respect to the degree of each node in Figure 2. 4-KCP is the graph which has 16 nodes and 24 edges. There are nodes with 2, 3 and 4 degrees. They are the portion of the whole graph respectively 25%, 50%, and 25%. The knights on the corner cells (orange) can attack to 2 cells located in the center. The cells on the edges (purple) with 3 degrees can attack 2 cells on the edges and 1 cell on the center. The cells on the center can attack 4 cells which are 2 of them on the edges and 2 of them on the corners (see Figure 1).



Color code	Degree	Percentage in the graph (%)
●	2	25
●	3	50
●	4	25

Figure 2. 4-KCP graph is shown by the degrees of nodes

Many algorithms are built on knight graphs to solve N-KCP [15]. The algorithms use the graph theory properties such as the independent set. In Figure 3, the solutions of 4-KCP are found by the independent set algorithm. In the presented solutions exactly 4 knights are placed to cover 4x4 board. The found solutions are rotationally symmetric. With similar utilization of graphs, in this study, we use modularity to analyze the 4-KCP graph to find solutions. The network analysis method divides the 4-KCP graph into densely connected clusters. The clustered nodes show a strong relationship between the knights. Thus, they highlight the knights which are less likely to be in the same solution. The details of the modularity and the algorithm is discussed in the following sections.

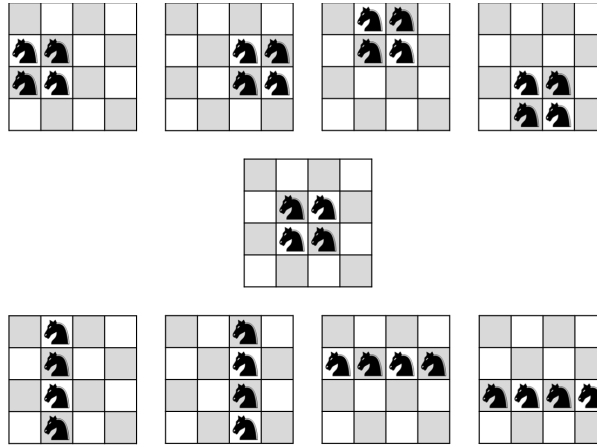


Figure 3. 4-KCP solutions by 4 knights only

2. Modularity

In the present study, we used the modularity to identify the close connected knights for the 4-KCP problem. The modularity score is formulated by various formulas. The formula which is utilized is as follows [32]:

$$Q = \frac{1}{2m} \sum_{i,j} \left(A_{ij} - \gamma \frac{k_i k_j}{2m} \right) \delta(c_i, c_j) \quad (1)$$

where δ -function is 1 if $c_i = c_j$; in other words, node i and j are in the same cluster. m stands for the number of edges in the graph. γ is the resolution. k_i is the degree of node i and k_j is the degree of node j . A_{ij} represents the weights of the edge between nodes i and j . It is the same for all since the effect of all knights is equal.

Our analysis is completed by the Gephi [33-35]. We applied the resolution from 0.2 to 3.2. The implementation and analysis will be given in the Results and Discussion section.

3. Results and Discussion

In the present study, we have investigated the relational information of the 4-KCP graph by modularity score. There are extracted communities from 1 to 8 respect to resolution.

The modularity phenomena built on the strong relationships between nodes. On the other hand, the N-KCP solutions are to place the knight which has weak/no relations. Thus, the extracted clusters show the list of positions that are the least likely to be in the same solution.

In **Figure 4**, modularity results on 4-KCP (for resolution = 0.2 - 3.2) graphs are presented. The resolution 3.2 is extracted 1 cluster in **Figure 4.p**. Thus, in the generated solutions shows that no two nodes could be included simultaneously in a solution. Also, there is no solution by one knight, so 17 permutations which include no knight are not solutions for 4-KCP. In **Figure 4.o**, 2 clusters are generated which are (1, 2, 7, 8, 9, 10, 15, 16) and (3, 4, 5, 6, 11, 12, 13, 14). Similarly, 2 nodes / 2 knights solutions do not exist for 4-KCP. 80 combinations of the two clusters are not the solutions. Likewise, modularity application for resolutions = 2.8, 2.6, 2.4, 2.2, 2.0, 1.8, and 1.6 cannot generate 4-KCP solutions. For the resolution = 1.4 in **Figure 4.g**, the 4-KCP graph is divided into 4 clusters. 8 out of 9 solutions with the length of 4 are generated by the permutation 499 combinations (See **Table 1**).

Table 1. The solution generated by modularity application for the resolution 1.4. 8 out of 9 solutions for length 4 are generated.

(2, 3, 6, 7)	(5, 6, 7, 8)	(7, 8, 11, 12)
(2, 6, 10, 14)	(5, 6, 9, 10)	(9, 10, 11, 12)
(3, 7, 11, 15)	(6, 7, 10, 11)	(10, 11, 14, 15)

3 clusters are introduced by the resolution 1.2, and there is no such solution with length 3. For the resolutions 1.0, 0.8 and 0.6, 4 clusters are generated. This modularity is similar to resolution 1.4, so the generated solutions. The modularity is divided into 6 clusters for the resolution 0.4. Clusters make 2159 combinations length varies from 1 to 6. This generates 13 solutions of 4-KCP.

The modularity by resolution 0.2 divides the particular graph to 8 clusters. The number of permutations is 6560 length varies from 1 to 8. This permutation includes all 31 solutions of 4-KCP.



Figure 4. Modularity is applied to 4-KCP graphs for various resolutions from 0.2 to 3.2

The applied modularity for various resolutions divided the 4-KCP graph to the various number of clusters. In **Figure 5**, pie charts are shown which are greater to highlight the direction of the increasing number of clusters. The decreasing resolutions divide the network into smaller clusters. The increasing number of clusters more likely to generate 4-KCP solutions. In **Figure 6**, the number of permutations is compared with the number of solutions for the resolution from 0.2 to 3.2. There are no solutions obtained for the resolutions 1.6-3.2. Similarly, resolution 1.2 divides the 4-KCP graph to insufficient clusters. The resolutions 1.4 (number of permutations = 499) and 0.6-1 (624) generates 8 solutions. Resolution 1.4 generates the same number of solutions by less number of permutations. Thus, resolution 1.4 extracts relatively more meaningful clusters. All the solutions are obtained by the maximum number of permutations. The maximum number of permutations are generated for resolution 0.2. The 4-KCP graph is divided into 8 clusters with two nodes for each. Thus, it approximates the permutation solution algorithm [15]. It is computationally more efficient than permutation solutions since reduces the number of permutations. Thus, we conclude the existence of an explicit correlation between generated permutations and related solutions.

Based on the modest comparison of the number of generated permutations with the number of found solutions, the computational efficiency of clustering is obtained with respect to the resolution in **Figure 7**. The computational efficiency is calculated as:

$$\text{Efficiency of the cluster} = \frac{\text{Number of found solutions} * 100}{\text{Number of permutations}} \quad (2)$$

Resolution 0.2 introduces the best clustering which obtains all solutions, but it is not computationally efficient (0.47256) because the highest number of permutations are generated. The most computationally efficient resolution is 1.4 by 1.60321. It finds 8 solutions by 499 permutations. All clustering could not identify a solution. Between the clusters which find a solution, resolution 0.4 is the least efficient (0.60213) since it finds 13 solutions in 2159 permutations.



Figure 5. Increase resolution causes to decrease to the number of communities for 4-KCP graph

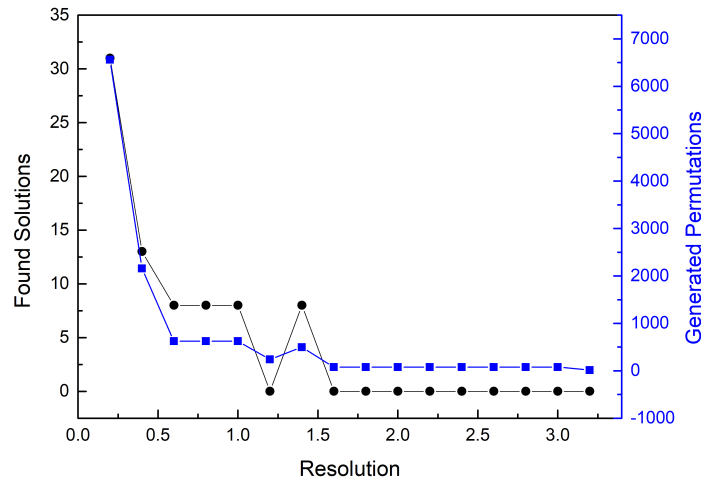


Figure 6. (Color online) Generated permutations have correlations with the found solutions

The modularity score which identifies the quality of clustering has no explicit correlation with the number of found solutions for the specified resolutions (**Figure 6** and **Figure 8**). The highest modularity score is 0.417 (for resolution = 0.6, 0.8, 1, and 1.4). Thus, clustering presents the best sub-communities.

Resolution 1.4 identifies computationally as the most efficient clustering to find solutions with fewer permutation. However, all solutions are found for resolution 0.2 which is the computationally least efficient between the clusters that can lead to some solution.

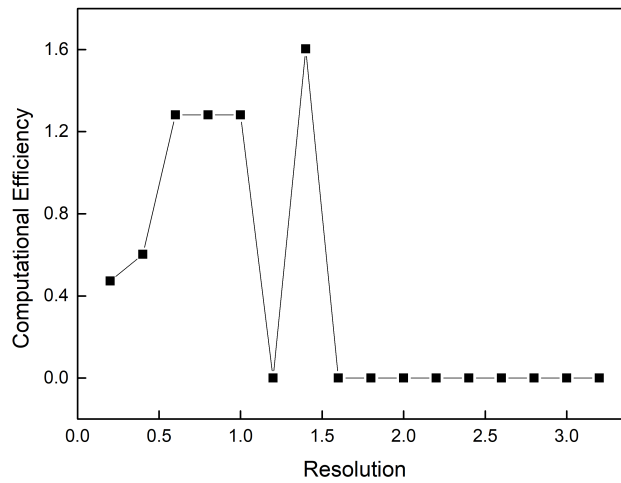


Figure 7. Computational efficient clustering is obtained by resolution 1.4. However, all solutions are obtained by the resolution 0.2 which is the computationally least efficient resolution between the solutions found

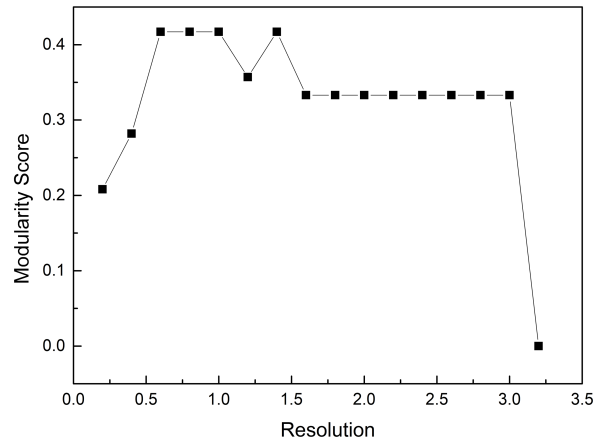


Figure 8. Modularity score versus Resolution

4. Conclusion

In this study, we have applied the Modularity 4×4 knight graph. Thus, an analysis is applied to solve the Knight Covering Problem (N-KCP). Our analysis is limited to the 4-KCP graph. The analyses show resolution 1.4 is the computationally optimal resolution to find some solutions of 4-KCP. Moreover, the analysis shows resolution 0.2 is the best resolution to find all solutions of 4-KCP.

Based on our analysis, the modularity is a promising method to solve N-KCP. Thus, in future studies, the analyses will be extended around the N-KCP with modularity.

5. Acknowledgment

The authors declare no conflict of interest.

References

- [1] S. Bai, G. Zhu, and J. Huang, "An Intelligent Algorithm for the (1,2,2)-Generalized Knight's Tour Problem," in *2013 Ninth International Conference on Computational Intelligence and Security*, 2013, pp. 583-588.
- [2] H. Jian and B. Sen, "An Efficient Algorithm for the Generalized (1,k)-Knight's Tours Problem," in *2009 First International Workshop on Education Technology and Computer Science*, 2009, vol. 1, pp. 697-701.

- [3] S. Bai, X. Liao, X. Qu, and Y. Liu, "Generalized Knight's Tour Problem and Its Solutions Algorithm," in *2006 International Conference on Computational Intelligence and Security*, 2006, vol. 1, pp. 570-573.
- [4] A. Philip, "A Generalized Pseudo-Knight's Tour Algorithm for Encryption of an Image," *IEEE Potentials*, vol. 32, no. 6, pp. 10-16, 2013.
- [5] J. Kumar and S. Nirmala, "Securing the contents of document images using knight moves and genetic approach," in *2015 International Conference on Advances in Computing, Communications and Informatics (ICACCI)*, 2015, pp. 1091-1095.
- [6] J. Delei, B. Sen, and D. Wenming, "An Image Encryption Algorithm Based on Knight's Tour and Slip Encryption-Filter," in *2008 International Conference on Computer Science and Software Engineering*, 2008, vol. 1, pp. 251-255.
- [7] D. C. Fisher, "On the $n \times n$ Knight Cover Problem," *Ars Comb.*, vol. 69, / 2003.
- [8] F. Rubin, "Improved Knight Coverings," *Ars Comb.*, vol. 69, / 2003.
- [9] F. Rubin, "Knight Covers for the 50x50 Chessboard," presented at the Mathfest 2004, Providence RI, 2004.
- [10] F. Rubin, "A Family of Efficient Knight Covering Patterns," *Journal of Recreational Mathematics*, Article vol. 33, no. 3, pp. 165-175, 2005.
- [11] F. Rubin, "An Improved Method for Finding Knight Covers," *Ars Comb.*, vol. 82, / 2007.
- [12] B. Lemaire, "Knights Covers on $N \times N$ Chessboards," *J. Recr. Math.*, vol. 31, pp. 87-99, 2003.
- [13] A. H. Jackson and R. P. Pargas, "Solutions to the $N \times N$ Knights Covering Problem," *J. Recr. Math.*, vol. 23, pp. 255-267, 1991.
- [14] F. Wei, "Research on Knight Covering Based on Breadth First Search Algorithm," (in English), *APPLIED MECHANICS AND MATERIALS*, vol. 686, pp. 377-380, 2014.
- [15] S. Güldal, M. Lipscomb, and M. M. Tanik, "Solving Knights Covering Problem: Backtracking, Permutation, Bipartite Graph, and Independent Set," presented at the Nineteenth Annual Early Career Technical Conference, Birmingham, Alabama USA, 2019
- [16] S. Güldal, M. M. Tanik, and M. M. Lipscomb, "Solving Knights Covering Problem by a Hybrid Algorithm," presented at the IEEE SouthEastConn, Huntsville, Alabama, April 11 - 14 2019,
- [17] S. Güldal, "Connectives of Knights Covering Problem By Girvan-Newman Clustering," presented at the SDPS 2019 Workshop, Madrid, Spain, 25-26, November 2019,
- [18] M. Gençer, "Sosyal Ağ Analizi Yöntemlerine Bir Bakış," *Yildiz Social Science Review*, vol. 3, pp. 19-34, 12/15 2017.
- [19] P. Nerurkar, M. Chandane, and S. Bhirud, "Understanding attribute and social circle correlation in social networks," *Turkish Journal of Electrical Engineering and Computer Sciences*, vol. 27, pp. 1228-1242, 03/22 2019.
- [20] N. Almolhem, Y. Rahal, and M. Dakkak, "Social network analysis in Telecom data," *Journal of Big Data*, vol. 6, 12/01 2019.
- [21] "Analysis of the Application of Artificial Intelligence in Computer Networks Technology," *IOP Conference Series: Materials Science and Engineering*, vol. 750, p. 012097, 03/24 2020.
- [22] C. Engström and S. Silvestrov, "PageRank for networks, graphs, and Markov chains," *Theory of Probability and Mathematical Statistics*, vol. 96, p. 1, 10/05 2018.
- [23] Y. L. Karpov, I. Volkova, A. A. Vylitok, L. Karpov, and Y. G. Smetanin, "Designing classes' interfaces for neural network graph model," *Proceedings of the Institute for System Programming of RAS*, vol. 31, pp. 97-112, 10/01 2019.
- [24] L. Johnsen, "Graph Analysis of Word Networks," <http://ceur-ws.org/Vol-2021/>, vol. 2021, 01/01 2017.
- [25] E. Hasanah and D. Agustini, "Analysis of 'Halal' Word in Social Media Using Text Mining and Word Networking." 2020.
- [26] R. Ozcelik, G. Uludoğan, S. Parlar, Ö. Bakay, O. Ergelen, and O. Yildiz, *User Interface for Turkish Word Network KeNet*. 2019, pp. 1-4.
- [27] K. Kugler, L. Mueller, A. Graber, and M. Dehmer, "Integrative Network Biology: Graph Prototyping for Co-Expression Cancer Networks," *PloS one*, vol. 6, p. e22843, 07/29 2011.
- [28] B. Eckman and P. Brown, "Graph data management for molecular and cell biology," *IBM Journal of Research and Development*, vol. 50, pp. 545-560, 12/01 2006.
- [29] V. Gadiyaram, S. Vishveshwara, and S. Vishveshwara, *From Quantum Chemistry to Networks in Biology: A Graph Spectral Approach to Protein Structure Analyses*. 2019.
- [30] S. Valverde, B. Vidiella Rocamora, R. Montañez Martínez, A. Fraile, S. Sacristán, and F. García-Arenal, "Coexistence of nestedness and modularity in host-pathogen infection networks," *Nature Ecology & Evolution*, pp. 1-10, 03/09 2020.

- [31] T. Shiino, "Phyldynamic analysis of a viral infection network," *Frontiers in microbiology*, vol. 3, p. 278, 07/31 2012.
- [32] M. E. J. Newman, "Analysis of weighted networks," *Physical Review E*, vol. 70, no. 5, p. 056131, 11/24/2004.
- [33] M. Bastian, S. Heymann, and M. Jacomy, "Gephi: an open source software for exploring and manipulating networks," in *International AAAI Conference on Weblogs and Social Media*, 2009.
- [34] V. D. Blondel, J.-L. Guillaume, R. Lambiotte, E. J. J. o. s. m. t. Lefebvre, and experiment, "Fast unfolding of communities in large networks," vol. 2008, no. 10, p. P10008, 2008.
- [35] R. Lambiotte, J.-C. Delvenne, and M. J. a. p. a. Barahona, "Laplacian dynamics and multiscale modular structure in networks," 2008.

The Change of The Magnitude of The Electric Field Vector (E_y/E_0) in The Ionosphere in The Magnetic Equator Through

A.Yeşil¹, O. Özcan¹, M. Inc¹, S. Sağır², K. Kurt¹, L.V. Tsamalashvili³, T.D. Kaladze³, and D.T. Kaladze⁴

¹Firat University, Science Faculty, Elazığ, Turkey

²Department of Physics, Faculty of Arts and Science, Mus Alparslan University, Mus, Turkey

³I. Vekua Institute of Applied Mathematics, I. Javakhishvili Tbilisi State University, 2 University Str., 0186 Tbilisi, Georgia

⁴E. Andronikashvili Institute of Physics, I. Javakhishvili Tbilisi State University, Tbilisi 0128, Georgia

*¹ avesil@firat.edu.tr, ¹ osmanozcan@firat.edu.tr, ¹ minc@firat.edu.tr, ² s.sagir@alparslan.edu.tr,
¹ kadrikurt@hotmail.com, ³ luba_tsamal@yahoo.com, ³ tamaz_kaladze@yahoo.com, ⁴ tamaz_kaladze@yahoo.com

(Geliş/Received: 22/08/2020;

Kabul/Accepted: 17/09/2020)

Abstract: The seasonal changes of (E_y/E_0), which was obtained from the WKB (Wentzel, Kramers, Brillouin) solution, for (-30°N; 30°S geographic latitudes and (390, 410, 450, 500, 550 and 600 Km) altitudes in the equatorial anomaly region were investigated. (E_y/E_0) ratio takes minimum value in latitudes, where the electron density is at maximum levels and takes maximum value in places where the electron density is at minimum levels, respectively. It is possible to say that in places where the electron density is at maximum, the wave transfers energy to the medium, otherwise it receives energy from the medium.

Key words: Ionosphere, WKB, Refractive index, Equatorial Anomaly.

Manyetik Ekvator Bölgesinde İyonosferde Elektrik Alan Vektörünün (E_y/E_0) Büyüklüğünün Değişimi

Öz: Ekvatorial anomali bölgesinde (390, 410, 450, 500, 550 and 600 Km) yüksekliklerinde (30°N; 30°S) coğrafik enlemler için WKB (Wentzel, Kramers, Brillouin) çözümünden elde edilen (E_y/E_0) mevsimsel değişimi araştırıldı. (E_y/E_0) değişimi elektron yoğunluğunun maksimum olduğu yüksekliklerde minimum, maksimum olduğu yerlerde minimum değer almaktadır. Elektron yoğunluğunun maksimum olduğu yerlerde dalgaya ortamdan enerji aktarılmakta, minimum olduğu durumlarda dalgadan enerji ortama aktarılmaktadır.

Anahtar kelimeler: İyonküre, WKB, Kırılma İndisi, Ekvatorial Anormallik.

1. Introduction

Electron density, which is the main backbone that characterizes the ionosphere, depends on parameters inside and outside the ionosphere such as solar activity, geomagnetic activity, geographic latitudes, local time and seasons [1-13; 31-36]. The electron density strongly affects the behavior of the electromagnetic wave in the ionosphere. The reflection of the waves from the ionosphere depends on the refractive index of the medium, the frequency of the wave and the vibration frequencies of the charged particles in the ionosphere. The highest wave frequency reflected from the ionosphere is called the critical frequency. The ionosphere acts like a very lossy medium during the day and a little lossy medium at night. This causes the waves to attenuation by creating differences in medium and long wave propagation [13-36]

F layer, which is the richest region in terms of electron density of ionosphere, exhibits different behaviors as anomalies, seasonal anomaly and semester-year changes, night F2-peak, equatorial anomaly under different time and geographical latitudes. Many anomalies of seasonal change at the value of NmF2 (maximum electron density in the F2 region) were recorded at noon. As a result of the observations, NmF2's winter values were found to be much larger than the summer values at noon. This is in contrast to the expectation that ion and electron production will be very small in winter. This situation is generally called either "seasonal anomaly" or "winter anomaly". Considering the annual change of NmF2 in the ionosphere, the electron density was measured to be 20% higher in December than in June. The Sun is the largest in January due to the change of distance between the Sun and Earth. This is called "annual anomaly" [19-22]. The behavior of the F2 region is quietly different at low latitudes. At some times, the electron density is greater at midnight compared to noon. There is not the vertical diffusion. Because ionization is not distributed from one side of the magnetic field lines of the earth to the other side, it is

* Corresponding author: avesil@firat.edu.tr. ORCID: *¹ 0000-0003-5997-897X, ¹ 0000-0003-3219-146, ¹ 0000-0003-4996-8373, ² 0000-0002-5698-0154, ¹ 0000-0002-6507-8234, ³ 0000-0002-4151-8792

distributed along the field lines. Actually, this distribution affects the latitude distribution of ionization. Besides, it affects the daily change of electron density in electromagnetic drift [1-11, 19-36].

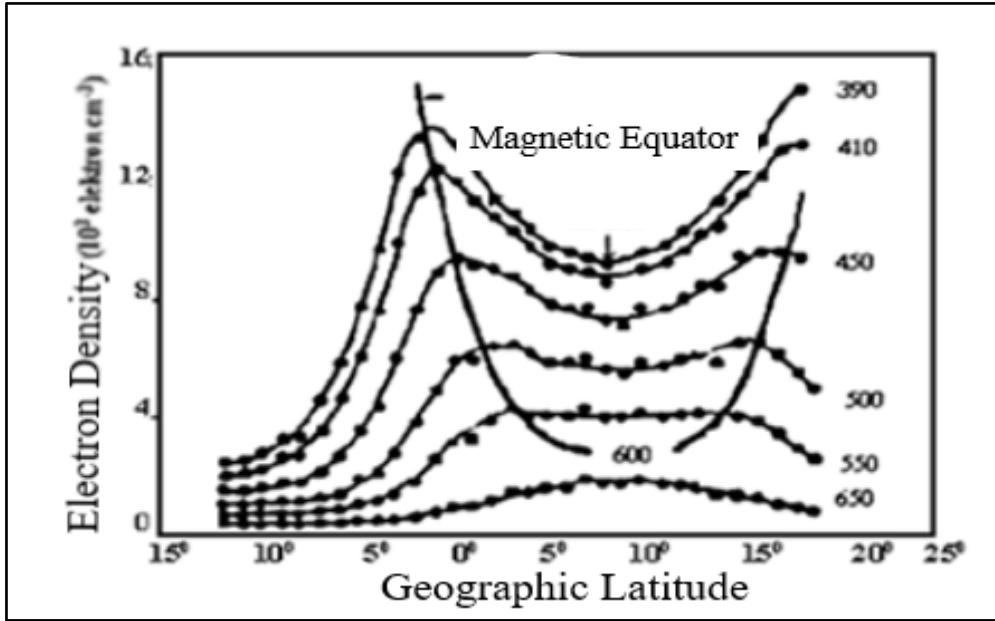


Figure 1. Equatorial peaks and cavities in the northern and southern hemispheres [19, 22].

According to figure 1, the values of NmF2 during the night as a function of the latitude exhibit a condition so-called "cavity" focused on the lowest magnetic point of Equator with "peaks" in 15°-20° latitudes in the northern and southern hemispheres. Electromagnetic drift ($\perp \mathbf{B}$) and diffusion ($\parallel \mathbf{B}$) combine and cause an upward increase in plasma motion like a "fountain". In this way, anomaly peaks are fed from the high regions on the Equator by diffusion. The production rate is very low here. However, plasma is drawn from lower levels around F2-peak, where the production rate is greater [7-11].

By this time, many researchers have conducted theoretical and experimental studies about the reciprocal interaction between electromagnetic wave and ionospheric plasma [3-13]. In this work, the variation of wave amplitude at the equatorial trough for some heights of the F2 region of an electromagnetic wave traveling in the z direction polarized in the y direction "in geographic latitudes where magnetic equatorial trough occurs" was investigated. We used the ordinary wave obtained before for the refractive index (n) of the medium, which is one of the most powerful parameters that characterizes the medium. Because this wave is independent of the magnetic field of the earth and forms the theoretical infrastructure of the working principles of the ionosonde.

2. Wave Equations and Refractive Index of The Plasma

According to Newton law, the force acting on an electron with mass m and velocity \mathbf{V} is described eqn. (1) as follow.

$$m \frac{d\mathbf{V}}{dt} = -e[\mathbf{E} + \mathbf{V} \times \mathbf{B}] - m\nu \mathbf{V} \quad (1)$$

In which, \mathbf{V} ; the velocity of the charged particle, \mathbf{E} and \mathbf{B} are electric and magnetic field, m; mass of particle ν : the collision frequency of electron-other particles, the velocity and fields change in accordance with $e^{i(\mathbf{k} \cdot \mathbf{r} - \omega t)}$. The wave in the northern hemisphere travels in the z direction. The magnetic field of the earth for this condition,

$$\mathbf{B} = B_x \mathbf{a}_x + B_y \mathbf{a}_y + B_z \mathbf{a}_z \quad (2)$$

where $B_x = B \cos I \sin D$, $B_y = B \cos I \cos D$ and $B_z = -B \sin I$. I is the lowest magnetic point and D is the magnetic declination angle. If the equation 2 is written within the equation 1, the current density is obtained as

$$\mathbf{J} = \sigma_0 \mathbf{E} - \frac{e}{m(\nu - i\omega)} \mathbf{J} \times \mathbf{B} \quad (3)$$

where $\sigma_0 = \frac{Ne^2}{m(\nu - i\omega)}$ is the parallel conductivity. According to this equation, if current is used as

$$\mathbf{J} = \sigma \mathbf{E} \quad (4)$$

conductivity tensor σ is obtained.

If Maxwell's equations are used to obtain the refractive index of the medium,

$$\nabla \times \mathbf{E} = i\omega \mathbf{B} \quad (5)$$

$$\nabla \times \mathbf{B} = \mu_0 \sigma \mathbf{E} - i\omega \mu_0 \mathbf{E} \quad (6)$$

and from here,

$$n^2 \mathbf{E} - n(\mathbf{n} \cdot \mathbf{E}) = \left[\mathbf{I} + \frac{i}{\epsilon_0 \omega} \sigma \right] \mathbf{E} \quad (7)$$

If solved by adding collisions and magnetic field to equation (7), the known waves as depending on magnetic field geometry and collisions are obtained for the plasma of the ionosphere.

As in vertical ion-probes, the wave propagates in the z direction ($\mathbf{k} // \mathbf{B}$). Therefore, the vertical component of Earth's magnetic field affects the propagation of the wave. When the wave moves parallel to the magnetic field, the wave creates two waves perpendicular to each other due to the double refraction structure of the ionosphere.

$$a) n_0^2 = 1 - \frac{X}{1 + Z^2} + iZ \frac{X}{1 + Z^2} \quad (8)$$

is an ordinary wave and it does not related to Earth's magnetic field. The other is an extraordinary wave,

$$b) n_{ex}^2 = 1 - \frac{aX(1 - X) + Z^2 X(2 - X)}{a^2 + b^2} + iZ \frac{X(1 - X)(2 - X) - aX}{a^2 + b^2} \quad (9)$$

Where $a = 1 - x - Yy^2 - Z^2$ ve $b = z(2 - x)$. The wave given by formula (9) is also seen in the x direction. Only the ones in a and b will be Y_y, Y_x . The first of these waves is known as the ordinary, which is independent of the magnetic field, and the second is called the extra-ordinary wave.

Consider an electromagnetic wave polarized in the y direction propagating in the z direction in the ionosphere. The propagating wave depends on the refractive index n of the medium [2]. If the wave normal (\mathbf{k}) is assumed to be constant and the polarization direction of the wave does not change, the linear polarized wave in the y direction is identified as [23],

$$E_y(z, t) \equiv E_y(z) \exp(-i\omega t) \quad (10)$$

and

$$B_x(z, t) \equiv B_x(z) \exp(-i\omega t) \quad (11)$$

When Maxwell's equations are resolved for these wave fields, For $E_y(z)$ and $B_x(z)$, the following equations are obtained:

$$\frac{d^2 E_y}{dz^2} + k_0^2 n^2 E_y = 0 \quad (12)$$

and

$$\frac{dB_x}{dz} = -ik_0^2 n^2 E_y \quad (13)$$

Where, $k_0 = \omega/c$ is the number of waves in space. The real number of waves is obtained as $\mathbf{k} = k_0 \mathbf{n}$. from WKB approaches, the values of E_y and magnetic field depending on the refractive index are founded as follows:

$$E_y \cong E_0 n^{1/2} \exp\left(\pm ik_0 \int^z n dz\right) \quad (14)$$

$$cB_x \cong E_0 n^{-1/2} \exp(\pm ik_0 \int^z n dz) \quad (15)$$

Solutions for non-uniform wave equations are usually related to WKB solutions. When a progressive wave normal reaches an interface, refractive index changes abruptly at this interface, where most of the wave is reflected.

WKB solutions, according to (14) - (15) equations, when the refractive index of the medium changes very slowly in the direction of the wave travel, the wave does not reflect in any way when it comes to the medium normally.

This refractive index is linear in the direction of wave propagation, even if it changes excessively. WKB solutions show that when the wave travels through the medium, its wavelength changes slowly. In fact, the wavelength at position z is approximately $\lambda(z) = 2\pi/k_0$. Solutions of the equations (14)-(15) shows that the amplitude of the wave gradually changes as the wave travels. In fact, the amplitude of the electric field component is inversely proportional to $n^{1/2}$, whereas the amplitude of the magnetic field component is directly proportional to $n^{1/2}$. However, $-(E_y B_x^* + E_y^* B_x) / (4\mu_0)$ given by the Poynting vector, the energy flux in the z direction remains constant (n is generally real)[30-36].

In fact, when the refractive index is a slowly changing function of the position, a wave entering the medium is subjected to a small amount of reflection. However, the ratio of reflected amplitude to incoming amplitude is at the level of $(dn/dz) / (k_0 n^2)$. The reflected wave is negligibly small as long as the radiation changes on a much longer scale than wavelength. Therefore, we expect a strong reflection of the wave that has reached such a point. Furthermore, WKB solutions disturb at a point where $n^2 \rightarrow \infty$, the B_x amplitude becomes infinite.

The equation (10) is a wave independent of the constant magnetic field, dependent only on the collisions of the particles and the plasma frequency. When the refractive index of this wave is used in the equation (16), it can be written as follows:

$$E_y \cong A \sqrt{n_o} \exp\left(\pm ik_0 \int^z n_o dz\right) = A \sqrt{n_o} e^{\left(\pm ik_0 \int^z n_o dz\right)} \quad (16)$$

3. Numerical Analysis and Discussion

In this study, we researched the electric field component of an electromagnetic wave with a linear polarization in the y direction and moving in the z direction, known as the WKB solution, in an medium with a slow change in the refractive index of the ordinary wave in the non-collision medium, which is given by equation (9) and generally constitutes the theoretical background of the ionosondes, in the equatorial anomaly region of the F2 region, at some altitudes (390, 410, 450, 500, 550 and 600 km), at 12.00 LT and for 21 March-December months.

In Figure 2, the change of electron density with latitude is given for the conditions accepted above. Electron density is the basic parameter for ionospheric plasma. In other words, the fundamental change either from outside (applying electric or magnetic field; neutral winds etc.) or within the ionosphere plasma (internal dynamics) in this medium occurs in the electron density and all ionosphere parameters (conductivity, refractive index, etc.) change accordingly. We have examined the electron density change for the conditions considered for electron peaks and cavities, where this interesting feature occurs. According to Figure 2, the change of electron density is consistent with the figure given in (Rishbeth, H.,1967).

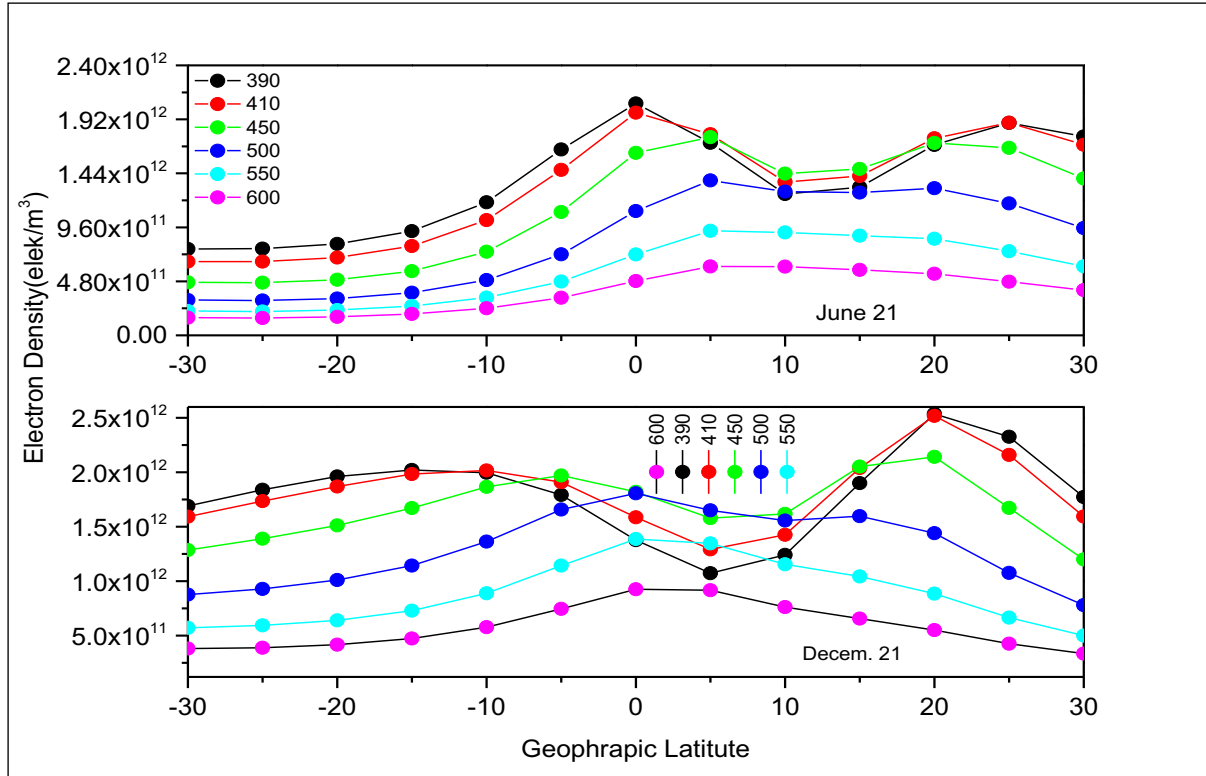


Figure 2. Change of electron density with low latitude in some F2 region altitudes (June 21st-December 2nd, Time: 12.00 LT)

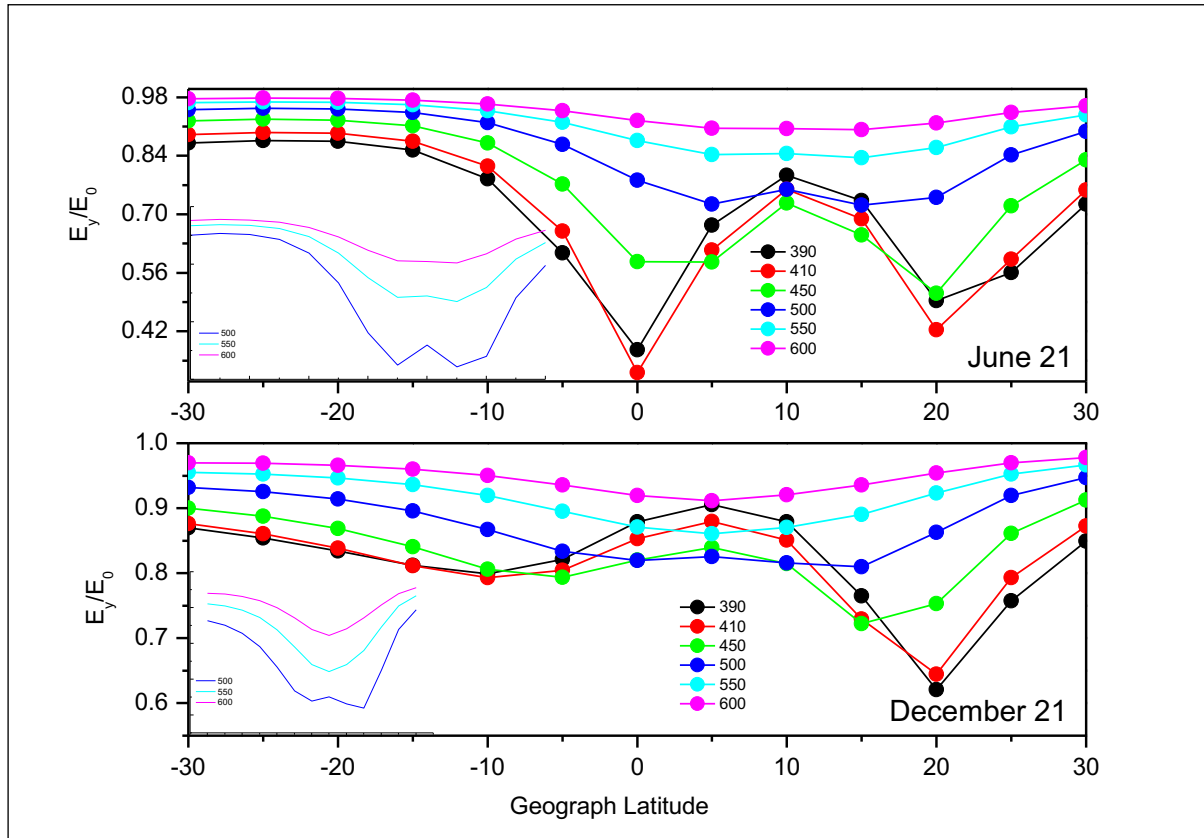


Figure 3. Change of (E_y/E_0) for some altitudes at low latitudes (Time: 12.00 LT)

In Figure 3, the cosine component of the equation is given in the cold plasma medium without collision with the expansion of the equation (11-16) for some conditions considered. Accordingly, the ratio of (E_y/E_0) exhibits an opposite behaviour with the change of electron density in both seasons in 0-150 geographical latitudes, where the equatorial anomaly occurs. Even though the electron density forms peaks at 0-150 latitudes, sharp decreases are observed at the same latitudes, especially at altitudes (390, 410, 450 km), for (E_y/E_0). This is also observed at other altitudes, but these decreases are not sharp. There is an increase in the ratio of (E_y/E_0) in both seasons between these latitudes. Considering the change of electron density given in Figure 2, it can be said that there is an opposite behaviour. This is same for both seasons for the altitudes considered. However, in Figure 2, electron density is higher in summer season (June 21st) than in winter (December 21st). In reality, this is not an expected result. Because electron production in summer is higher and losses are less depending on the Sun. In winter, this is vice versa. This is called winter anomaly. In Figure 3, the ratio of (E_y/E_0) is higher in winter (December 21st) than in summer (June 21st). The magnitude of (E_y/E_0) is parallel to the behaviour of electron density in both seasons. However, it is in contrast with the change of electron density as a trend.

4. Results

In this study, which is conducted in accordance with the conditions accepted, the magnitude of (E_y/E_0) at lower altitudes is higher in winter (December 21st) than in summer (June 21st). This conclusion is in line with the literature. Because the change of electron density with latitude is higher in December than in June. However, (E_y/E_0) takes the lowest values in the peaks and the highest values around the magnetic equator for all altitudes in the latitudes with anomaly. In this regard, the ratio of (E_y/E_0) gets the minimum values at points, where the electron density is at the maximum level and vice versa. When this electron density increases, (E_y/E_0) the values decrease or otherwise. as the density increases, the wave transfers more energy to the medium and the kinetic energy of electrons increases. The increase of (E_y/E_0) magnitude can be interpreted as taking the energy of the wave from the medium.

Acknowledgements. The carried out investigation is supported through the grant No. 04/01 of 2017 Joint Call of Shota Rustaveli National Science Foundation of Georgia and the Scientific and Technological Research Council of Turkey (TUBITAK).

References

- [1] Kurt, K., Yeşil, A., Sağır, S., Atici, R. The relationship of stratospheric QBO with the difference of measured and calculated NmF2, *Acta Geophysica* 2016; 64 (6): 2781-2793.
- [2] Unal, I., Senalp, E.T., Yeşil, A., Tulunay, Y., Tulunay, E. Performance of IRI-based ionospheric critical frequency calculations with reference to forecasting, *Radio Science* 2011; 46 (01): 1-10.
- [3] Yeşil, A., Sağır S., Kurt, K., The Behaviour of the Classical Diffusion Tensor for Equatorial Ionospheric Plasma, *Journal of Science* 2016; 13:123-127.
- [4] Yeşil, A., Unal, I., Electromagnetic Wave Propagation in Ionospheric Plasma, *Behaviour of Electromagnetic Waves in Different Media and Structures* 2011; 189.
- [5] Yeşil, A., Sağır, S., Updating Conductivity Tensor of Cold and Warm Plasma for Equatorial Ionosphere F2-Region in The Northern Hemisphere, *Iranian Journal of Science and Technology, Transactions A: Science* 2019; 43 (1): 315-320.
- [6] Sağır, S., Yeşil, A., The Relation Between the Refractive Index of the Equatorial Ionospheric F2 Region and Long-Term Solar Indices, *Wireless Personal Communications* 2018; 102 (1): 31-40.
- [7] Yeşil, A., Sağır, S., Kurt, K., The Behavior of the Classical Diffusion Tensor for Mid-Latitude Ionospheric Plasma, *Bitlis Eren Üniversitesi Fen Bilimleri Dergisi* 2016; 5 (2).
- [8] Sağır, S., Karatay, S., Atici, R., Yeşil, A., Özcan, O., The relationship between the Quasi Biennial Oscillation and Sunspot Number, *Advances in Space Research* 2015; 55(1): 106-112.
- [9] Yeşil, A., The Effect of the cold plasma on the propagation of the electromagnetic waves, *Firat University, Elazığ*, 1995
- [10] Yeşil, A. and Unal, I. The Electromagnetic waves in the fully ionized plasma, *Firat University, Elazığ*, 2002.
- [11] Yeşil, A., The Effect of the Electron Temperature on the Electric Polarization Coefficient of Ionospheric Plasma, *International Journal of Science & Technology* 2006; 1 (2):125-130.
- [12] Kaladze, T., Tsamalashvili, L., Kaladze, D., Özcan, O., Yeşil, A., Inc, M., Modified KdV equation for magnetized Rossby waves in a zonal flow of the ionospheric E-layer, *Physics Letters A* 2019; 383 (32): 125888.
- [13] Sağır, S., Atici, R., Akalin, Y., Yeşil, A., The assessment in terms of QBO of NeQuick 2 model, *The Egyptian Journal of Remote Sensing and Space Science* 2019; 22 (1): 67-72.
- [14] Timucin, E., Unal, I., Yeşil, A., The Effect of the Midlatitude Electron Density Trough on the Ionospheric Conductivities, *Iranian Journal of Science and Technology, Transactions A: Science* 2019; 43 (1): 297-307.
- [15] Yeşil, A., Kurt, K., Calculation of electric field strength in the ionospheric F-region, *Thermal Science* 2019; 22 (Suppl. 1): 159-164.
- [16] Timocin, E., Yeşil, A., Unal, I., The effect of the geomagnetic activity to the hourly variations of ionospheric foF2 values at low latitudes, *Arabian Journal of Geosciences* 2014; 7 (10): 4437-4442.
- [17] Sağır, S., Yaşar, M., Atici, R. The Relationship between Dst, IMF-Bz and Collision Parameters for O+ +N2 NO+ + N Reactive Scattering in the Ionosphere, *Geomagnetism and Aeronomy* 2019; 59: 1003–1008.
- [18] Swanson, D.G., *Plasma waves*, Academic Press, New York, 1989.
- [19] Whitten, R.C., Poppoff, I.G., *Fundamentals of Aeronomy*, John Wiley and Sons, New York, 1971.
- [20] Budden, K.G., *The Propagation of Radio Waves*, Cambridge University Press, Cambridge, 1988.
- [21] Budden, K.G., Stott, G.F., Rays in magneto-ionic theory-II, *Journal of Atmospheric and Solar Terrestrial Physics*, 1980; 42: 791–800.
- [22] Richard, F. *The physics of Plasma*, CRC press, New York 2014; 50–140.
- [23] Hunsucker, R.D. and Hargreaves, J., K., *The High-Latitude Ionosphere and its Effects on Radio Propagation*, Cambridge University Press, 2003; 1-50.
- [24] Aydoğdu M, Yeşil A, Güzel E, The Group Refractive Indices of HF Waves in the Ionosphere and Departure From the Magnitude Without Collisions, *Elazığ*, 2003.
- [25] Özcan, O., Aydoğdu, M., Yeşil, A., Güzel, E., The Damping of Radio Waves in the Ionospheric Plasma over Elazığ, *F. Ü. Fen ve Müh. Bilimleri Dergisi* 1996; 113–123.
- [26] Rishbeth, Henry, *Physics and Chemistry of the Ionospheric Contemp*, *Phys* 1973; 14: 229-240
- [27] Rishbeth, H. ve Garriot, O.K., *Introduction to Ionospheric Physics*, Academic Pres, New York 1969.
- [28] Bailey, G. J., Su, Y. Z. and Oyama, K.-I., Yearly Variations In The Low-Latitude Topside Ionosphere, *Ann. Geophysicae* 2000; 18: 789-798.
- [29] Rishbeth, H., A Review of Ionospheric F Region Theory, *Proceedings of The Iee* 1967; 55: 16-35.
- [30] Zhang, S. R., Oliver, W. L., Fukao, S. and Otsuka, Y., A Study of The Forenoon Ionospheric F2-Layer Behavior Over The Middle And Upper Atmospheric Radar, *Journal of Geophysical Research* 2000; 15: 823-833.
- [31] Millward, G. H., Rishbeth, H., Fuller-Rowell, T. J., Aylward, A. D., Quegan, S. and Moffett, R. J., Ionospheric F2-Layer Seasonal And Semiannual Variations, *Journal of Geophysical Research* 1996; 101: 5149-5156.
- [32] Rapoport, Z. Ts. and Sinel'nikov, V. M., Experimental Electron Concentration Profiles Of The Midlatitude Lower Ionosphere And The Winter Anomaly, *International Journal of Geomagnetism and Aeronomy* 1998; 1: 2-7.
- [33] Chien-Chih Lee, Bodo W. Reinisch, Quiet-Condition hmF2, NmF2, and BO variations at Jicamarca and comparison with

The Change of The Magnitude of The Electric Field Vector (E_y/E_0) in The Ionosphere in The Magnetic Equator Through

- IRI-2001 during solar maximum, *Journal of Atmospheric and Solar-Terrestrial Physics* 2006; 68(18): 2138-2146.
- [34] Rawer, K, *Wave Propagation in the Ionosphere* , Kluwer Academic Publishers, London 1993.
- [35] Budden K G, *The Propagation of Radio Waves*, Cambridge University Pres, Melbourne Sydney 1985.
- [36] Fitzpatrick R, *The Physics of Plasmas*, The Univ

Correlation Based Regression Imputation (CBRI) Method for Missing Data Imputation

Uğur ÜRESİN^{1*}

¹ Industrial Engineering, Faculty of Management, Istanbul Technical University, Istanbul, Turkey

*¹ uresin15@itu.edu.tr

(Geliş/Received: 12/11/2020;

Kabul/Accepted: 31/01/2021)

Abstract: To complete missing values in a dataset is crucial for data mining and machine learning applications. If a parameter of a dataset has missing values, the values of the other parameters corresponding to those missing values should not be excluded from the dataset to prevent information in the dataset. Missing values should be handled carefully to avoid their affecting analyses and to prevent loss of information. There are many methods and practical applications to predict missing values (imputation) in a dataset. Most of the methods that consider other parameters to predict missing values generally require lots of observations. These methods do not give successful results for datasets with a low number of observations according to the number of parameters. In this study, an algorithm is proposed for small datasets to predict missing values. The performance of the proposed method is compared with methods that are generally used for small datasets. The proposed method (CBRI) was tested with real data on how much the dimensions of vehicle bodies produced by an automotive manufacturer deviated from design specifications. Some of the values deliberately and randomly removed from the real data were predicted by the proposed method and the standard error of the predictions was calculated. The results were compared with the arithmetic mean assignment and median value assignment methods using the same data, and much more successful results were obtained with the proposed method.

Keywords: Missing data, imputation, data manipulation

Eksik Veriler için Korelasyona Dayalı Regresyon Yöntemi İle Değer Atama

Öz: Veri madenciliği ve makine öğrenmesi uygulamalarında eksik verilerin tamamlanması oldukça önemlidir. Bir veri setinin herhangi bir parametresinde eksik değerler varsa, o eksik değerlere karşılık gelen diğer parametrelere ait değerlerin ölçümünden çıkarılmaması gerekir. Aksi takdirde bilgi kaybı meydana gelecektir. Söz konusu bilgi kaybının oluşmaması için eksik veriler uygun bir şekilde tamamlanmalıdır. Bir veri kümesindeki eksik değerleri tahmin etmek (değer atamak) için birçok yöntem ve pratik uygulama vardır. Eksik değerleri tahmin etmek için diğer parametreleri dikkate alan yöntemlerin çoğu genellikle çok sayıda gözlem gerektirir. Bu yöntemler, parametre sayısına göre az sayıda gözlem içeren veri setlerinde başarılı sonuçlar vermemektedir. Bu çalışmada, eksik değerleri tahmin etmek için küçük veriler için bir algoritma önerilmiştir. Önerilen yöntemin performansı, genellikle küçük veri kümeleri için kullanılan yöntemlerle karşılaştırılmıştır. Önerilen yöntem, bir otomotiv üreticisinin ürettiği taşıt gövdelerindeki boyutların, dizayn spesifikasyonlarından ne kadar sapıp içerden gerçek bir veri ile test edilmiştir. Gerçek veriden kasıtlı ve rasgele olarak silinen değerler, önerilen yöntem ile tahmin edilmiş ve tahminlerin standard hatası hesaplanmıştır. Sonuçlar, aynı veri kullanılarak yapılan aritmetik ortalama atama ve medyan değer atama yöntemleri ile kıyaslanmış ve önerilen yöntem ile çok daha başarılı sonuçlar elde edilmiştir.

Anahtar kelimeler: Eksik veri, eksik değer atama, veri işleme

1. Introduction

The first process of data science and machine learning applications is the data wrangling process which consists of data gathering, assessment and cleaning. One of the tasks in this process is called imputation. The imputation method involves replacing the missing value with a value predicted based on data mining from existing information in the data set [1]. Missing data is a serious problem for researchers in many disciplines. Because traditional statistical methods and software assume that all variables are measured for all observations [2]. Besides missing data reduces the accuracy of the statistical models and produces biased predictions of a model, leading to invalid results [3]. In particular, missing observations are frequently encountered in raw data generated by collecting data from different sources. Missing observations are also encountered in the raw data generated intermittently due to physical constraints. Removing an observation with missing values in one or more parameters from the raw data may result in the loss of existing information drastically. Therefore, it is crucial to complete the missing data rationally.

* Corresponding author: uresin15@itu.edu.tr. ORCID Number of the author: ¹ 0000-0002-9100-9697

There are different methods in the literature to predict missing observations. The selection of the appropriate method depends on incomplete observation mechanisms. These mechanisms are examined in three categories in the literature. These categories are 'missing completely at random' (MCAR), missing at random (MAR) and 'not negligible' (NI) [4,5]. It is assumed that missing observations depend entirely on chance, and an X variable is not dependent on any other variable and X variable itself [5]. Incomplete observation due to chance is the incomplete observation of an X variable, it is dependent on other variables in the data set but not itself. That is, the absence of observation is that it depends on other variables except itself. The non-negligible missing case is that the missing value in an X variable depends on all variables in the data set, including the X variable. In other words, missing data is not due to chance.

The method of assigning the mean value is to replace the missing observations of a variable with the arithmetic mean of the complete observations for the variable. As a result of this operation, the arithmetic mean obtained for complete and assigned observations will be equal to the arithmetic mean obtained with complete observations. The positive aspect of this method is that it is easy to apply and takes into account all observations with complete information. The disadvantage of this method is that since all observations in the variables are replaced by a single value, the actual distribution of the variables changes and the variance in the data set decreases artificially. Correlation between this variable and other variables depending on the decrease in variance. In this approach, the data should be incomplete (MCAR) depending on the chance [6].

Another method frequently used for incomplete observation is the minimum assignment method where the value in the variable is used instead of the missing observation for the variable with missing observations. Another method is the maximum assignment method. In the maximum assignment method, for the variable with missing observations, the largest value in that variable is used [7].

In the median (median value) assignment method, it is used instead of the missing observation left in the middle after the observations in the variable containing missing observations are listed in order from small to large. If the size of the data set is odd, the median is the middle observation; If the number of observations is double, the median is the average of the two values in the middle [8].

Another method is the regression value assignment method. This method is used to predict missing values by establishing regression equations on variables that do not contain missing values. This method calculates multiple linear regression estimation and has options to increase the estimation with random components. In the first step of the regression value assignment method, regression equations that predict the missing value variables are obtained from the variables without missing values. In the second step, the values of the variables with missing values are predicted. These predictive values are used in place of missing values. Thus, a data set without missing values is created. In this method, the regression method is used as a tool to predict missing observations. If the missing observations are random (MCAR) and depend on other independent variables that do not contain missing observations, the least-squares coefficients are consistent [9]. Besides, this method gives almost unbiased results in large samples. This method is based on the assumption that there is a high correlation relationship between the variable with missing data and other variables. If this relationship is not sufficient, it is recommended to use other methods such as substituting the mean value instead of this method. However, it is very difficult for each parameter to have a high correlation relationship with each other for datasets with many parameters. If the parameters are not correlated with each other, the error rate of the created multiple regression models will be very high and the error of the predicted missing value will also be very high. Therefore, it is extremely critical to establish regression models correctly.

In this study, for the prediction of the missing observations, a simple regression model was established among the parameter that has the highest correlation and the parameter that has the missing observations. To test this method, dimensional data generated in a quality control process in the automotive industry were used. The dimensional data is a numerical data that includes how much certain points on a manufactured vehicle deviate from design specifications. Thus, measurement points on the vehicle are parameters of the data. Therefore, points that are physically close to each other are expected to be parameters that correlate with each other. This data was divided into two as training and test data to create regression models and to test the created model, and some values in the test data were randomly removed from the data, and the success of the regression models created with training data was tested. While creating the regression models here, not all parameters, but the parameter values with the highest correlation with the parameter with the missing observation value were used. The success of the results obtained from this approach was compared with the median and mean value assignment methods which are commonly used methods in practice when the number of observations is not much.

2. The Proposed Method and Algorithm

The proposed method is an application of simple linear regression-based imputation. In this study, different from the simple linear regression imputation, a criterion for determining the independent variable in the regression model is added. Pearson's pairwise correlation matrix was used to determine the dependent and independent variables of the regression model. This method is called Correlation Based Regression Imputation (CBRI for short) in this paper.

The flowchart for the algorithm is shown in Figure 1. When fitting a simple linear regression model, the 'parameter i' (contain a missing value or multiple missing values) is the dependent variable, the 'parameter j' (According to Pearson's pairwise correlation matrix, the parameter with the highest correlation with 'parameter i') is the independent variable. Also, outliers in these parameters are subtracted from the training data used to create the regression model. Unlike multiple regression, only the parameter with the highest correlation is considered for the missing value prediction in the CBRI method. Because it's expected that independent variables (or features) are uncorrelated. Therefore, As a matter of fact, including all indepent variables except the independent variable with missing data into the model will increase the standard error of the prediction.

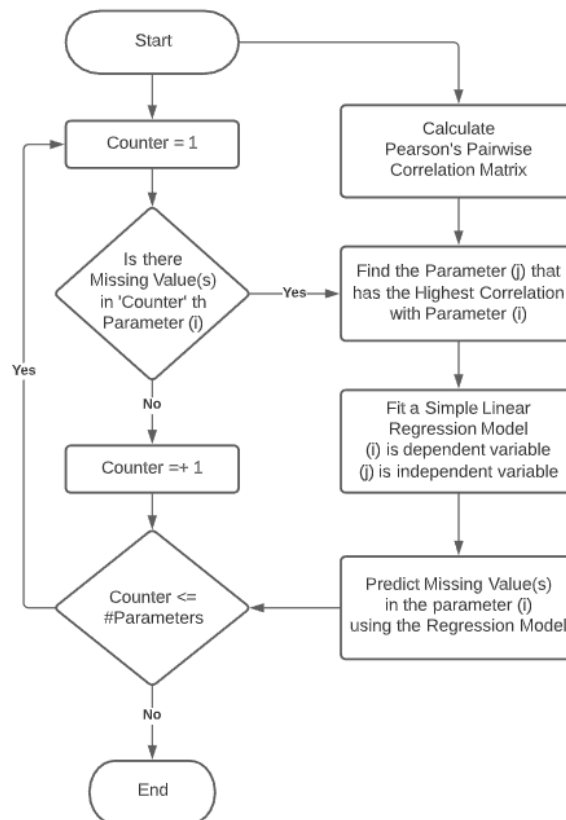


Figure 1. The flowchart of the CBRI algorithm

Besides, separate models are created for each missing value to decrease the standard error of the prediction. Therefore, fitting a simple linear regression model is repeated for each parameter that contains missing value or values. Thus, the high pairwise correlation relationship requirement for the regression imputation is ensured and that the parameters that are unrelated to each other do not affect the prediction of missing data. The difference between the proposed method and imputation using multiple regression model is that only the most correlated is considered to predict a parameter's missing values. Therefore, irrelevant features are not considered. Besides, multiple regression models require many observations per number of features. For regression models, there must be 10 observations per predictor variable at least [10]. In some cases, it is not always possible to collect 10 observations per predictor. If this is the case, fitting multiple regression models to predict missing values is likely

to yield high standard errors. However, the CBRI method predicts missing values by using just one predictor so that this method allows us to make good predictions even with a small number of observations.

3. Experimental study and results

To test the proposed method (CBRI) a real dataset was used. The data is called vehicle body dimensional data that includes how much the measured some assembly points on the vehicle body deviate from the design specifications. Vehicle body dimensional data is created in two steps. First, certain points on a vehicle body are measured with a device called CMM (Cartesian Measuring Modeling) just after the production of the vehicle body. Second, the deviations between measurement data and design specifications are calculated. These two processes are repeated on a large number of vehicle bodies to create data called vehicle body dimensional data.

The measurement points that are close to each other on the vehicle body have correlations due to their physical relationships. For example, there are some measurement points on the roof of the vehicle body and since most of the roof sections are continuous, close points are likely to have a high correlation for the bodies produced on same production day. Because the measurement pace is lower than the production pace, not all previously defined points can be measured. However, estimating unmeasured points with a reasonable standard error is especially important for the quality process. Therefore, this data is appropriate to use for the proposed method (CBRI) in this study.

3.1. Descriptive statistics of the dataset

The dimensional dataset consists of 66 parameters (measurement points) and 382 observations. All parameters contain float values. The descriptive statistics of some (since there are so many) parameters of the data are given in Table 1. In the dataset, some measurement points (parameters) that are close to each other show a high correlation relationship due to their physical and mechanical relationships.

Table 1. The descriptive statistics of some parameters in the data

Parameter	Min	1st Qua.	Median	Mean	3rd Qua.	Max
1	-1,85	-0,7875	-0,27	-0,1874	0,2775	2,07
5	-2,46	-0,7975	-0,245	-0,2466	0,2775	2,03
10	-5,47	-0,9375	0,155	-0,01976	0,905	2,66
15	-1,64	-0,3975	0,24	0,2161	0,6975	2,29
20	-2,31	-0,0575	0,600	0,5674	1,2775	3,49
25	-3,49	-0,76	-0,185	-0,351	0,01	3,61
30	-2,28	-0,63	-0,055	-0,2572	0,06	1,54
35	-2,00	-0,5975	0,295	0,4522	1,4225	3,61
40	-2,96	-1,24	-0,835	-0,709	0,045	1,48
45	-0,9	0,04	0,23	0,2385	0,44	1,21
50	-1,63	-0,1675	0,27	0,3429	0,7675	2,8
55	-3,61	-1,1475	-0,68	-0,7883	-0,33	0,8
60	-0,94	-0,3575	-0,1	-0,07872	0,1975	2,04
65	-3,1	-0,595	0,235	0,1897	1,0075	3,09

The descriptive statistics for all variables (66) in the data used in this study are shown in Figure 2. The minimum, maximum, median and mean values are given (the distributions of Quarter1 and Quarter3 values are not added to the figure to make the figure easily readable).

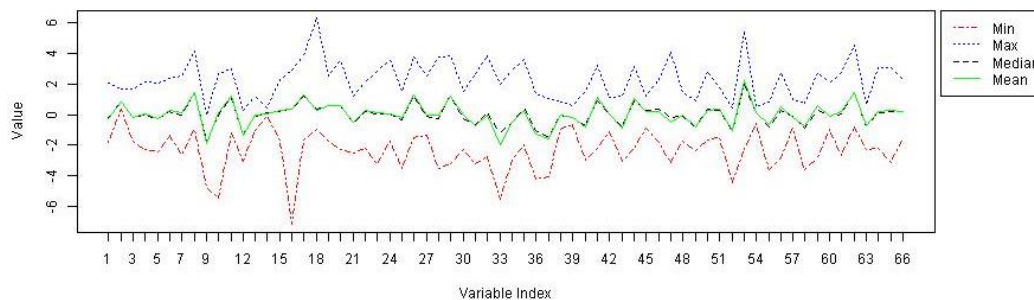


Figure 2. Some descriptive statistics values for all variables in the data

Considering, and the number of parameters, it can be said that this dataset contains a small number of observations. Therefore it's suitable for the proposed method (CBRI) to predict missing values in the dataset. In the next section, the results are presented.

3.2. Results and Discussion

In this study, 20 random values (using sample.int() method in R programming language) are removed. The missing (removed) values are predicted Using the proposed method (CBRI),. These values are also predicted using the median assignment and mean assignment methods. Then standard errors are calculated. Random value removal was performed 5 times (5 iterations) to ensure randomness. The standard errors of the predictions for 5 iterations are shown in Figure 3 and Figure 4.

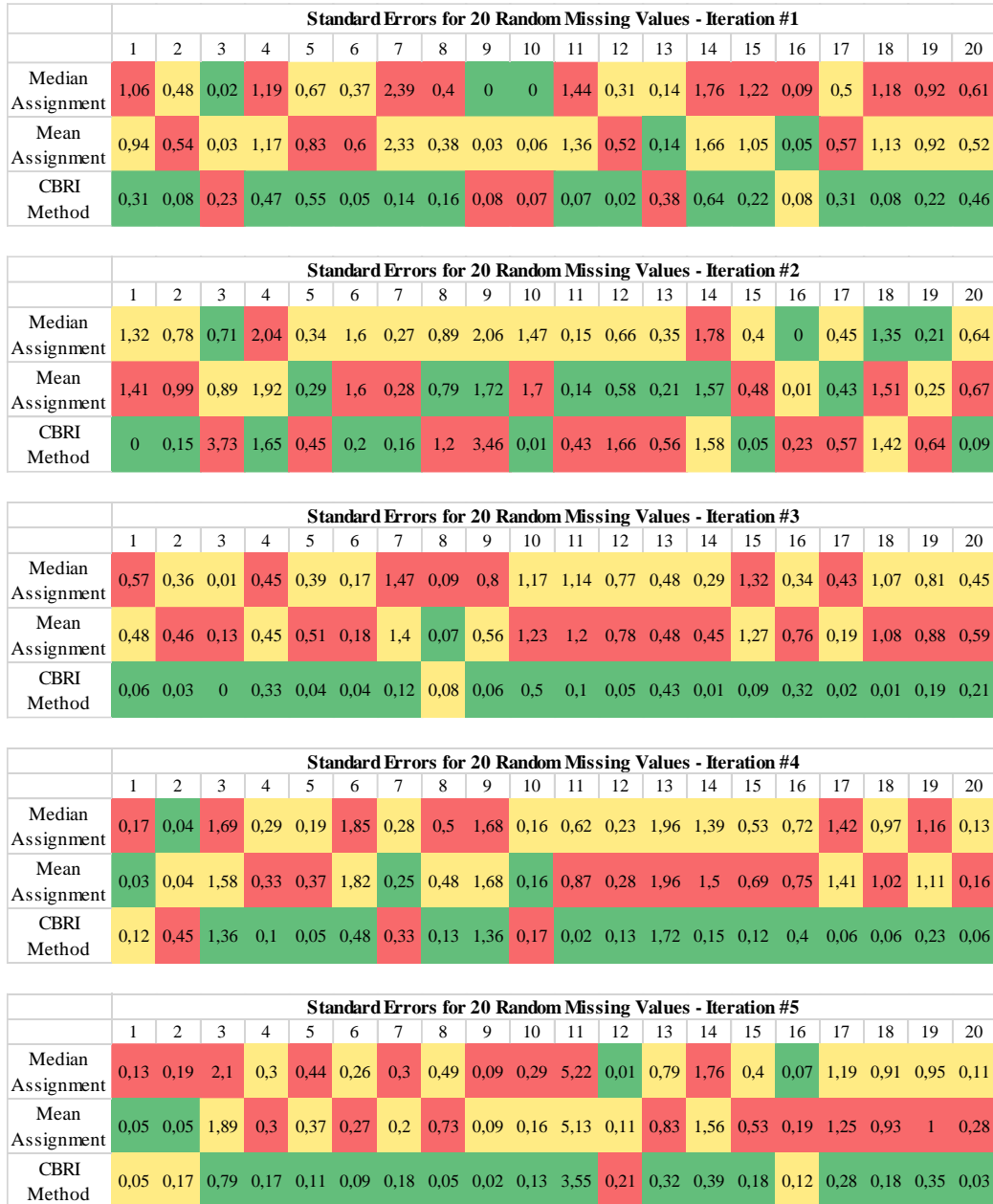


Figure 3. Standard errors of the predictions for the 20 missing values (red is the maximum standard error, yellow is the moderate standard error, green is the lowest standard error)
a)Iteration #1 b)Iteration #2 c)Iteration #3 d)Iteration #4 e)Iteration#5

Correlation Based Regression Imputation (CBRI) Method for Missing Data Imputation

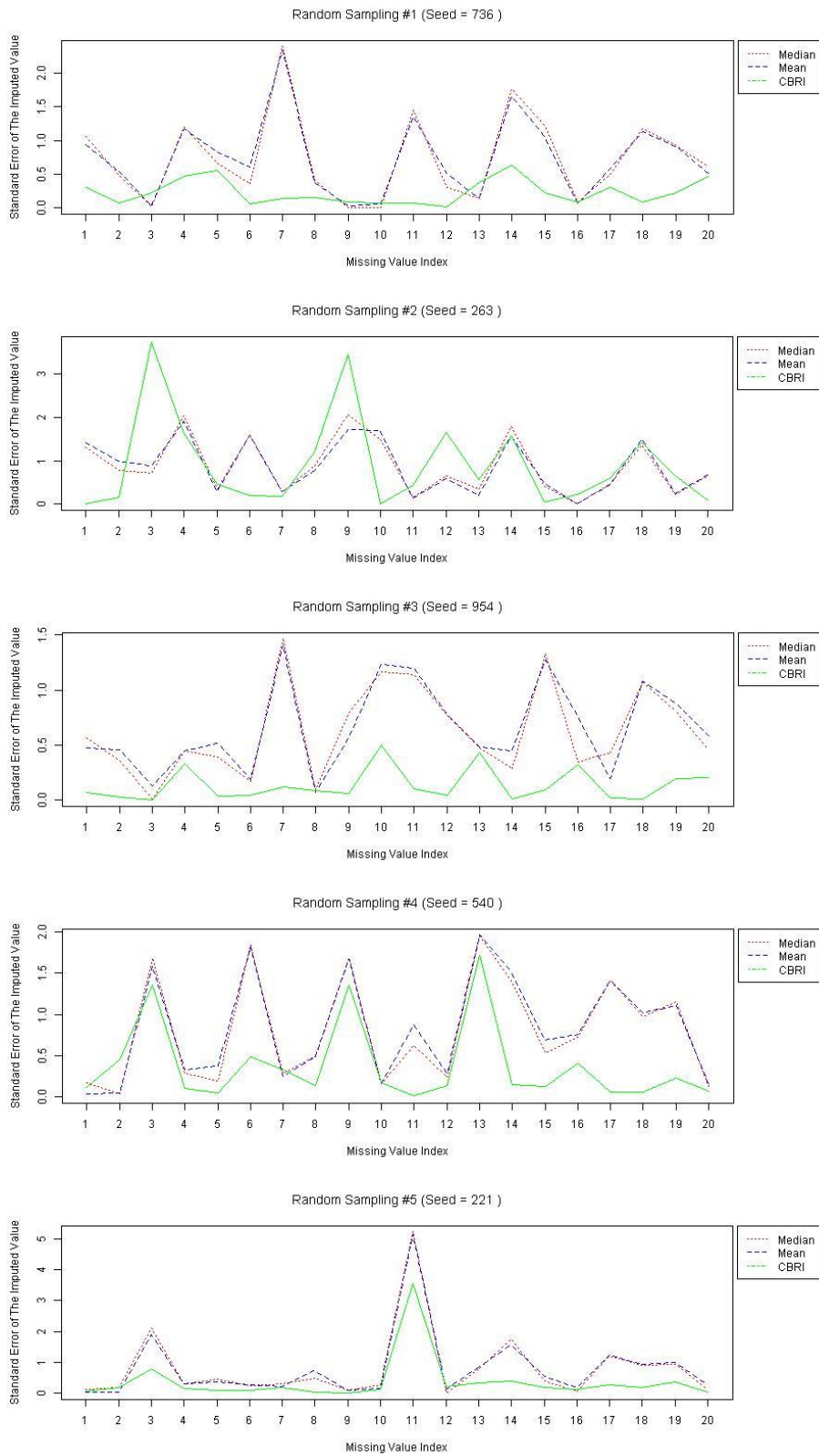


Figure 4. Comparison of the standard errors
a)Iteration #1 b)Iteration #2 c)Iteration #3 d)Iteration #4 e)Iteration#5

As shown in Figure 3 and Figure 4, assigning the median value and assigning the mean value methods yielded similar standard errors in the iterations of missing value prediction. In most of the iterations, the proposed method (CBRI) yielded a much less standard error. In the 5 iterations, a total of 100 randomly removed values were predicted using CBRI, mean assignment and median assignment methods. In 74% of the predictions, the CBRI method yielded the best prediction in terms of the minimum standard error. Since the volume of the data is very small (only 382 observations for the 66 parameters), it is very likely that a value that is randomly removed from the data is equivalent or very close to the mean and median value.

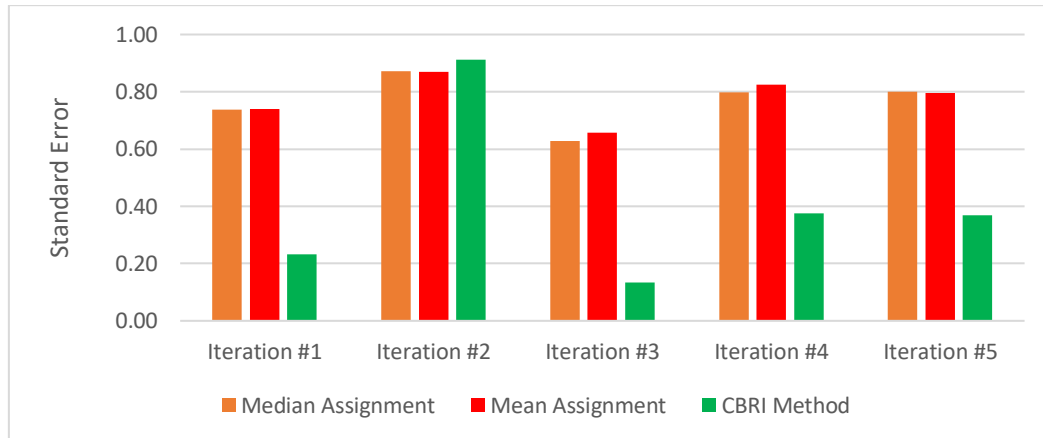


Figure 5. Comparison of the average standard errors in the iterations

In Figure 5, the average of the standard errors for the predictions in the iterations are shown. Considering the difference between the standard errors, CBRI is much better than median assignment and mean assignment methods in 4 of the 5 iterations. In iteration #2, although the CBRI method is not the best in terms of the average standard error, the difference between the average standard errors are significantly low. Thus, CBRI yielded better results in terms of both standard errors of the particular predictions and average standard errors of the predictions in the iterations.

5. Conclusion

In this study, a missing value assignment (imputation) method (CBRI) is proposed that takes into account the Pearson's pairwise correlations between parameters in a dataset. The proposed method has been tested using a real and relatively small data. The results are compared with the median assignment and mean assignment methods. 20 randomly chosen measurement values were removed from the data and these values were predicted by 3 methods and the standard errors of the predictions were compared. In conclusion, the proposed method (CBRI) was found more successful than median assignment and mean assignment methods.

As long as the distribution of data is not uniform, as the number of observations in the data increases, the probability that a missing value will differ from the mean or median value increases. Thus, the CBRI method is quite likely to perform much better in relatively larger data compared to mean and median assignment. In future, researchers may test the CBRI method's performance in bigger datasets and compare with more complex methods instead of mean and median assignment methods.

References

- [1] Zain A.M., Ali N.A., Sallehuddin R. A Review On Missing Value Estimation Using Imputation Algorithm. *Journal of Physics Conference Series* 892(1):012004. 2017.
- [2] Alkan B., Alkan N. Investigation of the Multiple Imputation Method in Different Missing Ratios and Sample Sizes. *Sakarya University Journal of Science*. 605-609. 2019.
- [3] Kang H. The prevention and handling of the missing data. *Korean J.Anesthesiol* 64 (5): 402–406, 2013.
- [4] Pelckmans K., Brabante, J.D., Suykens J.A.K., Moor B.D. Handling missing values in support vector machine classifiers. *Neural Networks*, 684-692. 2005.
- [5] Jerez, J.M., Molina I., Subirats J.L., Franco L., Missing data imputation in breast cancer prognosis. *Processing of the fourth IASTED International Conference Biomedical Engineering*. 2006.

- [6] Mohamed S. & Marwala T., Neural Network Based Techniques for Estimating Missing Data in Databases. 16th Annual Symposium of the Pattern Recognition Association of South Africa. 2005.
- [7] Alpar, R., Uygulamalı Çok Değişkenli İstatistiksel Yöntemler. 135-157. Nobel Kitabevi. 2010.
- [8] Bal C., Özdamar K. Eksik Gözlem Sorununun Türetilmiş Veri Setleri Yardımıyla Çözümlemesi. Osmangazi Üniversitesi Tıp Fakültesi Dergisi, 26 (2): 67-76. 2004.
- [9] Menengiç Y. The Comparison of Missing Value Analysis Methods. MSc, Ondokuz Mayıs University, Samsun, Turkey, 2015.
- [10] VanVoorhis C.R, Morgan B.L. Understanding Power and Rules of Thumb for Determining Sample Sizes. Tutorials in Quantitative Methods for Psychology vol. 3 (2), 43-50. 2007.

Enhancing The Data Security by using Audio Steganography with Taylor Series Cryptosystem

Muharrem Tuncay GENÇOĞLU^{1*}, Mehmet VURAL²

¹ Vocational School of Technical Sciences, Fırat University, Elazığ, Türkiye

² Fırat University, Elazığ, Türkiye

*¹ mt.gencoglu@firat.edu.tr ² mvural002@gmail.com

(Geliş/Received: 10/12/2020;

Kabul/Accepted: 14/01/2021)

Abstract: Especially in recent years, the security of information and computer systems appears to be a very important issue. Because the heavily used communication network has made life easier as well as accompany serious security problems. To solve these problems, cryptography and steganography have been widely used. To present a more secure model for audios, a simple and secure stego-crypto method is presented. In this work, the hidden data is encrypted by the proposed Taylor series based encryption method and the encrypted data are hidden audio signals by applying the least significant bit (LSB) method. A real-world application is implemented in the proposed model. According to the results, the used encryption model is more efficient than AES. The results and findings demonstrated that this model can be used in a communication security system.

Key words: Cryptography, Audio Steganography, Data Steganography, Text Steganography

Taylor Serisi Kriptosistem ile Ses Steganografisi Kullanılarak Veri Güvenliğinin Arttırılması

Öz: Özellikle son yıllarda bilgi ve bilgisayar sistemlerinin güvenliği oldukça önemli bir konu olarak karşımıza çıkmaktadır. Çünkü yoğun bir şekilde kullanılan iletişim ağı, hayatı kolaylaştırdığı gibi ciddi güvenlik sorunlarına da beraberinde getirmektedir. Bu sorunların çözümü için kriptografi ve steganografi yaygın olarak kullanılmıştır. Çalışmamızda Ses steganografisinde daha güvenli bir model oluşturmak için basit ve güvenli bir stego-kripto yöntemi sunulmuştur. Bu çalışmada, gizli veriler önerilen Taylor serisi tabanlı şifreleme yöntemi ile şifrelenmiş daha sonra şifrelenen veriler en az önemli bit (LSB) yöntemi uygulanarak ses sinyallerine gömülmüştür. Önerilen modelde gerçek bir uygulama yapılmış ve bu uygulamada kullanılan şifreleme modelinin AES'den daha verimli olduğu gözlemlenmiştir. Sonuçlar ve bulgular, bu modelin bir iletişim güvenlik sisteminde kullanılabileceğini göstermiştir.

Anahtar kelimeler: Kriptografi, Ses Steganografisi, Veri Steganografisi, Metin Steganografisi.

1. Introduction

Security is considered as the most basic factor in any communication system. This issue poses an important threat, as failure to ensure the confidentiality of information will negatively affect individuals, communities and states. For this reason, new applications and new system protection mechanisms have emerged along with the developing technology to prevent data hiding and changing. In these applications, many encryption algorithms have been created and existing algorithms continue to be developed to further increase the security of the data, and even new algorithms are being created.

The main purpose of cryptographic protocols is to ensure the integrity and confidentiality of the data. While examining a protocol, just like algorithms, we are concerned with basic operating principles rather than what kind of device we will implement[1].

Data we want to be protected; It is sent after being rendered incomprehensible with the aid of a key and the specified encryption algorithm. However, the fact that encrypted data in this way can be cracked by crypto analysts over time indicates that encryption alone is not sufficient for secure communication. For this reason, encryption and information hiding methods have started to be used as hybrid with encryption algorithms. It has been shown that it is possible to provide secure communication, especially using Steganography[6,10,14,16,17].

Data hiding and data communication security is a very important issue. The purpose of hiding data is the third person noticing during communication. In cryptographic encryption, the third party is aware of the secret data being sent. However, when data communication is made between the two people using steganographic methods, the third person cannot realize that there is a hidden communication between them. Steganography is the art of

* Corresponding author: mt.gencoglu@firat.edu.tr. ORCID Number of authors: ¹ 0000-0002-8784-9634, ² 0000-0003-1768-5117

hiding information with other information. Encryption turns data into an incomprehensible format, making it difficult to access real data, but cannot ensure the privacy of communication. In that case, we can express the difference between steganography and cryptography as follows; While cryptography scrambles the data, steganography completely hides the data[3-7].

Steganography, which is very important in hiding information, has been frequently used in recent years to protect the data in digital media by embedding it in text, audio, video and image files. In some techniques, the hybrid model is used[2].

Steganography started to use many methods with the development of technology. With this development, many steganographic methods started to need different algorithms. A different algorithm and a different method are used in each steganographic method. Each steganographic method has a distinctive steganalysis method. Steganography is done by hiding data into text, sound, picture, video files[12-15,17-24]. Similarly, a text file can also be stored in an audio or video file[8-10]. Therefore, steganography is not an encryption method, but a complementary element to encryption[11].

1.1. Motivation and Contribution

In this study, encryption and data hiding techniques are used to ensure the security of communication. A Taylor series based encryption algorithm, previously developed by Gençoğlu, was used to demonstrate that mathematical functions can be used to increase the robustness of the algorithms used in encryption[17]. Then, sound steganography, one of the steganography techniques, was used to hide the presence of data encoded with the proposed algorithm.

1.2 Organization

In the second chapter of this study, brief information about the necessity of the proposed method was given. Then, information was given about the proposed algorithm technique and comparison was made. In the third chapter, the application steps of the proposed algorithm technique are shown. In the fourth chapter, experimental results are given. In the fifth chapter, the performance analysis of the proposed method was made. In the sixth chapter, the obtained results and suggestions were included.

2. Proposed Method

Initially, with an eight-character key, the message is encrypted, subject to several rules and using the Taylor series in the encryption algorithm. Then, the obtained data is sent to the most meaningless bit of the voice by hiding with a proprietary code that will receive the encrypted message. The encryption diagram is shown in Fig. 1 and the decryption diagram is shown in Fig. 2.

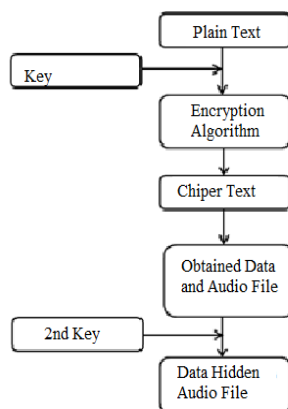


Fig. 1 The encryption diagram of the proposed model.

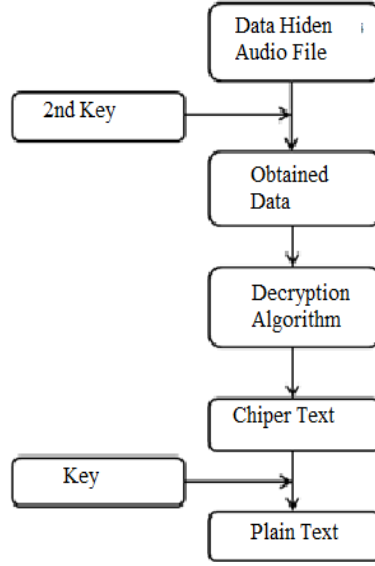


Fig. 2 The decryption diagram of the proposed model.

2.1. Encryption Algorithm

First of all in the encryption algorithm, after the message is encrypted using a set of rules with the key, the obtained data is subjected to hiding by sound steganography. The working principle of the encryption algorithm is as follows:

- The message to be encrypted is processed with the key in octal blocks.
- The key to be used must have eight characters.
- Taylor series is used in encryption, mod 256 is used in calculations.
- All of the key and the message are processed by converting them into Binary in octal blocks.
- Taylor series is used in the encryption algorithm for the Laplace transform to be used in the algorithm. The expanded Taylor series is taken with e^t .
- $f(x) = f(a) + \frac{f'(a)}{1!}(x-a) + \frac{f''(a)}{2!}(x-a)^2 + \dots + \frac{f^n(a)}{n!}(x-a)^n + \dots$

$$= \sum_{n=0}^{\infty} \frac{f^n(a)}{n!} (x-a)^n \text{ [16] and } f(t) \text{ is obtained;}$$

$$f(t) = \sum_{n=0}^{\infty} K_n \frac{t^{n+3}}{n!} .$$

From hence;

$$[f(t)](h) = T\left[\sum_{n=0}^{\infty} K_n \frac{t^{n+3}}{n!}\right](h)$$

$$= T\left[K_0 \frac{t^3}{0!} + K_1 \frac{t^4}{1!} + K_2 \frac{t^5}{2!} + K_3 \frac{t^6}{3!} + K_4 \frac{t^7}{4!} + K_5 \frac{t^8}{5!} + K_6 \frac{t^9}{6!} + K_7 \frac{t^{10}}{7!}\right](h)$$

$$\sum_{n=0}^{\infty} K_n (n+3)! \frac{h^{n+3}}{n!} \tag{2.1}$$

From here, the dividend and remainder values of the coefficients according to mod 256 are found.

Step 1.

After the 1st character of the key and 1st character of the message has been converted to binary;

- a) If the number of 0 in the 1st character of the key is more than or equal to the number of 1;
 - The last bit, the 1st character of the key, is taken first (a_1).
 - The first bit, the 1st character of the message, is taken to the end.
- b) If the number 0 in the 1st character of the key is less than the number 1;
 - The leading bit, the 1st character of the key, is taken to the end (a_1).
 - The last bit, the 1st character of the message, is taken first (m_1).
 - The transformed version (a_1) of the 1st character of the key with the transformed version of the 1st character of the message (m_1) by XOR the first character of the message is encrypted in step 1 (x_1).

Step 2.

After the 2nd character of the key is converted into binary;

- a) If the number of 0 in the 2nd character of the key is more than or equal to the number of 1;
 - The last bit, the 2nd character of the key, is taken first (a_2).
 - The first bit(x_1), the 1st character of the message, the encrypted value at the end of step 1, is taken to the end (m_2).
- b) If the number of 0 in the 2nd character of the key is less than the number of 1;
 - The leading bit, the 2nd character of the key, is taken to the end (a_2).
 - The last bit (x_1), the 1st character of the message, the encrypted value at the end of step 1, is taken first (m_2).
 - The transformed version (a_2) of the 2nd character of the key with the transformed version of the 2nd character of the message in step 2 (m_2) by XOR the first character of the message is encrypted in step 2 (x_2).

Step 3.

After the 3rd character of the key has been converted to binary;

a) If the number of 0 in the 3rd character of the key is more than or equal to the number of 1;

- The last bit, the 3rd character of the key, is taken first (a_3).
- The first bit of the encrypted value at the end of step 2(x_2), the 1st character of the message, is taken to the end (m_3).

b) If the number of 0 in the 3rd character of the key is less than the number of 1;

- The leading bit, the 3rd character of the key, is taken to the end (a_3).
- The last bit of the encrypted value at the end of step 2(x_2), the 1st character of the message, is taken to the top (m_3).
- The transformed version (a_3) of the 3rd character of the key with the transformed version of the message in step 3 (m_3) by XOR the first character of the message is encrypted in step 3 (x_3).

By doing similar operations in steps 4,5,6,7 and 8, x_4, x_5, x_6, x_7 and x_8 encrypted values are found.

- At the end of step 8, the encryption process is completed in the first character of the message. Other characters of the message are similarly encrypted, but before processing, each character is subjected to XOR processing by the encrypted format of the previous character. In this way, the message is encrypted in octal blocks.
- Encryption is completed by taking from previously random generated Tab. 1 the equivalent of the value obtained at the end of each step (first 4 numbers rows, last 4 numbers columns).

Table. 1 S-box List

	0000	0001	0010	0011	0100	0101	0110	0111	1000	1001	1010	1011	1100	1101	1110	1111
0000	1	181	120	169	38	245	76	242	230	39	72	78	47	33	239	249
0001	49	7	37	64	68	160	237	32	58	48	14	203	35	114	110	143
0010	119	23	6	12	220	109	44	61	215	202	159	45	29	250	157	235
0011	24	184	170	22	150	28	149	133	129	198	219	13	145	56	63	204
0100	212	97	201	5	15	177	234	122	50	0	113	102	253	106	36	168
0101	192	65	57	104	226	3	174	101	84	151	42	128	140	60	224	112
0110	207	53	46	95	131	243	87	118	175	164	69	55	178	247	79	126
0111	158	134	217	229	139	73	93	30	254	92	142	59	27	52	248	153
1000	240	121	189	196	138	165	130	228	11	144	34	147	25	194	137	100
1001	180	135	99	222	156	241	161	208	18	20	80	197	67	105	244	124
1010	221	74	211	167	85	115	183	251	111	51	16	108	200	233	205	66
1011	41	152	214	125	163	31	86	62	155	166	176	26	75	21	188	172
1100	232	96	4	216	238	54	107	210	171	9	195	103	8	88	141	10
1101	117	2	91	123	154	43	191	236	162	116	185	81	127	19	173	193
1110	82	252	246	83	190	187	186	136	223	71	70	218	182	225	89	146
1111	40	209	98	179	255	132	17	199	77	231	213	206	227	90	94	148

The parties are previously recorded by agreement a standard value of the person, who will receive the message, into the file with the extension *.txt and use this file as the second key. Using audio steganography's LSB (Least Significant Bit) most meaningless bit technique, they hide the obtained dividend-remainder values in any sound file. Since the hidden data is hidden in the most meaningless bit of the audio file, the changed audio will not display a frequency feature that can be heard with the ear. Besides, any change in sound frequency will be observed(Fig. 3 and Fig. 4)

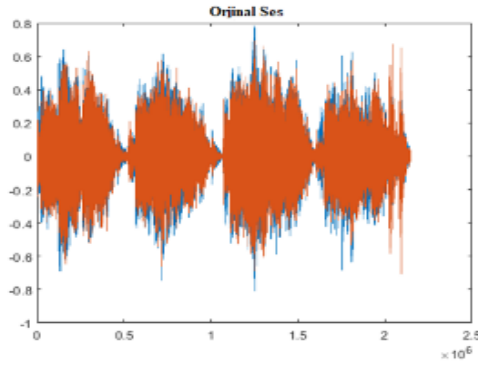


Fig. 3 A sample sound of the used dataset.

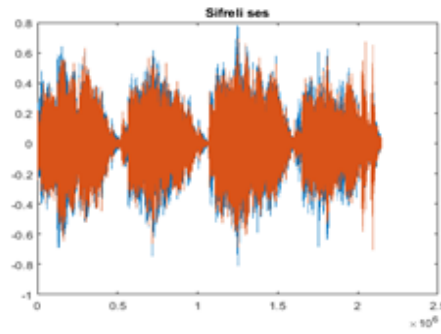


Fig. 4 The stego sound.

2.2. Decryption Algorithm

The decryption process is to decipher by applying in the reverse direction of steps in the encryption algorithm. The working principles of the decryption algorithm are as follows:

- The encrypted message is processed by the key in octal blocks.
- The entire key is implemented by converting the encrypted message into Binary in octal blocks.
- Using the LSB technique, to reach the hidden dividend - remainder values, the previously agreed standard value is saved in the file with the extension *.txt and the second key is entered into this file.

$$\text{➤ } A_n = \frac{K_n - K'_n}{256}$$

$$x_1 = 256 * dividend_1 + remainder_1$$

$$x_2 = 256 * dividend_2 + remainder_2$$

$$x_3 = 256 * dividend_3 + remainder_3$$

$$x_4 = 256 * dividend_4 + remainder_4$$

$$x_5 = 256 * dividend_5 + remainder_5$$

$$x_6 = 256 * dividend_6 + remainder_6$$

$$x_7 = 256 * dividend_7 + remainder_7$$

$$x_8 = 256 * dividend_8 + remainder_8$$

$$\sum_{n=1}^{\infty} K_n (n+3)! \frac{h^{n+3}}{n!} [16] \tag{2.1}$$

$$\sum_{n=1}^{\infty} K_n (n+3)! \frac{h^{n+3}}{n!} = x_1 h^4 + x_2 h^5 + x_3 h^6 + x_4 h^7 + x_5 h^8 + x_6 h^9 +$$

$$x_7 h^{10} + x_8 h^{11} [16] \tag{2.2}$$

For each value obtained from the Taylor equation above, their equivalents in Tab. 1 are found.

Step 1.

After the 8th character of the key is converted to binary (a_8), it is processed with the value (m_8) from Tab. 1;

a) If the number of 0 in the 8th character of the key is more than or equal to the number of 1;

- The last bit, the 8th character of the key, is taken first (a_8).
- The 1st value from Tab. 2.1 with the key is XOR (m_8).
- The transformed version (a_8) of the 8th character of the key and the transformed version (m_8) of the 1st value from Tab. 1 is XOR. Taking the last bit of the found value first, the 1st character of the message (1st step) is decoded (m_7).

b) If the number of 0 in the 8th character of the key is less than the number of 1;

- The leading bit of the 8th character of the key is taken to the end (a_8).
- With the key, XOR is applied to the first value from Tab.4 (m_8).
- The transformed version of the key's 8th character (a_8) and the transformed version of the 1st value from Tab. 1 (m_8) is XOR. Taking the first bit of the found value last, the 1st character of the message(1st step) is decoded (m_7).

The first character of the message is reached by performing similar operations with the other characters of the key.

After reaching the 1st character of the message, before the above steps are applied to the characters 2,3,4,5,6,7 and 8, XOR is performed with the value of the previous character from Tab. 1. Then, if the above steps are applied, the message is reached.

2.3. Comparison of Embedding and Decoding Time

The time analysis of the messages with AES into the audio file and embedding/decoding of the messages encrypted with the proposed method (PM) into the audio file and embedding/decoding was made according to the file sizes, the results are given in Tab. 2 and Tab. 3.

The graphics of these data are shown in Fig. 5 and Fig. 6.

Tab. 2 Data Embedding Time Analysis

File Name	File Size (Byte)	Embedding Time (Sec)	
		AES	PM
Test-1	50	50	80
Test-2	150	170	210
Test-3	300	440	460

Tab. 3 Audio decoding Time Analysis

File Name	File Size (Byte)	Decoding Time (Sec)	
		AES	PM
Test-1	50	161	140
Test-2	150	260	277
Test-3	300	392	365

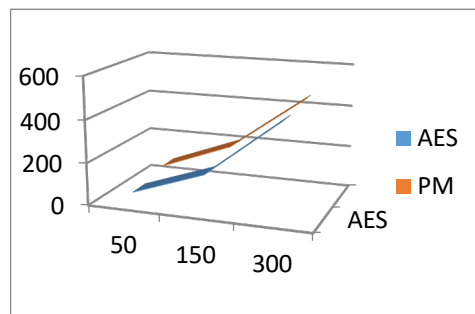


Fig. 5 Embedded Time/File Size

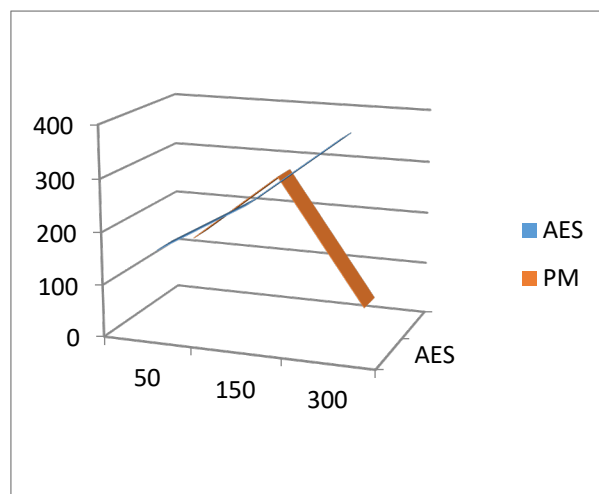


Fig. 6 Audio Decoding/File Size

2.4. Encryption

Key = Flr@tb3y Message = Steganog

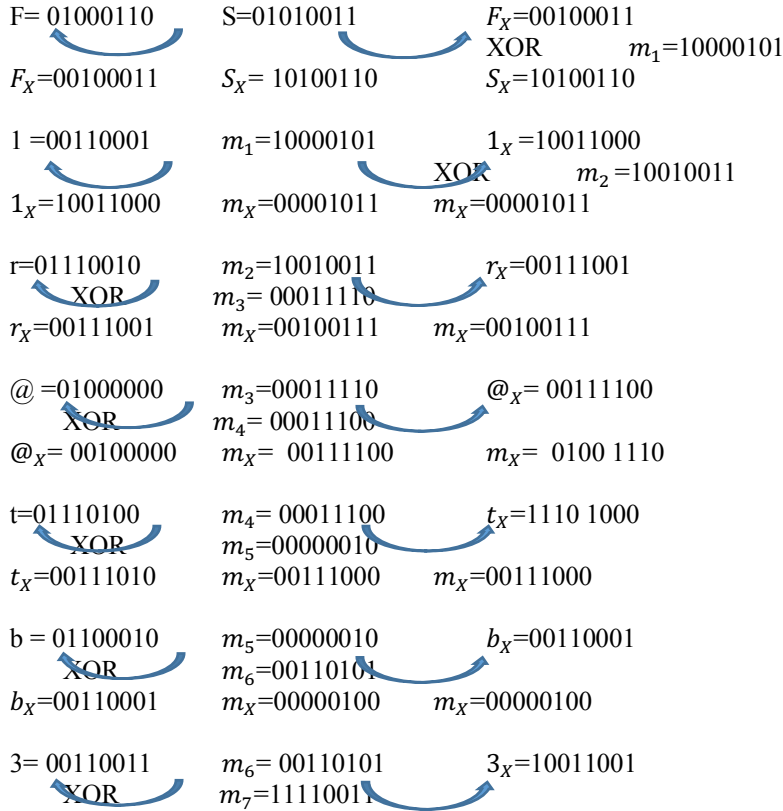
F=01000110 1=00110001 r =01110010 @=01000000
 t=01110100 b=01100010 3=00110011 y=01111001
 S=01010011 t=01110100 e=01100101 g=01100111
 a=01100001 n=01101110 o=01101111 g=01100111

The number of 0 and 1 numbers in the characters used as keys in the application is shown in Tab. 4.

Tab. 4 Number of 0 and 1 numbers in the key

		0 Number	1 Number
F	01000110	5	3
1	00110001	5	3
r	01110010	4	4
@	01000000	7	1
t	01110100	4	4
b	01100010	5	3
3	00110011	4	4
y	01111001	3	5

Step 1.



$$3_x = 10011001 \quad m_x = 01101010 \quad m_x = 01101010$$

$$y = 01111001 \quad m_7 = 11110011 \quad y_x = 11110010$$

XOR $m_8 = 00001011$ (1st Character)

$$y_x = 11110010 \quad m_x = 11111001 \quad m_x = 11111001$$

Step 2.

After the second character of the message with the result is XOR, it is processed with the key again.

$$t = 01110100 \quad \text{XOR} \quad t_x = 01111111$$

$$m_8 = 00001011$$

$$F = 01000110 \quad t_x = 01111111 \quad F_x = 00100011$$

XOR $m_1 = 11011101$
 $m_2 = 00100011$

$m_3 = 01111111$
 $m_4 = 11011110$

$m_5 = 10000111$
 $m_6 = 00111110$
 $m_7 = 11100101$

$$m_8 = 00000000 \text{ (2nd Character)}$$

Step 3.

After the third character of the message with the result is XOR, it is processed with the key again.

$$m_1 = 11101001$$

$$m_2 = 01001011$$

$$m_3 = 10101111$$

$$m_4 = 01111111$$

$$m_5 = 11000100$$

$$m_6 = 10111000$$

$$m_7 = 11101000$$

$$m_8 = 10000110 \text{ (3rd Character)}$$

In this way, $m_8 = 11111010$ (8th Character) is obtained in step 8.

Step 9.

The obtained results are equivalent to the s-box table (Tab. 5). The first 4 numbers are taken as rows and the last 4 numbers as columns.

Tab. 5 S-box List

	0000	0001	0010	0011	0100	0101	0110	0111	1000	1001	1010	1011	1100	1101	1110	1111
0000	1	181	120	169	38	245	76	242	230	39	72	78	47	33	239	249
0001	49	7	37	64	68	160	237	32	58	48	14	203	35	114	110	143
0010	119	23	6	12	220	109	44	61	215	202	159	45	29	250	157	235
0011	24	184	170	22	150	28	149	133	129	198	219	13	145	56	63	204
0100	212	97	201	5	15	177	234	122	50	0	113	102	253	106	36	168
0101	192	65	57	104	226	3	174	101	84	151	42	128	140	60	224	112
0110	207	53	46	95	131	243	87	118	175	164	69	55	178	247	79	126
0111	158	134	217	229	139	73	93	30	254	92	142	59	27	52	248	153
1000	240	121	189	196	138	165	130	228	11	144	34	147	25	194	137	100
1001	180	135	99	222	156	241	161	208	18	20	80	197	67	105	244	124
1010	221	74	211	167	85	115	183	251	111	51	16	108	200	233	205	66
1011	41	152	214	125	163	31	86	62	155	166	176	26	75	21	188	172
1100	232	96	4	216	238	54	107	210	171	9	195	103	8	88	141	10
1101	117	2	91	123	154	43	191	236	162	116	185	81	127	19	173	193
1110	82	252	246	83	190	187	186	136	223	71	70	218	182	225	89	146
1111	40	209	98	179	255	132	17	199	77	231	213	206	227	90	94	148

- 1st Character = 00001011 - 78
- 2nd Character = 00000000 - 1
- 3rd Character = 10000110 - 130
- 4th Character = 10100111 - 251
- 5th Character = 01101110 - 79
- 6th Character = 11011111 - 193
- 7th Character = 11110011 - 179
- 8th Character = 11111010 - 213

Step 10.

Taylor series is used in the encryption algorithm for the Laplace transform to be used in the algorithm. Firstly, the expanded Taylor series is taken with e^t .

$$f(x) = f(a) + \frac{f'(a)}{1!}(x - a) + \frac{f''(a)}{2!}(x - a)^2 + \dots + \frac{f^n(a)}{n!}(x - a)^n + \dots$$

$$= \sum_{n=0}^{\infty} \frac{f^n(a)}{n!}(x - a)^n \tag{3.1}$$

$$e^t = 1 + \frac{t}{1!} + \frac{t^2}{2!} + \frac{t^3}{3!} + \dots = \sum_{n=0}^{\infty} \frac{t^n}{n!} \tag{3.2}$$

Then, if it is expanded with t^3 , equation(3.3) is obtained;

$$t^3 e^t = t^3 + \frac{t^4}{1!} + \frac{t^5}{2!} + \frac{t^6}{3!} + \dots = \sum_{n=0}^{\infty} \frac{t^{n+3}}{n!} \tag{3.3}$$

As a result, $f(t)$ is obtained;

$$f(t) = \sum_{n=0}^{\infty} K_n \frac{t^{n+3}}{n!} .$$

The plain text "Steganag" to be encrypted corresponds to the numbers 78, 1, 130, 251, 79, 193, 179, 213.

$$K_0 = 78, K_1 = 1, K_2 = 130, K_3 = 251, K_4 = 79, K_5 = 193, K_6 = 179, K_7 = 213$$

$$\begin{aligned}
 f(t) &= \sum_{n=0}^{\infty} K_n \frac{t^{n+3}}{n!} \\
 &= K_0 \frac{t^3}{0!} + K_1 \frac{t^4}{1!} + K_2 \frac{t^5}{2!} + K_3 \frac{t^6}{3!} + K_4 \frac{t^7}{4!} + K_5 \frac{t^8}{5!} + K_6 \frac{t^9}{6!} \\
 &\quad + K_7 \frac{t^{10}}{7!}
 \end{aligned} \tag{3.4}$$

From hence;

$$\begin{aligned}
 [f(t)](h) &= T\left[\sum_{n=0}^{\infty} K_n \frac{t^{n+3}}{n!}\right](h) \\
 &= T\left[K_0 \frac{t^3}{0!} + K_1 \frac{t^4}{1!} + K_2 \frac{t^5}{2!} + K_3 \frac{t^6}{3!} + K_4 \frac{t^7}{4!} + K_5 \frac{t^8}{5!} + K_6 \frac{t^9}{6!} + K_7 \frac{t^{10}}{7!}\right](h) \\
 &= 78.3!h^3 + 1.4!h^4 + 130.5! \frac{h^5}{2!} + 251.6! \frac{h^6}{3!} + 79.7! \frac{h^7}{4!} + 193.8! \frac{h^8}{5!} + 179.9! \frac{h^9}{6!} + 213.10! \frac{h^{10}}{7!} \\
 &\quad \sum_{n=0}^{\infty} K_n (n + 3)! \frac{h^{n+3}}{n!} \\
 &= 468h^3 + 24h^4 + 7800h^5 + 30120h^6 + 16590h^7 + 64848h^8 + 90216h^9 + 153360h^{10}
 \end{aligned} \tag{3.5}$$

According to mod (256) in the series 468, 24, 7800, 30120, 16590, 64848, 90216, 153360;

Dividend; 1, 0, 30, 117, 64, 253, 352, 599

Remainder; 212, 24, 120, 168, 206, 80, 104, 16.

Step 11.

The obtained data is hidden in an audio file selected by LSB technique by using the 2nd key through a file with the extension * .txt.

2.5. Decryption

Step 1.

Using the 2nd key, the encrypted message is extracted from the audio file by the file with the * .txt extension.

As a result of the above steps, Dividends and Remainders are obtained as follow;

Dividend; 1, 0, 30, 117, 64, 253, 352, 599

Remainder; 212, 24, 120, 168, 206, 80, 104, 16.

Step 2.

$$\begin{aligned}
 A_n &= \frac{K_n - K'_n}{256} \\
 256 * 1 + 212 &= 468 \\
 256 * 0 + 24 &= 24 \\
 256 * 30 + 120 &= 7800 \\
 256 * 117 + 168 &= 30120 \\
 256 * 64 + 206 &= 16590
 \end{aligned}$$

$256 * 253 + 80 = 64848$
 $256 * 352 + 104 = 90216$
 $256 * 599 + 16 = 153360$
 468, 24, 7800, 30120, 16590, 64848, 90216, 153360 values are obtained.

$$\sum_{n=0}^{\infty} K_n(n+3)! \frac{h^{n+3}}{n!} \tag{3.6}$$

$$\begin{aligned}
 &= 468h^3 + 24h^4 + 7800h^5 + 30120h^6 + 16590h^7 + 64848h^8 + 90216h^9 + 153360h^{10} \\
 &= 78.3!h^3 + 1.4!h^4 + 130.5!h^5 + 251.6!h^6 + 79.7!h^7 + 193.8!h^8 + 179.9!h^9 + 213.10!h^{10}
 \end{aligned}$$

If we apply the Reverse Extended Force Series Transformation to both sides of the equation (3.6), equation (3.7) is obtained.

$$T^{-1} \left[\sum_{n=0}^{\infty} K_n(n+3)! \frac{h^{n+3}}{n!} \right] \tag{3.7}$$

$$= T^{-1} [78.3!h^3 + 1.4!h^4 + 130.5!h^5 + 251.6!h^6 + 79.7!h^7 + 193.8!h^8 + 179.9!h^9 + 213.10!h^{10}]$$

$$\sum_{n=0}^{\infty} K_n \frac{t^{n+3}}{n!} = 78.t^3 + 1.t^4 + 130.\frac{t^5}{2!} + 251.\frac{t^6}{3!} + 79.\frac{t^7}{4!} + 193.\frac{t^8}{5!} + 179.\frac{t^9}{6!} + 213.\frac{t^{10}}{7!}$$

Step 3.


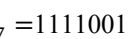






For each value obtained from the equation (3.7) equivalents in Table 3.2 are found.

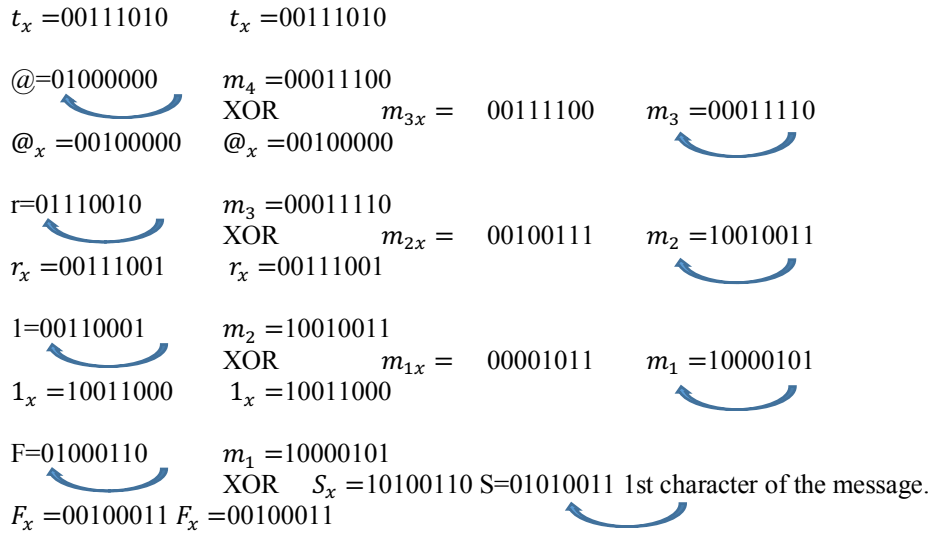
- 1st character = 78 - 00001011
- 2nd character = 1 - 00000000
- 3rd character = 130 - 10000110
- 4th character = 251 - 10100111
- 5th character = 79 - 01101110
- 6th character = 193 - 11011111
- 7th character = 179 - 11110011
- 8th character = 213 - 11111010

Step 4.

Key = Flr@tb3y

- 1st character = 00001011 2nd character = 00000000 3rd character = 10000110
- 4th character = 10100111 5th character = 01101110 6th character = 11011111
- 7th character = 11110011 8th character = 11111010

y=01111001	$m_8 = 00001011$		
	XOR	$m_{7x} = 11111001$	$m_7 = 11110011$
$y_x = 11110010$	$y_x = 11110010$		
3=00110011	$m_7 = 11110011$		
	XOR	$m_{6x} = 01101010$	$m_6 = 00110101$
$3_x = 10011001$	$3_x = 10011001$		
b=01100010	$m_6 = 00110101$		
	XOR	$m_{5x} = 00000100$	$m_5 = 00000010$
$b_x = 00110001$	$b_x = 00110001$		
t=01110100	$m_5 = 00000010$		
	XOR	$m_{4x} = 00111000$	$m_4 = 00011100$
			



Each character of the message is reached one by one by performing similar operations among other characters.

3. Experimental Results

Firstly, the message is encrypted then the encrypted message is hidden in the audio file. While the decryption process is being done, first the encrypted message is extracted from the audio file and then the encrypted message is decrypted. Data encryption based on the proposed algorithm has been performed in Fig. 7.

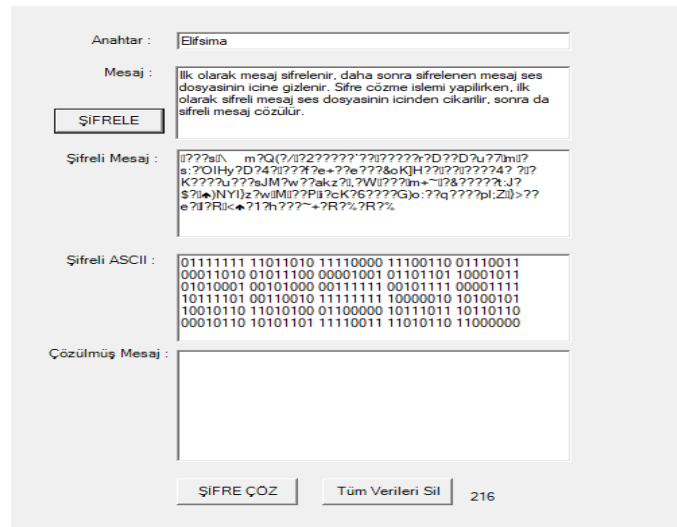


Fig. 7 Encryption screenshot

The encrypted data based on the proposed algorithm has been hidden in the audio file in Fig. 8.



Fig. 8 Screenshot of hiding encrypted data into audio.

4. Performance Analysis

In this technique, measures were taken against language frequency analysis attacks, which is one of the cryptanalysis techniques, by using the Taylor series. Various experimental attacks on the message encryption and hiding technique have been carried out. These attacks against the technique did not give any negative results. The equivalent of the same letter used in a word or a sentence is different values. Therefore, precautions were taken against the attacks of the language analysis method, which is one of the crypto attack techniques.

The encrypted data based on the proposed algorithm was attacked with the language analysis method in Fig. 9.

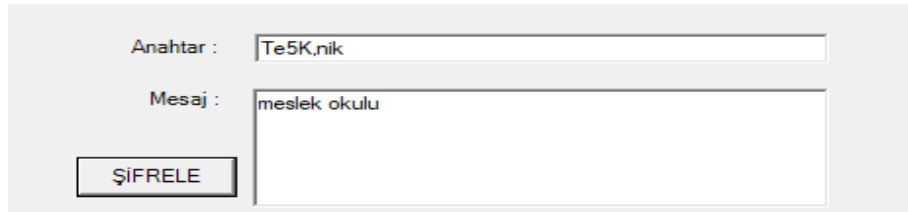


Fig. 9 Language analysis screenshot

12-3 | 104-7 | 92-28 | 56-64 | 2-73 | 224-301 | 40-179 | 112-413 | 64-866 | 112-1268 | 252-1038 | 72-213 | 32-853 | 192-2703 | 16-4064 | 32-478 as seen in the results of the examination, although the letters "e", "u", "l" are used twice in the sentence, all results show different values.

If against plain text attacks, which is another cryptanalysis method, first, the text is encrypted and then hidden in the audio, plain text attacks cannot be done. Even if the data hidden in the audio is reached, it has been tested that it is a powerful algorithm against plain text attacks thanks to the developed algorithm.

The encrypted data based on the proposed algorithm was attacked with plain text method in Fig. 10.

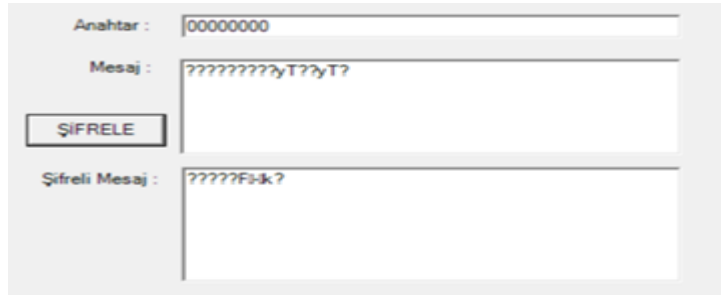


Fig. 10 Plain text attached screenshot

Since the encrypted message is concealed in the most meaningless bit of the sound, when the frequency analysis of the sound is made, no changes that can be seen with the eye as an image are encountered. This sentence is Turkish.

“Steganografinin amacı bilginin varlığın gizlemek veya bilgiyi fark edilmeden başka verinin içerisine yerleştirmektir. Güvenli şekilde gönderilmek istenen veriyi, dikkat çekmeyen görünüme sahip bir başka ortamda gizleyerek üçüncü şahısların gönderilen mesajın varlığından haberdar olması engellenir. Bu işlemler ile metin, ses, resim, video dosyaları içerisine veri gizleyebilmek mümkündür. Bu veriler herhangi bir metin dosyası olabileceği gibi, herhangi bir görüntü içerisine başka bir görüntüyü gizleme şeklinde de olabilmektedir. Yine aynı şekilde bir ses veya video dosyasının içine bir metin dosyası da saklanabilmektedir” text is encrypted as an application. Then this encrypted text is hidden in the audio file “ney sesi. wav”.

First, the data based on the proposed algorithm are encrypted and then hidden inside the sound using the LSB technique in Fig. 11.

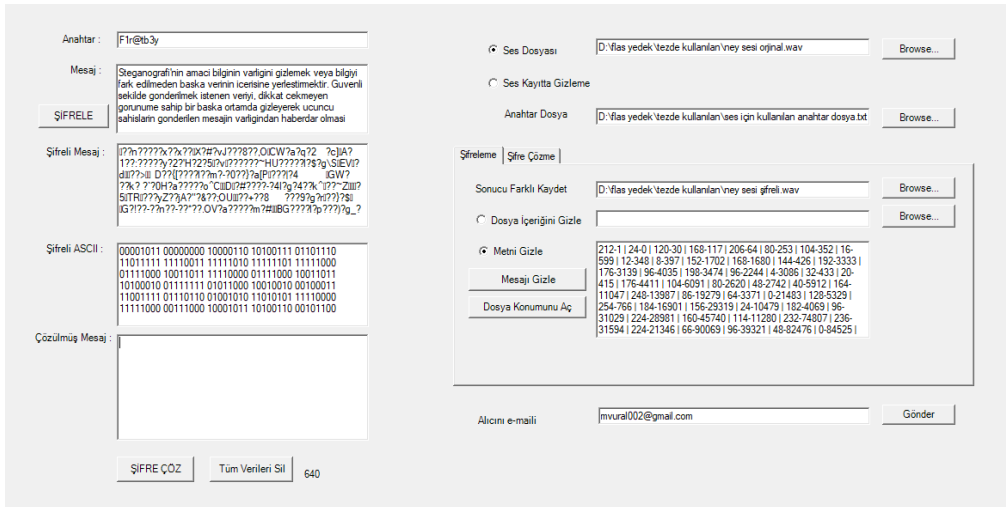


Fig. 11 Practice screenshot

The encrypted message can be hidden in the newly recorded audio file by opening the voice recorder instantly via the program as it is recorded in the audio file.

After saving the encrypted message in a file, optionally, the encrypted message can be hidden into sound in a file from (*.txt, *.xls, *.doc, etc.).

Thanks to the software written, when the program is taken over by unauthorized people, it can be determined who used the program and to whom the data was sent. This process has been added as a security measure. These follow-ups are performed only when used by unauthorized persons.

6. Conclusion and Discussion

By combining cryptography and steganography, a different perspective on cryptology has been introduced with this obtained hybrid model. In applications made with the proposed algorithm, it has been proven once again that mathematics is vital in the field of cybersecurity. Also, by expanding the proposed algorithm; It can be turned into an important defense system that can be used in cyber defense. Moreover, the mobile application of the proposed algorithm can be developed and presented as a commercial product, especially for use in instant communication. Plain text attacks have prevented with the proposed algorithm. Using the Taylor Series in the algorithm, the language analysis attack also has prevented.

Since the message encrypted with this developed algorithm is hidden, the data will not be available in the attacks. Even if hidden data are reached, meaningless values will be obtained because the data are encrypted using the mathematical function. This developed algorithm will make a significant contribution to data security. This is a hybrid model and is open to development. An attack was made with language frequency attack, explicit text attack and sound analysis methods to a text that was encrypted and hidden with the proposed method, as a result, our method was observed to be resistant to these attacks. Other attack techniques can be used to test the reliability of the algorithm. A new crypto device can be produced using the proposed method. Also, the developed algorithm can be used in biometric encryption or decryption.

Ethical approval: This article does not contain any studies with human participants performed by any of the authors.

References

- [1] Yıldırım M. Kriptolojiye Giriş Ders Notları, Uygulamalı Matematik Enstitüsü, 2004.
- [2] Vural M, Gençoğlu MT. Embedded Audio Coding Using Laplace Transform For Turkish Letters. Journal of the Technical University - Sofia Plovdiv branch, Bulgaria “Fundamental Sciences and Applications”,2018; 24:109-116.
- [3] Gençoğlu MT. Importance of Cryptography in Information Security. IOSR Journal of Computer Engineering, 2019; 21(1): 65-68.
- [4] Murray AH, Burchfield RW. The Oxford English Dictionary: Being a Corrected Re-issue. Clarendon Press, Oxford, 1933.
- [5] Weiss M. Principles of Steganography, Math 187: Introduction to Cryptography Professor Kevin O’Bryant, 2004.
- [6] Kadry S, Nasr S. New Generating Technique for Image Steganography. Lecture Notes on Software Engineering, 2013; 1(2):190-193.
- [7] Gençoğlu MT, Baleanu D. [Nonlinear Systems and Complexity](#) book series. In: Power Series Transform In Cryptology and ASCII, *Mathematical Methods In Engineering*. Springer, pp 67-74, 2018.
- [8] Memon N, Wong P. Protecting digital media content. Communications of the ACM 41(7): 34–43,1998.
- [9] Wang H, Wang S. Cyber Warfare: Steganography vs. Steganalysis, Communications of the ACM, 2004; 47(10): 6-82. <https://doi.org/10.1145/1022594.1022597>
- [10] Gençoğlu MT. Programming Encryption Algorithms with steganography. International Conference on Engineering Technology and Innovation, Sarajevo, 2017; 22-26 march, 58.
- [11] Anderson RJ, Petitcolas FAP. On the Limits of Steganography. IEEE Journal of Selected Areas in Communications, 1998; 16(4):474-481.
- [12] Bennett K. Linguistic steganography- survey, analysis and robustness concerns for hiding information in text. Tech Report, Purdue University, 2004.
- [13] Shahreza MS, Shahreza, MHS. Text steganography in SMS. International Journal of Network Security & Its Applications, 2007; 5(1): 2260-2265.
- [14] Gençoğlu MT. Combining Cryptography with Steganography. ITM Web of Conferences, 2017; <https://doi.org/10.1051/itmconf/01010>
- [15] Bhattacharyya S, Banerjee I, Sanyal G. A Novel Approach of Secure Text-Based Steganography Model using Word Mapping Method (WMM). International Journal of Computer and Information Engineering, 2010; 4(2): 96-103.
- [16] Gençoğlu MT. Embedded image coding using Laplace Transform for Turkish letters. Multimedia Tools and Applications, 2019; 78(13): 17521–1753.

- [17] Sellars D. An Introduction to Steganography, 1999. <http://www.cs.uct.ac.za/courses/CS400W/NIS04/papers99/dsellars/index.html>. Date of access: 01 January 2020.
- [18] Petitcolas FAP, Anderson RJ, Kuhn MG. Information Hiding- A Survey. *Process of IEEE*, 1999; 87(7): 1062-1078.
- [19] Huang X, Kawashima R, Segawa N, Abe Y. The Real-Time Steganography Based on Audio-to-Audio Data BitStream. Technical report of IEICE, ISEC, 2006; 106:15-22.
- [20] Jayaram P, Ranganatha HR, Anupama HS. Information hiding using audio steganography – a survey. *The International Journal of Multimedia & Its Applications*, 2011; 3(3):86-96. <https://doi.org/10.5121/ijma.2011.3308>
- [21] Cvejic N, Seppben T. Increasing the capacity of LSB-based audio steganography. Media Team Oulu Information Processing Laboratory University of Oulu FIN- 90014 Finland, 2002.
- [22] Qi YC, Ye L, Liu C. Wavelet domain audio steganalysis for multiplicative embedding model. *Proceedings of the International Conference on Wavelet Analysis and Pattern Recognition*, 2009; 429-432. <https://doi.org/10.1109/ICWAPR.2009.5207432>
- [23] Shahreza SS, Shalmani MTM. High capacity error-free wavelet domain speech steganography. *Acoustics, Speech and Signal Processing IEEE International Conference*, 2008; 223-227. <https://doi.org/10.1109/ICASSP.2008.4517963>
- [24] Choudry KN, Akash W. A Survey Paper on Video Steganography. *International Journal of Computer Science and Information Technologies*, 2015; 6 (3):2335-2338.

Performance Analysis of Various Classification Algorithms for Computer-Aided Breast Cancer Diagnosis System Using Thermal Medical Images

Muhammet BAYKARA

Software Engineering, Technology Faculty, Firat University, Elazig, Turkey
mbaykara@firat.edu.tr

(Geliş/Received: 03/01/2021;

Kabul/Accepted: 31/01/2021)

Abstract: One of the most widespread cancer types is breast cancer all over the world. It affects both women and men. Detection of cancer in early-stage is very critical in terms of treatment success. Many studies have been done in image processing, for the detection of cancer using computer-aided diagnosis systems. In this study, the performance of various classification algorithms in cancer detection was analyzed on a thermal image dataset. For this purpose, a graphical user interface based system was developed using MATLAB. The developed system uses five different algorithms; Decision Tree, Support Vector Machine (SVM), Logistic Regression Analysis, K Nearest Neighborhood (kNN), Linear Discriminant Analysis (LDA). According to the obtained results, kNN and SVM provide the best performance. The developed system can be used as an assistant system to produce an objective result for the expert in breast cancer diagnosis with the 98.8% success rate. This study contributes to the literature by using different methods compared to studies using the same dataset and increasing the performance of existing methods with hybrid approaches.

Key words: Image processing, breast cancer detection, thermal image analysis, image classification, feature extraction.

Termal Tıbbi Görüntüler Kullanılarak Bilgisayar Destekli Meme Kanseri Tanı Sistemi İçin Çeşitli Sınıflandırma Algoritmalarının Performans Analizi

Öz: Tüm dünyada en yaygın kanser türlerinden biri meme kanseridir. Hem kadınları hem de erkekleri etkiler. Kanserin erken dönemde tespiti tedavi başarısı açısından çok önemlidir. Görüntü işleme kanserin bilgisayar destekli teşhis sistemleri kullanılarak saptanması için birçok çalışma yapılmıştır. Bu çalışmada, kanser tespitinde çeşitli sınıflandırma algoritmalarının performansı termal bir görüntü veri setinde analiz edilmiştir. Bu amaçla, MATLAB kullanılarak grafik kullanıcı ara yüzü tabanlı bir sistem geliştirilmiştir. Geliştirilen sistem beş farklı algoritma kullanır; Karar Ağacı, Destek Vektör Makinesi (DVM), Lojistik Regresyon Analizi, K En Yakın Komşu (kNN), Lineer Diskriminant Analizi. Elde edilen sonuçlara göre kNN ve DVM en iyi performansı sağlar. Geliştirilen sistem, %98,8 başarı oranı ile meme kanseri teşhisinde uzmana objektif bir sonuç üretmek için yardımcı sistem olarak kullanılabilir. Bu çalışma literatüre, aynı verisetini kullanan çalışmalara göre farklı yöntemler kullanması ve mevcut yöntemlerin hibrit yaklaşımlarla başarılarının artırılması yönüyle katkı sağlamaktadır.

Anahtar kelimeler: Görüntü işleme, meme kanseri tespiti, termal görüntü analizi, görüntü sınıflandırma, özellik çıkarma.

1. Introduction

Today, breast cancer is still one of the most widespread cancer types [1], especially for women. Early detection of breast cancer is very vital in diagnosis and treatment. Studies have shown that new cancer cases and death rates due to cancer have been decreasing. This decrease is thought to be due to improvements in treatment, increased awareness, and early detection by screening [2]. To provide early detection many different biomedical imaging methods are used in cancer diagnosis. These methods include ultrasonography [1], mammography [2-4], thermography, tomography, and etc. techniques.

In this study, a novel software tool was developed to detect breast cancer using thermal images. This paper also presents a performance evaluation of classification algorithms for a computer-aided diagnosis system on thermal mammography images. For this purpose Decision Tree, SVM, Logistic Regression Analysis, kNN, Linear Discriminant Analysis algorithms are compared according to their accuracy performance. The aim of this paper is to develop a computer-aided diagnostic system that can detect cancer in the thermal breast image. In the proposed system, Machine Learning (ML) algorithms are used in the detection of cancer images and high performance is obtained. The developed system can provide high accuracy, autonomous control, speed, and objective evaluation for experts.

* Corresponding author: mbaykara@firat.edu.tr. ORCID: 0000-0001-5223-1343¹

Breast cancer is the most frequently encountered type of cancer in women today. Therefore, it is the leading cause of death due to cancer. Early diagnosis of it increases the effectiveness of treatment and increases the probability of complete healing. In the detection and diagnosis of it; mammography, ultrasonography, and magnetic resonance imaging are used [1-3, 5]. Cancer symptoms can be detected by mammogram images obtained using low-level X-ray radiation [6, 7]. For this reason, it is aimed to make use of methods such as image processing techniques, classification methods, and texture analysis and so on to diagnose this cancer early and go to the treatment part without wasting time. Many studies based on computer evaluation have been performed to help the expert physician in the interpretation of radiological images. This computer-assisted detection and diagnosis system (CAD) provides an increased success rate in the identification of diseases, such as breast cancer, for a specialist physician [8].

This paper is organized as follows. Section 2 provides a literature review on breast cancer detection with various techniques. Section 3 describes the proposed methodology and application. Evaluation and benchmarking of the results and relevant studies are given in Section 4. The conclusions are given in the last section.

2. Related Work

Recently, several studies have been done to detect breast cancer. These studies used different imaging techniques [1-4]. Huang et al. developed a web-based application [1] for the early detection and diagnosis of breast cancer. The main goal here is to interpret ultrasound images of the breast for enhancing the skills of the physicians on interpretation. Chougrad et al. [2] analyze the importance of transfer learning instead of random initialization for previously proposed CNN models and explore the effect of a well-adjusted number of layers on the results. They achieved 97.35% accuracy on the Digital Database for Screening Mammography (DDSM) database, 95.50% accuracy on the INbreast database, and 96.67% accuracy on the Breast Cancer Digital Repository (BCDR) database. Dhahbi et al. [3] investigated various gray-level texture analysis algorithms for the characterization of mammograms. This study emphasized that gray level texture features should be used together in order to reduce the false-positive level in cancer diagnosis systems.

Rezk et al. [4] developed a new data sampling method used to create samples on data distribution of binary patterns. Their method was applied in the classification of breast cancer images. The results show that their proposed method is efficient. Aswathy et al. [5] presented the current status and future possibilities for the detection of breast cancer. They specified that a new algorithm called visiopharm is used recently for a more objective diagnosis. Khalilabad et al. [6] focused on the detection of breast cancer type in their study. For this purpose, they developed a system to classify raw data related to cancer from microarray images and they achieved an accuracy of 95.23% in diagnosis.

It is difficult to evaluate mammographic X-ray images at first. An image defect occurs in images that are transferred from analog media to digital media. Various image filtering methods are used to enhance these images or reduce noise in these images [9-14]. Some of these filtering types are “imnoise”, “average”, “unsharp”, “gaussian”, and median filtering [15-17]. Filtering is basically obtained from the result of evaluating new values generated by changing pixel values. According to the new pixel values created in the images, the image can be made healthier by providing blurring, sharpening, increasing the brightness, understanding the color levels, and so on [18-21].

These images, which are brought to a healthy state, are then kept for processing by many classification methods. There are many types of classifications in the literature. One of these classification types is Artificial Neural Networks (ANN), which only work with digital information, have features such as information storage, learning using examples and generating information about unknown examples, classification, and shape completion. ANN can be applied to many fields from financial matters to engineering science, from production applications to fault detection and analysis in our daily life, and it has an important use in medical science. The predictive feature that ANNs are used extensively is used to estimate output from input values [23-27]. ANN uses the information provided to the network to estimate the output value corresponding to this information. ANN is used in the classification stage to remove tumors from mammographic images. Nowadays, many ANN models (Perceptron, Adaline, MLP (multilayer perceptron), LVQ (Learning vector quantization), Hopfield, Recurrent, SOM (Self-organizing map), ART (Adaptive resonance theory), and PCA (Principal component analysis)) have been developed for use with specific purposes and in various fields [28-32].

In addition, the Random Forest (RF) decision tree used in breast cancer detection distinguishes all nodes from each other by choosing the best of the randomly acquired attributes in each node, instead of dividing nodes selected from the best attributes in the data set. Each dataset is generated with displacement from the original dataset. Trees are developed using random property selection and there is no pruning. This is the reason why the RF is faster and more accurate than the other algorithms [3, 6, 12].

The most common methods used to classify medical images and diagnose the disease are kNN, SVM, and MLP [3, 4, 9, 15, 17]. Among other preferred methods, the C4.5 algorithm is a sort of decision tree-based classifier that takes the source from Quinlan's ID3 algorithm. The classifier constructs decision trees from a set of tagged training data using the concept of information gain. C4.5 is an algorithm generally used in medical data analysis. KNN is a classifier often used in pattern recognition. It uses similarity information to find neighbors [16]. In order to be able to say that a patient in breast cancer diagnosis belongs to a cancer patient, most of the k nearest neighbors must have cancerous specimens. SVM is not only for an early diagnosis of breast cancer but is also successful in many other classification problems [19, 23, 33-35].

Digitization and processing of pathologic data allow obtaining faster and more accurate results with computerized image analysis. With these techniques, diagnostic breast pathology assisted software has been continuously developed for years. In the literature, many techniques such as artificial intelligence, SVM, deep learning, ML, K-Nearest Neighbor algorithm (kNN), Naive Bayes, Linear Discriminant Analysis, and Logistic Regression have been used to achieve more accurate results [24, 33]. As can be seen from the literature studies, there are many systems used to provide datasets such as UCI [36-40]. In some studies, it has been focused on feature extraction methods and classification for malignant masses on mammograms image. For this purpose, methods such as the GLCM (gray level co-occurrence matrix), contourlet, discrete wavelet, ridgelet, and curvelet transform have been used additionally to help classification [8, 10, 11, 14].

The classification has an important place in ML and data mining. A decision tree is also one of the most popular learning models in data mining. Actually, the effectiveness of each algorithm used in classification depends on various configurations such as input property types and model parameters. Methods used to overcome model performance limitation, using a classification-based learning algorithm such as SVM to reduce diagnostic variance and improve diagnostic accuracy have been extensively used in breast cancer diagnosis [40-43].

Thermography is an imaging technique that can easily detect cancerous masses more quickly than conventional mammography. Progress in the IR (infrared) cameras used to obtain thermal images of the breasts and in the calculation tools used to accurately model the heat transfer within the breast has significantly increased the accuracy of the thermography [36]. Current studies have also explored the progress of using thermal and benefited from this progress. Ultrasonography techniques such as ultrasonography elastography, contrast-enhanced ultrasound, 3-D ultrasound, automated breast ultrasound and chest ultrasound have also been used in the studies. In proposed knowledge-based systems, many clinical decision support systems have been developed to assist health practitioners. In addition, ultrasound-guided breast biopsy and other imaging modalities, especially MRI (Magnetic resonance imaging) and ultrasound fusion have been used to detect chest diseases [24, 25, 26, 27, 34].

Although the most frequently used method for detecting breast cancer is the investigation of mammography, thermography performs better in the analysis of dense tissues. However, in the last two decades, many computer-assisted diagnostic systems have been proposed for the early detection of cancer. Mammogram-based classification, which consists of many stages such as feature extraction, classification, and segmentation, is an important and effective way to diagnose breast cancer in computer-aided diagnosis. Ultrasound used in CAD systems is one of the most commonly used methods to detect and diagnose breast tumors due to its inoffensiveness and low cost [37-42].

These studies suggest that ML approaches to diagnosing breast cancer are a powerful alternative to clinical methods and new studies are needed for better results [44-48]. In this context, Logistic Regression Analysis and LDA methods, which are not used in the literature, have also been used in this study. In the developed study, the most successful result with a 98.8% success rate was found with kNN.

3. Proposed Methodology and Application

Mammography is the most important imaging method that can be used for the early detection of cancer. With the use of images obtained by mammography, even small changes that cannot be detected by palpation can be

detected early. Therefore, mammography images should be analyzed in detail for the diagnosis of the disease. In the detection phase, breast cancer is often misdiagnosed by radiologists. Because mammograms are two-dimensional projections of a three-dimensional object. So superimposed textures may also produce some symptoms, as well as hide symptoms that do not exist. Hence, radiologists cannot detect real patients, and every year a certain number of patients suffer from it. Many biomedical image processing applications have been developed in order to simplify the work of the radiologists and to short the examination period.

In this study, a computer-aided diagnosis system was developed using thermal mammography images. Database for Mastology Research (DMR) database was used in the developed system. There are 3340 images of 287 people in the dataset images (Fig. 1), each with .txt extension at 640x480 pixels, taken at different numbers and angles. In the first stages of the study, various operations were performed on these images. These operations are preparation, pre-processing and segmentation, feature extraction, and classification. The aim of this section is to provide detailed information about these steps.

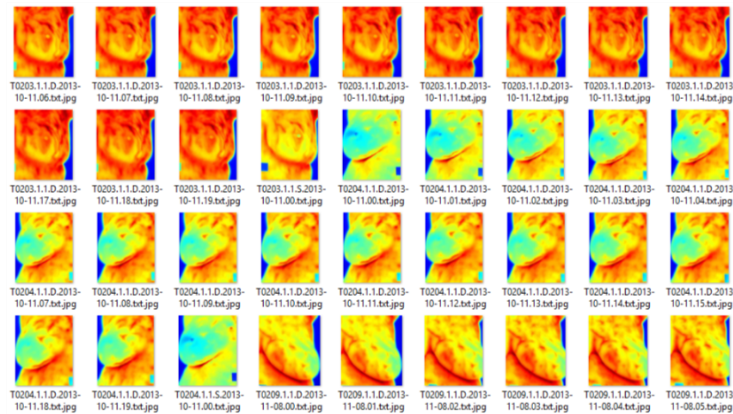


Figure 1. Image database.

During the preparation phase (step 1), filtering processes were performed for 3340 image files with the .txt extension in the dataset. First, the data in the form of a text file with a float value of 640x480 size has been imported into the system. This imported data is then transformed into a picture. However, when we convert the txt file to Image, it will be a grayscale image because it is a one-dimensional array. Since the operations will not perform on a grayscale image, the txt file will be read first and the highest value will be converted to red and the lowest value will be converted to blue to build an image file. Thus, thermal images will be obtained. After that, these thermal images cut out from the neck region and from the lower part in order to focus on the chest area. The obtained image is saved to use after the last phase of step 2, called "Horizontal projection analysis"

At the pre-processing and segmentation phase (step 2), it is aimed to obtain the image quality necessary for the system to be more accurate by eliminating the difficulties in diagnosis (noise, low contrast, etc.) on the digitized image. In addition, features not used on the image are removed. Cleaning the background noise will be useful for improving the image on the mammograms while protecting the details of the suspicious areas that can be detected as a tumor. For pre-processing, the image that was first converted to a thermal image was considered, and filtration was carried out. With filtering, each pixel value is recalculated as though there is a filter on the image. Filtering has done the processes such as sharpening the image, extracting certain details, smoothing the image, edge sharpening or edge detection. The obtained original image was converted to a gray tone to clearly select the chest area required for the detection step, and then noise removal was performed by centering the values of the pixels with this median filter method on the gray tone image. After the noise removal process, a clean image is obtained. It is then necessary to fill in the gaps in the image. For this, before the edge detection, the image is converted to a gray level. Later, the gray level image has been filled with white areas under the 50-pixel threshold. With the threshold process, objects in the image are separated from the image background. For thresholding, the image histogram that shows the gray level distributions in the image is utilized. After this method, edge detection is performed in the gray level image and the protrusions on the image are detected and the chest area is clearly

determined by Sobel Edge Detection. Then, a graph was created using the Horizontal Projection Analysis method and the pixel values at the peak points were determined, and then the chest region was clearly extracted by “imcrop” method by matching on the original thermal image that was mentioned in the last step of Step 1. After this process, the resulting image is divided into two parts using the “imcrop” method to be used in the feature extraction phase. A general working diagram is given in Fig. 2.

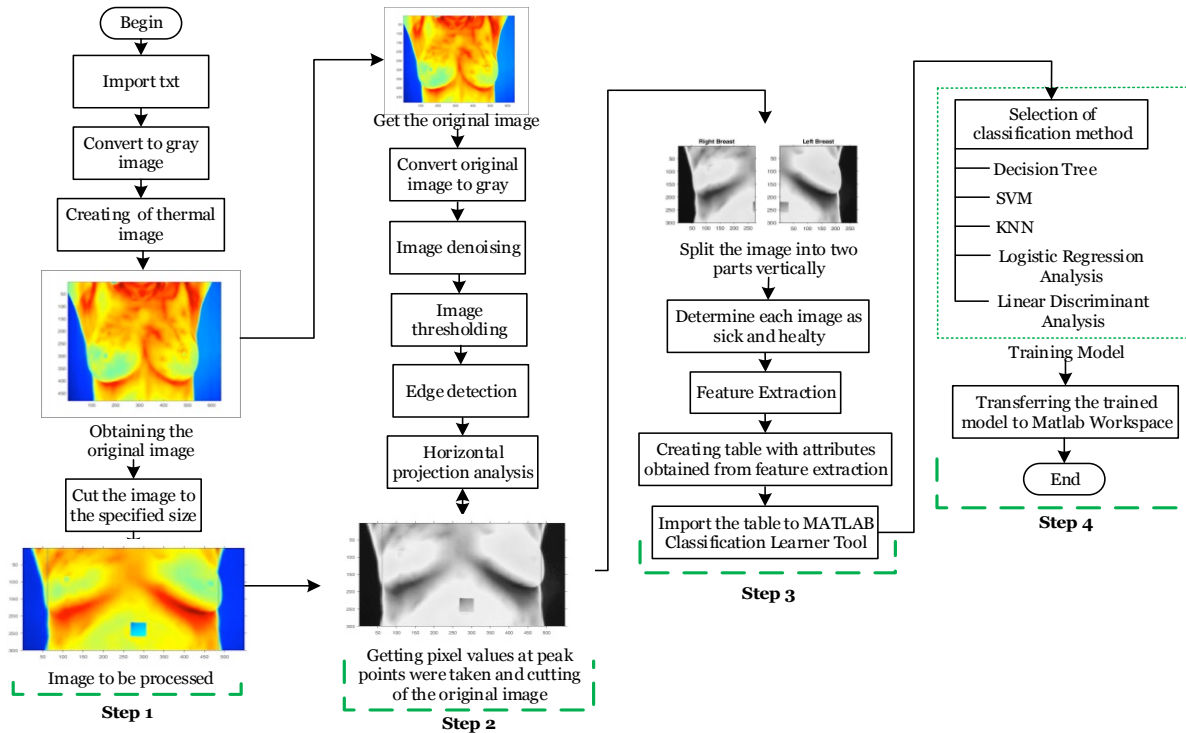


Figure 2. General working diagram of the developed system.

In the feature extraction section (step 3), feature extraction is performed on images divided into two parts. In the first phase of this section; Firstly, the images were compared with excel manually, looking at the ID numbers before dividing the images into two parts. According to the ID number of the patient whose breast was biopsied, the breast was determined to be sick. In other words, the breast that was biopsied determined as sick, and the others were determined as healthy by examining the attributes on excel. Thus, by dividing a patient's image into two, the total number of data, which has doubled in number, has become 3895. Here, in comparison with the excel table, 3098 healthy breasts and 797 diseased breasts were identified. After these operations, various textural attributes of each breast were obtained such as entropy, variance, standard deviation, contrast, homogeneity, kurtosis, skewness, correlation, energy. The obtained values were recorded in a table. The table was imported into the MATLAB Classification Learner Tool. The values calculated in the feature extraction stage are briefly explained in this section.

Entropy is the measure of image complexity. Complex tissues have higher entropy. Entropy is a statistical computation of randomness. It can be used to specify the texture of an image. Entropy is defined as $-\sum(p_i \cdot \log_2(p_i))$, where p_i defines the normalized histogram counts returned from the function of imhist.

Variance is the sum of the squares of the deviations of the data from the arithmetic mean. In other words, the variance is defined as the square of the standard deviation. The formula bellowed can be given as a definition of variance for a feature vector called A made up of N scalar observations.

$$V = \frac{1}{N-1} \sum_{i=1}^N |A_i - \mu|^2 \quad (1)$$

In this equation, μ is the mean of A.

$$\mu = \frac{1}{N} \sum_{i=1}^N A_i. \quad (2)$$

Kurtosis is a measure of the probability distribution of a real-valued random variable and an indication of the amount of change in the class. Kurtosis includes different ways of quantification for a theoretical distribution and appropriate estimation methods from a population sample.

$$k = \frac{E(x-\mu)^4}{\sigma^4} \quad (3)$$

Skewness is defined as the measure of the asymmetry of the data around the sample mean. When the skewness is negative, the spread of the data is greater towards the left of the center relative to the right. When the skewness is positive, spread to the right is greater. The skewness for a normal distribution or any perfectly symmetric distribution is zero. We can define the disruption of distribution as follows:

$$s = \frac{E(x-\mu)^3}{\sigma^3} \quad (4)$$

Mean returns the average values of items in an array along their different dimensions. In the form, it is shown that for a random variable vector of N scalar observations, the average is found.

$$\mu = \frac{1}{N} \sum_{i=1}^N A_i. \quad (5)$$

Standard deviation can be defined as the square root of the average of the differences of each number on a group of numbers with the mean. To calculate the standard deviation;

- The arithmetic mean of the numbers is calculated.
- For each number, the difference from the arithmetic means is calculated.
- The square of each difference is calculated.
- The squares of the differences are summed.
- The sum obtained is divided by the previous number of the total count of the elements in the series
- The square root of the found number is taken.

$$S = \sqrt{\frac{1}{N-1} \sum_{i=1}^N |A_i - \mu|^2} \quad \text{where } \mu \text{ is the mean of A} \quad (6)$$

RMS (root mean square) is a statistical value used to measure the magnitude of varying amounts. It is useful in waves where the change is positive and negative. A changing function can be calculated for the continuous value series. The square root comes from taking the square root of the average of the mean squares. The average square root level of an x vector:

$$x_{RMS} = \sqrt{\frac{1}{N} \sum_{n=1}^N |x_n|^2} \quad (7)$$

It is expressed as the sum performed over the specified dimension.

Contrast is a calculation of image variation and image contrast.

$$\sum_{i,j} |i - j|^2 p(i,j) \quad (8)$$

Correlation: Correlation is the calculation of image linearity. Linear structures in the Φ direction lead to large correlation values in this direction.

$$\frac{\sum_i \sum_j (i - \mu_i)(j - \mu_j) N_d[i,j]}{\sigma_i \sigma_j} \quad (9)$$

Energy is the measure of image homogeneity. For the more homogeneous image, energy has a larger value.

$$\sum_{i,j} p(i,j)^2 \quad (10)$$

Homogeneity is a measure of similarity in different regions of the image. As the object size gets smaller, the homogeneity in the object will increase accordingly. The heterogeneous structure of different spectral properties and classes in these objects during the selection of large objects influences the classification accuracy.

$$\sum_i \sum_j \frac{N_d[i,j]}{1+|i-j|} \quad (11)$$

In the classification section (step 4) ML methods are used. ML is a kind of method that aims to give computers the ability to learn. ML provides learning skills such as prediction, diagnosis, detection and recognition using statistics, optimization, programming and many more disciplines. ML is basically divided into two groups such as supervised and unsupervised learning. Firstly data is given to the system in supervised learning, then data that the system has never seen is expected to be known over the previous data, similar to the artificial neural network. In unsupervised learning, data is clustered with the help of the distribution of the data features, similar to k-means clustering. Artificial neural networks, Bayesian decision theory, clustering, statistical discriminant analysis, multi-layered networks, and hidden Markov models have widely used ML techniques, and each technique has its advantages and disadvantages in terms of performance.

As mentioned in the previous section, a total of 11 different features were extracted from each image. There are 3895 images in the image database. The size of the dataset is totally 3895x12 because one extra column is for the result (Fig. 3). The cross-validation method has been preferred to train and test the system.

With cross-validation, the data set is divided into a number of parts, one of which is used for testing, and the other parts are used for training. In this study, k value was chosen as 5 for cross validation. In the next stage, another part is used for testing while the other parts are used for training. As can be seen in Figure 4 this process continues for all parts.

Data set

Workspace Variable: Features (3895x12 table)

Response: Diagnosis (double, 0 .. 1)

	Name	Type	Range
<input type="checkbox"/>	Diagnosis	double	0 .. 1
<input checked="" type="checkbox"/>	Entropy	double	5.57542 .. 6.84208
<input checked="" type="checkbox"/>	Variance	double	7467.98 .. 12844.9
<input checked="" type="checkbox"/>	Kurtosis	double	1.15414 .. 1.87034
<input checked="" type="checkbox"/>	Skewness	double	-0.561238 .. 0.557481
<input checked="" type="checkbox"/>	Mean	double	97.925 .. 164.167
<input checked="" type="checkbox"/>	StandartDeviation	double	86.4175 .. 113.335
<input checked="" type="checkbox"/>	RMS	double	12.0586 .. 15.541
<input checked="" type="checkbox"/>	Contrast	double	0.068665 .. 0.387312
<input checked="" type="checkbox"/>	Correlation	double	0.980064 .. 0.996436
<input checked="" type="checkbox"/>	Energy	double	0.173037 .. 0.351346
<input checked="" type="checkbox"/>	Homogeneity	double	0.934846 .. 0.981837

Validation

Cross-Validation
Protects against overfitting by partitioning the data set into folds and estimating accuracy on each fold.

Cross-validation folds: 5 folds

Holdout Validation
Recommended for large data sets.

Percent held out: 25%

No Validation
No protection against overfitting.

Response variable is numeric. Distinct values will be interpreted as class labels.

Figure 3. Feature extraction from the dataset.

Diagnosis	Entropy	Variance	Kurtosis	Skewness	Mean	Standard	RMS	Contrast	Correlatio	Energy	Homogeneity
1	6.382179	9864.648	1.606388	-0.42113	152.6657	99.32071	14.32094	0.143684	0.991052	0.221453	0.969636816
1	6.294064	10354.97	1.508547	-0.3921	150.8107	101.7591	14.2102	0.104337	0.993821	0.222368	0.97326389
1	6.368711	9875.018	1.601532	-0.41447	152.1913	99.3729	14.29881	0.139078	0.991331	0.218729	0.970520497
1	6.273599	10343.87	1.508562	-0.3888	150.6141	101.7046	14.20311	0.103589	0.993855	0.222208	0.973894538
1	6.374852	9907.613	1.586333	-0.40043	151.4516	99.53676	14.2854	0.136741	0.991516	0.217708	0.970858363
1	6.279064	10413.14	1.492118	-0.38101	150.2886	102.0445	14.20555	0.103589	0.9939	0.223405	0.973470132
1	6.361803	9962.298	1.575009	-0.39503	151.0938	99.81108	14.26819	0.13698	0.991539	0.217335	0.970815717
1	6.27979	10459.7	1.482115	-0.37376	149.8565	102.2725	14.18872	0.102717	0.993978	0.223671	0.973913576
1	6.351475	10010.05	1.565464	-0.39162	150.9	100.05	14.25539	0.136549	0.991609	0.217478	0.970576034
1	6.277286	10462.69	1.479804	-0.36981	149.6448	102.287	14.18216	0.103839	0.993923	0.223418	0.973634181
1	5.868081	12422.43	1.218631	-0.19014	136.5699	111.4557	13.14352	0.090005	0.995528	0.292125	0.976404999
1	5.851778	12057.31	1.24339	-0.08595	130.4701	109.8055	12.97495	0.083451	0.995685	0.270957	0.975639049
1	6.110144	11314.2	1.368582	-0.28159	140.7132	106.368	13.41375	0.120606	0.993391	0.245043	0.963403044
1	6.228667	10802.83	1.41381	-0.23446	140.3816	103.9364	13.70881	0.123852	0.992893	0.230497	0.960153091
1	6.056771	11356.39	1.355762	-0.25235	139.1217	106.5661	13.35642	0.116476	0.99362	0.245642	0.964977037
1	6.235295	10893.77	1.393537	-0.21308	139.4956	104.373	13.68237	0.115629	0.993415	0.232331	0.962122779
1	6.079482	11353.37	1.341554	-0.21388	137.2334	106.5519	13.32566	0.118209	0.993528	0.24369	0.965118772
1	6.204321	11005.77	1.366239	-0.16311	136.9302	104.9082	13.6167	0.121007	0.993179	0.233309	0.962171623
1	6.075595	11344.29	1.341034	-0.20553	136.8762	106.5093	13.32264	0.11754	0.993552	0.242865	0.96575132
1	6.219178	11039.37	1.35722	-0.14943	136.2226	105.0682	13.605	0.121663	0.993169	0.233526	0.962218907
1	6.09722	11334.78	1.331888	-0.17159	135.2493	106.4647	13.31197	0.118848	0.993482	0.241913	0.964717418
1	6.217624	11149.85	1.334054	-0.11128	134.3651	105.5926	13.56511	0.118137	0.993444	0.234807	0.962471386
1	6.078416	11339.16	1.330881	-0.16457	134.8649	106.4853	13.29332	0.11702	0.993575	0.241284	0.96555677
1	6.207025	11166.33	1.333252	-0.10741	134.0603	105.6706	13.54251	0.1195	0.993374	0.235983	0.963168223
1	6.094008	11331.42	1.326978	-0.14622	134.0085	106.4489	13.28987	0.119184	0.993457	0.24006	0.964445255
1	6.201555	11214.58	1.324655	-0.09479	133.4761	105.8987	13.53539	0.118556	0.993456	0.236914	0.962901423
1	6.085801	11341.99	1.327341	-0.14967	134.1805	106.4985	13.29307	0.116594	0.993606	0.241707	0.965302876
1	6.208531	11213.94	1.3243	-0.09649	133.5159	105.8956	13.53364	0.119507	0.993402	0.236406	0.962853717

Figure 4. Feature values of the images from GLCM method.

3.1 Decision Tree

Decision trees are a commonly used data mining approach to classification and estimation. Although other methodologies, such as neural networks, can be used for classification, decision trees provide an advantage for decision-makers in terms of ease of interpretation and intelligibility. The decision tree technique is a two-step process using learning and classification. In the developed project, training data which is known in the learning step is analyzed by the classification algorithm in order to construct the model. The learned model is shown as a classification rule or decision tree. In the classification step, the test data is used to determine the accuracy of the classification rules or decision tree. If accuracy is acceptable, rules are used to classify new data. It should be determined which areas in the training data will be used in which order to build the tree. The most commonly used measurement for this purpose is entropy. The result obtained using the area where the entropy measure higher, is uncertain and unstable. For this reason, at the root of the decision tree, the fields with the least Entropy measure are used [3], [6].

3.2 Support Vector Machine

SVM is a ML algorithm based on convex optimization working by the principle of structural risk minimization. The SVM algorithm is a distribution independent learning algorithm because it does not need any joint distribution function knowledge related to the data. In this algorithm, each data item is drawn as a point in n-dimensional space (where n is the number of properties we have), along with the value of each feature whose value is a specific coordinate value. The classification is then performed by finding the hyperplane, which distinguishes the two classes very well. The SVM developed for binary classification essentially separates the data with a plane that can be expressed by a linear equation such as $wTx+b=0$. Here, w defines the d-dimensional coefficient vector, x defines the data, and b defines an offset value. Linear SVM provides finding the separation plane with optimizing the objective function using quadratic optimization [17, 19].

SVM is a structured learning procedure in statistical learning theory. Instead of minimizing the squared error of the data sets, SVM minimizes the limit on the generalization error. Therefore, it gives successful results also for the data apart from the training set. There are three main stages in SVM classification: (1) defining the training cells as feature vectors, (2) mapping feature vectors to feature space using kernel functions, and (3) creating n-dimensional hyperplanes that best separate classes. SVMs have been proposed for solving classification and curve-fitting problems based on statistical learning theory and minimizing the structural risk. This learning method is considered as supervised learning method. In supervised learning, it is known that the data belong to which classes. The SVM separates the data provided as input into two classes [23].

3.3 Logistic Regression Analysis

It is a regression method in which the expected values of the response variable are obtained as probabilities according to the explanatory variables. Simple and multiple regression analyses are used to analyze the mathematical relationship between the dependent variable and the explanatory variable or variables. Logistic regression analysis is a regression method that helps to perform classification and assignment. There is no assumption of normal distribution and continuity. The effects of the explanatory variables on the dependent variable are obtained as probabilities and the risk factors are determined as probabilities. Discriminant analysis is a method of classifying data and assigning it to specific classes according to certain possibilities. It is possible to determine the effects of the variables in the data set to the classification by the logistic regression [45, 46].

3.4 K Nearest Neighborhood (kNN)

KNN algorithm is in the supervised learning category between ML algorithms. KNN algorithm can be used for classification. In this algorithm, the output is a class membership. An element is classified by a majority vote of its neighbors, with the element being assigned to the class most common among its k nearest neighbors. It can also be used for the prediction of continuous values. This value is the average of the values of its k nearest neighbors.

The kNN algorithm can be summarized as [17]:

1. k value is specifies as a positive integer value
2. The k entries are selected among our data which is closest to the new sample (Euclidean distance)
3. The most common classification of these entries is found. The distances are sorted and k objects are selected at the nearest distance.
4. This is the classification that is given to the new sample

3.5 Linear Discriminant Analysis

LDA is a classification method developed by R. A. Fischer in 1936. Although it is a simple method, it provides good results in complex problems. Discriminant analysis is a common classification algorithm, and it is fast, accurate and easy to interpret. It is also good for large data sets. The discriminant analysis assumes that different classes form data based on different Gaussian distributions. To train a classifier, it estimates the parameters of a Gaussian distribution for each class. There are two discriminant types such as linear and quadratic discriminant. The LDA defines the following score function [47, 48].

$$Z = \beta_1 x_1 + \beta_2 x_2 + \dots + \beta_d x_d \quad (12)$$

$$S(\beta) = \frac{\beta^T \mu_1 - \beta^T \mu_2}{\beta^T C \beta} \quad (\text{Score function}) \quad (13)$$

$$S(\beta) = \frac{\bar{Z}_1 - \bar{Z}_2}{\text{The variance of } Z} \quad (14)$$

Score function, predicts the linear coefficients that maximize the problem score. Formulation: where β is linear model coefficients; C_1, C_2 are covariance matrices; μ_1, μ_2 are average vectors

$$\beta = C^{-1}(\mu_1 - \mu_2) \quad \text{Model coefficients} \quad (15)$$

$$C = \frac{1}{n_1 + n_2} (n_1 C_1 + n_2 C_2) \quad \text{Covariance matrices} \quad (16)$$

The way to determine the best discrimination is to calculate the Mahalanobis distance between the two groups. The fact that Mahalanobis distance is less than three indicates that the probability of misclassification is very small.

$$\Delta^2 = \beta^T (\mu_1 - \mu_2), \quad (17)$$

Δ : Mahalanobis difference between two groups

Finally, if the following condition is satisfied, a new incoming property is classified.

$$\beta^T \left(x - \left(\frac{\mu_1 + \mu_2}{2} \right) \right) > \log \frac{p(c_1)}{p(c_2)}, \quad (18)$$

Here, β is a coefficient vector, x is a data vector, μ_1, μ_2 are average vectors, p is class probabilities.

3.6 Using Gabor Filter for Feature Extraction

The Gabor filter method, developed by Dennis Gabor, describes the signals of frequency and time (or space) with minimum uncertainty. Gabor filters are band-pass filters that can select frequency and direction. Gabor filter is the product of Gaussian function and sinusoidal plane wave. The Gabor function is calculated by multiplying the Gaussian function with a complex exponential function. Gabor filters have different uses for an application in computer vision and image processing. Examples include tissue recognition and classification, type identification, texture separation, edge detection, image compression, motion estimation, object identification and shape recognition in the tissue. Visual cortex using the direction-selective feature of the Gabor filter performed increased the use of these methods in computer vision and digital image processing. The Gabor filter also allows access to local frequency information from an image. In contrast to the Fourier analysis, which determines the representation of a global frequency area of the whole image, the Gabor filter gives a result in the spatial field, calculating the power of certain frequency belts and the predictions in each position on the image. The number of Gabor filters varies for different applications. 5-scale and 10-oriented 39x39 filters are used for filtering. These filters, images to be feature extracted, and the number of steps are sent to the Gabor function for the feature extraction operation. The length of the property vector is calculated as $(m * n * u * v) / (d1 * d2)$. “m” and “n” represents the x and y dimension of the image. “u” represents the number of scales and v represents the number of orientations in the filters. “d1” and “d2” represent the sub-sampling factor along the row and column.

In the previous part, breast images were divided into two groups as right and left. The sizes of these images were not very important for feature extraction. However, when sub-sampling with the Gabor filter, the number of properties (or feature vector size) extracted from each image is variable due to the size of these images. For this reason, while x features were extracted from an image, x + y (y ≠ 0) or x - y (y = 0) features were extracted from another image. When these properties were extracted and collected in a data set, the resultant part of the data set in a given column or row was different in the feature vector.

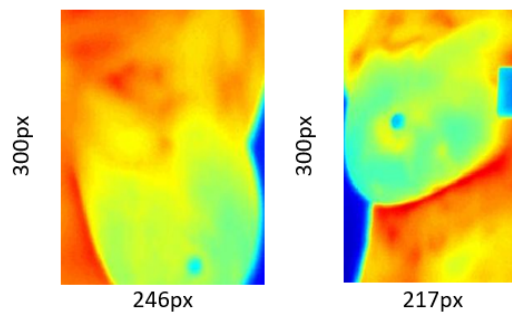


Figure 5. Preparing images for Gabor filter.

3000 features were taken from constant Gabor variables determined from Figure 5, Image 1 above, while 2700 different properties were extracted from the 2nd image using the same variables. The dataset formed by feature vectors has an irregular structure as all images may vary in size. To solve this problem, the average height and width values of all images were taken. These values were observed to be 300x220. The image size is resized to 300x220 before the feature is extracted from an image. Thus, data should be recovered from the irregular form as given in Table 1. So it is made regular as in Table 2.

Table 1. Non-Uniform dataset

X1	X2	X3	X4	...	y
X1	X2	...	y		
X1	X2	X3	...	y	

Table 2. Uniform dataset

X1	X2	X3	X4	...	y
X1	X2	X3	X4	...	y
X1	X2	X3	X4	...	y

Gabor filter is created after all the images are fixed to the same size. This filter takes 4 variables. These variables are (m, n, u, v).

- u: Number of scales (generally set to 5)
- v: Number of directions (generally set to 8)
- m: Number of lines in the 2-D Gabor filter (generally set to 39 and preferred to be an odd number)
- n: Number of columns in a 2-D Gabor filter (generally set to 39 and preferred to be an odd number)

In this section, the parameters m, n, u, v are set as 5, 10, 39, 39 respectively. Figure 6 shows Gabor Filters with five scale and ten orientations.

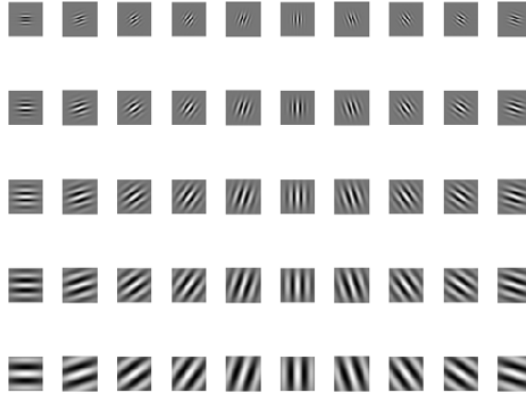


Figure 6. Gabor filters

These filters are sent to the Gabor feature extraction function. This function takes 4 parameters as input and returns the feature vector. These parameters which taken as input are named as I, Gabor Filter, d1, and d2 respectively. Here "I" represents the image, "gaborFilter" represents the filters created in the previous function, "d1" and "d2" represent the sub-sampling factor to be applied across the rows and columns of the image. In addition, this function accepts a grayscale image as input. Filters are applied to the image in the matrix in which the filters are kept.

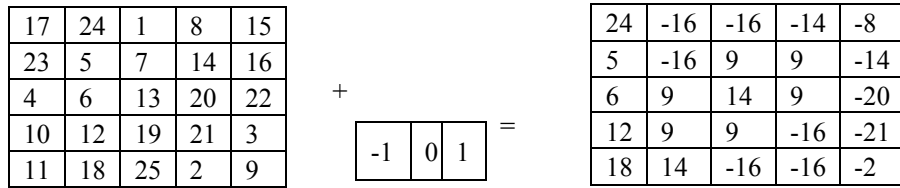


Figure 7. Gabor filter example.

As it can be seen in Figure 7, the last two cells of the filter and the values in the first two pixels of the image are multiplied first and then collected and written to the first pixel of the filtered image. So $(17 * 0) + (24 * 1) = 24$ is in the form. Then the filter is shifted one step to the right and the same operation is repeated. It continues as like $(17 * (-1)) + (24 * 0) + (1 * 1) = -16$. In this section, all the filters created in the mammography image are applied in order (Figure 8).

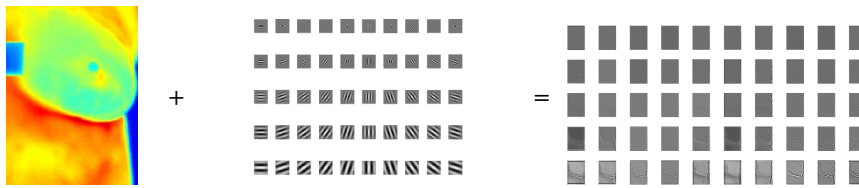


Figure 8. Gabor filter application to the mammography image.

The following operations are applied to the filtered images. (Step 1-5)

1. The absolute value of the image is taken. This eliminates negative values in the pixel values.
2. Sub-samples of all rows are taken according to the $d1$ variable specified in the image.
3. Transpose of sub-samples are made, and sub-samples are taken according to $d2$ variable.
4. The obtained two-dimensional sub-sample space is made one-dimensional and added to the feature vector.
5. Move to the next filtered image and the same steps are performed.

The above application of operations is as follows. Consider the image in row 5 and column 1 of the filtered images.

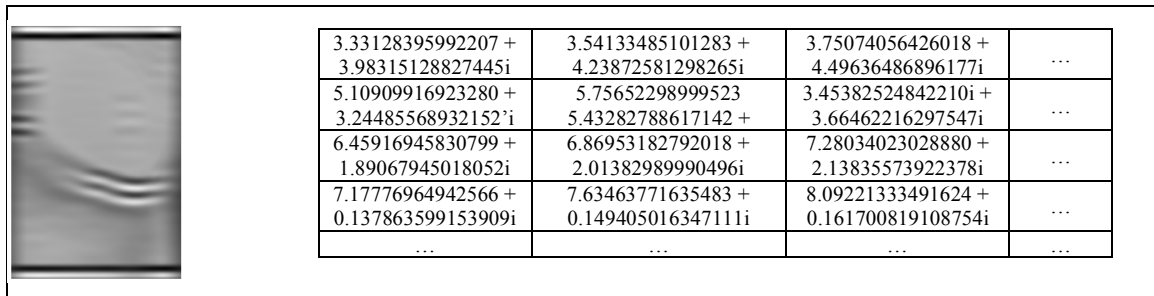


Figure 9. The pixel values of the filtered image.

As shown in Figure 9, the pixel values of the filtered image consist of complex numbers. The absolute value of the image is taken to eliminate this complexity. The absolute value for complex values is defined as

$$|a+bi| = \sqrt{a^2 + b^2} \tag{19}$$

5.19258577270 674	5.52339108199 333	5.85536948579 851	...
6.05243610173 437	6.43774243717 468	6.82400267670 776	...
6.73019605022 571	7.15862964543 911	7.58787975235 724	...
7.17909350212 043	7.63609945711 143	8.09382874866 381	...
...

Figure 10. Absolute value for the image.

The sub-samples are taken at the d1 rate of each column of the absolute value as given in Figure 10. “d1” and “d2” were taken as 8 in this section. The sub-samples will be taken as 1., 9., 17., 25...., and all values will be taken by increasing in d1 ratio. In this way, only the rows with multiples of 8 will be kept. As a result of this process, a picture with a size of 300x220 is reduced to a size of 38x300. Transposition of the 38x300-sized image created in “Step 2” is taken. The result is 300x38-sized. The same steps as in step 2 are performed again. But the ratio here is “d2” and may differ from “d1”. D1 is the same for this project. As a result of the process, a 28x38 image was created. This image matrix will then be called the future. The values in the 2-dimensional (28x38) matrix created in step 3 are converted to a one-dimensional matrix. As a result of this process, a 1064x1 matrix is formed. This matrix is the feature vector obtained from the filtered image. The next filtered image is selected and all steps are repeated. The feature vector of that filtered image obtained in “Step 4” is added to the feature vector of the actual image. These operations continue and the feature vector of the image (actual image) to which the filters are applied is obtained. In total (1064+1064+...) x1 = 53200 features are obtained. The above steps continue with the next image. After all the images are completed, a feature vector consists of 3895 x 53200. After this step, the column 53201 is added to decide whether the breast is diseased or not. (0 for patient breasts, 1 for healthy breasts). This data set is divided into a 5-fold cross-validation method and training and test data are separated by the Fine kNN algorithm. As a result of the training, 98.7% (Figure 11) success rate was achieved.

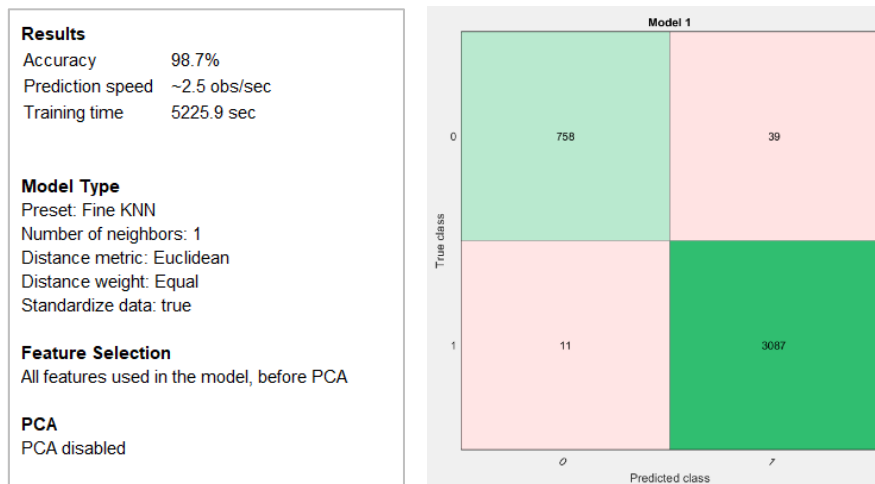


Figure 11. The accuracy result of Gabor-Fine kNN.

In order to increase the success rate, a second training was carried out on the same data set. In this training, 69% of the data using PCA were kept in those with a variance of 69%. In the above study, the number of the nearest neighbors in the kNN algorithm was 1, while this rate was 3 in the second training. At the end of the second

Performance Analysis of Various Classification Algorithms for Computer-Aided Breast Cancer Diagnosis System Using Thermal Medical Images

training, the success rate increased from 98.7% to 98.8% (Figure12). The details of the second training are given below.

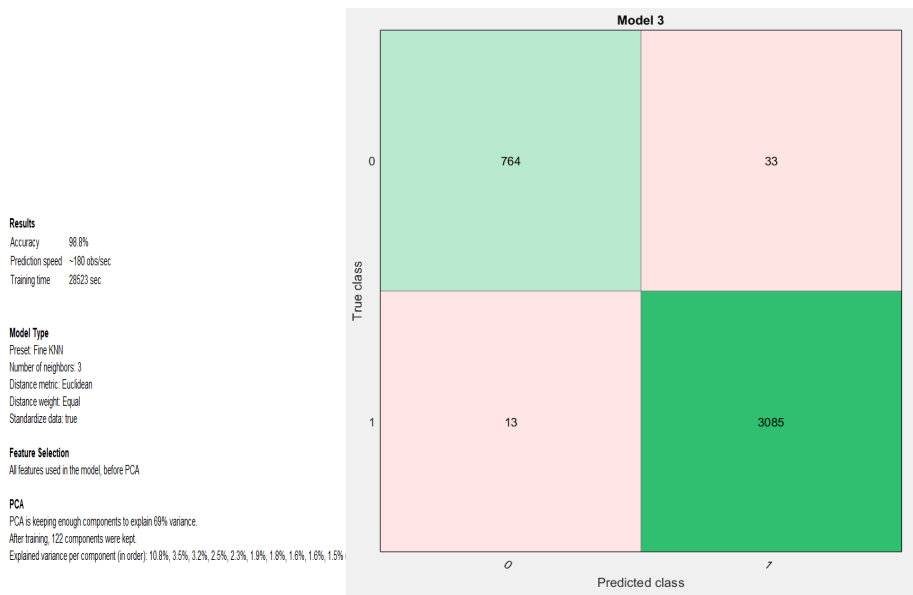


Figure 12. The accuracy result of Gabor-Fine kNN with PCA.

Figure 13 shows the implementation of the 2D-Gabor filter and kNN. Figure 14 shows the MATLAB GUI for the developed software.

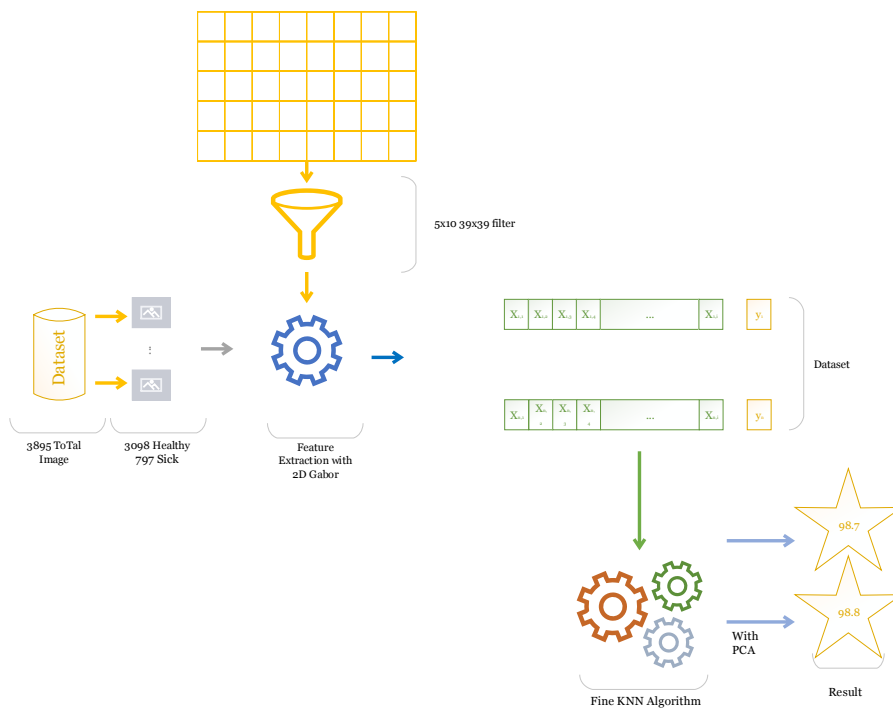


Figure 13. Implementation of 2D-Gabor filter and kNN.

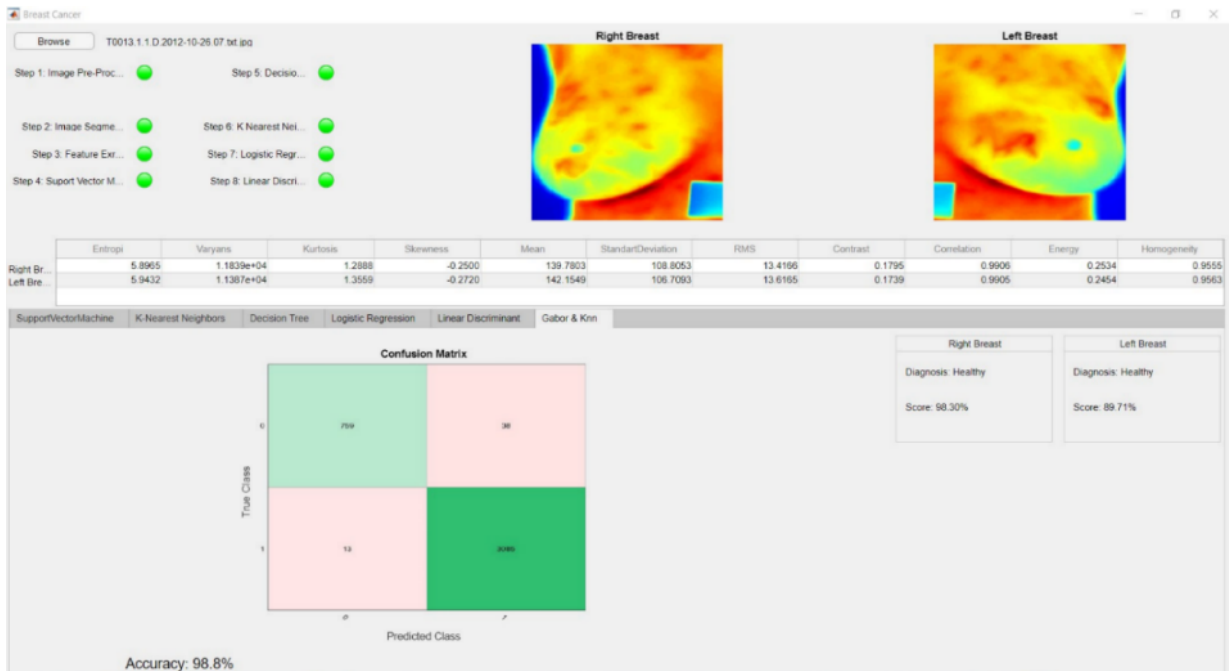


Figure 14. MATLAB GUI for the developed software

4. Evaluation and Benchmarking

In the classification of medical images and disease diagnosis; kNN, SVM and MLP are widely used. Of the preferred methods, the C4.5 algorithm is a sort of decision-tree-based classifier originating from the Quinland ID3 algorithm. The classifier constructs decision trees from a set of labeled training data using the concept of knowledge gain. C4.5 is an algorithm commonly used in medical data analysis. kNN is a classifier based on majority voting, which is commonly used in pattern recognition. KNN, which is classified according to the class of neighbors, uses similarities in finding neighbors. In order to be able to tell that a patient is a cancer patient in the diagnosis of breast cancer, most of the nearest neighbors should be cancerous. When the studies were examined, it was observed that the SVM method was not only useful for the result in early diagnosis of breast cancer but also many other classification problems. In addition, studies in the literature have shown that ML approaches in breast cancer diagnosis provide a strong alternative to clinical methods and new studies are needed for better results. Table 3 gives a detailed comparison between the studies have done before and the current study present in this paper. In this study, methods such as Logistic Regression Analysis and LDA which were not used before in early diagnosis of breast cancer were used.

In this study, both GLCM and Gabor were investigated and performed in the feature extraction section. Similarly, many methods have been tried in the classification phase. When GLCM is used in feature extraction, performance is lower (96.1%). So Gabor filter is more effective than the GLCM. The most successful result with the 98.8% performance rate was obtained with kNN in the classification. Table 4 gives a comparison of the performance analysis of the relevant studies. As can be seen from Table 3 and Table 4, the current study has more methods than the others. And the performance is higher than the related studies.

Table 3. A comparison of the relevant studies on breast cancer detection

Author(s)	Year	Specification	Used Database	Method	Application Environment
Chougrad H. et al. [2]	2018	Computer-aided Diagnosis (CAD) to help classify mammography mass lesions	DDSM, BCDR, INbreast, The Merged Dataset (MD)	Convolutional Neural Networks (CNN)	Breast Cancer
Dhabbia S. et al. [3]	2018	Reducing false positives in CAD systems for cancer diagnosis	DDSM	Random Forest, SVM, Decision Tree	Breast Cancer
Rezk E. et al. [4]	2017	Data sampling and classification for cancer	MITOS 2012 dataset3	NB, SVM, Pattern net (PN), Cascade forward net (CFN), Feed forward net (FFN)	Breast Cancer
Aswathy M. A. et al. [5]	2016	Cancer detection on digital images	Special Collected Data	General Classifier Neural Network (GCNN)	Breast Cancer
Khalilabad N. D. et al. [6]	2016	Fully automatic classification of microarray images	Stanford Microarray Database (Stanford, 2015)	Decision Tree	Breast Cancer
Saha M. et al. [7]	2017	Efficient deep learning model for mitosis detection	MITOS-ATYPIA-14, ICPR-2012, AMIDA-13	F-score	Breast Cancer
Wang P. et al. [9]	2016	Automatic quantitative image analysis technique of BCH images	Dataset not specified	Wavelet decomposition and multi-scale region-growing (WDMR), Double-strategy splitting model (DSSM), Curvature Scale Space (CSS), SVM, Chain-like agent genetic algorithm (CAGA).	Breast Cancer
Berbar M. A. et al. [11]	2018	Hybrid methods for feature extraction in classification	DDSM, MIAS	ST-GLCM, GLCM, Wavelet-CT1 and Contourlet (CT2)	Breast Cancer
Carvalho E. D. et al. [12]	2018	Method of differentiation of benign and malignant masses in digital mammograms using texture analysis based on phylogenetic diversity	DDSM, MIAS	Random Forest, Neural Network, MLP, SMO	Breast Cancer
Sun W. et al. [15]	2017	A graph based semi-supervised learning scheme using deep CNN for cancer detection	L denote labeled dataset and U denote unlabeled dataset	ANN, SVM and CNN algorithms	Breast Cancer
Majid A. et al. [17]	2014	Prediction of breast and colon cancers from imbalanced data	Cancer/non-cancer (C/NC), breast/nonbreast cancer (B/NBC) and colon/non-colon cancer (CC/NCC)	K-Nearest Neighbor and SVM	Breast and Colon Cancers
Sampaio W. B. et al. [19]	2015	Detection of masses in mammograms with adaption to breast density	DDSM	Genetic Algorithm, Phylogenetic Trees, LBP and SVM	Breast Cancer
Cheng H.D. et al. [23]	2010	Automated detection and classification using ultrasound images	Dataset not specified	Linear classifiers, Artificial neural networks, Bayesian neural networks, Decision tree, SVM, Template matching, Human classifier	Breast Cancer
Nilashi M. et al. [26]	2017	A knowledge-based system	Wisconsin Diagnostic Breast Cancer (WDBC) and Mammographic mass datasets	Fuzzy logic method	Breast Cancer
Rastghalam R. et al. [28]	2016	Cancer detection using MRF-based probable texture feature and decision-level fusion-based classification using HMM on thermography images	Dataset not specified	Hidden Markov Model (HMM)	Breast Cancer
Mohammed M. A. et al. [32]	2018	Neural network and multi-fractal dimension features	Dataset of Breast Cancer Department of the Oncology Specialist Hospital in Baghdad, Iraq	Neural network and multi-fractal dimension features	Breast Cancer
Lee M. Y. et al. [34]	2010	For breast cancer diagnosis using standardized thermograph images	Thermograph images of unspecified sources	Entropy and decision tree induction	Breast Cancer
Francis S. V. et al. [35]	2014	Detection of cancer from rotational thermography images	Dataset not specified	SVM	Breast Cancer
EtehadTavakol M. et al. [36]	2013	Cancer detection thermal images using bispectral invariant features	Dataset not specified	Adaboost classifier	Breast Cancer
Abdel-Nasser M. et al. [37]	2016	Automatic nipple detection in breast thermograms	Proeng database	Multi-layer perceptron (MLP)	Breast Cancer
Elyasi I. et al. [41]	2016	Speckle reduction in breast cancer ultrasound images	Dataset not specified	Homogeneity Modified Bayes Shrink (HMBS)	Breast Cancer
Singh B. K. et al. [43]	2017	Risk stratification of 2D ultrasound-based breast lesions		Back-propagation artificial neural network (BPANN) and SVM	Breast Cancer

				The database of 178, B-mode breast ultrasound images			
Baykara M.* [current study]	2021	Computer assist system design in breast cancer diagnosis	DMR (Database Mastology Research)	For	Decision Tree, Regression Analysis, Discriminant Analysis	SVM, kNN, Linear	Logistic Breast Cancer

Table 3. A comparison of the performance analysis of the relevant studies

Relevant Studies	Classification Method				
	SVM	kNN	Decision Tree	Logistic Regression	Linear Discriminant
Baykara M. [Current Study]	95,6	98,8	91,2	80,3	80,5
Dhahbia S. et al. [3]	80,01	X	79,12	X	X
Rezk E. et al. [4]	78	X	X	X	X
Khalilabad N. D. et al. [6]	X	X	95,23	X	X
Wang P. et al. [9]	96,19	X	X	X	X
Sun W. et al. [15]	85,52	X	X	X	X
Majid A. et al. [17]	95,18	93,47	X	X	X
Sampaio W. B. et al. [19]	92,99	X	X	X	X
Cheng H.D. et al. [23]	94,25	X	96	X	X
Lee M. Y. et al. [34]	X	X	90	X	X
Francis S. V. et al. [35]	83,3	X	X	X	X
Singh B. K. et al. [43]	94,4	X	X	X	X

5. Conclusion

Image processing methods provide the development of a computer-aided diagnostic system to assist the expert in cancer diagnosis. With the use of intelligent methods, the performance of these diagnostic systems is increasing in recent years. In particular, methods such as ANN, CNN, and SVMs are the most popular methods that increase diagnostic success.

In this study, new effective software is developed for detecting breast cancer. Additionally, this paper presents a performance evaluation of classification algorithms for a computer-aided diagnosis system on thermal mammography images. The implemented software can be used detection and diagnosis of breast cancer in an early stage. It provides an objective result with good accuracy for the expert in breast cancer diagnosis. In order to reach the best classification results in this study, very different structures have been tried both as a feature extraction method and as a classification method. In the feature extraction phase, both the GLCM-derived properties and the Gabor filter were used. For classification, SVM, kNN, Decision Tree, Logistic Regression, Linear Discriminant methods were used given in Table 4. In the study, feature extraction was first done with GLCM and the classification was done by the methods mentioned above. Then the attributes extracted by the Gabor filter are used for feature extraction and the classification was done by the methods mentioned above. The success rates achieved by using the GLCM method are lower. This means that the values obtained with Gabor are enhancing the classification performance.

The developed system is a sufficiently high-performance expert system to classify thermal medical images. In future works, it is planned to develop high-performance computer-aided diagnostic systems by using some deep learning methods.

References

- [1]. Huang, Q., Huang, X., Liu, L., Lin, Y., Long, X., & Li, X. (2018). A case-oriented web-based training system for breast cancer diagnosis. *Computer Methods and Programs in Biomedicine*, 156, 73–83. <http://doi.org/10.1016/j.cmpb.2017.12.028>.

- [2]. Chougrad, H., Zouaki, H., & Alheyane, O. (2018). Deep Convolutional Neural Networks for breast cancer screening. *Computer Methods and Programs in Biomedicine*, 157, 19–30. <http://doi.org/10.1016/j.cmpb.2018.01.011>
- [3]. Dhahbi, S., Barhoumi, W., Kurek, J., Swiderski, B., Kruk, M., & Zagrouba, E. (2018). False-positive reduction in computer-aided mass detection using mammographic texture analysis and classification. *Computer Methods and Programs in Biomedicine*, 160, 75–83. <http://doi.org/10.1016/j.cmpb.2018.03.026>
- [4]. Rezk, E., Awan, Z., Islam, F., Jaoua, A., Al Maadeed, S., Zhang, N., Rajpoot, N. (2017). Conceptual data sampling for breast cancer histology image classification. *Computers in Biology and Medicine*, 89(July), 59–67. <http://doi.org/10.1016/j.compbiomed.2017.07.018>
- [5]. Aswathy, M. A., & Jagannath, M. (2016). Detection of breast cancer on digital histopathology images: Present status and future possibilities. *Informatics in Medicine Unlocked*, 8(October 2016), 74–79. <http://doi.org/10.1016/j.imu.2016.11.001>
- [6]. Khalilabad, N. D., Hassanpour, H., & Abbaszadegan, M. R. (2016). Fully automatic classification of breast cancer microarray images. *Journal of Electrical Systems and Information Technology*, 3(2), 348–359. <http://doi.org/10.1016/j.jesit.2016.06.001>
- [7]. Saha, M., Chakraborty, C., & Racoceanu, D. (2018). Efficient deep learning model for mitosis detection using breast histopathology images. *Computerized Medical Imaging and Graphics*, 64(June 2017), 29–40. <http://doi.org/10.1016/j.compmedimag.2017.12.001>
- [8]. Robertson, S., Azizpour, H., Smith, K., & Hartman, J. (2018). Digital image analysis in breast pathology—from image processing techniques to artificial intelligence. *Translational Research*, 194, 19–35. <http://doi.org/10.1016/j.trsl.2017.10.010>
- [9]. Wang, P., Hu, X., Li, Y., Liu, Q., & Zhu, X. (2016). Automatic cell nuclei segmentation and classification of breast cancer histopathology images. *Signal Processing*, 122, 1–13. <http://doi.org/10.1016/j.sigpro.2015.11.011>
- [10]. Peng, L., Chen, W., Zhou, W., Li, F., Yang, J., & Zhang, J. (2016). An immune-inspired semi-supervised algorithm for breast cancer diagnosis. *Computer Methods and Programs in Biomedicine*, 134(61472092), 259–265. <http://doi.org/10.1016/j.cmpb.2016.07.020>
- [11]. Berbar, M. A. (2018). Hybrid methods for feature extraction for breast masses classification. *Egyptian Informatics Journal*, 19(1), 63–73. <http://doi.org/10.1016/j.eij.2017.08.001>
- [12]. Carvalho, E. D., de Carvalho Filho, A. O., de Sousa, A. D., Silva, A. C., & Gattass, M. (2018). Method of differentiation of benign and malignant masses in digital mammograms using texture analysis based on phylogenetic diversity. *Computers & Electrical Engineering*, 67(November 2017), 210–222. <http://doi.org/10.1016/j.compeleceng.2018.03.038>
- [13]. Cherif, W. (2018). Optimization of K-NN algorithm by clustering and reliability coefficients: application to breast-cancer diagnosis. *Procedia Computer Science*, 127, 293–299. <http://doi.org/10.1016/j.procs.2018.01.125>
- [14]. Li, Y., Chen, H., Rohde, G. K., Yao, C., & Cheng, L. (2015). Texton analysis for mass classification in mammograms. *Pattern Recognition Letters*, 52, 87–93. <http://doi.org/10.1016/j.patrec.2014.10.008>
- [15]. Sun, W., Tseng, T. L. B., Zhang, J., & Qian, W. (2017). Enhancing deep convolutional neural network scheme for breast cancer diagnosis with unlabeled data. *Computerized Medical Imaging and Graphics*, 57, 4–9. <http://doi.org/10.1016/j.compmedimag.2016.07.004>
- [16]. Yassin, N. I. R., Omran, S., El Houbby, E. M. F., & Allam, H. (2018). Machine learning techniques for breast cancer computer-aided diagnosis using different image modalities: A systematic review. *Computer Methods and Programs in Biomedicine*, 156, 25–45. <http://doi.org/10.1016/j.cmpb.2017.12.012>
- [17]. Majid, A., Ali, S., Iqbal, M., & Kausar, N. (2014). Prediction of human breast and colon cancers from imbalanced data using nearest neighbor and support vector machines. *Computer Methods and Programs in Biomedicine*, 113(3), 792–808. <http://doi.org/10.1016/j.cmpb.2014.01.001>
- [18]. Sayed, A. M., Zaghoul, E., & Nassef, T. M. (2016). Automatic Classification of Breast Tumors Using Features Extracted from Magnetic Resonance Images. *Procedia Computer Science*, 95, 392–398. <http://doi.org/10.1016/j.procs.2016.09.350>
- [19]. De Sampaio, W. B., Silva, A. C., De Paiva, A. C., & Gattass, M. (2015). Detection of masses in mammograms with adaption to breast density using genetic algorithm, phylogenetic trees, LBP and SVM. *Expert Systems with Applications*, 42(22), 8911–8928. <http://doi.org/10.1016/j.eswa.2015.07.046>
- [20]. Dora, L., Agrawal, S., Panda, R., & Abraham, A. (2017). Optimal breast cancer classification using Gauss–Newton representation based algorithm. *Expert Systems with Applications*, 85, 134–145. <http://doi.org/10.1016/j.eswa.2017.05.035>
- [21]. Pak, F., Kanan, H. R., & Alikhassi, A. (2015). Breast cancer detection and classification in digital mammography based on Non-Subsampled Contourlet Transform (NSCT) and Super Resolution. *Computer Methods and Programs in Biomedicine*, 122(2), 89–107. <http://doi.org/10.1016/j.cmpb.2015.06.009>

- [22]. Dehghan Khalilabad, N., & Hassanpour, H. (2017). Employing image processing techniques for cancer detection using microarray images. *Computers in Biology and Medicine*, 81(December 2016), 139–147. <http://doi.org/10.1016/j.compbimed.2016.12.01>
- [23]. Cheng, H. D., Shan, J., Ju, W., Guo, Y., & Zhang, L. (2010). Automated breast cancer detection and classification using ultrasound images: A survey. *Pattern Recognition*, 43(1), 299–317. <http://doi.org/10.1016/j.patcog.2009.05.012>
- [24]. Bhardwaj, A., & Tiwari, A. (2015). Breast cancer diagnosis using Genetically Optimized Neural Network model. *Expert Systems with Applications*, 42(10), 4611–4620. <http://doi.org/10.1016/j.eswa.2015.01.065>
- [25]. Kandlikar, S. G., Perez-Raya, I., Raghupathi, P. A., Gonzalez-Hernandez, J. L., Dabydeen, D., Medeiros, L., & Phatak, P. (2017). Infrared imaging technology for breast cancer detection – Current status, protocols and new directions. *International Journal of Heat and Mass Transfer*, 108, 2303–2320. <http://doi.org/10.1016/j.ijheatmasstransfer.2017.01.086>
- [26]. Nilashi, M., Ibrahim, O., Ahmadi, H., & Shahmoradi, L. (2017). A knowledge-based system for breast cancer classification using fuzzy logic method. *Telematics and Informatics*, 34(4), 133–144. <http://doi.org/10.1016/j.tele.2017.01.007>
- [27]. Guo, R., Lu, G., Qin, B., & Fei, B. (2018). Ultrasound Imaging Technologies for Breast Cancer Detection and Management: A Review. *Ultrasound in Medicine and Biology*, 44(1), 37–70. <http://doi.org/10.1016/j.ultrasmedbio.2017.09.012>
- [28]. Rastghalam, R., & Pourghassem, H. (2016). Breast cancer detection using MRF-based probable texture feature and decision-level fusion-based classification using HMM on thermography images. *Pattern Recognition*, 51, 176–186. <http://doi.org/10.1016/j.patcog.2015.09.009>
- [29]. Karabadjji, N. E. I., Seridi, H., Bousetouane, F., Dhifli, W., & Aridhi, S. (2017). An evolutionary scheme for decision tree construction. *Knowledge-Based Systems*, 119, 166–177. <http://doi.org/10.1016/j.knosys.2016.12.011>
- [30]. Wang, H., Zheng, B., Yoon, S. W., & Ko, H. S. (2018). A support vector machine-based ensemble algorithm for breast cancer diagnosis. *European Journal of Operational Research*, 267(2), 687–699. <http://doi.org/10.1016/j.ejor.2017.12.001>
- [31]. Kaymak, S., Helwan, A., & Uzun, D. (2017). Breast cancer image classification using artificial neural networks. *Procedia Computer Science*, 120, 126–131. <http://doi.org/10.1016/j.procs.2017.11.219>
- [32]. Mohammed, M. A., Al-Khateeb, B., Rashid, A. N., Ibrahim, D. A., Abd Ghani, M. K., & Mostafa, S. A. (2018). Neural network and multi-fractal dimension features for breast cancer classification from ultrasound images. *Computers and Electrical Engineering*, 0, 1–12. <http://doi.org/10.1016/j.compeleceng.2018.01.033>
- [33]. Karabatak, M. (2015). A new classifier for breast cancer detection based on Naïve Bayesian. *Measurement: Journal of the International Measurement Confederation*, 72, 32–36. <http://doi.org/10.1016/j.measurement.2015.04.028>
- [34]. Lee, M. Y., & Yang, C. S. (2010). Entropy-based feature extraction and decision tree induction for breast cancer diagnosis with standardized thermograph images. *Computer Methods and Programs in Biomedicine*, 100(3), 269–282. <http://doi.org/10.1016/j.cmpb.2010.04.014>
- [35]. Francis, S. V., Sasikala, M., Bhavani Bharathi, G., & Jaipurkar, S. D. (2014). Breast cancer detection in rotational thermography images using texture features. *Infrared Physics and Technology*, 67, 490–496. <http://doi.org/10.1016/j.infrared.2014.08.019>
- [36]. Etehadtavakol, M., Chandran, V., Ng, E. Y. K., & Kafieh, R. (2013). Breast cancer detection from thermal images using bispectral invariant features. *International Journal of Thermal Sciences*, 69, 21–36. <http://doi.org/10.1016/j.ijthermalsci.2013.03.001>
- [37]. Abdel-Nasser, M., Saleh, A., Moreno, A., & Puig, D. (2016). Automatic nipple detection in breast thermograms. *Expert Systems with Applications*, 64, 365–374. <http://doi.org/10.1016/j.eswa.2016.08.026>
- [38]. Li, J. B., Wang, Y. H., & Tang, L. L. (2012). Mammogram-based discriminant fusion analysis for breast cancer diagnosis. *Clinical Imaging*, 36(6), 710–716. <https://doi.org/10.1016/j.clinimag.2012.01.041>
- [39]. Li, J. B., Peng, Y., & Liu, D. (2013). Quasiconformal kernel common locality discriminant analysis with application to breast cancer diagnosis. *Information Sciences*, 223, 256–269. <https://doi.org/10.1016/j.ins.2012.10.016>
- [40]. Shi, Y., Dai, D., Liu, C., & Yan, H. (2009). Sparse discriminant analysis for breast cancer biomarker identification and classification. *Progress in Natural Science*, 19(11), 1635–1641. <https://doi.org/10.1016/j.pnsc.2009.04.013>
- [41]. Elyasi, I., Pourmina, M. A., & Moin, M. S. (2016). Speckle reduction in breast cancer ultrasound images by using homogeneity modified bayes shrink. *Measurement: Journal of the International Measurement Confederation*, 91, 55–65. <https://doi.org/10.1016/j.measurement.2016.05.025>
- [42]. Amin, K. M., Shahin, A. I., & Guo, Y. (2016). A novel breast tumor classification algorithm using neutrosophic score features. *Measurement: Journal of the International Measurement Confederation*, 81, 210–220. <https://doi.org/10.1016/j.measurement.2015.12.013>

- [43]. Singh, B. K., Verma, K., Thoke, A. S., & Suri, J. S. (2017). Risk stratification of 2D ultrasound-based breast lesions using hybrid feature selection in machine learning paradigm. *Measurement: Journal of the International Measurement Confederation*, 105, 146–157. <https://doi.org/10.1016/j.measurement.2017.01.016>
- [44]. Fenster, A., Surry, K., Smith, W., & Downey, D. B. (2004). The use of three-dimensional ultrasound imaging in breast biopsy and prostate therapy. *Measurement: Journal of the International Measurement Confederation*, 36(3–4), 245–256. <https://doi.org/10.1016/j.measurement.2004.09.013>
- [45]. Masamha, T., Mnkandla, E., Jaison, A. (2017, September). Logistic regression analysis of information communication technology projects' critical success factors: A focus on computer networking projects. In *AFRICON*, IEEE, pp. 963-967, 2017.
- [46]. Hai, Y., Wong, S. Y., Yuen, K. Y., Cheng, V. C., Tsui, K. L. (2011, July). Logistic regression analysis for Predicting Methicillin-resistant Staphylococcus Aureus (MRSA) in-hospital mortality. In *Intelligence and Security Informatics (ISI)*, 2011 IEEE International Conference, pp. 349-353, 2011.
- [47]. Li, M., Yuan, B., 2D-LDA: A statistical linear discriminant analysis for image matrix. *Pattern Recognition Letters*, 26(5), 527-532, 2005.
- [48]. Gyamfi, K. S., Brusey, J., Hunt, A., Gaura, E., Linear classifier design under heteroscedasticity in Linear Discriminant Analysis. *Expert Systems with Applications*, 79, 44-52, 2017.
- [49]. Internet: Database for Mastology Research, <http://visual.ic.uff.br/dmi/>.

Energy and Exergy Analysis of Drying Behavior for a Fish

Murat ERDEM¹, Fethi KAMISLI², Yasin VAROL^{3*}, Hakan Fehmi OZTOP⁴

¹ Technical Vocational School, Firat University, Elazig, Turkey

² Department of Chemical Engineering, Engineering Faculty, Firat University, Elazig, Turkey

³ Department of Automotive Engineering, Technology Faculty, Firat University, Elazig, Turkey

⁴ Department of Mechanical Engineering, Technology Faculty, Firat University, Elazig, Turkey
muratrdm01@gmail.com, yvarol@gmail.com, fkamisli@firat.edu.tr, hfoztop1@gmail.com

(Geliş/Received: 05/01/2021;

Kabul/Accepted: 28/01/2021)

Abstract: The drying of rainbow trout in a square cross-sectional drier is examined to analyze the system in terms of energy and exergy by considering a thin-layer drying approach. In the experiments, the inlet velocity of air was kept to be constant at 1.5 m/s while varying the temperature of inlet air of 38, 46, and 53 °C with relative moisture ranged from 28 to 43 percent. In the beginning, the moisture content of specimen (fish) on wet basis was found to be around 75 %. Fish with an average weight of 200 grams were used in the experiments. The energy analysis on the consumed energy for the drying process was performed by considering the energy balance. Moreover, the exergy analysis was actualized by considering the second law of thermodynamics to identify the efficiency of the device and the magnitude of energy losses. At the beginning of the drying, the energy consumption was high on account of the large moisture content and decreased with decreasing moisture content. The exergy for inflow and outflow was observed to be increased with increasing the air temperature used for the drying process. Furthermore, it was observed that the lower temperature of the drying air, the lower exergy losses for the entire drying period in the range of 0-900 minutes.

Key words: Energy, Exergy analysis, Convective dryer, Drying, Fish drying.

Bir Balık için Kuruma Davranışının Enerji ve Ekserji Analizi

Öz: Bu çalışma, kare-kesitli bir kurutucuda kurutulan gökkuşuğu alabalığının ince tabaka kurutma işleminin enerji ve ekserji analizini ele almaktadır. Deneyler, 1.5 m/s giriş havası hızında, ancak 38, 46 ve 53 °C'lik farklı giriş hava sıcaklığında yüzde 28-43 bağıl nem aralığında gerçekleştirilmiştir. Başlangıçta yaş temele (w.b.) göre nem içeriği % 75 olarak belirlenmiş ve balıklar için uygun olan seviyeye düşürmeyi amaçlanmıştır. Deneylerde, ortalama 200 gram ağırlığına sahip balıklar kullanılmıştır. Termodinamiğin birinci kanunu kullanılarak kurutma işlemi sırasında kullanılan enerji dikkate alınarak analiz yapılmıştır. Ayrıca termodinamiğin ikinci yasası uygulanarak sistemin tipi ve ekserji kayıplarının büyüklüğü ile kurutma işlemi sırasında ekserji verimliliğini belirlemek için ekserji analizi yapılmıştır. Yüksek nem içeriğinden dolayı kurutma işleminin başlangıcında enerji kullanımının yüksek olduğu ve azalan nem içeriği ile düştüğü görülmüştür. Ekserji girişi ve çıkışı, artan kurutma hava sıcaklığı ile artar. Ayrıca en düşük ekserji kayıplarının tüm kurutma süresi boyunca en düşük kurutma hava sıcaklığında gerçekleştiği ve en yüksek ekserji kayıplarının 0-900 dakika kuruma süresi aralığında en yüksek kurutma sıcaklığıyla meydana geldiği görülmüştür. Ancak en yüksek ekserji verimi en yüksek kurutma havası sıcaklığında elde edilmiştir.

Anahtar kelimeler: Enerji, Ekserji analizi, Taşınımlı kurutucu, Kurutma, Balık kurutma.

1. Introduction

Preservation of the agricultural and animal nutrients by drying has been known in the early ages. This preservation technique can be implemented in several kinds of food. To consume fish later, the fish have to be preserved by some preservation method such as drying since fish must be consumed within a short period of time. Fish and other food items are, the most of time, required to be dried in closed areas since those nutrients can be protected from the harm of insects, dust, and rain. Thereby, it can be considered that drying nutrients in closed areas is healthier than under the sun in open areas [1-4].

The available energy in a system at various stages can be determined by the exergy analysis. The exergy method offers valuable information in designing a system to choose the required component configuration and operation procedure. The knowledge of the application of exergy analysis is far more effective in evaluating the

* Corresponding author: yvarol@gmail.com. ORCID Numbers of Authors: ¹0000-0003-0287-1881, ²0000-0002-1796-3785, ³0000-0003-2989-7125, ⁴0000-0002-2161-0639

configuration, running costs, and energy conservation [5]. In this respect, it is possible to list the works of some studies as follows. Prommas et al. [6] studied energy and exergy analysis in the drying porous media to determine a suitable size and drying conditions. They suggested that the effects of energy and exergy analysis can be applied to determine the effects of porosity and grain size in different drying processes of porous materials. Akpınar et al. [7] studied the drying of potato slices in a cyclone type dryer and examined the energy and exergy. They pointed out that the 1st tray in which the available energy was less used during the single-layer drying method acts as an exergy loser. In another study, Akpınar [8] examined the drying of red pepper slices using exergy and energy analysis. The exergies for inflow, outflow, and thus losses were observed to be increased while the rising temperature of the air used in the drying process. Dincer and Sahin [9] developed a new model for the exergy analysis for a drying process by using the first and the second law of thermodynamics. Corzo et al. [10] dried cordoba slices at various temperatures and velocities of air and the energy and exergy analysis was performed for the thin-layer drying process. In energy and exergy research, Boulemtafes-Boukadoum and Benzaoui [11] conducted a research about the drying of mint in the solar drier. The drying of pumpkin slices in cyclone dryers was examined by Akpınar et al. [12]. Aghbashlo et al. [13] performed a study about the microencapsulation drying process for fish oil by performing an energy and exergy analysis. The drying of green olives in a tray drier was investigated by Colak and Hepbasli [14] using the method of exergy analysis at various air temperatures and constant air humidity of 15 percent. It was reported that the performance values for the exergy were varied in the range of 68.65-91.79 percent for the considered drying air temperatures while varying flow rates between 0.01 kg/s-0.015 kg/s. In addition, there have recently been encountered some investigations related to energy and exergy analysis of drying some products in the solar collectors in the literature [15,16].

Today, energy consumption is increasing at the same rate in parallel with the increase in the human population. Researchers are constantly doing research to reduce energy consumption in every aspect of life. Thereby, it is very important to execute an exergy analysis besides energy use for drying processes. Furthermore, there have been few studies related to drying of fish in the tunnel drier in terms of energy and exergy analysis in the related literature. It is considered that the data obtained in the present study are crucial for researchers who will study on this subject and in this respect, the present investigation can make some contributions to the literature about drying of fish and drying systems. Therefore, the aim in the present paper is to examine the energy and exergy analysis of the thin-layer drying process of a kind of fish in a tunnel drier of the square cross-section at different inlet air temperatures. Methods for increasing the energy efficiency in the present dryer can be implemented to dry other products in the same drier.

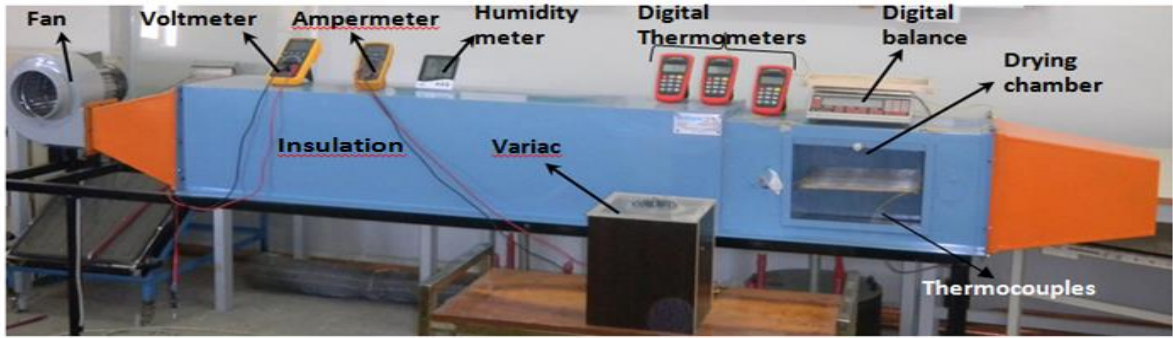
2. Material and Procedure

2.1 Material

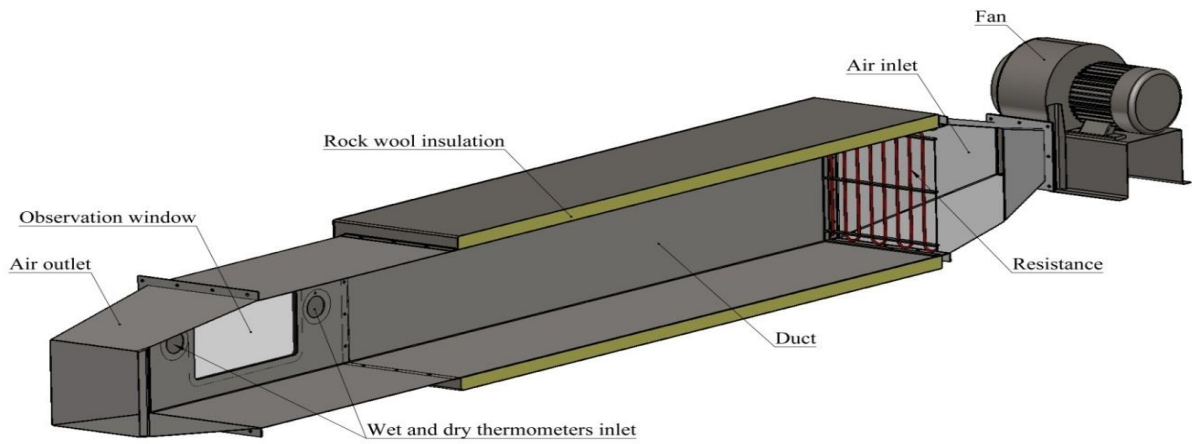
The fish used in the experiments were obtained from fresh waters (Keban dam) in Elazig in Turkey. The samples used in the experiments were chosen to be about the same size, an average weight of 200 grams, in order to obtain the accurate experimental results.

2.2. Experimental set-up

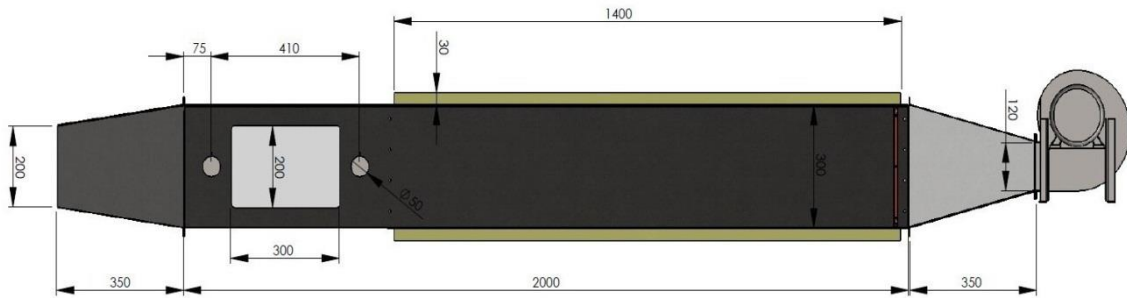
The set-up of the drier system for the present study is represented in Figure 1. As can be seen in the figure, a 375 W electric fan, drying chamber, heater resistance, and some instruments for measuring some variables such as temperature, weight, etc. are the main parts of this drier. The heating system consists of an electric heater which is mounted in the duct (maximum power of 1000 W). The heater power control regulates the drying chamber temperature. The fan velocity control unit regulates the inlet airflow rate. The drying duct of the square cross-section was made of a sheet of st-52 steel and has a length of 2000 mm, a width of 300 mm, a height of 300 mm, and a drying chamber length of 590 mm as well. The instruments used for temperature measurement are three K-type thermocouple numbers that can be operated manually with a two-channel digital thermometer (CHY, 806 AW, with the accuracy of $\pm 0.1^\circ\text{C}$). A digital anemometer (RAM DT-619, m/s - range: 0.4 - 3 m/s, precision: 3 percent) measures the air velocity lasting from inside the device. A digital balance (Avery Berkel, Model CC061) registers the amount of moisture loss at an interval of 10 minutes during the drying process and those data were used to calculate the rate of moisture removal. The digital balance with the range in between 0 and 6000 g having the accuracy of $\pm 0.1\text{g}$ was used to record weigh losses of samples. The power consumed by the heater was measured by the Wattmeter connected to the electrical supply side of the heater.



a)



b)



c

Figure 1. Experimental set up: a) experimental set-up, b) the schematic presentation of the experimental set-up, c) the dimensions of the experimental set-up.

2.3. The mathematical formulation for drying curves

According to wet basis (w.b.), the moisture content is carried out with the following equation [17].

$$M_{wb} = \frac{M_w}{M_i} \quad (1)$$

Where, M_{wb} is moisture content, M_i the weight of fish at the beginning, M_w , the amount of water. Equation (2) is the differential form of the drying velocity.

$$\lim_{\Delta t \rightarrow 0} \left(\frac{M_{t+\Delta t} - M_t}{\Delta t} \right) = - \frac{dM}{dt} \quad (2)$$

Here, M_t and $M_{t+\Delta t}$, stand for the weight of the sample (rainbow trout) at the time of t and $t+\Delta t$, respectively and dM/dt drying rate.

3. Analysis

A single-layer drying approach for energy and exergy analysis proposed by Midilli and Kucuk [5] was implemented in the present research study. The single-layer drying process is known to be a steady-flow process in the drying system in which the first and second thermodynamic laws are used to analyze the system.

3.1. The first law analysis

Energy analysis for drying of the fish in the tray dryer was applied to find the amount of energy and parameters of the single-layer drying using the first law of thermodynamics. In this process, steady-state conditions for conservation of mass and energy can be used to model air conditioning processes [5]. The following equations are usually used to determine the mass, the energy, the relative humidity, and the enthalpy and energy analysis for the single-layer drying processes [5, 18]:

Equation (3) states that the mass conservation for the drying process.

$$\sum \dot{m}_{dai} = \sum \dot{m}_{dao} \quad (3)$$

In this equation, \dot{m}_{dai} and \dot{m}_{dao} stand for mass flow rates of the inlet and outlet flows in the drier, respectively. Equation (3) with a little detail can be written as follows. In other words, the mass conservation for the drying air process can be expressed with Equation (4) also.

$$\sum (\dot{m}_{wi} + \dot{m}_{mp}) = \sum \dot{m}_{wo} \quad \text{or,} \quad \sum (\dot{m}_{dai} w_i + \dot{m}_{mp}) = \sum \dot{m}_{dai} w_o \quad (4)$$

In this equation, \dot{m}_{mp} stands for the mass flow of moisture of the product, and \dot{m}_{wi} and \dot{m}_{wo} denote the mass flow rates of humidity of the inlet and the outlet air flows, respectively. w_i and w_o represent specific humidity for the inlet and the outlet flows, respectively.

Equation (5) represents energy conservation for the system at hand.

$$\dot{Q} - \dot{W} = \sum \dot{m}_{dao} \left(h_o + \frac{v_o^2}{2} \right) - \sum \dot{m}_{dai} \left(h_i + \frac{v_i^2}{2} \right) \quad (5)$$

In this equation h shows enthalpy; v , air rate; \dot{Q} , heat; \dot{W} , work.

The relative humidity of the air used for the drying process can be found from Equation (6).

$$\phi = \frac{\omega P}{(0.622 + \omega) P_{sat@T}} \quad (6)$$

The potential and kinetic energy can be ignored in the entire drying process except for the fan's kinetic energy. Equations (7) - (9) were used for the calculation of the enthalpy of drying air while calculating the energy and exergy for the system.

$$h = c_{pda}T + wh_{sat@T} \quad (7)$$

The following equation is used to calculate the fan outlet enthalpy [19] in the present study.

$$h_{fo} = \left[\left(\dot{W}_f - \frac{V_{fo}^2}{2 \cdot 1000} \right) \left(\frac{1}{\dot{m}_{da}} \right) \right] + h_{fi} \quad (8)$$

h_{fi} and h_{fo} , characterize enthalpies for the drying air at the inlet and the outlet of the fan, respectively. \dot{W}_f , fan energy, V_{fo} is the velocity of drying air at the fan outlet and \dot{m}_{da} , the air mass flow rate. By taking into account the enthalpy and dry-bulb temperature, Akpınar [7] used Eq. (8) to find the relative and specific humidity of the drying air at the outlet of the ventilator. The heater's inlet conditions and the outlet conditions of the fan are taken to be equal to one another in the calculations. As a convection heat source, the useful energy obtained from the heater described in Equation (9) enters the drying chamber.

$$\dot{Q}_u = \dot{m}_{da}c_{pda}(T_{ho} - T_{hi}) \quad (9)$$

Here, T_{ho} and T_{hi} are temperatures of outlet and inlet air flows in the heating portion, respectively. In the drying chamber, the inlet conditions were determined according to the drying air humidity and temperatures. For the drying air, the mass flow rate was calculated by considering the inlet conditions. The specific humidity of outlet flow at the drying chamber is determined using Equation (10) [6].

$$w_{pbo} = w_{pbi} + \frac{\dot{m}_{wp}}{\dot{m}_{da}} \quad (10)$$

In this equation, while \dot{m}_{wp} shows the mass flow rate of the removed moisture, w_{pbi} and w_{pbo} stand for the specific humidity at the inlet and outlet of the chamber, respectively. Equation (11) is used to calculate the heat consumed for the humidification process in the drying chamber.

$$\dot{Q}_{pb} = \dot{m}_{da} (h_{pbi@T} - h_{pbo@T}) \quad (11)$$

3.2. The second law analysis

The thermal systems are usually analyzed using the second law of thermodynamics in terms of evaluation of exergy. In a system, the exergy can be taken into account as measuring of the available energy at various points. Exergy can be considered as an indicator of quality or energy grade that can be lost in the system in which the energy is consumed for processes. It is known that some of the energy that enters a thermal system by any means of energy sources is lost in the system on account of irreversibility. The available energy in a thermal system or the lost energy and thus, the efficiency of the system can be determined using the second law analysis. While performing the exergy analysis of the chamber, it was assumed that the steady-state condition at each point is valid. Energy consumption for the process at hand was determined by using an energy balance that is expressed as follows [20]. Equation (12) is utilized to perform the exergy balance.

$$\begin{aligned} Exergy = & \underbrace{(u - u_\infty)}_{\text{Internal energy}} - T_\infty \underbrace{(s - s_\infty)}_{\text{entropy}} + \underbrace{\frac{P_\infty}{J}(v - v_\infty)}_{\text{work}} + \underbrace{\frac{V^2}{2gJ}}_{\text{momentum}} + \underbrace{(z - z_\infty) \frac{g}{g_c J}}_{\text{gravity}} \\ & + \underbrace{\sum_c (\mu_c - \mu_\infty) N_c}_{\text{Chemical}} + \underbrace{E_i A_i F_i (3T^4 - T_\infty^4 - 4T_\infty T^3)}_{\text{radiation emission}} + \dots \end{aligned} \quad (12)$$

Here the reference conditions are shown by the subscript ∞ . Only some terms shown in Equation (12) are used to perform the exergy analyses for many systems because the available energy source can be magnetic fields, electric current flow, and material diffusion flow. One common simplification can be made by substituting enthalpy for PV terms and the internal energy into Eq. (12). The gravity and momentum terms are commonly disregarded in Eq. (12) during the evaluation of exergy. The further simplification can be done in Eq. (12) by ignoring pressure changes in the system by virtue of $v \approx v_\infty$. Therefore, Eq. (12) reduces to the following equation [18]:

$$\text{Exergy} = \bar{c}_p \left[(T - T_\infty) - T_\infty \ln \frac{T}{T_\infty} \right] \quad (13)$$

Eq. (13) can be used for the calculation of exergies for the inflow and outflow by taking into account of the inlet and outlet temperatures in the drying chamber. Thereby, the loss of exergy was calculated using Eq. (14).

$$\sum Ex_L = \sum Ex_i - \sum Ex_o = \bar{c}_{p_{da}} \left[(T_{dci} - T_{dco}) - T_\infty \ln \frac{T_{dci}}{T_{dco}} \right] \quad (14)$$

The exergy for inlet airflow in the drying chamber is determined from the following equation:

$$Ex_{dci} = Ex_{pbi} = \bar{c}_{p_{da}} \left[(T_{dci} - T_\infty) - T_\infty \ln \frac{T_{dci}}{T_\infty} \right] \quad (15)$$

The exergy for outlet airflow in the drying chamber is obtained from the following equation:

$$Ex_{dco} = Ex_{pbo} = \bar{c}_{p_{da}} \left[(T_{dco} - T_\infty) - T_\infty \ln \frac{T_{dco}}{T_\infty} \right] \quad (16)$$

The exergy efficiency can be defined as the ratio of the exergy of the product to that of the inlet flow in the drying chamber.

$$\text{Exergy Efficiency} = \frac{\text{Exergy inflow} - \text{Exergy loss}}{\text{Exergy inflow}} \quad (17)$$

When splitting operation is done, Eq. (17) becomes as follows:

$$\eta_{Ex} = 1 - \frac{Ex_L}{Ex_i}, \text{ or } \eta_{Ex} = \frac{Ex_o}{Ex_i} \quad (18)$$

4. Results and Discussion

4.1. Energy and Exergy Analysis

The rainbow trout fish was dried at the constant inlet air velocity of 1.5 m/s and various inlet air temperatures (38, 46, and 53 °C) in a tray dryer of cross-sectional area to actualize the energy and exergy analyses using a thin-layer drying approach and determine optimum conditions for the drier. In the present work, the magnitudes of energy consumption and exergy losses, the exergy of inlet flow and the outlet flow, and the efficiency of exergy were calculated depending on the drying time. Moreover, the rate of removed moisture of fish samples was depicted as a function of temperature. As mentioned previously, the adequate data concerning the drying behavior of the rainbow trout do not exist in the related literature. For this reason, the experimental results obtained from the present study are crucial for future investigations about the subject.

The moisture content depending on the drying rate for various inlet air temperatures ($T = 38, 46, 53$ °C) at the constant velocity ($V=1.5$ m/s) of the inlet air is illustrated in Figure 2. The maximum rate for the drying process takes place at the beginning of the drying process in which fish samples have the highest moisture contents as evidenced in the figure.

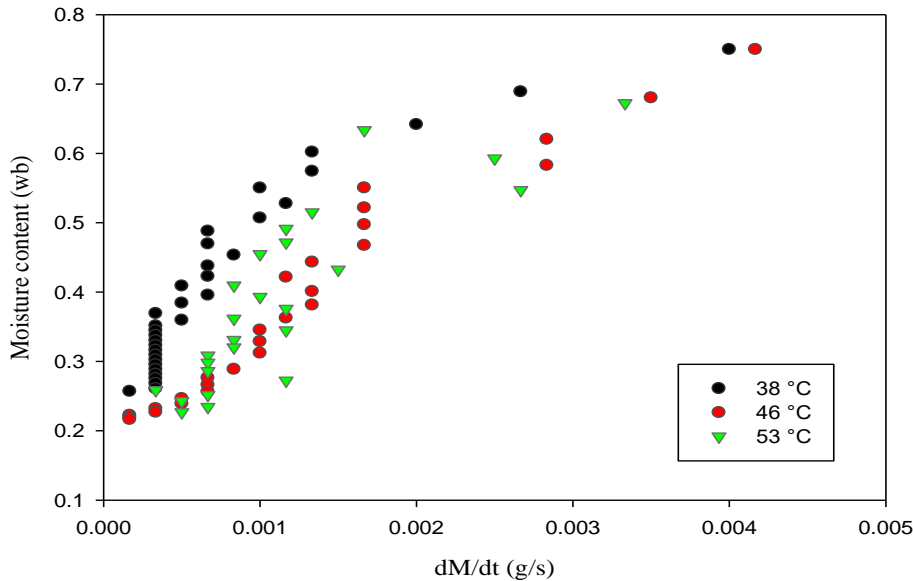


Figure 2. The moisture content depending on the drying rate for various inlet air temperatures at the constant inlet air velocity of ($V=1.5$ m/s).

Although it is not seen in Figure 2, both the moisture content of the specimen and drying rate reduces with increasing drying time. Figure 2 illustrates the relationship between moisture content and drying rate. Figure 3 illustrates the variations of energy utilization with the drying time for different inlet temperatures of 38, 46, and 53 °C at the constant velocity (1.5 m/s) of the drying air. The figure indicates that the use of energy by heater was large and becoming larger at the first stages of the drying process by virtue of the large amount of moisture content of the specimens, but it is observed that it lessens fast with increasing drying time on account of the low moisture content of the fish specimens at the ends of the drying. The use of the energy for drying processes varied depending drying temperatures and those were determined to be, respectively, between 0.0925-0.8480 kW, 0.2104-0.9770 kW and 0.1324-1.0297 for the drying carried out at 38 °C, 46 °C and 53 °C and at the constant velocity of 1.5 m/s. The figure shows that the lowest energy utilization occurs at the largest drying air temperature (53 °C) and the drying time in a range of 200 – 1200 min.

Changes of input and output exergy as a function of the drying time for various inlet temperatures ($T = 38, 46, \text{ and } 53$ °C) at a constant velocity ($V=1.5$ m/s) of the inlet air are shown in Figure 4. The ambient air temperatures (T_{∞}) were measured to be 26.1 °C, 26.4 °C and 26.8 °C for drying air temperatures of 38 °C, 46 °C, and 53 °C, respectively. By considering the ambient and inlet temperatures, Eq. (15) was used to evaluate the exergy for inlet flow. On the other hand, the exergy for outlet flow was obtained from Eq. (16) with the use of the ambient and outlet temperatures. As expected when inlet temperature increased, the exergy for inlet flow increased. The exergy for inlet flow in the drying chamber changed between 0.2321-1.0893 kJ/kg depending on the temperatures of inlet air. Exergy for outlet flow was observed to be increased with increasing drying air temperatures and the values for those were found to be between 0.0679-0.2321 kJ/kg at 38 °C, 0.2803-0.5352 kJ/kg at 46 °C, 0.5936-1.0295 kJ/kg at 53 °C. These temperature values are the drying air temperatures. The exergy for inlet and outlet flows increases with increasing drying air temperature and the lowest energy losses take place at the lowest drying air temperature at present operation temperatures as proved in Figure 4. The data illustrated in Figure 4 are qualitatively in agreement with the results given in Figure 4 at the Ref. [8] in which different material was dried. During the experiments, sometimes the inlet temperature could change slightly due to voltage fluctuations. However, this negligible fluctuation was ignored and the inlet temperatures were taken to be the constant in the calculations.

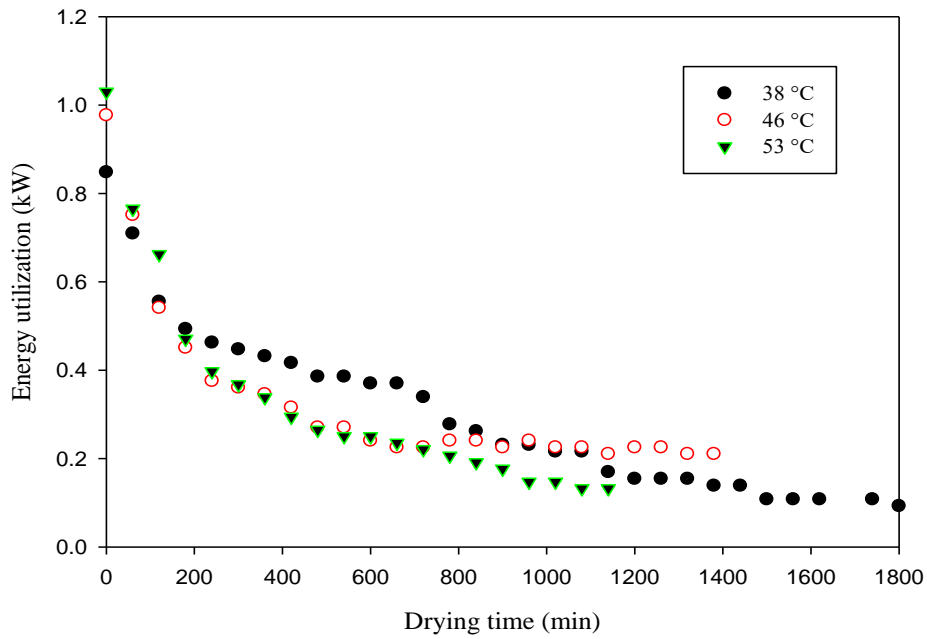


Figure 3. Changes of energy use as a function of drying time for various temperatures of the inlet air at the constant velocity ($V=1.5$ m/s).

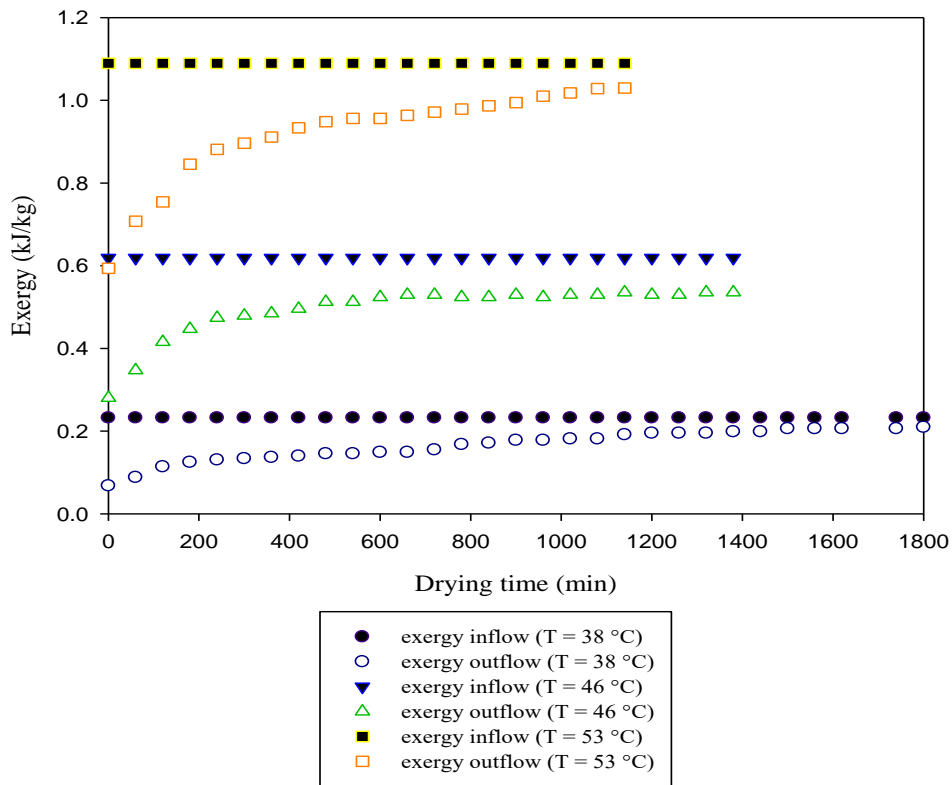


Figure 4. Changes of exergy depending on the drying time for various inlet temperatures in the drying chamber at the constant inlet velocity ($V=1.5$ m/s).

Figure 5 demonstrates the changes of exergy losses as a function of drying time for various values of inlet temperatures ($T = 38, 46, \text{ and } 53 \text{ }^{\circ}\text{C}$) at the constant velocity of 1.5 m/s . The figure indicates that the larger temperature of inlet air temperature causes larger exergy losses. Exergy losses at each drying temperature were calculated from Eq. (14) and found to be in ranges of $0.0225\text{-}0.1642 \text{ kJ/kg}$ at $38 \text{ }^{\circ}\text{C}$, $0.0837\text{-}0.3386 \text{ kJ/kg}$ at $46 \text{ }^{\circ}\text{C}$, $0.0598\text{-}0.4957 \text{ kJ/kg}$ at $53 \text{ }^{\circ}\text{C}$. The figure points out that the lowest exergy losses occur at the lowest drying air temperature and the largest exergy losses happen at the highest drying temperature ($53 \text{ }^{\circ}\text{C}$) at drying time in a range of $0 - 900 \text{ min}$. In this context, Figure 6 agrees with Figure 5. Figure 6 illustrates the changes in exergy efficiency as a function of the drying time for various inlet temperatures ($T = 38, 46, 53 \text{ }^{\circ}\text{C}$) at constant velocity ($V=1.5 \text{ m/s}$). The exergy efficiency increases with drying time as evidence in Figure 6. For the drying chamber, the exergy efficiencies were obtained in ranges of $29.27\text{-}94.50 \%$ for various air temperatures at the constant velocity. As can be seen from the figure the efficiency of exergy increases with an increase in the drying air temperature. So, the highest exergy efficiency was obtained at the largest drying air temperature. Also, during the drying processes, interior temperatures of products were calculated to be between $22.5\text{-}33.5 \text{ }^{\circ}\text{C}$ at $38 \text{ }^{\circ}\text{C}$, $24.5\text{-}40.5 \text{ }^{\circ}\text{C}$ at $46 \text{ }^{\circ}\text{C}$, and $23\text{-}46 \text{ }^{\circ}\text{C}$ at $53 \text{ }^{\circ}\text{C}$. As mentioned previously $38 \text{ }^{\circ}\text{C}$, $46 \text{ }^{\circ}\text{C}$ and $53 \text{ }^{\circ}\text{C}$ are the drying air temperatures.

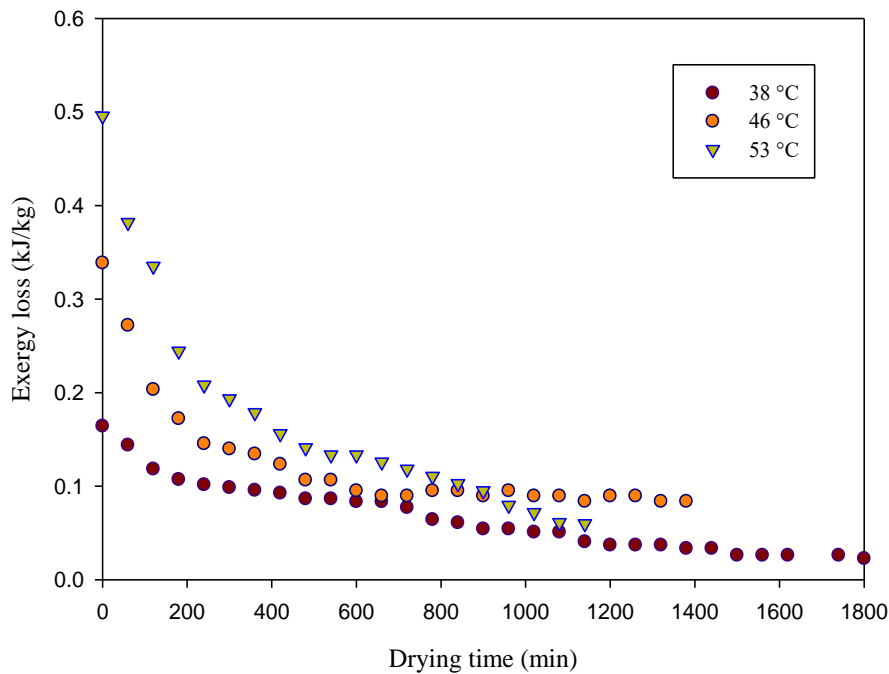


Figure 5. Changes of exergy losses in the drying chamber as a function of drying time for inlet temperatures at the constant velocity ($V=1.5 \text{ m/s}$).

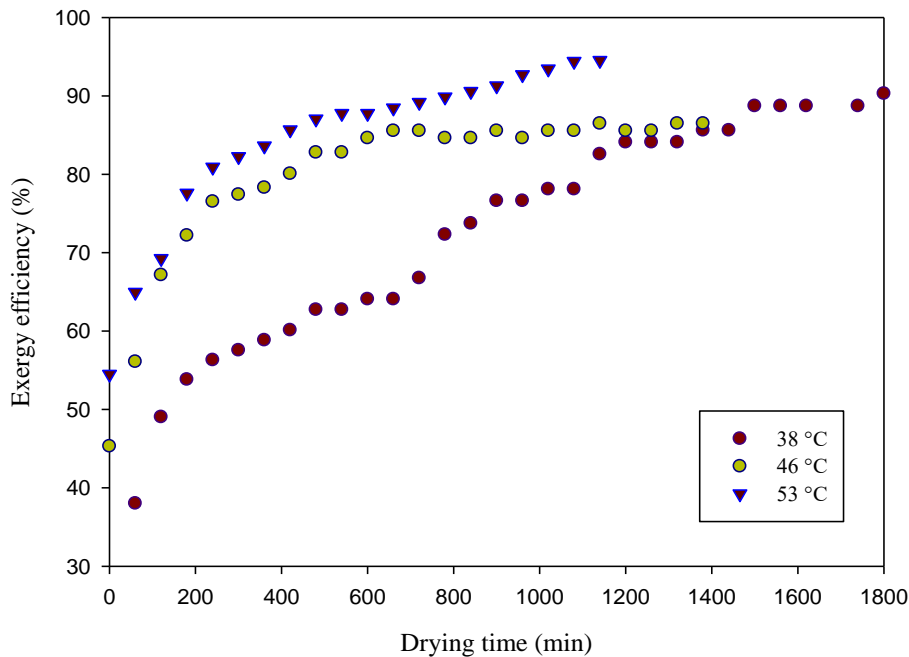


Figure 6. Changes of exergy efficiency in the drying chamber as a function of drying time for various inlet temperatures at the constant velocity ($V=1.5$ m/s).

4.2. Uncertainty for Experimental Study

It is expected that some errors can be occurred during the experimental study on account of instruments used in measuring effective parameters, electronic oscillations, and unknown causes, etc. The following equation [21] can be used for analysing errors that happened during performing experiments.

$$W_x = [(x_1)^2 + (x_2)^2 + \dots + (x_n)^2]^{1/2} \tag{19}$$

Table 1. Uncertainties for the parameters measured in the present work.

Parameter	Unit	Total error
The temperature	°C	±0.07
The inlet velocity	m/s	±0.025
Mass for moisture	g	±0.1
The moisture content in dimensionless form	min	±0.2
Moisture loss	min	±0.17

As can be seen from Table 1 total error of the measured parameters is quite low.

5. Conclusions

In the present study, drying of fish samples in the tray dryer of cross-sectional area has examined by performing energy and exergy analysis using the thin layer drying approach. The effects of drying temperatures namely the inlet air temperature at the constant air velocity on the drying process were examined using the first and second law of thermodynamics. It is noticed that the surface of the samples does not change with the variation of inlet air temperature considered here.

The present study may lead to the following conclusions.

- While the inlet airflow exergies depending on drying air and ambient temperatures were found to be between 0.2321 - 1.0893 kJ/kg, those for outlet flow were obtained to be between 0.0679-0.2321 kJ/kg at 38 °C, 0.2803-0.5352 kJ/kg at 46 °C and 0.5936-1.0295 kJ/kg at 53 °C.
- The efficiency of exergy depending on the inlet air temperature (38, 46, and 53 °C) varied from 29.27 to 94.5% at a constant air velocity of 1.5 m/s.
- The largest use of energy was observed to be occurred at the first stages of the drying owing to the large moisture content of the specimen and decreased according to decreasing moisture content that lessens with drying time.
- Although the lowest exergy losses were observed to be taken place at the lowest drying air temperatures, the largest exergy efficiency was found at the highest drying air temperature at the considered operation temperatures.
- The exergy losses as a function of air temperature (38, 46, and 53 °C) were found to be in the range of 0.0225-0.4957 kJ/kg at the constant air velocity of 1.5 m/s.
- It was observed that the use of energy at all considered drying air temperatures reduced with an increase in the drying time.
- It can be said that the moisture content is almost proportional to the drying rate.

It can be suggested that to get a higher exergy efficiency and lower exergy loss, some parts of the experimental set-up can be improved.

References

- [1] Erdem M, Öztöp HF, Varol Y, Kanişlı F. Tepsili bir kurutucuda kurutulan alabalığın üzerinde hava giriş sıcaklığı etkisinin deneysel olarak incelenmesi. Dicle Üniversitesi 2. Anadolu Enerji Sempozyumu, (2-4 Mayıs 2013) Bildirileri, H. Bayındır (Editor), Diyarbakır, 2013: 741-745.
- [2] Erdem M. Balığın tepsili kurutucuda kurutma davranışının deneysel olarak incelenmesi. Yüksek Lisans Tezi, Fırat Üniversitesi Fen Bilimleri Enstitüsü 2011; 67s.
- [3] Erdem M, Varol Y. Alabalığın kurutulması ve tuzlanması üzerine deneysel bir çalışma. Termodinamik Dergisi 2014; 264: 92-102.
- [4] Erdem M, Varol Y, Öztöp HF, Türkbay İ. Balığın Kuruma Davranışı Üzerinde Parça Etkisi ve Sistemin Enerji Gereksiniminin İncelenmesi. Fırat Üniversitesi Mühendislik Bilimleri Dergisi 2016; 28 (2): 89-98.
- [5] Midilli A, Kucuk H. Energy and exergy analysis of solar drying process of pistachio. Energy 2003; 28: 539-556.
- [6] Prommas R, Rattanadecho P, Cholaseuk D. Energy and exergy analysis in drying process of porous media using hot air, Int. commun Heat Mass Transfer 2010; 37: 372-378.
- [7] Akpınar EK, Midilli A, Bicer Y. Energy and exergy of potato drying process via cyclone type dryer. Energy Conver Manag 2005; 46: 2530-2552.
- [8] Akpınar EK. Energy and exergy analyses of drying of red pepper slices in a convective type dryer. Int commun in Heat Mass Transfer. 2004; 31: 1165-1176.
- [9] Dincer I, Sahin AZ. A new model for thermodynamic analysis of a drying process. Int J Heat Mass Transfer. 2004; 47: 645-652.
- [10] Corzo O, Bracho N, Vasgues A, Pereira A. Energy and exergy analyses of thin layer drying of coroba slices. J Food Eng. 2008; 86: 151-161.
- [11] Buolemtafes-Boukadoum A, Benzaoui A. Energy exergy analysis of solar drying of mint. Energy Procedia 2011; 6: 583-591.
- [12] Akpınar EK, Midilli A, Bicer Y. The first and second law analyses of thermodynamic of pumpkin drying process. J Food Engineer 2006; 72: 320-331.
- [13] Aghbashlo M, Mobli H, Rafiee S, Madadlou A. Energy and exergy analyses of the spray drying process of fish oil microencapsulation. Biosystems Engineer 2012; 111: 229-241.
- [14] Colak N, Hepbasli A. Performance analysis of drying of green olive in a tray dryer. J Food Engineer 2007; 80: 1188-1193.
- [15] Mol da Silva G, Ferreira, Rogério Morouço Coutinho AG, Cristiana Brasil Maia AG. Energy and exergy analysis of the drying of corn grains. Renewable Energy 2021; 163: 1942-1950.
- [16] Erick César, LV, Ana Lilia CM, Octavio, GV, Orlando SS, Niño Alfredo D. Energy and exergy analyses of a mixed-mode solar dryer of pear slices (*Pyrus communis* L). Energy 2021; 220: 119740.
- [17] Gokoglu N. Aquatic products processing technology. Istanbul, Turkey 2002.
- [18] Cengel YA, Boles MA. Thermodynamics: An engineering approach. McGraw-Hill, Inc. New York 1994.
- [19] Bejan A. Advanced Engineering Thermodynamics. John Wiley and Sons, New York 1998.
- [20] Ahern JE. The exergy method of energy systems analysis. John Wiley, New York 1980.
- [21] Holman J. Experimental methods for engineers, second edition. McGraw-Hill New York 1994.

Quantum Cryptography, Quantum Communication and Quantum Computing Problems and Solutions

Muharrem Tuncay GENÇOĞLU*

Vocational School of Technical Science, Fırat University, Elazığ, Turkey

*mt.gencoglu@firat.edu.tr

(Geliş/Received: 27/01/2021;

Kabul/Accepted: 13/02/2021)

Abstract: : The development of quantum technologies will open up new perspectives in the use of quantum algorithms, the creation and modeling of complex physical and biological systems, new physical methods of transmitting, receiving and processing information. In turn, this will give impetus to the development of a large number of applications in the scientific, technical, economic and social spheres of society. Quantum cryptography is a communication protection method based on certain phenomena of quantum physics. Unlike traditional cryptography, which uses mathematical methods to ensure the secrecy of information, quantum cryptography focuses on physics, where information is carried using objects of quantum mechanics. The process of sending and receiving is always carried out by physical means, for example using electrons in an electric current, or photons in fiber-optic communication lines. In this process, the current situation was determined and the problems encountered and the solution suggestions for these problems were tried to be addressed.

Key words: Quantum cryptography, quantum communication, quantum computing, quantum problems, quantum solutions.

Kuantum Kriptografi, Kuantum İletişim ve Kuantum Hesaplama Problem ve Çözümler

Öz: Kuantum teknolojilerinin gelişimi, kuantum algoritmalarının kullanımı, karmaşık fiziksel ve biyolojik sistemlerin oluşturulması ve modellenmesi, bilgi iletimi, alımı ve işlenmesi için yeni fiziksel yöntemler konusunda yeni bakışaçıları ortaya koyacaktır. Bu da, toplumun bilimsel, teknik, ekonomik ve sosyal alanlarda çok sayıda uygulamanın geliştirilmesine katkı sağlayacaktır. Kuantum kriptografi, kuantum fiziğinin belirli ilkelerine dayanan bir iletişim koruma yöntemidir. Bilginin gizliliğini sağlamak için matematiksel yöntemler kullanan geleneksel kriptografinin aksine, kuantum kriptografi, bilginin, kuantum mekaniği nesnelere kullanılarak, taşındığı fiziksel alana odaklanır. Gönderme ve alma işlemi her zaman, örneğin bir elektrik akımındaki elektronlar veya fiber-optik iletişim hatlarındaki fotonlar kullanılarak, fiziksel yollarla gerçekleştirilir. Bu süreçteki mevcut durum tespiti yapılarak karşılaşılan sorunlar ve bu sorunlara yönelik çözüm önerilerine değinilmeye çalışılmıştır.

Anahtar kelimeler: Kuantum kriptografi, kuantum iletişim, kuantum hesaplama, kuantum problemler, kuantum çözümler.

1. Introduction

Quantum information processing is a new area of expertise with tremendous potential leading to breakthroughs in many areas of science and technology. It uses fundamentally new methods of computation and communication, based on the principles of quantum mechanics, rather than classical physics. This promises tremendous computing power, far beyond the capabilities of any classical computer, guarantees secure communication, and also stimulates the development of nascent quantum and related Technologies[6].

The development of quantum technologies will open up new perspectives in the use of quantum algorithms, the creation and modeling of complex physical and biological systems, new physical methods of transmitting, receiving and processing information. In turn, this will give impetus to the development of a large number of applications in the scientific, technical, economic and social spheres of society.

Considerable interest in the world in this topic is manifested in the increase in funding for quantum information technologies in the USA, Canada, Australia, the European Union, China, Singapore, Japan and many other countries. An example is similar long-term programs adopted in the United States (QIST) and the European Union (QIPS), the creation of Centers and target laboratories for developments in the field of COIKS. Certain areas of KOIKS are funded by law enforcement agencies of many states (DARPA, ARDA, NASA, ONR, ESA, GACICN, etc.). Leading scientists in the field of quantum physics, mathematics, computing, biology, and others are involved in the development. Such large firms as Microsoft, IBM and Lockheed Martin, as well as NASA, have created special research units that develop quantum information technologies. Leading

* Corresponding author: mt.gencoglu@firat.edu.tr. ORCID: 0000-0002-8784-9634

scientists in the field of quantum physics, mathematics, microelectronics, computer technology, biology, etc. are involved in these developments[7,8].

Such technologies are based on priority fundamental research, which covers the following areas:

- 1) Quantum communications, including quantum cryptography;
- 2) Quantum computing;
- 3) Technologies aimed at creating a component base for quantum communications and computing.

The goal of research in the selected priority areas is to create a fundamental foundation for the development of computing and communication technologies at a fundamentally new level and the creation of appropriate new materials and devices[10].

Quantum cryptography is a communication protection method based on certain phenomena of quantum physics. Unlike traditional cryptography, which uses mathematical methods to ensure the secrecy of information, quantum cryptography focuses on physics, where information is carried using objects of quantum mechanics. The process of sending and receiving is always carried out by physical means, for example using electrons in an electric current, or photons in fiber-optic communication lines[1].

History of quantum cryptography The idea of using quantum objects to protect information from counterfeiting and unauthorized access was first expressed by Stefan Weisner in 1970. In 1984, Charles Bennett of IBM and Gilles Brassard of the University of Montreal, who were familiar with Weisner's work, suggested that photons could be used in cryptography to obtain a fundamentally secure channel. To represent zeros and ones, they decided to take photons polarized in different directions and proposed a simple quantum encryption key distribution scheme, which they called BB84. In 1989, Bennett and Brassard at the IBM Research Center built the first working quantum cryptographic system. It consisted of a quantum channel containing transmitters at the ends (traditionally called Bob's and Alice's transmitters) placed on an optical bench about[2].

In the second part of the study, the idea and applications of quantum cryptography are mentioned. In the third section, the current situation is determined and the problems are classified. While the results are included in the fourth chapter, solution suggestions are given for the problems identified in the fifth chapter.

2. Implementation of the idea of quantum cryptography

The method of quantum cryptography is based on the observation of quantum states of photons. The sender sets these states, and the receiver registers them. It uses the Heisenberg quantum uncertainty principle when two quantum quantities cannot be measured simultaneously with the required accuracy. Thus, if the sender and the receiver have not agreed between themselves which type of polarization of quanta to take as a basis, the receiver can destroy the signal sent by the sender without receiving any useful information. These features of the behavior of quantum objects formed the basis of the BB84 quantum key propagation protocol.

This scheme uses a quantum channel through which users (Alice and Bob) exchange messages, transmitting them in the form of polarized photons.

The BB84 circuit works as follows. First, Alice generates and sends to Bob a sequence of photons, the polarization of which is chosen at random and can be 0, 45, 90 and 135 °. Bob takes these photons and for each of them randomly decides whether to measure its polarization as perpendicular or diagonal. On the open channel, Bob announces for each photon what type of measurements he made (perpendicular or diagonal), but does not report the result of these measurements, for example, 0, 45, 90 or 135 °. Through the same open channel, Alice tells him whether the correct type of measurements has been chosen for each photon. Alice and Bob then discard any cases where Bob made incorrect measurements. If the quantum channel was not intercepted, the remaining types of polarization will be shared between Alice and Bob the secret information, or the key. This stage of the operation of a quantum cryptographic system is called primary quantum transmission.

The next important step is to evaluate attempts to intercept information in a quantum-cryptographic communication channel. This can be done by Alice and Bob over an open channel by comparing and discarding subsets of the data they receive randomly. If such a comparison reveals the presence of an interception, Alice and Bob discard all their data and begin re-executing the primary quantum transfer. Otherwise, they leave the same polarization, taking photons with horizontal or 45 ° polarization for binary "0", and with vertical or 135 ° polarization - for binary "1". According to the uncertainty principle, an attacker cannot measure both rectangular and diagonal polarizations of the same photon. Even if he makes a measurement for any photon and sends this photon to Bob per the result of his measurements, then in the end the number of errors will greatly increase, and this will become noticeable to Alice. This will lead to 100% confidence of Alice and Bob in the interception of photons.

A more efficient check for Alice and Bob is the parity check performed over the open channel. For example, Alice might report, "I looked at the 1st, 4th, 6th, 8th... and 998th of my 1000 bits, and they contain an even number of ones." Then Bob counts the number "1" in the same positions. It can be shown that if Bob's and Alice's data are different, parity checking a random subset of that data will reveal the number of errors. It is enough to repeat this test 20 times with 20 different random subsets to calculate the error rate. If there are too many errors, then it is considered that an interception was made in a quantum cryptographic system. If Alice and Bob are not going to use the key they received immediately, then they face a new problem - how to keep the key secret? In 1991, Artur Ekert proposed a protocol to solve both of these problems of key distribution and storage. Ekert's protocol is based on the coupling effect of quantum particles. Linked particles behave unusually: if you measure one of them, then the other (no matter how far away it is) will necessarily "go over" into a state opposite to the state of the first particle. The paradox is that information about the state of a particle is transmitted at a speed that exceeds the speed of light. Nevertheless, this phenomenon is demonstrated experimentally by physicists and can be used to encrypt information[3-5].

In a somewhat simplified form, Ekert's protocol assumes that Alice generates a certain number of pairs of concatenated photons. She sends one photon from each pair to Bob and keeps the other. Some of the particles are immediately measured by Alice and Bob to determine if the interception was performed: if so, the consistency of the states of the particles will disappear. The rest of the particles are stored by Alice and Bob in perfectly reflecting boxes. When the need arises to exchange messages, they will measure the state of a certain number of particles stored in them, and receive a secret key[11,12].

3. Current state and problems

Quantum cryptography as a market segment is just beginning to emerge, and for now, both global computer corporations and small start-up companies can play on equal terms. Interest in quantum cryptography from commercial and military organizations is growing, as this technology can guarantee absolute security. Today, quantum cryptography has been available for commercial use for several years. But the technology is only practical in the hands of government organizations and large private sectors that can afford to have their fiber-optic networks.

But besides the successful creation and commissioning of quantum key distribution systems, there are also successful experiments on their cracking. For example, in 2007, physicists from the University of Toronto (Canada) performed an experimental demonstration of undetectable message interception in a quantum key distribution system implemented by the Swiss company ID Quantique.

3.1. Scientific and technical problems in the field of quantum communications

- Development of new protocols of quantum communication and quantum cryptography, research of their properties and experimental implementation;
- Development of methods for preparation, measurement, control and transformation of quantum states of light, including states of high dimension, macroscopic entangled states, etc.
- Search and study of effective light-matter interfaces, a study of the interaction of non-classical states of light with individual quantum objects and ensembles.
- Development of principles and methods of quantum metrology;
- Development of relativistic quantum information theory and quantum communication based on combining the concepts of relativistic quantum theory and information theory.

3.2. Scientific and technical problems in the field of quantum computing

Creation, analysis and implementation of elements of quantum computing devices and quantum simulators using:

- Spin states in specially designed condensed media having specially created ensembles of atoms or molecules with electronic or nuclear spin. For example, these can be shallow donors or in single crystals of isotopically pure ^{28}Si , NV-complexes in diamond, etc .;
- States of ensembles of ions, neutral atoms or molecules (including highly excited Rydberg states) in electromagnetic (for example, optical) traps or inert media;
- Semiconducting and superconducting quantum multicomponent structures demonstrating relaxation to the ground state through "quantum annealing", including phenomena and devices based on hybrid

semiconducting or superconducting quantum structures with weakly interacting molecules included in them;

- Opto-nanomechanical and magneto-nanomechanical quantum systems;
- States of linear and nonlinear optical (including microwave) systems in high-quality resonators;
- States of specially synthesized molecular and supramolecular systems, in particular, polynuclear complexes, hybrid systems with charge separation;
- Topological quantum states, condensates of various particles and quasiparticles, structures based on new carbon materials, etc.

3.3. Scientific and technical problems in the field of architecture and algorithms and quantum computing

- Development of algorithms for quantum computing (including algorithms for quantum modeling and quantum tomography; correction of quantum errors to compensate for the loss of coherence; accuracy assessment);
- Development of architectural and software principles of hybrid supercomputers containing quantum computers;
- Development of methods for collecting and analyzing large amounts of data from quantum computing devices using supercomputers;
- Qualitative and quantitative characterization of confused multi-qubit quantum states as the main information resource in quantum informatics;
- Synthesis and optimization of quantum circuits (including the synthesis of reversible circuits for calculating Boolean functions; reduction of the depth of a quantum circuit; quantum technologies for testing and repairing digital circuits on crystals).

4. Conclusion

The use of photons, both for transmission and for information processing, presupposes the creation of new principles and technologies of integrated photonic devices both for distributed quantum communication lines and for classical optoelectronic or all-optical integrated devices. It is also necessary to develop atomic-scale technologies, with the use of which it is possible to "assemble" elements of systems from individual atoms or molecules. In this regard, the development of new physical principles and approaches are required to create the necessary materials and structures, new experimental methods and metrological support.

Cryptography is an important component of the modern world and is necessary primarily for the preservation of personal data and important information. Since its inception, it has undergone many modifications and is now a security system that practically cannot be hacked. It is difficult to overestimate its potential for humanity. Modern methods of cryptography are used in almost all industries in which there is a need for secure transmission or storage of data. Based on the fact that the latest developments in the field of quantum cryptography make it possible to create systems that provide almost 100% protection of the key and key information, it can be assumed that shortly all cryptographic information protection and key distribution will be based on quantum cryptographic systems[9,10].

5. Discussion and Suggestions

- Development and creation of photon sources, including one, two and N-photon, the creation of photon detectors, including single-photon, the creation of optical and microwave amplifiers with a quantum level of input noise, high-Q resonators "on a chip", quantum systems for coherent photon conversion, etc.,
- Development and creation of new materials and basic elements for problems of quantum communication and quantum information processing, including photonic materials, structures and fiber systems for the generation of special quantum states of light;
- Development and creation of quantum memory systems (including photonic ones) and the creation of practically significant quantum memory with high efficiency, long lifetime, high information capacity, as well as the ability to work at room temperature;
- Development and creation of quantum generators of random bit sequences;

- Design and creation of quantum interfaces, i.e. elements for setting the initial state of "qubits" before computation and elements for reading quantum states of "qubits" after computation. (For example, to read the state of spin qubits, one-electron transistors with a Coulomb blockade or devices based on spin-dependent transport and spin-dependent reactions can be used);
- Design and creation of "quantum wires" for the transfer of a quantum state between registers in a quantum computer.

References

- [1] Cryptography and data encryption - everything you need to know. [Electronic resource]. - Access mode: <https://prostocoin.com/blog/cryptography>. - Date of access: 15.04.2020.
- [2] Hardware Quantum Cryptography. [Electronic resource]: <http://fkn.ktu10.com>. - Date of access: 15.04.2020.
- [3] Journal of Science and Technology "Popular Mechanics" [Electronic resource] - Access mode: https://www.popmech.ru/technologies/235655_kvantovayakriptografiya-chto-eto-takoe. - Date of access: 15.04.2020.
- [4] Quantum cryptography, or how light generates encryption keys. [Electronic resource] - Access mode: <https://www.osp.ru/school>. - Date of access: 15.04.2020.
- [5] Krasavin, V. Quantum cryptography [Electronic resource] - Access mode: <https://ru.b-ok.cc/book/628590/bbd531>. - Date of access: 15.04.2020.
- [6] Imre, S. Gvongyosi, L. Advanced Quantum Communications: An Engineering Approach, John Wiley & Sons, 2012.
- [7] Segienko, A. V. Quantum Communications and Cryptography, CRC Press, 2018.
- [8] Imre, S Quantum Communications: Explained for Communication Engineers, IEEE Communications Magazine 51(8), 2013.
- [9] Xin, S. Conti, A. Long, G. Muller, P. Sayeed, A. Yuan, J. Hanz, L. Guest Editorial Advances in Quantum Communications, Computing, Cryptography, and Sensing, IEEE Journal on Selected Areas in Communications 38(3), 2020.
- [10] Arun, G. Mishra, V. A review on quantum computing and communication, 2nd International Conference on Emerging Technology Trends in Electronics, Communication and Networking, 2014.
- [11] Morimae, T. Nishimura, H. Rational proofs for quantum computing 20(3-4), 181-193, 2020.
- [12] Mavroeidis, V. Vishi, K. Zych, M.D. Jøsang, A. The Impact of Quantum Computing on Present Cryptography, International Journal of Advanced Computer Science and Applications, 9(3), 2018.

Classification of 40 Different Human Movements with CNN Architectures and Comparison of Their Performance

Muhammed YILDIRIM^{1*}, Ahmet ÇINAR

¹ Computer Engineering Department, Engineering Faculty, Firat University, Elazığ, Turkey

² Computer Engineering Department, Engineering Faculty, Firat University, Elazığ, Turkey

*¹ 171129205@firat.edu.tr, ² acinar@firat.edu.tr

(Geliş/Received: 27/01/2021;

Kabul/Accepted: 09/02/2021)

Abstract: Detection of human movements has become one of the current issues with the developing technology. Recognition of human movements is used in many areas such as security systems, human computer interaction, human robot interaction. Due to the increase in data stored in databases, deep learning methods have recently become one of the most frequently used methods. At this study, it is aimed to classify human movements by using Convolutional Neural Network (CNN) architectures. Images are classified with InceptionV3, Googlenet and Alexnet architectures using a data set with 40 different motion classes. The highest accuracy rate with 76.15% was obtained in InceptionV3 architecture. Increasing the amount of data in CNN networks is a parameter that closely concerns the network uptime. Since 40 different motion classes are used in this study, the results obtained in the related architectures are obtained in different times.

Key words: Deep Learning, Human movements, Alexnet, Googlenet, Inceptionv3.

40 Farklı İnsan Hareketinin CNN Mimarileriyle Sınıflandırılması ve Başarım Oranlarının Karşılaştırılması

Öz: İnsan hareketlerinin tespit edilmesi gelişen teknolojiyle birlikte güncel konulardan biri haline gelmiştir. İnsan hareketlerinin tanınması güvenlik sistemleri, insan bilgisayar etkileşimi, insan robot etkileşimi gibi birçok alanda kullanılmaktadır. Veri tabanlarında saklanan verilerin artmasından dolayı son zamanlarda derin öğrenme yöntemleri en sık kullanılan yöntemlerden biri haline gelmiştir. Bu çalışmada Convolutional Neural Network (CNN) mimarileri kullanılarak insan hareketlerinin sınıflandırılması amaçlanmıştır. 40 farklı hareket sınıfına sahip olan bir veri seti kullanılarak InceptionV3 Googlenet ve Alexnet mimarileriyle görüntüler sınıflandırılmıştır. En yüksek doğruluk oranı %76.15 ile InceptionV3 mimarisinde elde edilmiştir. CNN ağlarında veri miktarının artması ağır çalışma süresini yakından ilgilendiren bir parametredir. Bu çalışmada 40 farklı hareket sınıfı kullanıldığından dolayı ilgili mimarilerde alınan sonuçlar farklı sürelerde elde edilmiştir.

Anahtar kelimeler: Derin Öğrenme, İnsan Hareketleri, Alexnet, Googlenet, Inceptionv3.

1. Introduction

After Alexnet architecture won the large-scale visual recognition (ILSVCR) competition in 2012, the Convolutional Neural Network (CNN) started a new era in image processing. Thanks to these deep learning-based neural networks, the classification process can be successfully performed today. In this study, Alexnet, who won the large-scale visual recognition competition in 2012, and the Googlenet and inceptionV3 architectures, which won the same competition in 2014, were used [1]. Classification of human movements has become an important issue with the developing technology. Recognition and classification of human movements are widely used in many areas such as security systems, human computer interaction, smart homes, object tracking, environment supported life, rehabilitation services in elderly care homes [2]. This situation makes the issue of recognition of human movements more and more important every day.

The purpose of the describe human movements is to try to recognize a human activity automatically using relevant images. In recent years, human movement recognition systems have been a major subject of study. It is very difficult to classify human movements with high accuracy, especially in studies involving more than one movement class [3]. The source of this difficulty lies in the similarity of most human movements. The fact that human movements are similar to each other complicates the result obtained in large-class data sets. The

* Corresponding author: 171129205i@firat.edu.tr. ORCID Number of authors: ¹0000-0003-1866-4721, ²0000-0001-5528-2226

performance rate may be higher in data sets with fewer classes. Since there are 40 different classes in the data set used in this study, the performance rate of the study decreases.

Many methods are used to classify human movements. Support Vector Machines (SVM) [4], Principal Component Analysis (PCA) [5], Histograms of Oriented Gradients(HOG) [6] are some of these methods used. However, methods based on deep learning have been used widely in the field of image classification in recent years [7]. In this study, it is aimed to classify 40 different human movements using the Stanford 40 Action data set taken from Stanford University. Alexnet, Googlenet and InceptionV3 models, which are CNN models, are used for the classification of this data. With these models, accuracy and loss curves are obtained separately. In addition, the performance rates of the models were calculated from the confusion matrix obtained and these models were compared with each other.

In the first part of the study, the classification of human movements is briefly mentioned. In the second chapter, the data set and used models are explained. In the third part, experimental results are evaluated. In the last section, the results are evaluated and future studies are mentioned.

2. Materials and Methods

Classification of human movements has become an important issue with the developing technology. In this study, it is aimed to classify 40 different human movements. CNN-based models are used to classify human movements. The test results obtained with Alexnet [8], Googlenet [9], Inceptionv3 [10] models were compared with each other.

2.1. Data set

In this study, 40 Action datasets taken from the Stanford University web page are used [11]. The data set consists of 40 different human movement classes. The number of pictures in each class is different for these movements. The classes used and the number of data in these classes are given in table 1.

Table 1. Data counts and image examples in 40 action classes.

Applauding (285 Image)	Blowing bubbles (259 Image)	Brushing teeth (200 Image)	Cleaning the floor (212 Image)	Climbing (295 Image)	Cooking (288 Image)	Cutting trees (203 Image)	Cutting vegetables (189 Image)
							
Drinking (256 Image)	Feding a horse (286 Image)	Fishing (273 Image)	Fixing a bike (228 Image)	Fixing a car (251 Image)	Gardening (199 Image)	Holding an umbrella (292 Image)	Jumping (295 Image)
							
Looking through a microscope (191 Image)	Looking through a telescope (203 Image)	Phoning (259 Image)	Playing guitar (289 Image)	Playing violin (260 Image)	Pouring liquid (200 Image)	Pushing a cart (235 Image)	Reading (245 Image)
							
Riding a bike (293 Image)	Riding a horse (296 Image)	Rowing a boat (185 Image)	Running (251 Image)	Shooting an arrow (214 Image)	Smoking (241 Image)	Taking photos (197 Image)	Texting message (193 Image)
							



Each class in the data set has an average of 180-300 images. The total number of images in 40 classes is 9532.

2.2. Models Used in the Paper

In this study, Alexnet, Googlenet and Inceptionv3, which are CNN models, are used.

2.2.1. Alexnet

The LeNet architecture, published by Yan LECun in 1998, is seen as the first study in deep learning. However, the most important factor in the popularization of deep learning is the Alexnet architecture. Alexnet architecture won the large-scale visual recognition (ILSVRC) competition published in 2012. After this success of the Alexnet architecture, deep learning architectures have become popular. With this success of the Alexnet architecture, the object identification error value of computers decreased from 26.2% to 15.4% [12].

2.2.2. Googlenet

It is the winning model of ImageNet 2014 competition. The combination of starter modules in the Googlenet model has a complex structure. Since the error rate in Googlenet architecture is 5.7%, it has achieved successful results in data sets. Googlenet has a structure of 144 layers in total. The starting layers in Googlenet have the ability to filter in different sizes. With this feature, it differs from the previously suggested models [13]. This architecture has the distinction of being one of the first Cnn works in which layers have moved away from an ordered structure.

2.2.3. Inceptionv3

We can define Inceptionv3 model as a model consisting of three parts. This parts Convolutional block, improved start up module and classifier [14]. This model takes the input data in 299x299 size. Inceptionv3 model consists of 315 layers in total. In the Inceptionv3 model, Relu is used as the activation function, batch normalization for normalization, and max pooling and average pooling are used together for pooling.

2.3. Layers of Convolutional Neural Networks

2.3.1. Input Layer

This layer is the first layer of the developed CNN models. Images are first read from the input layer [15]. The entrance dimensions of the models used in the application are given in table 2.

Table 2. Input size of models

	Alexnet	Googlenet	InceptionV3
Input Size	227 227 3	224 224 3	299 299 3

2.3.2. Convolutional Layer

Convolution layer, which is considered as the main layer of CNN architecture, is the process of applying different filters such as 2x2, 3x3, 5x5 on the image. The filter operator is scrolled through the image. The main purpose of this process is to obtain feature maps [16]. The application of a 3x3 size filter to an 8x8 size image is shown in figure 1.

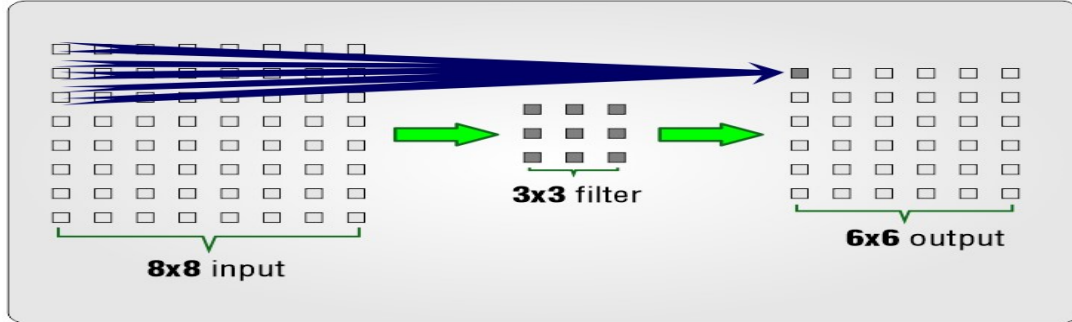


Figure 1. Applying a 3x3 filter to the 8x8 input image

Calculation of the output size is given in equation 1.

$$o = ((i - k) + 2p) / s + 1 \quad (1)$$

i: Input Size, k: filter size, s: number of steps, p: padding process, o: output size

2.3.3. Activation Function (RELU)

With the activation process, a linear filter is obtained with a nonlinear function applied to each component of a feature map. Relu is an activation function commonly used in CNN networks. It is also used in sigmoid and tangent activation functions [17]. Relu equation 2, Sigmoid equation 3 and Tanh equation 4 are presented.

$$\text{Relu} = f(x) = \begin{cases} 0, & x < 0 \\ x, & x \geq 0 \end{cases}, f'(x) = \begin{cases} 0, & x < 0 \\ 1, & x \geq 0 \end{cases} \quad (2)$$

$$\text{Sigmoid} = f(x) = \frac{1}{1+e^{-x}}, f'(x) = f(x)(1 - f(x)) \quad (3)$$

$$\text{Tanh} = f(x) = \tanh(x) = \frac{2}{1+e^{-2x}} - 1, f'(x) = 1 - f(x)^2 \quad (4)$$

2.3.4. Normalization

This layer, where the normalization process is performed, mostly normalizes the values produced by the Fully Connected and convolution layers. After the normalization process, the training time of the network is shortened and the learning process of the network faster [18].

2.3.5. Dropout

One of the problems with CNN architectures is that the network is memorized. In CNN architectures, node dilution is performed to prevent memorization. In this process, some nodes of the network are removed randomly. The original structure of the network is shown in Figure 2.a, and its shape after the node dilution step is shown in Figure 2.b [19].

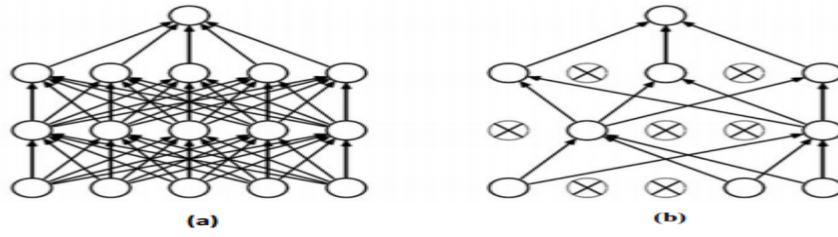


Figure 2. Dropout process

2.3.6. Pooling Layer

In the pooling layer, the data size is reduced and calculation costs are lowered. It is tried to prevent the network from memorizing. Since the data volume decreases in the pooled image, there is a shrinkage. The height and width of the image are reduced. As a result of this process, there is no change in the depth of the image [20]. In an image that has been pooled, the size of the new image is calculated by equation 5.

$$Y = \frac{W-F}{S} + 1 \quad (5)$$

Y=Size of the new image, W=Image_size, F=Filter_size, S=Number of steps.

2.3.7. Fully Connected

The classification stage comes after the feature extraction stage in CNN networks. Fully Connected takes feature maps as input and prepares them for classification. The matrix obtained from the feature maps in a multi-dimensional form is made unidimensional in this layer and given as input to the classifier [21].

2.3.8. Softmax and Classification

This layer comes after the Fully Connected layer and classification is done on this layer. The output value of this layer is equal to the number of objects to be classified [22].

3. Application and Results

In the study, it is aimed to classify human movement images belonging to 40 different classes with CNN models. While 80% of the Stanford 40 actions dataset used is used for training the model, the remaining 20% is reserved for testing the model. The study is carried out in a Matlab environment in a computer with 8GB RAM memory of the 8th generation.

There are many parameters that measure the success rate of working in CNN architectures. Most of these parameters are obtained using a Confusion matrix [23]. An example of the Confusion matrix is given in table 3.

Table 3. Confusion Matrix

	A	B
A	TruePositive(TP)	FalsePositive(FP)
B	FalseNegative(FN)	TrueNegative(TN)

The success rates of the models are compared according to the accuracy matrix. Accuracy ratio is calculated by equation 6.

$$Accuracy = \frac{TP+TN}{TP+TN+FP+FN} \quad (6)$$

Other parameter values used in the study are given in table 4.

Table 4. Used parameters and their values

Software	Model	MaxEpochs	Optimization	MiniBatchSize	LearningRate	ValidationFrequency
Matlab	AlexNet GoogleNet InceptionV3	5	Stochastic Gradient Descent (SGD)	16	10^{-5}	6

The accuracy and loss curves of the model trained using the Alexnet model are given in figure 3. 59.59% accuracy value is obtained with Alexnet. Confusion matrix created with the Alexnet architecture is as in figure 4. By looking at the confusion matrix, we can see which data is placed in which class.

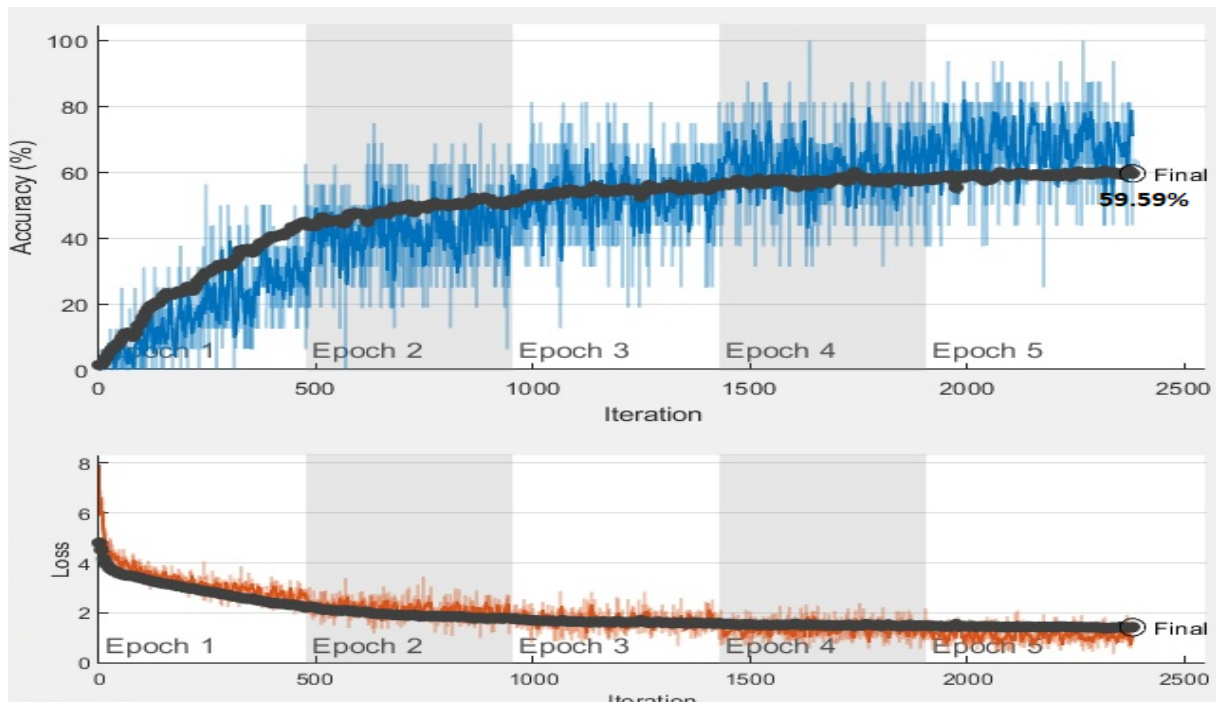


Figure 3. Alexnet's accuracy and loss curves

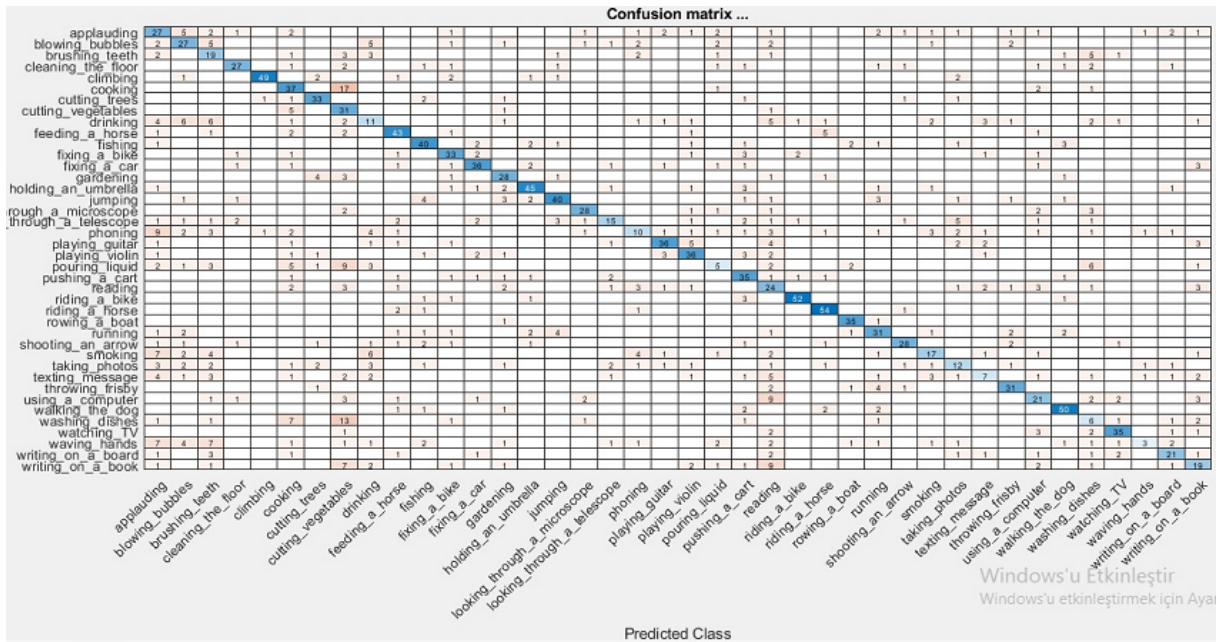


Figure 4. Alexnet’s confusion matrix.

The accuracy and loss curve acquired with the Googlenet model is as in figure 5. 71.02% accuracy is achieved with Googlenet. The confusion matrix obtained with Googlenet is as in figure 6.

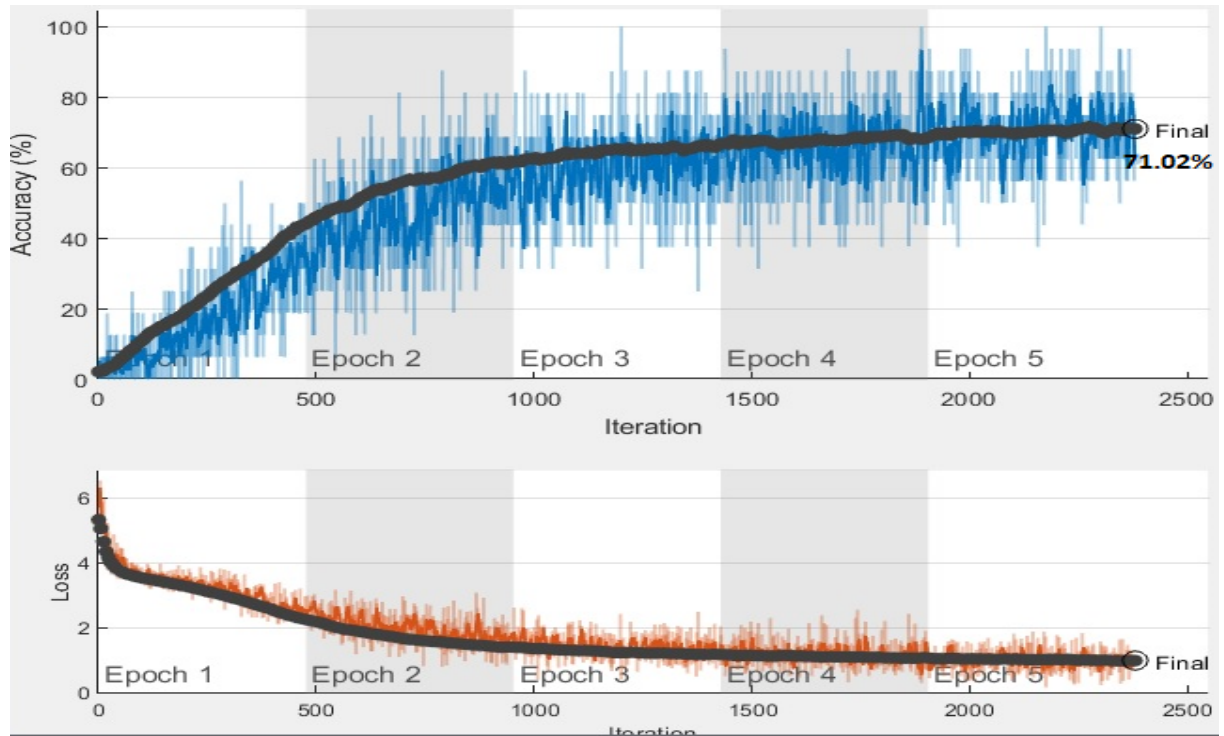


Figure 5. Googlenet’s accuracy and loss curves.

Classification of 40 Different Human Movements with CNN Architectures and Comparison of Their Performance

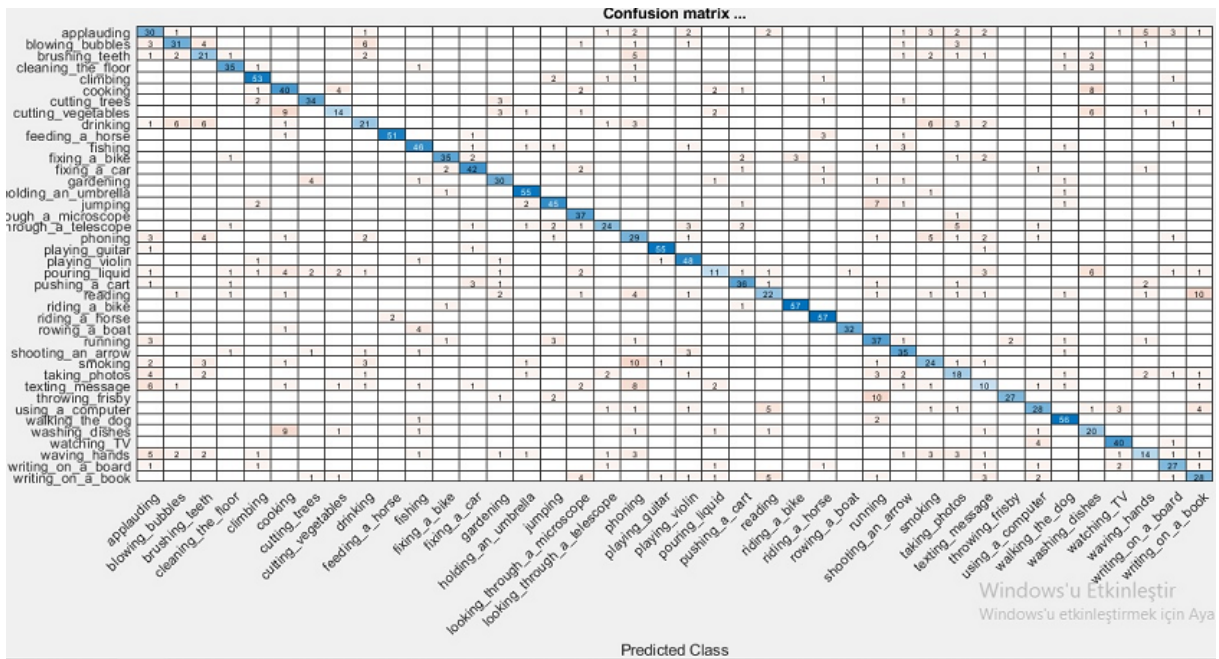


Figure 6. GoogLeNet’s confusion matrix.

The accuracy and loss curve obtained with the InceptionV3 model is as in figure 7. An accuracy of 76.15% is achieved with InceptionV3. This rate is the highest accuracy rate among the architectures used. The confusion matrix obtained with InceptionV3 is as in figure 8.

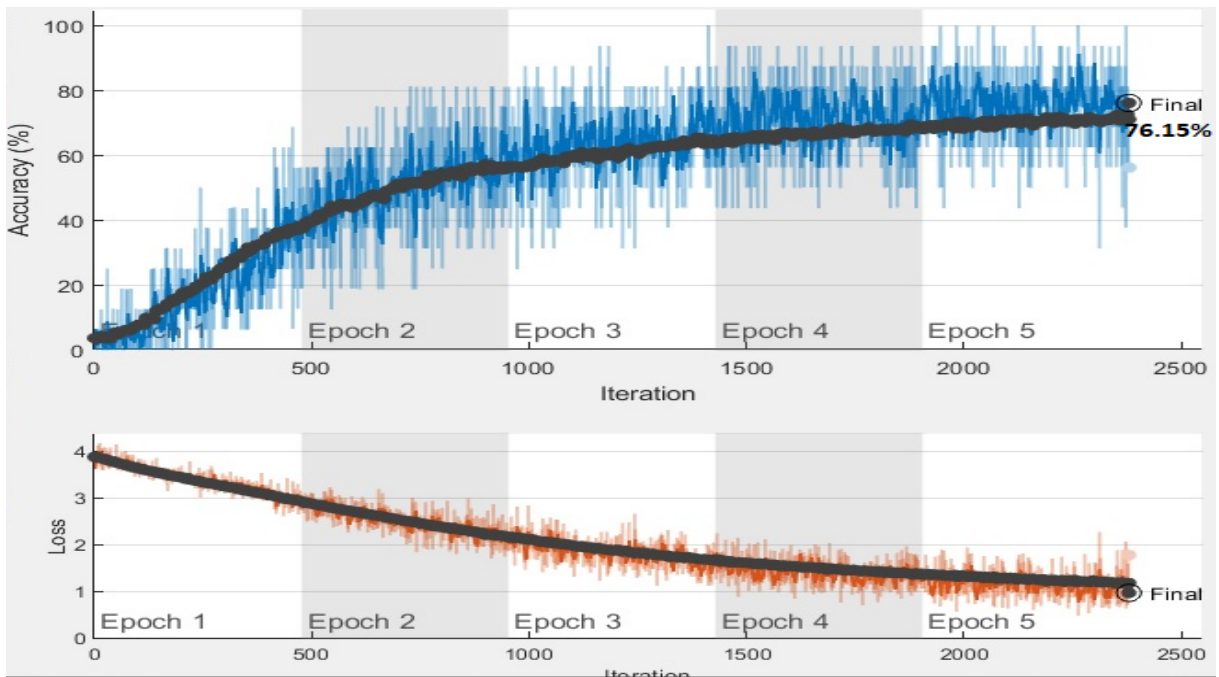


Figure 7. InceptionV3’s accuracy and loss curves.

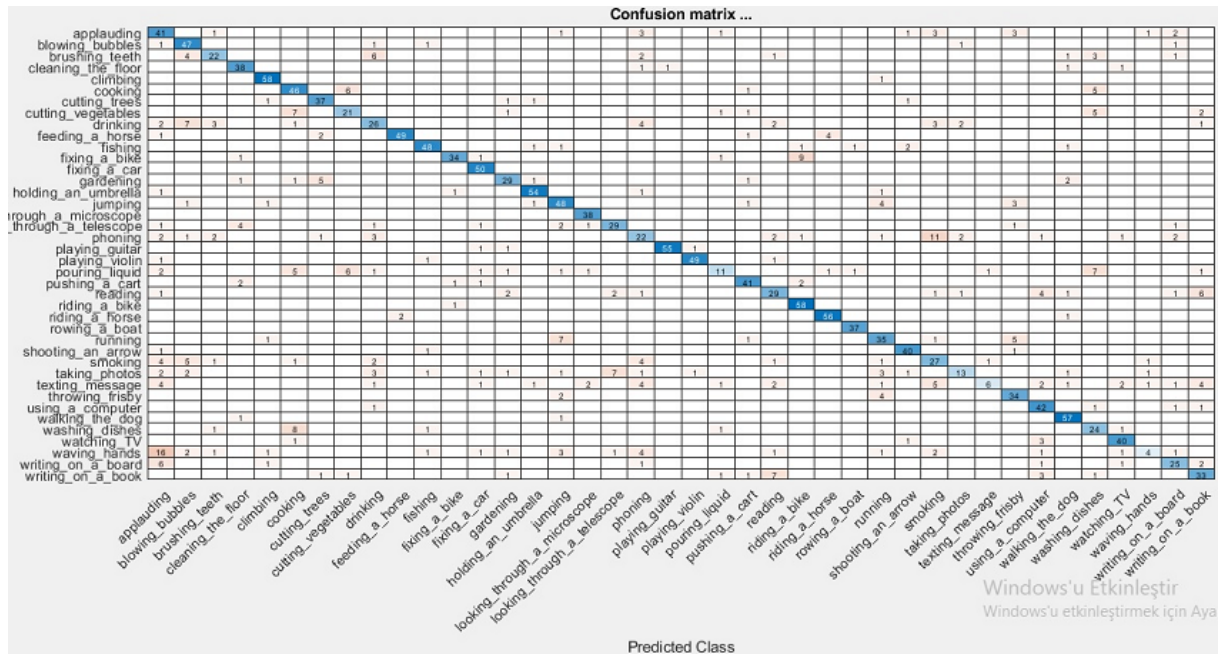


Figure 8. Inceptionv3’s confusion matrix.

Classification of human movements is a difficult subject of study due to the large number of human movement class and the similarity of these movements.

4. Conclusions

With the advancing technology, the process of classifying human movements has become an important issue. With the development of technology in recent years, it is of great importance to use confidential data and make inferences from this data. After deep learning architectures became popular, human computer interaction has become one of the most current topics in recent times. There are many studies on the classification of human movements. Classification of human movements is used in many areas from health to safety, from sports to social life, from object tracking to the game industry. In this study, Alexnet, Googlenet and Inceptionv3 models from CNN models were used to classify images of human movements. The highest accuracy value is obtained in InceptionV3 model with 76.15%. Accuracy values of 59.59% are obtained in the Alexnet model and 71.02% in the Googlenet model. In future studies, a new architecture will be studied to improve performance in classifying human movements.

References

- [1] Ebrahim, M., Al-Ayyoub, M., & Alsmirat, M. A. (2019, June). Will Transfer Learning Enhance ImageNet Classification Accuracy Using ImageNet-Pretrained Models?. In 2019 10th International Conference on Information and Communication Systems (ICICS) (pp. 211-216). IEEE. DOI: 10.1109/IACS.2019.8809114
- [2] AYDIN, İ., & AŞICI, B. (2020). İnsan Hareketlerinin Tanınması için Parçacık Sürü Optimizasyonu Tabanlı Topluluk Sınıflandırıcı Yöntemi. Fırat Üniversitesi Mühendislik Bilimleri Dergisi, 32(2), 381-390. <https://doi.org/10.35234/fumbd.671403>
- [3] Murad, A., & Pyun, J. Y. (2017). Deep recurrent neural networks for human activity recognition. Sensors, 17(11), 2556. <https://doi.org/10.3390/s17112556>
- [4] Batool, M., Jalal, A., & Kim, K. (2019, August). Sensors Technologies for Human Activity Analysis Based on SVM Optimized by PSO Algorithm. In 2019 International Conference on Applied and Engineering Mathematics (ICAEM) (pp. 145-150). IEEE. DOI: 10.1109/ICAEM.2019.8853770
- [5] Altun, K., & Barshan, B. (2010, August). Human activity recognition using inertial/magnetic sensor units. In International workshop on human behavior understanding (pp. 38-51). Springer, Berlin, Heidelberg. https://doi.org/10.1007/978-3-642-14715-9_5
- [6] Ke, S. R., Thuc, H. L. U., Lee, Y. J., Hwang, J. N., Yoo, J. H., & Choi, K. H. (2013). A review on video-based human activity recognition. Computers, 2(2), 88-131. <https://doi.org/10.3390/computers2020088>

- [7] Yildirim, M., Çinar, A. (2019). Classification of white blood cells by deep learning methods for diagnosing disease. *Revue d'Intelligence Artificielle*, Vol. 33, No. 5, pp. 335-340. <https://doi.org/10.18280/ria.330502>
- [8] Krizhevsky, A., Sutskever, I., & Hinton, G. E. (2012). Imagenet classification with deep convolutional neural networks. In *Advances in neural information processing systems* (pp. 1097-1105).
- [9] Szegedy, C., Liu, W., Jia, Y., Sermanet, P., Reed, S., Anguelov, D., ... & Rabinovich, A. (2015). Going deeper with convolutions. In *Proceedings of the IEEE conference on computer vision and pattern recognition* (pp. 1-9).
- [10] Szegedy, C., Vanhoucke, V., Ioffe, S., Shlens, J., & Wojna, Z. (2016). Rethinking the inception architecture for computer vision. In *Proceedings of the IEEE conference on computer vision and pattern recognition* (pp. 2818-2826).
- [11] Stanford University, <http://vision.stanford.edu/Datasets/40actions.html>
- [12] Özkan, İ. N. İ. K., & Ülker, E. (2017). Derin öğrenme ve görüntü analizinde kullanılan derin öğrenme modelleri. *Gaziosmanpaşa Bilimsel Araştırma Dergisi*, 6(3), 85-104.
- [13] YILDIZ, O. (2019). Derin öğrenme yöntemleriyle dermoskopi görüntülerinden melanom tespiti: Kapsamlı bir çalışma. *Gazi Üniversitesi Mühendislik Mimarlık Fakültesi Dergisi*, 34(4), 2241-2260. <https://doi.org/10.17341/gazimmfd.435217>
- [14] Lin, C., Li, L., Luo, W., Wang, K. C., & Guo, J. (2019). Transfer learning based traffic sign recognition using inception-v3 model. *Periodica Polytechnica Transportation Engineering*, 47(3), 242-250. <https://doi.org/10.3311/PPtr.11480>
- [15] Çinar, A., Yildirim, M. (2020). Classification of malaria cell images with deep learning architectures. *Ingénierie des Systèmes d'Information*, Vol. 25, No. 1, pp. 35-39. <https://doi.org/10.18280/isi.250105>
- [16] Yildirim, M., Çinar, A. (2020). A deep learning based hybrid approach for COVID-19 disease detections. *Traitement du Signal*, 37(3): 461-468. <https://doi.org/10.18280/ts.370313>
- [17] Pei, J.Y., Shan, P. (2019). A micro-expression recognition algorithm for students in classroom learning based on convolutional neural network. *Traitement du Signal*, Vol. 36, No. 6, pp. 557-563. <https://doi.org/10.18280/ts.360611>
- [18] Jiang, X., Chang, L., & Zhang, Y. D. (2020). Classification of Alzheimer's disease via eight-layer convolutional neural network with batch normalization and dropout techniques. *Journal of Medical Imaging and Health Informatics*, 10(5), 1040-1048. <https://doi.org/10.1166/jmihi.2020.3001>
- [19] Öztürk, Ş., Yigit, E., & Özkaya, U. Fused Deep Features Based Classification Framework for Covid-19 Classification with Optimized MLP. *Konya Mühendislik Bilimleri Dergisi*, 8, 15-27. <https://doi.org/10.36306/konjes.821782>
- [20] Çinar, A., Yildirim, M. (2020). Detection of tumors on brain MRI images using the hybrid convolutional neural network architecture. *Medical Hypotheses*, 139: 109684. <https://doi.org/10.1016/j.mehy.2020.109684>
- [21] Kanda, Y., Sasaki, K. S., Ohzawa, I., & Tamura, H. (2020). Deleting object selective units in a fully-connected layer of deep convolutional networks improves classification performance. *arXiv preprint arXiv:2001.07811*.
- [22] Kadam, V. J., Jadhav, S. M., & Vijayakumar, K. (2019). Breast cancer diagnosis using feature ensemble learning based on stacked sparse autoencoders and softmax regression. *Journal of medical systems*, 43(8), 1-11. <https://doi.org/10.1007/s10916-019-1397-z>
- [23] Zeng, G. (2020). On the confusion matrix in credit scoring and its analytical properties. *Communications in Statistics-Theory and Methods*, 49(9), 2080-2093. <https://doi.org/10.1080/03610926.2019.1568485>

The Helix and Slant Helices Generated by non-Degenerate Curves in $M^3(\delta_0) \subset E_2^4$

Fatma ALMAZ¹, Mihriban ALYAMAÇ KÜLAHÇI²

^{1,2}Department of Mathematics, Science Faculty, Firat University, Elazığ, Turkey

¹ fb_fatalmaz@hotmail.com, ² maryamac@firat.edu.tr

(Geliş/Received: 29/01/2021;

Kabul/Accepted: 14/02/2021)

Abstract: In this paper, we investigate helix and slant helices using non-degenerate curves in term of Sabban frame in de Sitter 3-space or Anti de Sitter 3-space $M^3(\delta_0)$. Furthermore, in $M^3(\delta_0)$ 3-space the necessary and sufficient conditions for the non-degenerate curves to be slant helix are given.

MSC[2000]: Primary 53A35; Secondary 53C25

Key words: Sabban frame, helix, slant helix, $M^3(\delta_0) \subset E_2^4$ 3-space.

$M^3(\delta_0) \subset E_2^4$ 3-Uzayında non-Dejenere Eğriler Tarafından Elde Edilen Helis ve Slant Helisler

Öz: Bu çalışmada, de Sitter veya Anti de Sitter $M^3(\delta_0) \subset E_2^4$ 3-uzayında dejenere olmayan eğrilerin helis ve slant helislerini Sabban çatısına göre inceledik. Ayrıca, $M^3(\delta_0)$ 3-uzayında non-dejenere eğrilerin slant helis olması için gerekli ve yeterli şartlar verildi.

Anahtar kelimeler: Sabban çatı, helis, slant helis, $M^3(\delta_0) \subset E_2^4$ 3-uzayı

1. Introduction

In the recent years, there has been remarkable interest in the slant helix and helices among or curve of geometrically constant slope, or so-called general helices are well-known curves in the classical differential geometry of space curves. Helices are characterized by the feature that the tangent makes a constant angle with a fixed straight line (the axis of the general helix), it is known that a curve x is called a slant helix if the principal normal lines of x make a constant angle with a fixed direction.

The concept of slant helix defined by Izumiya and Takeuchi [8, 9]. The geometry of helix and slant helices have been represented in a different ambient spaces by many mathematicians. In [1], the authors studied timelike B_2 -slant helices in Minkowski 4-space E_1^4 . Ahmad studied the position vectors of a spacelike general helix with reference to the standart frame in E_1^3 , [2]. In [3], the notion of a k-type slant helix in Minkowski 4-space E_1^4 was introduced by the authors. In [4], they gave necessary and sufficient conditions to be a slant helix in the Euclidean n-space and they expressed some integral characterizations of such curves in reference to curvature functions. In [14], the authors expressed helices and slant helices in lightlike cone. Camcı and et al. examined some characterizations for a non degenerate curve α to be a generalized helix by using its harmonic curvatures, [6]. Ferrandez and et al. obtained a Lancret-type theorem for null generalized helices in Lorentz-Minkowski space L^n , [7]. Ilarslan and et al. studied the position vectors of a timelike and a null helix in Minkowski 3-space E_1^3 , [10]. In [11], the authors examined spherical images the tangent indicatrix and binormal indicatrix of slant helix. In [15], they gave some characterizations for spacelike helices in Minkowski space-time E_1^4 . In [17], Turgut and et al. they examined the concept of a slant helix in Minkowski spacetime.

In this paper, we study helix and slant helices according to Sabban frame in de Sitter or Anti de Sitter 3-space.

* Corresponding author: fb_fatalmaz@hotmail.com. ORCID Number of authors: ¹0000-0002-1060-7813, ²0000-0002-8621-5779

2. Preliminaries

Let E_2^4 be the 4 –dimensional semi Euclidean space with index two with the metric

$$G(a, b) = \langle a, b \rangle = -a_1b_1 - a_2b_2 + a_3b_3 + a_4b_4$$

for all $a = (a_1, a_2, a_3, a_4), b = (b_1, b_2, b_3, b_4) \in \mathbb{R}^4$. Let $\{e_1, e_2, e_3, e_4\}$ be pseudo-orthonormal basis for E_2^4 . Then δ_{ij} is Kronecker-delta function such that $\langle e_i, e_j \rangle = \delta_{ij}\varepsilon_i$ for $\varepsilon_1 = \varepsilon_2 = -1, \varepsilon_3 = \varepsilon_4 = 1$. A vector $x \in E_2^4$ is said to be as spacelike, timelike and lightlike(null) if $\langle x, x \rangle > 0$ (or $x = 0$), $\langle x, x \rangle < 0$ and $\langle x, x \rangle = 0$ ($x \neq 0$), respectively. The norm of a vector $x \in E_2^4$ is given as $\|x\| = \sqrt{|\langle x, x \rangle|}$. The signature of a vector x is 1(or 0, -1) if x is spacelike(or null, timelike). Also, de Sitter 3-space with index 2 and Anti de Sitter 3-space in E_2^4 are given as

$$S_2^3 = \{x \in E_2^4: g(x, x) = 1\}; H_1^3 = \{x \in E_2^4: g(x, x) = -1\}, \quad (2.1)$$

respectively. The pseudo vector product of vectors a, b and c is given by

$$a \wedge b \wedge c = \begin{vmatrix} -e_1 & -e_2 & e_3 & e_4 \\ a_1 & a_2 & a_3 & a_4 \\ b_1 & b_2 & b_3 & b_4 \\ c_1 & c_2 & c_3 & c_4 \end{vmatrix},$$

where $\{e_1, e_2, e_3, e_4\}$ is the canonical basis of E_2^4 and $a = (a_1, a_2, a_3, a_4), b = (b_1, b_2, b_3, b_4), c = (c_1, c_2, c_3, c_4) \in \mathbb{R}_2^4$. Also, it is clear that $\langle w, a \wedge b \wedge c \rangle = \det(w, a, b, c)$ for any $w \in \mathbb{R}_2^4$. Hence, $a \wedge b \wedge c$ is pseudo-orthogonal to each of the vectors a, b and c . Unless otherwise stated for the sake of brevity, we will use the notation $M^3(\delta_0)$ instead of the symbols S_2^3 or H_1^3 . If $\delta_0 = 1$ or $\delta_0 = -1$, then $M^3(1) = S_2^3$ or $M^3(-1) = H_1^3$, respectively.

Let $x: I \subset \mathbb{R} \rightarrow M^3(\delta_0)$ be regular curve, where $\text{sign}(x(t)) = \delta_0$ for $\forall t \in I$. For non-degenerate curves in $M^3(\delta_0)$. The regular curve x is called as spacelike or timelike if x' is a spacelike or timelike vector where $x'(t) = dx/dt$ at any $t \in I$. The such curves are said to be non-degenerate curve. Let x be a non-degenerate curve, with arc length parametrization $s = s(t)$, that is the curve $x(s)$ is a unit speed curve. Also, the unit tangent vector of x is defined as $t(s) = x'(s)$. Also,

$$\langle x(s), x(s) \rangle = \delta_0, \langle x(s), t'(s) \rangle = -\delta_1; \delta_1 = \text{sign}(t(s)) \quad (2.2)$$

The vector $t'(s) + \delta_0\delta_1x(s)$ is pseudo-orthogonal to both $x(s)$ and $t(s)$. Moreover, since $\langle x''(s), x''(s) \rangle \neq \delta_0$ and $t'(s) + \delta_0\delta_1x(s) \neq 0$, the principle normal vector and the binormal vector of x is written as $n(s) = \frac{t'(s) + \delta_0\delta_1x(s)}{\|t'(s) + \delta_0\delta_1x(s)\|}$ and $b(s) = x(s) \wedge t(s) \wedge n(s)$, respectively. In addition, the geodesic curvature of x are given by $\kappa_g(s) = \|t'(s) + \delta_0\delta_1x(s)\|$. Therefore, pseudo-orthonormal frame field $\{x(s), t(s), n(s), b(s)\}$ of \mathbb{R}_2^4 along x is said to be the Sabban frame of non-degenerate curve x on $M^3(\delta_0)$, then

$$\begin{aligned} t(s) \wedge n(s) \wedge b(s) &= -\delta_0\delta_3x(s); n(s) \wedge b(s) \wedge x(s) = \delta_1\delta_3t(s); \\ b(s) \wedge x(s) \wedge t(s) &= -\delta_2\delta_3n(s); x(s) \wedge t(s) \wedge n(s) = b(s), \end{aligned}$$

where

$$\begin{aligned} \langle t(s), t(s) \rangle &= \text{sign}(t(s)) = \delta_1; \langle n(s), n(s) \rangle = \text{sign}(n(s)) = \delta_2 \\ \langle b(s), b(s) \rangle &= \text{sign}(b(s)) = \delta_3, \det(x, t, n, b) = -\delta_3. \end{aligned} \quad (2.3)$$

Also, let $x: I \rightarrow M^3(\delta_0)$ be an immersed spacelike (timelike) curve with k_g, τ_g with respect to the Sabban frame $\{x, t, n, b\}$, such that,

- If $\tau_g = 0$, x is said to be as planar curve in $M^3(\delta_0)$.
- If $k_g = 1$ and $\tau_g = 0$, x is called a horocycle in $M^3(\delta_0)$.
- If both $k_g \neq 0$ and $\tau_g \neq 0$ are constant, it is said to be as helix in $M^3(\delta_0)$.

Now, let's assume that $\langle x''(s), x''(s) \rangle \neq \delta_0$. Then, Frenet-Serret formulas of x is given as

$$\begin{aligned} x'(s) &= t(s) \\ t'(s) &= -\delta_0\delta_1x(s) + k_g n(s) \\ n'(s) &= -\delta_2\delta_1k_g t(s) - \delta_1\delta_3\tau_g b(s) \\ b'(s) &= \delta_1\delta_2\tau_g n(s), \end{aligned} \quad (2.4)$$

where the geodesic torsion of x is given by $\tau_g = \frac{\delta_1 \det(x, x', x'', x''')}{k_g^2}$, [18].

Definition 1. Let x be according to the frenet frame $\{t, n, b\}$ in M^3 . If there exists a constant vector field $W \neq 0$ in M^3 such that

$$\langle t(s), W_i(s) \rangle = \text{constant},$$

for $\forall s \in I$, then it is called a helix in M^3 and $W(s)$ is said to be an axis of $x(s)$, [9].

Remark 1 The condition $\langle x''(s), x''(s) \rangle \neq \delta_0$ is equivalent to $k_g(s) \neq 0$. Moreover, it may express that $k_g(s) = 0$ and $t'(s) + \delta_0 \delta_1 x(s) = 0$ if and only if the non-degenerate curve x is a geodesic in $M^3(\delta_0)$, [5].

3. Helix and Slant Helices in $M^3(\delta_0)$

In this section, the helices and slant helices in $M^3(\delta_0)$ space are expressed using sabban frame.

Definition 3. Let x be a non-degenerate curve with arc length according to the Sabban frame $\{x, t, n, b\}$ in $M^3(\delta_0)$. If there exists a constant vector field $W_i \neq 0$ in $M^3(\delta_0)$ such that

$$\langle t(s), W_i(s) \rangle = \text{constant},$$

for $\forall s \in I$, then x is called a helix in $M^3(\delta_0)$ and $W_i(s)$ is called as axis of $x(s)$.

Theorem 1. Let x be a helix in $M^3(\delta_0)$. Then the axis of the helices x are given as

$$W_i(s) = (\delta_0 A s + c_1)x(s) + \frac{A}{\delta_1}t(s) + \left(\frac{A(\delta_0 s + c_2)}{\delta_0 \delta_1 k_g}\right)n(s) + \left(\frac{A\delta_3}{\delta_2} \int (\delta_0 s + c_2)\tau_g(s)ds\right)b(s),$$

where $A, c_i \in \mathbb{R}_0^+$.

Proof. Let $W(s)$ be an axis of helix x with the Sabban frame $\{x, t, n, b\}$. Then, $W(s)$ can be written as

$$W_i = m_0^j x + m_1^j t + m_2^j n + m_3^j b, \tag{3.2}$$

where $m_i^j, i \in \{0,1,2,3\}$ are differentiable functions and from definition of the helix, we have $\langle t(s), W_i(s) \rangle = A, A \in \mathbb{R}_0^+$. Furthermore, from (2.2), (2.3) and (3.2), we can write

$$\delta_0 m_0^j = \langle x, W_i \rangle, m_1^j \delta_1 = \langle t, W_i \rangle = A, m_3^j \delta_3 = \langle b, W_i \rangle = A, m_2^j \delta_2 = \langle n, W_i \rangle, \forall s \in I. \tag{3.3}$$

By differentiating on both sides of (3.2) and using (2.4), we get

$$m_0^{j'} - m_1^j \delta_0 \delta_1 = 0, \tag{3.4a}$$

$$m_0^j + m_1^{j'} - m_2^j \delta_2 \delta_1 k_g = 0, \tag{3.4b}$$

$$m_1^j k_g + m_2^{j'} + m_3^j \delta_2 \delta_1 \tau_g = 0, \tag{3.4c}$$

$$-m_2^j \delta_3 \delta_1 \tau_g + m_3^{j'} = 0. \tag{3.4d}$$

Substituting $m_1^j \delta_1 = A$ into (3.4a), we have

$$m_0^j = \delta_0 A s + c_1. \tag{3.5}$$

After the necessary calculations from (3.4b) and (3.4d) the following equations (3.6) and (3.7) are obtained respectively.

$$m_2^j = \frac{A(\delta_0 s + c_2)}{\delta_0 \delta_1 k_g}. \tag{3.6}$$

$$m_3^j = \frac{A\delta_3}{\delta_2} \int (\delta_0 s + c_2)\tau_g(s)ds; c_i, A \in \mathbb{R}_0^+. \tag{3.7}$$

Hence, using (3.3) and $m_i^j, i \in \mathbb{R}$, we have

$$W_i = (\delta_0 A s + c_1)x + \frac{A}{\delta_1}t + \left(\frac{A(\delta_0 s + c_2)}{\delta_0 \delta_1 k_g}\right)n + \left(\frac{A\delta_3}{\delta_2} \int (\delta_0 s + c_2)\tau_g(s)ds\right)b. \tag{3.8}$$

Theorem 2. Let x be a non-degenerate curve with arc length in $M^3(\delta_0)$. Then x is a helix if and only if

$$k_g + \frac{d}{ds} \left(\frac{\delta_0 s + c_2}{k_g}\right) \frac{1}{\delta_2} + \delta_3 \tau_g \int (\delta_0 s + c_2)\tau_g ds = 0. \tag{3.9}$$

Proof. Using the equation (3.4c) and the equations $m_i^j, i \in \{0,1,2,3\}, j=n,b$. Hence, we get (3.9). Conversely, assume that (3.9) holds, we obtain define a vector field W_i . Therefore, from definition of helix, we write $W_i' = 0, \langle t, W_i \rangle = A, A \in \mathbb{R}_0^+$.

Corollary 1. Let $x: I \rightarrow M^3(\delta_0)$ is an helix curve with k_g and τ_g relative to the Sabban frame $\{x, t, n, b\}$

- 1) If the helix x is a horocycle in $M^3(\delta_0)$, x is non-degenerate curve in H_1^3 ,
- 2) If the helix x is a planar curve in $M^3(\delta_0)$, since $\tau_g = 0$ the following equation holds

$$\frac{k_g}{\sqrt{k_g^2 + \delta_0}} = \frac{c_4}{\delta_0 s + c_2}.$$

3.1 n-type Slant Helix

Definition 4. Let $x(s)$ be a non-degenerate curve with the Sabban frame $\{x, t, n, b\}$ in $M^3(\delta_0)$. If there exists a constant vector field W_n in $M^3(\delta_0)$ such that

$$\langle n, W_n \rangle = D, D \in \mathbb{R}_0^+,$$

for $\forall s \in I$. Then x is called a helix and W_n is called the n -axis of x .

Theorem 3 Let x be n -type slant helix in $M^3(\delta_0)$. Then the n -axes of x are

$$W_n = -D\delta_0\delta_1\delta_3 \left(\int \frac{\tau_g}{k_g} \int \tau_g ds ds \right) x - D\delta_3 \frac{\tau_g}{k_g} \left(\int \tau_g ds \right) t + \frac{D}{\delta_2} n + \frac{D\delta_3\delta_1}{\delta_2} \left(\int \tau_g ds \right) b, \quad (3.10)$$

where $D \in \mathbb{R}_0^+$.

Proof. Let W_n be an axis of n -type helix x with the Sabban frame $\{x, t, n, b\}$. From definition of the n -type helix, we have $\langle n(s), W_n(s) \rangle = D, D \in \mathbb{R}_0^+$. Thus, from equations (3.4), we get

$$\begin{aligned} m_0^n &= -D\delta_0\delta_1\delta_3 \int \frac{\tau_g}{k_g} \int \tau_g ds ds; \quad m_1^n = -D\delta_3 \frac{\tau_g}{k_g} \int \tau_g ds; \\ m_2^n &= \frac{D}{\delta_2}; \quad m_3^n = \frac{D\delta_3\delta_1}{\delta_2} \int \tau_g ds, \end{aligned} \quad (3.11)$$

Considering (3.11) we obtain (3.10).

Theorem 4. For the non-degenerate curve x to be n -slant helix in $M^3(\delta_0)$ the necessary and sufficient condition the following equation is provided

$$\delta_0\delta_1\delta_3 \int \frac{\tau_g}{k_g} \int \tau_g ds ds + \delta_3 \left\{ \frac{d}{ds} \left(\frac{\tau_g}{k_g} \right) \int \tau_g ds + \frac{\tau_g^2}{k_g} \right\} + \delta_1 k_g = 0. \quad (3.12)$$

Proof. Using the equation (3.4b), we get (4.12). Conversely, assume that (4.12) holds, we can define a vector field W_n as (3.10). Hence, from definition of n -slant helix, we can write $W_n' = 0, \langle n, W_n \rangle = \text{constant}$.

Corollary 2. Let $x: I \rightarrow M^3(\delta_0)$ is n -slant helix curve with k_g and τ_g as regards the Sabban frame $\{x, t, n, b\}$. If the n -slant helix x is a planar curve in $M^3(\delta_0)$, since $k_g = 0$ the curve x is also geodesic non-degenerate curve.

3.2 b-type Slant Helix

Definition 5. Let x be non-degenerate curve with the Sabban frame $\{x, \alpha, \beta, \gamma\}$ in $M^3(\delta_0)$. If there is a $W_b \neq 0$ constant vector field in $M^3(\delta_0)$ such that

$$\langle b, W_b \rangle = B, B \in \mathbb{R}_0^+.$$

Then x is called b -type slant helix and W_b is called the b -axis of x .

Theorem 5. Let x be b -type slant helix in $M^3(\delta_0)$. Then the b -axes of x are given as follows

$$W_b(s) = \left(-B \frac{\delta_0\delta_2}{\delta_3} \int \frac{\tau_g}{k_g} ds + c_3 \right) x(s) - B \frac{\delta_1\delta_2}{\delta_3} \frac{\tau_g}{k_g} t(s) + \frac{B}{\delta_3} b(s), \quad (3.13)$$

where $c_3, B \in \mathbb{R}_0^+$.

Proof. From definition of the b -type slant helix and (3.4), we get

$$m_0^b = -B \frac{\delta_0\delta_2}{\delta_3} \int \frac{\tau_g}{k_g} ds + c_3; \quad m_1^b = -B \frac{\delta_1\delta_2}{\delta_3} \frac{\tau_g}{k_g}; \quad m_2^b = 0; \quad m_3^b = \frac{B}{\delta_3}, \quad (3.14)$$

where $c_3, B \in \mathbb{R}_0^+$. Considering (3.14), we have (3.13).

Theorem 6. For the non-degenerate curve x to be b -slant helix in $M^3(\delta_0)$ the necessary and sufficient condition the following equation is provided

$$\delta_0 \int \frac{\tau_g}{k_g} ds + \delta_1 \frac{d}{ds} \left(\frac{\tau_g}{k_g} \right) + c_4 = 0, c_4 \in \mathbb{R}_0^+. \quad (3.15)$$

Proof. From definition of b -type slant helix and using (3.4b), we get (3.15). Conversely, assume that (3.15) holds, we can write a vector field W_b as (3.13). Since $W_b' = 0$, we obtain $\langle b, W_b \rangle = B$. Hence, the theorem is provided.

Example 1. Let us consider a non-degenerate curve in $M^3(\delta_0)$ given by

$$x(s) = \left(0, \frac{1-\sqrt{5}}{2} \sinh s, \pm \sqrt{\frac{-1+\sqrt{5}}{2}}, \frac{-1+\sqrt{5}}{2} \cosh s \right),$$

the Sabban frame of x is given as

$$t(s) = \left(0, \frac{1-\sqrt{5}}{2} \cosh s, 0, \frac{-1+\sqrt{5}}{2} \sinh s \right); Q = \sqrt{\frac{-1+\sqrt{5}}{2}},$$

$$n(s) = \left(0, \frac{1-\sqrt{5}}{2Q} (\cosh s + \delta_0 \delta_1 \sinh s), \pm 1, \frac{-1+\sqrt{5}}{2Q} (\sinh s + \delta_0 \delta_1 \cosh s) \right); b(s) = ((3-\sqrt{5})\delta_0 \delta_1, 0, 0, 0),$$

according to Theorem 1, Theorem 3 and Definition 3, Definition 4, the curve x holds helix and n -type helices whose axes are satisfied the following equations

$$\int (\delta_0 s + c_2) \tau_g(s) ds = \frac{c \delta_3}{\sinh s \delta_2} - \frac{\coth s \delta_2}{\delta_1 \delta_3},$$

$$\int \tau_g(s) ds \left(\frac{\tau_g}{k_g} (\cosh s + \delta_0 \delta_1 \sinh s) + \frac{\delta_1}{\delta_2} (\sinh s + \delta_0 \delta_1 \cosh s) \right) = c + \frac{d}{\delta_3 \delta_2}; c, d \in \mathbb{R}$$

3. Conclusion

In this study, we examine helix and n -type (and b -type) slant helices due to the Sabban frame given in de Sitter 3-space or Anti de Sitter 3-space $M^3(\delta_0)$. We show that some results of the helix and slant helix curves generated by the Sabban frame in $M^3(\delta_0)$ are given above. We find parameter equation of axis of W of n -type (and b -type) slant helices in terms of the Sabban frame's vector fields.

References

- [1] Ali AT, Lopez R. Timelike B_2 -Slant Helices in Minkowski Space E_1^4 . *Archivum Mathematicum(BRNO) Tomus*, 2010; 46: 39-46.
- [2] Ali AT. Position vectors of spacelike general helices in Minkowski 3-Space. *Nonlinear Analysis* 2010; 73: 1118-1126.
- [3] Ali AT, Lopez R, Turgut M. k -type partially null and pseudo null slant helices in Minkowski 4-Space. *Math. Commun.* 2012; 17: 93-103.
- [4] Ali AT, Turgut M. Some Characterizations of slant helices in the Euclidean E^n . arXiv: 0904.1187v1 2009; 8 pp.
- [5] Barros M, Ferrandes A, Lukas P, Mero.no MA. General helices in the three dimensional Lorentzian space forms. *Rocky Mountain J. Math* 2001; 31(2): 373-388.
- [6] Camci C, Ilarslan K, Kula L, Hacisalihoglu HH. Harmonic curvatures and generalized helices in E^n . *Chaos, Solitons and Fractals* 2009; 40: 2590-2596.
- [7] Ferrandez A, Gimenez A, Lucas P. Null generalized helices in Lorentz-Minkowski Spaces. *Journal of Physics A: Math. and General* 2002; 35(39): 8243-8251.
- [8] Gluck H. Higher curvature of curves in Euclidean space. *Amer. Math. Monthly* 1996; 73: 699-704.
- [9] Izumiya S, Takeuchi N. New special curves and developable surface. *Turk J. Math.* 2004; 28: 153-163.
- [10] Ilarslan K, Boyacioglu O. Position vectors of a timelike and a null helix in Minkowski 3-Space. *Chaos Solitons and Fractals* 2008; 38: 1383-1389.
- [11] Kula L, Yayli Y, On slant helix and its spherical indicatrix. *App. Math. and Computation* 2005; 169: 600-607.
- [12] Kulahci M, Bektaş M, Ergüt M. Curves of AW(k)-type in 3-dimensional null cone. *Physics Letters A* 371 2007; 275-277.
- [13] Kulahci M, Almaz F. Some characterizations of osculating curves in the lightlike cone. *Bol. Soc. Paran. Math.* 2017; 35(2): 39-48, 2017.
- [14] Kulahci MA, Almaz F, Bektaş M. On helices and slant helices in the lightlike cone. *Honam Mathematical J.* 2018; 40(2): 305-314.
- [15] Liu H. Curves in the lightlike cone. *Contributions to Algebra and Geometry Volume* 2004; 45(1): 291-303.
- [16] Millman RS, Parker GD. *Elements of differential geometry*, Prentice-Hall Inc. Englewood Cliffs, N. J., 1977.
- [17] Onder M, Kocayigit H, Kazaz M. Spacelike helices in Minkowski 4-Space E_1^4 *Ann Univ. Ferrara* 2010; 56: 335-343.
- [18] O'Neill B. *Semi-Riemannian Geometry*, Academic Press, New York, 1983.
- [19] Turgut M, Yilmaz S. Some Characterizations of type-3 slant helices in Minkowski Space-time. *Involve* 2009; 2(1): 115-121.

Poisonous Mushroom Detection using YOLOV5

Emine CENGİL^{1*}, Ahmet ÇINAR²

¹ Computer Engineering Department, Firat University, Elazığ, Turkey

² Computer Engineering Department, Firat University, Elazığ, Turkey

*¹ ecengil@firat.edu.tr, ² acinar@firat.edu.tr

(Geliş/Received: 03/02/2021;

Kabul/Accepted: 23/02/2021)

Abstract: Mushroom is a nutritious food that is grown and consumed in many countries around the world. It is preferred for consumption due to its easy acquisition, the benefit to human health and taste. Although edible ones are beneficial for health, there are also poisonous types. It is difficult for people who are not familiar with this subject to distinguish which mushrooms are edible. Therefore, it will be useful to provide this process automatically. The study aims to identify poisonous mushrooms. In this context, a dataset containing the eight most poisonous mushroom species is created. The dataset created is trained with the fine tuning method using the pre-trained YOLOV5 algorithm. Precision, recall, and mAP metrics are used to demonstrate the performance of the method. The fine-tuned model enables the recognition of eight different types as 0.77 mean Average Precision.

Key words: Object detection, YOLOV5, Poisonous mushroom detection.

YOLOV5 Kullanarak Zehirli Mantar Tespiti

Öz: Mantar dünyadaki birçok ülkede yetişen ve tüketilen besin değeri yüksek bir gıdadır. Kolay edinilmesi, insan sağlığına faydalı olması ve lezzeti sebepleriyle tüketim için tercih edilmektedir. Yenilebilir olanları sağlık açısından faydalı olmakla beraber zehirli türleri de bulunmaktadır. Mantarların hangilerinin yenilebilir olduğunu ayırt etmek bu konuda bilgi sahibi olmayan kişiler için zordur. Dolayısıyla bu işlemin otomatik olarak sağlanması faydalı olacaktır. Çalışma, zehirli mantarların tanınmasını sağlamaktır. Bu kapsamda, en zehirli 8 mantar türünü içeren bir veri seti oluşturuldu. Oluşturulan veri seti, ön eğitilmiş YOLOV5 algoritması kullanılarak ince ayar yöntemi ile eğitildi. Yöntemin başarımını göstermek için precision, recall ve mAP kriterleri kullanıldı. İnce ayarlanmış model, sekiz farklı türün tanınmasını 0.77 mean Average Precision olarak sağlamıştır.

Anahtar kelimeler: Nesne bulma, YOLOV5, Zehirli mantar tespiti.

1. Introduction

Mushroom is a very nutritious fungus. It contains vitamins B, C, and D, minerals such as copper, beta-glucans, potassium, selenium, sodium, calcium, phosphorus, magnesium and a large amount of protein [1]. They support preventing diseases such as cancer and diabetes. Also, it has benefits such as preventing weight loss and strengthening immunity [2]. There are many types of mushrooms in nature. The number of edible mushrooms is high. There are also types of poisonous mushrooms. Headaches, allergies, anxiety can be seen as side effects of eating poisonous mushrooms. While only a few of the around 80 types of poisonous mushrooms are deadly when eaten, most of these deadly mushrooms have a resemblance to edible species and are therefore particularly dangerous. For these reasons, it is important to distinguish poisonous mushrooms.

Studies have been done to classify poisonous mushrooms. S Alkronz et al. [3] used multilayer sensors to divide mushrooms into two groups as poisonous and edible. Using the "JustNN" software, they achieved 99.25% accuracy in their study with 8124 samples. Y. Wang et al. [4] emphasized the importance of recognizing poisonous mushrooms, Logistic regression, support vector machine and multi-grained cascade forest classifier methods were tried to distinguish poisonous mushrooms. The highest accuracy was achieved as 98% with multi grained cascade forest. P. Maurya et al. [2] used five different classifiers in their study in which they focused on mushroom classification using the texture feature based on a machine learning approach. Among these, SVM provided 76.6% accuracy performance by showing higher accuracy than other classifiers.

In [5], a method using the PCA algorithm is proposed to distinguish edible from inedible mushrooms. The performance of the proposed method showed a success rate of about 85% ~ 96% increasing with the number of training images. S. Beniwal et al. [6], were tested Naive Bayes, ZeroR, and Bayes net classifiers with the WEKA tool to classify the mushroom dataset. Bayes has shown the highest accuracy. I. T. Ayorinde et al. [7] develop a

* Corresponding author: ecengil@firat.edu.tr. ORCID Number of authors: ¹ 0000-0003-4313-8694, ² 0000-0001-5528-2226

deep learning model using a multi-layer perceptron neural network. Two different models, the first model with MLP and the model with PCA, were developed and applied using TensorFlow. The result shows that the model with PCA performs better than the first model with 98.34% accuracy. In [8], aimed to classify mushrooms according to whether they are edible or poisonous. In the method in which many classification algorithms are investigated, the decision tree method has shown the highest performance. M.A. Ottom et al. [9] aimed to classify mushrooms using the dataset they created from the internet. In the experiments performed with different machine learning algorithms, their methods showed 87% accuracy with the KNN classifier. In [10], a mobile application has been developed to recognize whether mushrooms are poisonous or not. In the application, the GrabCut algorithm is used for segmentation and probabilistic neural network as a classifier. The method using 133 images achieved 92% accuracy. In the literature, besides classification by looking at an image and numerical feature information, some studies make classification by using smell information. In [11], the authors proposed an electronic nose to classify the amanita mushroom species. Data were analyzed using PCA, LDA, and ANN algorithms. Classification of mushroom species provided 80-100% accuracy.

In the study, images of the 8 most poisonous mushroom species were collected from the internet. These images are manually labeled using the labelImg tool [12]. After the dataset acquisition, the related poisonous mushroom images were classified and localized using pre-trained yolov5 architecture.

The contributions of the study can be listed as follows:

- 1) To our knowledge, studies in the literature have treated mushrooms by dividing them into two groups as edible and poisonous. We group and detect the most poisonous mushrooms.
- 2) A dataset of eight categories including the most poisonous mushroom species was generated.
- 3) The Yolov5 architecture is trained with fine-tuning to enable the recognition of poisonous mushrooms. In addition to classification, location information is also provided with bounding boxes.

The organization of the study is as follows. Section 2 introduces basic object detection algorithms using deep learning methods. Section 3 explains the material and methods including dataset, model development, performance metrics, and experimental results. Finally, section 4 presents the conclusions of the paper.

2. Deep Learning Based Object Detection Approaches

Object detection finds the object in an image or video and then draws a box around the found object. Image classification aims to predict the class of the object in the image. Object localization involves determining the position of an object in an image. Object detection combines these two tasks, localizing and classifying objects in the image. An effective object detection extraction pipeline plays an important role in providing consistent and high quality labeled output [13].

Traditional methods were used before using deep learning algorithms for object detection problems. Methods developed for object detection consisted of the stages of proposal generation, feature vector extraction, and region classification [14]. Impressive results were obtained thanks to the advances in feature vector representations and classification models in the period they were used. However, using light variants of these models over the period 2007-2012 achieved slight gains [13].

Following the success of deep convolutional neural networks in image classification [15], object detection techniques based on deep learning have been developed [16] and have made significant progress in recent years. CNN-based detectors have replaced these detectors as they show better results than traditional detectors.

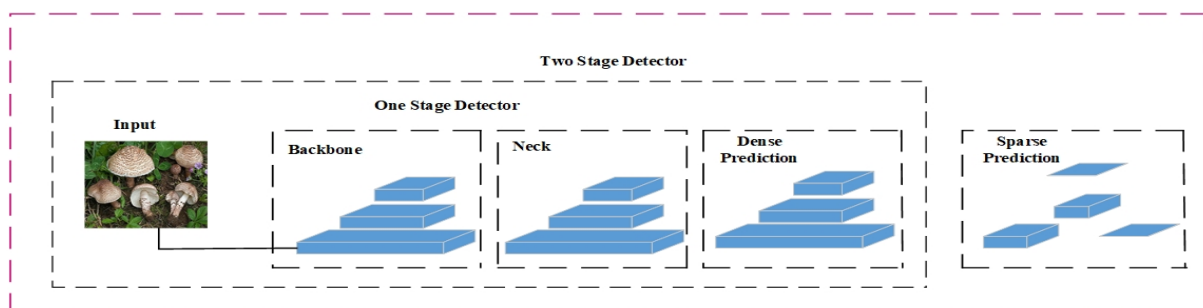


Figure 1. One-stage and two-stage object detectors

Generally, the convolutional neural network-based object detection approaches can be divided into two types. Figure 1 gives a summary of the two different approaches. The first type creates the region proposal network (RPN) as a branch to find category-independent candidate regions of interest (ROIs). The ROI-pooling layer is then added to create fixed-length feature representations. Another branch of the network is learned to classify and localize objects of various classes. These multi-stage detectors always require additional ROI-Pooling operations for better localization performance [17]. RCNN [16], Faster RCNN [17], Mask RCNN [18], Light-head RCNN [19], Cascade RCNN [20] are examples of multi-step object detectors.

The second type, called single-stage object detectors, finds objects in different categories through a sliding window [21]. The input images are gridded and the anchors correspond to spatially localized regions. The CNN outputs of these regions are used to distinguish objects from the background. These detectors are simple and effective in design and training. But there is a problem of unbalanced classification. SSD [21], DSSD [23], FSSD [24], MDSSD [25], DSOD [26], M2Det [27], RetinaNet [28], CornerNet [29], Reppoints [30], YOLO [31], YOLO9000 [32], YOLOV3 [33], YOLOV4 [34], DC-SPP-YOLO [35], YOLOV5 [36] can be cited as some of the one-step object detectors. Yolov5, the latest version of YOLO, one of the single-step object detectors from many existing architectures, was preferred in the study. We prefer it because it provides better performance in terms of accuracy and speed criteria [36].

3. Material and Methods

3.1. Dataset

There are thousands of mushroom species in the world. Although most of these are edible, there are also poisonous species. In the article written by Melissa Petruzzello, a dataset of 7 species [37], which are said to be the most poisonous species in the world, and fly agaric mushrooms, another poisonous species not mentioned in the article, were created. These species are; “Autumn Skullcap (*Galerina marginata*)”, “Destroying Angels”, “*Conocybe Filaris*”, “Deadly Dapperling”, “Death Cap”, “*Podostroma Cornu-damae*”, “Fly Agaric”, and “Webcaps”. An example of each category of images in the dataset is as illustrates in Figure 2.



Figure 2. Sample images of each category in our dataset [37]

Images were obtained from the internet. It is not possible to train images as we first downloaded them. Images of different formats and sizes have been converted to the same format. Then the images are labeled in YOLO format with the labelImg tool. The number of images concerning the classes is not equal. Besides, the number of images given to training and validation for each class was also kept different. In this way, it was aimed to observe the effect of the number of images on the training results. The number of images belonging to each category is as in table 1.

Table 1. The number of images in the dataset

	Autumn Sculp	Destroying angel	Conocybe Filaris	Deadly Dapperling	Death Cap	Podostroma Cornu-damae	Fly Agaric	Webcaps
Train	27	79	23	74	82	80	77	72
Validation	14	19	21	15	17	15	22	7
Total	41	98	44	89	99	95	99	79

3.2. Model Development

The YOLO algorithm is one of the one-step object detectors. Many versions of the algorithm have come out since the day it was published. Yolov5 was used in the study. The pipeline consists of three parts: backbone, neck, and head. In the model; CSPNET is preferred as a backbone. It extracts important features from the input image. The neck is used to produce feature pyramids. PANET is used here. The head is used to decide the final part. YOLOv5 uses the same head structure as the previous YOLOV3 [36].

Yolov5 has four different models: yolov5s, Yolov5m, Yolov5l and yolov5x. These models are pre-trained with an 80 class MSCOCO dataset. We used the largest model, Yolov5x, to get more accuracy. We trained the model with our poisonous mushrooms dataset. While 70% of the data was used for the training process, the remaining 30% was used for validation. The training process was carried out in a computer environment with Nvidia Geforce Gtx 950M GPU support. Other details of the training are as shown in table 2.

Table 2. Training details of Yolov5x model

Input Size	Model Parameters	Software Language	Environment	Library	Epoch	Optimizer	Activation Function
640x640	89M	Python	Spyder	Torch	40	SGD	Leaky RELU & Sigmoid

3.3. Performance Metrics

There are many measurement criteria used to evaluate the performance of an object detection model. Intersection over Union (IoU) Precision, Recall, Average Precision (AP), and mean Average Precision (mAP) can be given as examples of the most used criteria [39].

Intersection over Union: A measurement that finds the difference between the ground truth annotations and the predicted bounding boxes. This metric is used in the state of the art object detection algorithms. In object detection, the model predicts multiple bounding boxes for each object and removes unnecessary boxes depending on the threshold value based on the confidence scores of each bounding box. A threshold value is determined according to requirements. If the IoU value is greater than the threshold value, it is taken as an object, otherwise, the box is removed [38]. Metric is calculated as given in equation (1).

$$\text{IOU} = \text{Area of union} / \text{Area of intersection} \quad (1)$$

Precision: Precision is the metric used to measure correct predictions. It is calculated as in equation (2).

$$\text{Precision} = \text{TP} / (\text{TP} + \text{FP}) \quad (2)$$

Recall: Recall is the true positive rate. It measures the probability that exact reference objects will be detected correctly [39]. It is calculated as in equation (3).

$$\text{Recall} = \text{TP} / (\text{TP} + \text{FN}) \quad (3)$$

Average Precision (AP): AP is another criterion used to evaluate the performance of object detectors. It includes precision and recall. It is a single number metric that summarizes the Precision-Recall curve by averaging the recall values from 0 to 1 [40]. It is calculated with the equation given in 11-point interpolated AP (4).

$$AP = \frac{1}{11} \sum_{r \in (0, 0.1, 0.2, \dots, 1)} P_{interp}(r) \quad (4)$$

mAP: If the dataset contains M class category while calculating mAP, it takes AP average over M classes [41]. mAP is calculated as in equation (5).

$$mAP = \frac{1}{M} \sum_{j=1}^M AP_j \quad (5)$$

3.4. Experimental Results

The precision-recall curve obtained after the training is given in figure 3. According to the figure, the mean average Precision value for all classes was found to be 0.778. In addition, AP values of each class are given as 0.818, 0.825, 0.610, 0.737, 0.826, 0.854, 0.993, 0.556, respectively. The images allocated training and validation for each class are given at different rates as can be seen in table 1. For “fly agaric” mushroom showing the highest performance, 77 images were used for training and 22 images for testing. For the “Conocybe filaris” strain showing a low performance with 0.610 AP, 23 were used for training and 22 for validation. Here, both the low number of images and the uneven distribution affected the performance badly.

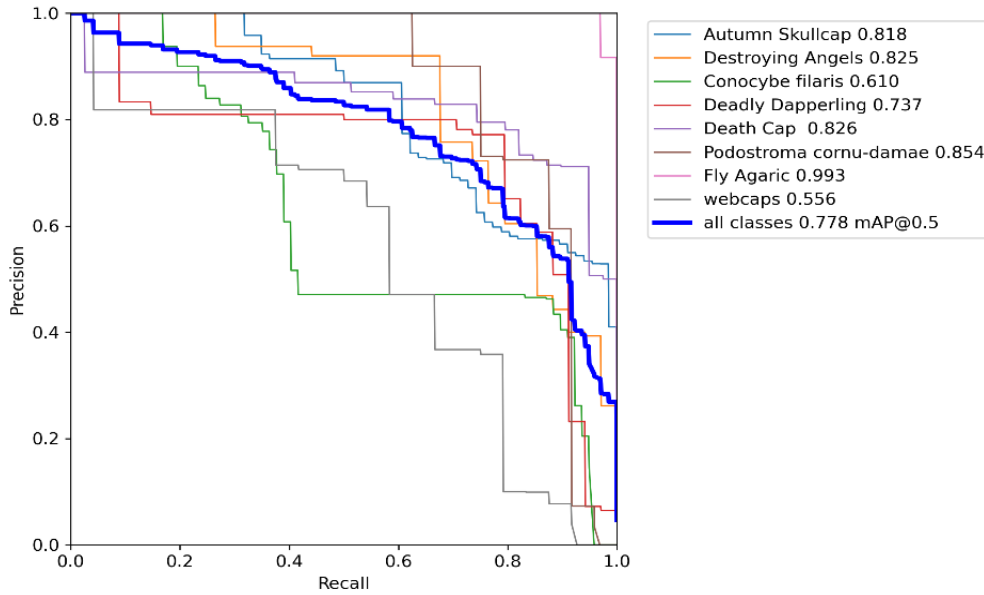


Figure 3. Precision-recall curve of the model

The precision, recall, and mAP curves of the training process are shown in figure 4. The training process is carried out in 40 epochs. Table 3 shows the Average Precision of each class after the training and validation process.

Table 3. Average Precision of each class in dataset

Mushroom Species	Autumn Skullcap	Destroying Angle	Cococybe Filaris	Deadly Dapperling	Death Cap	Podostroma Cornu-Damae	Fly Agaric	Webcaps
AP	0.818	0.825	0.610	0.737	0.826	0.854	0.993	0.556
mAP	0.778 mAP@0.5							



Figure 4. Precision, recall and mAP curve of the model



Figure 5. Images where mushroom species are correctly detected

130 images were used to test the model. Although the mushroom species in these images were mostly predicted correctly, some mushrooms were wrongly predicted or not seen. Figure 5 shows the images containing the correct mushrooms. Figure 6 gives images that are misclassified. Two mushrooms of the “Autumn skullcap” type were found as death cap. In the other image, the death cap mushroom was predicted as destroying angels.



Figure 6. Images where mushroom species are incorrectly detected

4. Discussions and Conclusions

In the literature, there are some studies made for mushroom classification. According to our knowledge, the studies are for the classification of edible and inedible mushrooms. In [10], authors worked with a ten-class dataset, and their purpose was to decompose edible mushrooms. Existing studies have used classification methods. The comparison of some studies made for mushroom classification is given in Table 4. In the study not only classifies certain types of poisonous mushrooms but also gives location information. YOLOV5 is used in real-time applications due to its speed and high accuracy rate. It is also good at finding small objects. As a future work is to apply our dataset in real-time, after enhancing it via images from internet. YOLOV5 was chosen for these reasons.

In this study where we focused on classifying poisonous mushroom species, a dataset including the most poisonous mushrooms was generated. It was prepared in YOLO format by labeling it with the labelImg tool. The study aimed to identify eight mushroom species known as poisonous species. Trained with yolov5x fine-tuning, the largest YOLOV5 model. As a result of our literature searches, no study classifies poisonous mushrooms according to their species and performs identification. Therefore, it has not had a chance to compare with other studies. But the success of working with a precision-recall curve, Average Precision, and Mean Average Precision metrics has been shown. Mean Average Precision of all classes is 0.77 and AP values of each class are 0.818, 0.825, 0.610, 0.737, 0.826, 0.854, 0.993, 0.556, respectively. The experimental results showed that with the image data used, a high success rate was achieved.

Table 4. Comparison of some studies made for mushroom classification

Ref. No/Year	Dataset/Samples	Number of Class	Method	Performance
[6]/2015	Mushroom dataset/8124	2	MLP+PCA	98.34% Acc.
[5]/2016	Collected from Internet/300	10	PCA	85%~96% Acc.
[9]/2019	Collected from Internet/380	2	KNN	87%~94% Acc.
[3]/2020	Mushroom dataset/8124	2	Multi-Layer ANN	99.25% Acc.
[4]/2020	Mushroom dataset/8124	2	Multi-Grained Cascade Forest	98% Acc.
Our/2021	Collected from Internet/644	8	Fine-tuned YOLO-V5	0.778 mAP

References

- [1] Krittanawong, C., Isath, A., Hahn, J., Wang, Z., Fogg, S. E., Bandyopadhyay, D., ..., Tang, W. W. Mushroom Consumption and Cardiovascular Health: A Systematic Review. *The American Journal of Medicine*. 2020.
- [2] Maurya, P., Singh, N. P. Mushroom Classification Using Feature-Based Machine Learning Approach. In *Proceedings of 3rd International Conference on Computer Vision and Image Processing*, 2020: (pp. 197-206). Springer, Singapore.
- [3] Sameh, A., Moghayer, M., Mohanad, G., Mohammad, A. Classification of Mushroom Using Artificial Neural Network. 2020.
- [4] Wang, Y., Du, J., Zhang, H., & Yang, X. Mushroom Toxicity Recognition Based on Multigrained Cascade Forest. *Scientific Programming*, 2020.
- [5] Subramaniam, A., Oh, B. J. Mushroom recognition using PCA algorithm. *International Journal of Software Engineering and Its Applications*. 2020; 10(1): 43-50.
- [6] Sunita, B., Bishan, D. Mushroom classification using data mining techniques. *International Journal of Pharma and Bio Sciences*. 2015; 6(1).
- [7] Ayorinde I. T., Badmos Z. O. Development of Deep Learning Model on Mushroom Dataset towards Classifying Poisonous Mushroom with Feature Selection. 3rd Biennial International Conference on Transition from Observation to Knowledge to Intelligence (TOKI), University of Lagos, Nigeria. 2019.
- [8] Ortega, J. H. J. C., Lagman, A. C., Natividad, L. R. Q., Bantug, E. T., Resurreccion, M. R., Manalo, L. O. Analysis of Performance of Classification Algorithms in Mushroom Poisonous Detection using Confusion Matrix Analysis. *International Journal*. 2020; 9(1.3).
- [9] Ottom, M. A., Alawad, N. A., & Nahar, K. M. Classification of Mushroom Fungi Using Machine Learning Techniques. *International Journal of Advanced Trends in Computer Science and Engineering*. 2019; 8(5): 2378-2385.
- [10] Lidasan, Johaira U., and Martina P. Tagacay. "Mushroom recognition using neural network." *International Journal of Computer Science Issues (IJCSI)*. 2018; 15.5 : 52-57.
- [11] Portalo-Calero, Francisco, et al. "Identification of Poisonous Mushrooms by Means of a Hand-Held Electronic Nose." *Multidisciplinary Digital Publishing Institute Proceedings*. Vol. 14. No. 1. 2019.
- [12] <https://github.com/tzatalin/labelimg>. Accessed January 2021.
- [13] Sharma, V., Mir, R. N. A comprehensive and systematic look up into deep learning based object detection techniques: A review. *Computer Science Review*. 2020; 38, 100301.
- [14] Wu, X., Sahoo, D., Hoi, S. C. Recent advances in deep learning for object detection. *Neurocomputing*. 2020; 396; 39-64.
- [15] Krizhevsky, Alex, Ilya Sutskever, Geoffrey E. Hinton. "Imagenet classification with deep convolutional neural networks." *Advances in neural information processing systems*. 2012.
- [16] Girshick, R., Donahue, J., Darrell, T., Malik, J. Rich feature hierarchies for accurate object detection and semantic segmentation. In *Proceedings of the IEEE conference on computer vision and pattern recognition*. 2014. pp. 580-587.
- [17] Cao, C., Wang, B., Zhang, W., Zeng, X., Yan, X., Feng, Z., ... , Wu, Z. An improved faster R-CNN for small object detection. *IEEE Access*. 2019. 7, 106838-106846.
- [18] He, K., Gkioxari, G., Dollár, P., Girshick, R. Mask r-cnn. In *Proceedings of the IEEE international conference on computer vision*. 2017. pp. 2961-2969.
- [19] Li, Z., Peng, C., Yu, G., Zhang, X., Deng, Y., Sun, J. Light-head r-cnn: In defense of two-stage object detector. 2017. *arXiv preprint arXiv:1711.07264*.
- [20] Cai, Z., Vasconcelos, N. Cascade r-cnn: Delving into high quality object detection. In *Proceedings of the IEEE conference on computer vision and pattern recognition*. 2018. pp. 6154-6162.
- [21] Liu, Y., Sun, P., Wergeles, N., & Shang, Y. A Survey and Performance Evaluation of Deep Learning Methods for Small Object Detection. *Expert Systems with Applications*. 2021. 114602.
- [22] Liu, W., Anguelov, D., Erhan, D., Szegedy, C., Reed, S., Fu, C. Y., Berg, A. C. Ssd: Single shot multibox detector. In *European conference on computer vision*. Springer, Cham. 2016. pp. 21-37.
- [23] Fu, C. Y., Liu, W., Ranga, A., Tyagi, A., Berg, A. C. Dssd: Deconvolutional single shot detector. 2017. *arXiv preprint arXiv:1701.06659*.
- [24] Li, Z., Zhou, F. FSSD: feature fusion single shot multibox detector. 2017. *arXiv preprint arXiv:1712.00960*.
- [25] Cui, L., Ma, R., Lv, P., Jiang, X., Gao, Z., Zhou, B., Xu, M. MDSSD: multi-scale deconvolutional single shot detector for small objects. 2018. *arXiv preprint arXiv:1805.07009*.
- [26] Shen, Z., Liu, Z., Li, J., Jiang, Y. G., Chen, Y., Xue, X. Dsod: Learning deeply supervised object detectors from scratch. In *Proceedings of the IEEE international conference on computer vision*. 2017. pp. 1919-1927.
- [27] Zhao, Q., Sheng, T., Wang, Y., Tang, Z., Chen, Y., Cai, L., Ling, H. M2det: A single-shot object detector based on multi-level feature pyramid network. In *Proceedings of the AAAI conference on artificial intelligence*. 2019. Vol. 33, No. 01; pp. 9259-9266.
- [28] Lin, T. Y., Goyal, P., Girshick, R., He, K., Dollár, P. Focal loss for dense object detection. In *Proceedings of the IEEE international conference on computer vision*. 2017. pp. 2980-2988.
- [29] Law, H., Deng, J. Cornernet: Detecting objects as paired keypoints. In *Proceedings of the European conference on computer vision (ECCV)*. 2018. pp. 734-750.

- [30] Yang, Z., Liu, S., Hu, H., Wang, L., Lin, S. Reppoints: Point set representation for object detection. In *Proceedings of the IEEE/CVF International Conference on Computer Vision*. 2019. pp. 9657-9666.
- [31] Redmon, J., Divvala, S., Girshick, R., Farhadi, A. You only look once: Unified, real-time object detection. In *Proceedings of the IEEE conference on computer vision and pattern recognition*. 2016. pp. 779-788.
- [32] Redmon, J., Farhadi, A. YOLO9000: better, faster, stronger. In *Proceedings of the IEEE conference on computer vision and pattern recognition*. 2017. pp. 7263-7271.
- [33] Redmon, J., Farhadi, A. Yolov3: An incremental improvement. 2018. *arXiv preprint arXiv:1804.02767*.
- [34] Bochkovskiy, A., Wang, C. Y., Liao, H. Y. M. Yolov4: Optimal speed and accuracy of object detection. 2020. *arXiv preprint arXiv:2004.10934*.
- [35] Huang, Z., Wang, J., Fu, X., Yu, T., Guo, Y., Wang, R. DC-SPP-YOLO: Dense connection. 2020.
- [36] Jocher, G., Nishimura, K., Mineeva, T., Vilariño, R.: YOLOv5 (2020). <https://github.com/ultralytics/yolov5>. Accessed january 2021
- [37] M. Petruzzello, <https://www.britannica.com/list/7-of-the-worlds-most-poisonous-mushrooms>. Accessed january 2021.
- [38] Rezatofighi, H., Tsoi, N., Gwak, J., Sadeghian, A., Reid, I., Savarese, S. (2019). Generalized intersection over union: A metric and a loss for bounding box regression. In *Proceedings of the IEEE/CVF Conference on Computer Vision and Pattern Recognition* (pp. 658-666).
- [39] Cengil, E., Çınar, A. Göğüs Verileri Metrikleri Üzerinden Kanser Sınıflandırılması. *Dicle Üniversitesi Mühendislik Fakültesi Mühendislik Dergisi*, 11(2), 513-519.
- [40] Padilla, R., Netto, S. L., da Silva, E. A. A survey on performance metrics for object-detection algorithms. In *2020 International Conference on Systems, Signals and Image Processing (IWSSIP)*. Niteroi, Brazil, 2020, pp. 237-24.
- [41] Henderson, P., Ferrari, V. End-to-end training of object class detectors for mean average precision. In *Asian Conference on Computer Vision*. 2016. (pp. 198-213). Springer, Cham.

Smart Arms Detection System Using YOLO Algorithm and OpenCV Libraries

Rayan KHALAF¹, Yaman AKBULUT^{2*}

^{1,2}Department of Software Engineering, Technology Faculty, Firat University, Elazig, Turkey
rayan.s.alhaddad@gmail.com, yamanakbulut@firat.edu.tr

(Geliş/Received: 04/02/2021;

Kabul/Accepted: 15/02/2021)

Abstract: The continuous development that the world is on must be pursued into human services, among these services provided by the modern world are the ability to detect faces, controlling and monitoring crowded places, the roads, auto-drive cars, and other smart systems that we can see through our daily life, these systems are known as object detection systems. This branch is getting development continuously and it gets big attention and support from international institutes, military institutions, and security companies. Object detection is a big branch and is used in many industries like medical, food production, plastic industries, controlling and monitoring roads, and more. In this paper we will explain information about object detection, its types, the YOLO algorithm, and a small idea that we made for controlling and monitoring arms showed by monitoring cameras or images that contain arms, we made it using the YOLO algorithm with the help of OpenCV and python libraries.

Keywords: YOLO, object detection, arms detection, monitoring, digital.

YOLO Algoritmasını ve Açık Kütüphanelerini Kullanan Akıllı Silah Algılama Sistemi

Öz: Dünyanın üzerinde bulunduğu sürekli gelişme, insan hizmetlerine dönüştürülmelidir, modern dünyanın sunduğu bu hizmetler arasında yüzleri algılama, kalabalık yerleri, yolları, otomatik sürüş arabaları ve diğer akıllı sistemleri kontrol etme ve izleme yeteneği vardır. günlük hayatımızda görebildiğimiz bu sistemler, nesne tespit sistemleri ile biliniyor. Bu şube sürekli gelişmekte ve uluslararası enstitülerden, askeri kurumlardan ve güvenlik şirketlerinden büyük ilgi ve destek almaktadır. Nesne algılama büyük bir daldır ve tıp, gıda üretimi, plastik endüstrisi, yolları kontrol etme ve izleme ve daha fazlası gibi birçok endüstride kullanılmaktadır. Bu çalışmada nesne algılama, türleri, YOLO algoritması ve el kollarını içeren kamera veya görüntüleri izleyerek gösterilen el kollarını kontrol etmek ve izlemek için yaptığımız küçük bir fikri açıklayacağız, YOLO algoritmasını kullanarak yaptık. opencv ve python kütüphanelerinin yardımı.

Anahtar kelimeler: YOLO, nesne algılama, silah tespiti, izleme, dijital.

1. Introduction:

The news circulating the world speaks of the constant struggle between development and ignorance, between reaction and backwardness, between light and darkness. And what the world is witnessing in terms of development in the field of science must be exploited by the leaders of the civilized world to make the world safer so that researchers and people, in general, can practice their normal lives without fear. From this standpoint, we found that devoting technology to serve humanity through smart systems that can monitor and control all vital, crowded places and state institutions is one of the responsibilities of the leaders of the civilized world. We began to search for a technology that can give a service to the community in a modern and smart way and we found it in computer vision.

Computer vision is a branch that is growing so fast and every day we find an invention or enhancement in its branches. It is a process that takes images as an array of digits, analyzes them depending on filters, and extracts their features. Then, it classifies them into a specific class or group [1]. Some problems appear in computer vision such as an image is 2D while the real world is 3D, the difference in point of view, the difference in size (near or far), the difference in color (like different clothes), the resolution, and the size of the image, the noise that appears in images because of the surrounding circumstances, etc. [1, 2].

A type of computer vision is object detection, one of the most modern and updated branches inside computer vision, also we can say is the most spread in computer vision. It differs or enhanced algorithm from classification types because in object detection we can detect more than one variable in the same image [3]. This type of computer vision has become widespread in multiple branches like medicine, industry, surveillance, and

* Corresponding author: yamanakbulut@firat.edu.tr. ORCID Number of authors: ¹ 0000-0002-9991-8844, ² 0000-0002-4760-4843

more others. The basic idea is to detect more objects in one image or frame especially in real-time, and our research will be in this branch (object detection in real-time), exactly in the YOLO algorithm.

Terrorist incidents are among the most common incidents that threaten the security of society. We found the idea of using technology as a weapon in the face of such incidents is a good idea and has great goals, one of which is to reduce the risk of a terrorist attack for any institution and also to support expertise and competencies to work intensively for more intelligent inventions. From this point, the idea of making this system we will talk about is coming. The system is an arms detector in a smart way built on a YOLO algorithm with OpenCV and python libraries

2. Deep Learning

Deep learning is a technology to analyze and extract features from data like images, frames, and sounds, this branch developed in fast steps to be more spread all around the world and it is divided into branches exploited in most of our daily life [15]. The name (deep) came from the structure of the algorithm layers, it is referred to the hidden layers of convolution used inside its structure [17]. One of the biggest deep learning branches is object detection, in the object detection branch, we are talking about voices, images, and frames and how this technology deals with them. The most popular technology used in this branch is CNN because of its characteristics [15]. The increase came to use in more branches like medicine, industry, and other branches after the growth of datasets, CPUs, and intelligent machines in general, this growth led to the use of deep learning to be responsible for making rapid and correct decisions depending on the dataset and an algorithm [16, 17].

2.1. Convolutional neural network

CNN One of the most advanced areas in machine learning and image processing, the name is taken from the analogy of human nerves and how the human brain works from convolutional neural networks [4]. Its history dates back to the 1990s when LeCun et al. used a gradient-based machine learning algorithm on CNN and he got successful outputs of classifying digits wrote by hands [5]. As the work of this technique is very like the work of the nerves of the human brain of complexity, accuracy, and the speed of processing and, above the human brain in some operations, new techniques in this field have proven superior to the human brain through the speed and accuracy of the human brain in parts of a second [4]. As it is a branch of NNs it gave good features to this branch, because it fixes many problems that appeared in NNs like the big number of parameters, the location of the specific object, besides the speed is an improvement [18]. This technique proved its success through more global applications like GoogLeNet, DeepFace, Go game, and others [4]. CNN's processing consists of convolution, pooling, and fully connected layers that are specialized to deal with different input dimensions with different layers as images, video frames, and voices [6, 19]. CNN's work on extracting Images features on many levels to give the processor enough information to detect the object in a fast and accurate way depending on its tools like loss function, convolution, and pooling [19]. There is a function Deep Convolutional Neural Networks (DCNN) uses to process faster than the traditional CNN's multiple times that is So-Called Rectified Linear Unit (SCRLU) [6]. This success goes to the invention of high-speed CPUs, GPUs, big datasets, and improved algorithms as we mentioned latterly, we will explain some of the big datasets and improved algorithms used lastly.

2.2. Object detection

This branch was invented in the 1990s, but its applications spread after that maybe in the 2000s. That is because in the 1990s we did not have big data sets, good algorithms; good funds specified to do AI studies like provided today from companies like Google, Amazon, Facebook, etc., and good CPUs and GPUs [7]. Generally, object detection is divided into two branches, one is classifying the image or frame in two stages like R-CNN, another one is taking the image in one step for classifying like YOLO [20]. We discovered how datasets are made and what are the contents of the dataset are; let's take an overview of the most popular algorithms used in these databases to achieve object detection and classification. The most popular object detection algorithms are:

- R-CNN
- Fast R-CNN

- Faster R-CNN
- Mask R-CNN
- Single Shot Detection
- You Only Look Once

2.3. You Only Look Once (YOLO)

Born of a new object detection approach after multiple improvements of object detection that uses bounding boxes of object detection instead of classifying whole image pixels (that have been used in object detection algorithms before), also is a real-time object detection because of the improvement in speed of recognition, the previous approaches did not provide it, they were slower than YOLO so it cannot detect real-time videos while YOLO did that, in YOLO algorithm takes a single look to the image and extract the objects that made YOLO much faster but this effects the accuracy too, the table below defines object detection approaches according to its born with its properties [8].

Table 1.1 Comparing YOLO with other object detection approaches [8].

Detection frameworks	Train	mAP	fps
Faster R-CNN	VOC 2007+2012	70.0	0.5
Faster R-CNN VGG16	VOC 2007+2012	73.2	7
Faster R-CNN Resnet	VOC 2007+2012	76.4	5
YOLO	VOC 2007+2012	63.4	45
YOLOv2 288 × 288	VOC 2007+2012	69.0	91
YOLOv2 352 × 352	VOC 2007+2012	73.7	81
YOLOv2 416 × 416	VOC 2007+2012	76.8	67
YOLOv2 480 × 480	VOC 2007+2012	77.8	59
YOLOv2 544 × 544	VOC 2007+2012	78.6	40

YOLO idea is cleverer than previous approaches like Deformable Part-based Method (DPM) because it takes region proposals inside an image with multiple class probabilities and processes it simultaneously to get faster (this is the idea from the name YOU ONLY LOOK ONCE). It takes several steps to do the best [8].

- Dividing an image into a grid of 13×13 cells
- Use bounded boxes with probable classes to predict objects
- Use a single CNN to optimize the RP's
- Loss function
- Non-maximal suppression and fast processing get to 45 fps.

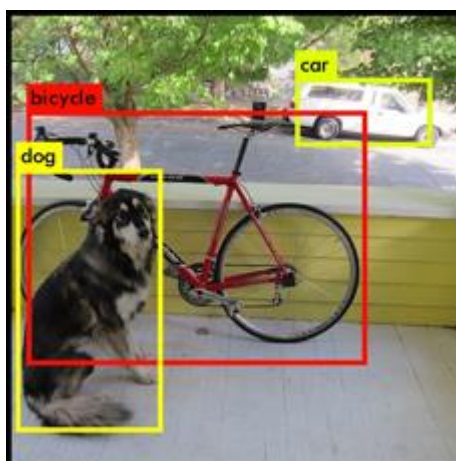


Figure 1. Regions remained that contained objects [8].

2.4. YOLO's vision to the image

YOLO's first step is dividing an image into a grid with 13×13 cells; cells that are the centers of the objects are responsible for detecting that object. This cell will predict the bounding of five cells [8].

So we have $13 \times 13 = 169$ cells, and every cell predicting its five bounding cells that lead to having 845 bounding cells. That is a big number of cells that need big time to process, but in YOLO it takes just that boxes having 30% or more of similarity (programmer can change this value depending on the accuracy needed) [8].

2.5. Loss Function

Loss function works on taking the bounding boxes that most, contain an object. As we can see in Figure 1 there are only three boxes that contain an object while the algorithm produces a big number of possibilities, but only detect three boxes that pass the percentage. This predicted boundary gives that what size and form of an object are beside of giving an exact bounded box (object size), in general, it defines objects through a formula that [14]:

$$pr(object) * iou_{pred}^{truth} \quad (1)$$

Where Pr denotes the proposal region and IOU denotes the intersection of a union. This formula gives the decision if there is an object or not, if there is no predicted object confidence score will be zero. If there is, it should take the IOU between our predicted box with a ground truth box [8, 13, and 14].

2.6. YOLO V3 the latest version

At the end of our research, we will talk about the last version of YOLO, which is YOLOV3 that is much faster and more accurate than the other versions. In this version, we will find small changes but it makes the detection operation more accurate [9]. Firstly the bounding boxes are the same as versions before, using anchors for making bounding boxes, the decision of having an object inside the RP or not is taken depending on assigning bounding box for each object, if not assigned it will be discarded [9]. In the prediction of class, they used independent logistic classification instead of softmax prediction that makes it faster than previous versions [9]. In the state of prediction they used three different scales of boxes, they tried it on the COCO dataset with the Darknet platform [9].

3. ARMS DETECTION EXPERIMENT

In this section, we will explain how YOLO is working with custom object detection, and we took a gun named Automatic refill Kalashnikov Modernized (AKM-47) as an example for gun detection.

Windows is a good platform to apply our idea of guns detection, but it needs some tools to be adaptive with the YOLO algorithm, as:

- Git tool: which is an open-source tool designed to help and handle small and big projects [10].
- Cygwin: this is a tool providing an environment like UNIX but on windows, also named GNU. This tool provides some functions that we need to build Darknet environment like (make, ssh, ssl, gcc-core, vim editor) [11].
- Installing Darknet: this is an open-source framework that supports neural networks and YOLO as a part of NN's, written in CUDA and C. supporting CPU and GPU too [12].

Now the environment is ready to install the YOLO algorithm.

3.1. Installing YOLO algorithm

First, we must download YOLO pre-trained weights that weights are provided by YOLO. If the installation is completed successfully we should test it before going to build our custom detection system. The most popular picture is below to know the system is installed successfully:

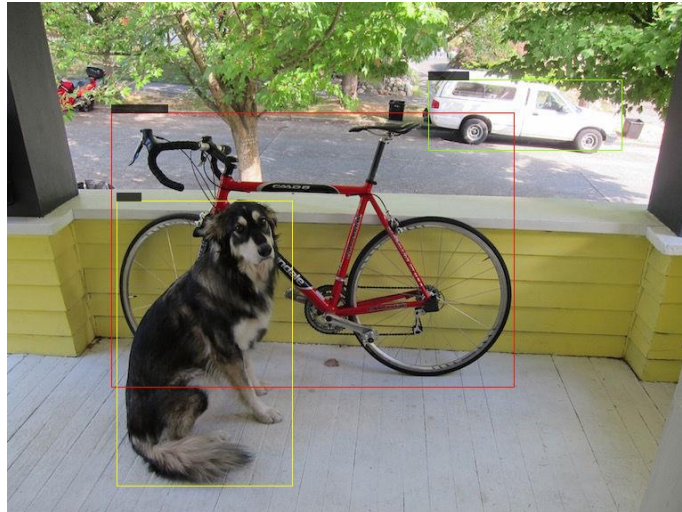


Figure 1. YOLO detection

YOLO is working now, the next step we will build our specific detection system (AKM-47).

3.2. Collecting images for AKM-47

The most important step when we decide to build a detection system on a specific object is collecting enough images about that object because it is the basic stone of building that system. In our experiment, we searched for images of AKM-47 on Google and we collected 100 different images, but this number of pictures is not enough for our system because of the bad resolution and the similarity. We decided to build our dataset by hand; we took 825 images of the object and prepared it to be ready to be a dataset. As we can see below:



Figure 2. AKM-47 dataset

We depended on the factors of resolution and the variety of angles in collecting and taking images, to make our dataset include most of the object angles and position sides. After collecting we need to resize all the images in the same size to make it through the processing. All images are resized to 180×180 pixels, the size we have chosen is to make the processor faster through the process of the weight. For resizing images to the specific size we used paint application to prepare it. All images are then collected in a folder named images to make it ready for the next step.

3.3. Labelling images

After collecting a dataset for AKM-47 we labeled all the images, labelling means making a txt file for every image, containing the height, width, X, Y for the object. We used the labeling tool as below:

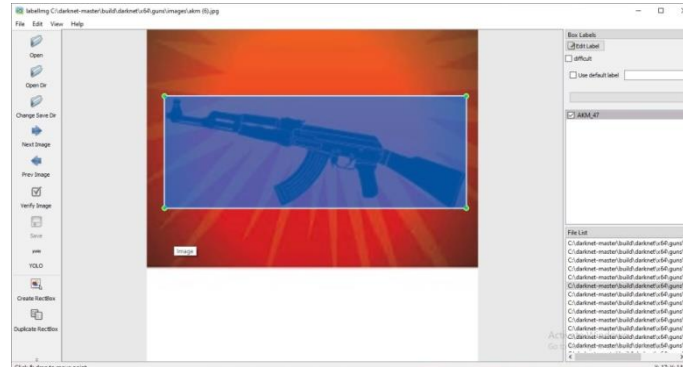


Figure 3. Labeling tool

This tool makes a text file for each image with the same name. It is a python function.

3.4. Making YOLO custom detection files

After collecting and labeling all images for the object, we must provide files that YOLO needs to process weights like:

- Configuration file: This file contains the steps of processing weights like the number of iterations, steps, number of classes, number of filters, and much other information.
- Names file: this file contains names of objects we want to detect, for example in our working it contains AKM-47.
- Data file: contain the number of classes we want to detect, the full path of training and test files, and where we must save our new weights.
- Training file: contains the full path of 70% of the dataset, these images will use for weight processing.
- Test file: contain the full path of remained images, also use it for weight processing.
- Pre-trained weights: weights YOLO provide it to users, for weights processing, its name is darknet53.conv.74

3.5. Weights processing

Now we prepared everything for weight processing, the last step is the process and it will be like below:

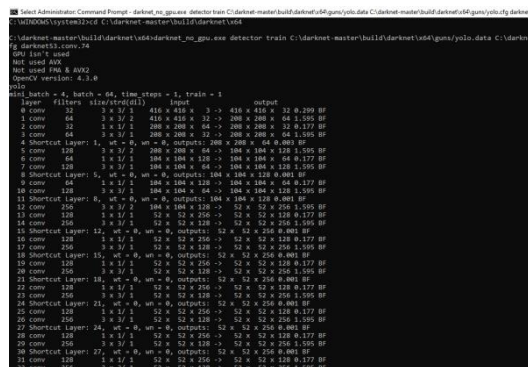


Figure 4. Weights processing

This step will take a long time depending on the CPU it works on, and if GPU is available or not. It takes 14 days if we are using CPU only, as we did in this project. The most important step is loss function and controlling how it works because detection depends on it. As below:

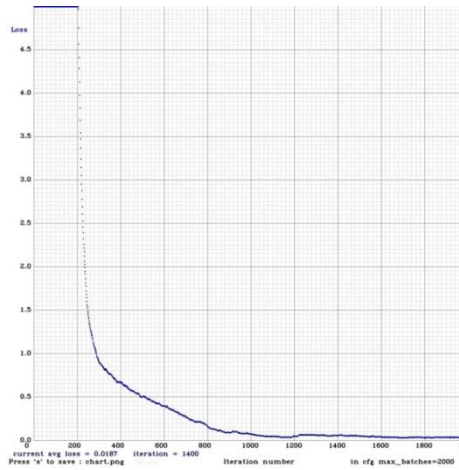


Figure 5. Loss function

The final step is testing our work using our weights instead of YOLO weights and test if it is detecting or not. As below:

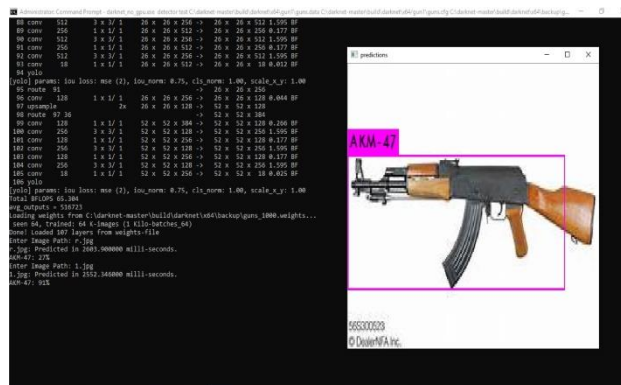


Figure 6. Testing the weights

As we note above the system detects AKM-47. Accuracy and speed depend on dataset and CPU, GPU, in our experiment the accuracy is reaching 90% in image detection within 2.5 seconds, and in the video, the accuracy is between 80% and 95% with a rate of 0.3 frames per second (fps).

4. Conclusion

Object detection with neural networks works very well inside controlling and surveillance systems, everything we can make with this technology means we can build monitoring systems for controlling vehicles, civil cars, persons, guns, etc. especially in military institutions because of its sensitivity. Our idea is simple but at the same time, it is a good idea if it is taken by institutions, government departments, or security companies, with a group of programmers, good computers, and technician persons.

There is another good idea for building a smart security system if it gets good care and support, the idea is connecting an X-ray to scan places and transfer the video to a guns detection system, in this manner the security will be 100% and the system will be smart enough to detect guns at all places, giving a piece of good information to the security managers.

There are new ideas always growing up, we hope in future we will perform smarter systems with better detection and more intelligence. We hope in future we can make an advanced system, contains more guns and

objects with good computers and bigger dataset, offer it to all military and public areas to control it from any terrorist attacks. Finally, we thank this modern technology for helping humans to be safer.

References

- [1] Kaehler, A., & Bradski, G. (2016). *Learning OpenCV 3: computer vision in C++ with the OpenCV library*. " O'Reilly Media, Inc."
- [2] Szeliski, R. (2010). *Computer vision: algorithms and applications*. Springer Science & Business Media.
- [3] Zafar, I., Tzanidou, G., Burton, R., Patel, N., & Araujo, L. (2018). *Hands-on convolutional neural networks with TensorFlow: Solve computer vision problems with modeling in TensorFlow and Python*. Packt Publishing Ltd.
- [4] Stuart, J., & Norvig, P. (2010). *Artificial Intelligence: a Modern Approach* Prentice-Hall. In *A Simon & Schuster Company Englewood Cliffs*.
- [5] Alom, M. Z., Taha, T. M., Yakopcic, C., Westberg, S., Sidike, P., Nasrin, M. S., ... & Asari, V. K. (2018). The history began from alexnet: A comprehensive survey on deep learning approaches. *arXiv preprint arXiv:1803.01164*.
- [6] Runia, T. F. H. (2015). *High-Speed Object Detection: Design, Study and Implementation of a Detection Framework using Channel Features and Boosting*, Master Thesis.
- [7] Ketkar, N., & Santana, E. (2017). *Deep learning with python* (Vol. 1). Berkeley, CA: Apress
- [8] Redmon, J., Divvala, S., Girshick, R., & Farhadi, A. (2016). You only look once: Unified, real-time object detection. In *Proceedings of the IEEE conference on computer vision and pattern recognition* (pp. 779-788).
- [9] Redmon, J., & Farhadi, A. (2018). Yolov3: An incremental improvement. *arXiv preprint arXiv:1804.02767*.
- [10] <https://git-scm.com>, access: 2 February 2020.
- [11] <https://www.cygwin.com>, access: 2 February 2020.
- [12] Redmon, J.. *Darknet: Open source neural networks in c*. 2013.
- [13] Atienza, R. (2020). *Advanced Deep Learning with TensorFlow 2 and Keras: Apply DL, GANs, VAEs, deep RL, unsupervised learning, object detection and segmentation, and more*. Packt Publishing Ltd.
- [14] <https://machinethink.net/blog/object-detection-with-yolo>, access: 18 April 2020.
- [15] Z. Zhang, P. Cui and W. Zhu, "Deep Learning on Graphs: A Survey," in *IEEE Transactions on Knowledge and Data Engineering*, doi: 10.1109/TKDE.2020.2981333.
- [16] Esteva, A., Robicquet, A., Ramsundar, B., Kuleshov, V., DePristo, M., Chou, K., ... & Dean, J. (2019). A guide to deep learning in healthcare. *Nature medicine*, 25(1), 24-29.
- [17] X. X. Zhu *et al.*, "Deep Learning in Remote Sensing: A Comprehensive Review and List of Resources," in *IEEE Geoscience and Remote Sensing Magazine*, vol. 5, no. 4, pp. 8-36, Dec. 2017, doi: 10.1109/MGRS.2017.2762307.
- [18] Albawi, S., Mohammed, T. A., & Al-Zawi, S. (2017, August). Understanding of a convolutional neural network. In *2017 International Conference on Engineering and Technology (ICET)* (pp. 1-6). Ieee.
- [19] T. Guo, J. Dong, H. Li and Y. Gao, "Simple convolutional neural network on image classification," 2017 IEEE 2nd International Conference on Big Data Analysis (ICBDA), Beijing, 2017, pp. 721-724, doi: 10.1109/ICBDA.2017.8078730.
- [20] Z. Zhao, P. Zheng, S. Xu and X. Wu, "Object Detection With Deep Learning: A Review," in *IEEE Transactions on Neural Networks and Learning Systems*, vol. 30, no. 11, pp. 3212-3232, Nov. 2019, doi: 10.1109/TNNLS.2018.2876865.

Classification of Brain Tumor Images using Deep Learning Methods

Harun BINGOL^{1*}, Bilal ALATAS²

^{1,2}Department of Software Engineering, Firat University, Elazig, Turkey

¹harun_bingol@hotmail.com, ²balatas@firat.edu.tr

(Geliş/Received: 04/02/2021;

Kabul/Accepted: 11/02/2021)

Abstract: Big data refer to all of the information and documents in the form of videos, photographs, text, created by gathering from different sources about a subject. Deep learning architectures are often used to reveal hidden information in the big data environment. Brain tumor is a fatal disease that negatively affects human life. Early diagnosis of the disease greatly increases the patient's chance of survival. For this reason, this study was conducted so that doctors could diagnose patients early. In this paper, deep learning architectures Alexnet, Googlenet, and Resnet50 architectures were used to detect brain tumor images. The highest accuracy rate was achieved in the Resnet50 architecture. The accuracy value of 85.71 percent obtained as a result of the experiments will be improved in our future studies. We will try to develop a new method based on convolutional neural network in the near future. With this model, we will try to achieve higher accuracy than any known deep learning method.

Key words: Brain tumor, deep learning, Alexnet, Resnet50, Googlenet.

Derin Öğrenme Yöntemleri Kullanılarak Beyin Tümörü Görüntülerinin Sınıflandırılması

Öz: Büyük veri bir konu hakkında farklı kaynaklardan toplanarak oluşturulan video, fotoğraf, metin formatındaki bilgi ve belgelerin tümünü ifade etmektedir. Büyük veri ortamında gizli bilgiyi ortaya çıkarmak için genellikle derin öğrenme mimarileri kullanılmaktadır. Beyin tümörü insan hayatını olumsuz etkileyen, ölümcül bir hastalıktır. Hastalığın erken teşhisi, hastanın yaşama şansını büyük oranda arttırmaktadır. Bu nedenle doktorların hasta olan kişileri erken teşhis edebilmesi için bu çalışma gerçekleştirilmiştir. Bu çalışmada beyin tümörü görüntülerini tespit etmek için derin öğrenme mimarilerinden olan Alexnet, Googlenet ve Resnet50 mimarileri kullanılmıştır. En yüksek doğruluk oranı Resnet50 mimarisinde elde edilmiştir. Deneysel sonucu elde edilen yüzde 85.71'lik doğruluk değeri, gelecek çalışmalarımızda iyileştirilecektir. Yakın zamanda evrimsel sinir ağı tabanlı yeni bir metot geliştirmeye çalışacağız. Bu model ile bilinen tüm derin öğrenme tabanlı modellerden daha yüksek doğruluk elde etmeyi deneyeceğiz.

Anahtar kelimeler: Beyin tümörü, derin öğrenme, Alexnet, Resnet50, Googlenet.

1. Introduction

Big data generally have a complex structure. Its complexity is due to the enormous amount of data they contain. [1]. Today, people generate huge amounts of data. Taking pictures of everything or videotaping everything is among the habits of people these days. The massive data produced by humans reach astronomical numbers and increase steadily. These data are not only produced by people using social media, but every professional person produces data about their expertise. Although medical science is very advanced today, it is still a problem that doctors cannot diagnose some diseases early. Doctors use brain tomography images and magnetic resonance images (MRI) to diagnose a brain tumor. These images from many patients are collected. Developing a system to diagnose the disease at an early stage is vital for patients. Brain tumor is a very dangerous, even fatal form of cancer. There are two known types of the disease, these are LGG (Low Grade Glioma) and HGG (High Grade Glioma). HGG patients usually die within 14 months of diagnosis. Treatment methods of the disease such as Radiotherapy and Chemotherapy are available [2]. Generally, this disease is tried to be treated with surgical intervention. The reason for this is that the tumor puts pressure on the brain.

Since brain tumors are tumors located in the skull, they can show distinct symptoms depending on the pressure increase. Severe headache, nausea and vomiting are among the most important symptoms. The disease can sometimes cause circulatory system disorders in patients and even paralyze these patients. Furthermore, different symptoms occur depending on the affected area of the brain. These are weakness, numbness, gait disturbance, vision loss, hearing loss, memory impairment, and difficulty speaking. It is not known exactly what causes brain tumors. However, it is known for certain that brain tumors can be seen in all age groups. As the world's population ages, more and more people will get this disease [3]. Since the disease is very dangerous, brain tumor diagnosis studies are a very active field of study [4]. In this study, a method was developed to help doctors diagnose the disease using a data set containing MRI images that are publicly available [5]. Also, with this study, it is aimed to

help early diagnosis of brain tumor disease in people living in rural areas where there are no specialist doctors. Another benefit of this study is to ease the workload of doctors. Again, with this study, it is aimed to prevent the doctors who are exhausted under excessive workload from making wrong diagnoses.

There are some studies in the literature for the detection of brain tumor. Dong et al. proposed a reliable segmentation method for automatic segmentation of brain tumor. They used the BRATS2015 data set in their experiments. They stated that the method they proposed gave promising results [6].

Amin et al. proposed an automatic system that detects whether the brain has a tumor or not from MRI images. Harvard, Rider, and Local datasets were used during the experiments and the highest accuracy rate obtained was 97.1 percent [7].

Wu et al. proposed a color-based segmentation to detect brain tumor. This method uses the k-means clustering method. They stated that the method could successfully achieve segmentation for MRI brain tumor images to help pathologists distinguish exactly lesion size and region [8].

Chandra et al. proposed a model for detection of brain tumor. This model was based on genetic algorithm. Tumor pixels on MRI images are detected with the help of a genetic algorithm [9].

The overall article organization is as follows: Section 2 defines materials and methods. Experimental results are demonstrated in Section 3. Conclusion of this paper is illustrated in Section 4. Again, in this section, information is given about the future studies.

2. Materials and Methods

The structure of the brain, the region where the tumor is located, the type of the tumor, and how much the brain and nerves are damaged are very important data for treatment. Revealing the information hidden in the MRI images is vital for early detection of the tumor.

2.1. Data Set

The data set used during the experiments was obtained from Kaggle [5]. This data set consists of two classes. There is no tumor in first-class data. The data in the second class are images of the patient with tumor. Figure 1 shows MRI images of a healthy individual on the left. Again, Figure 1 shows MRI images of a person with a brain tumor on the right.

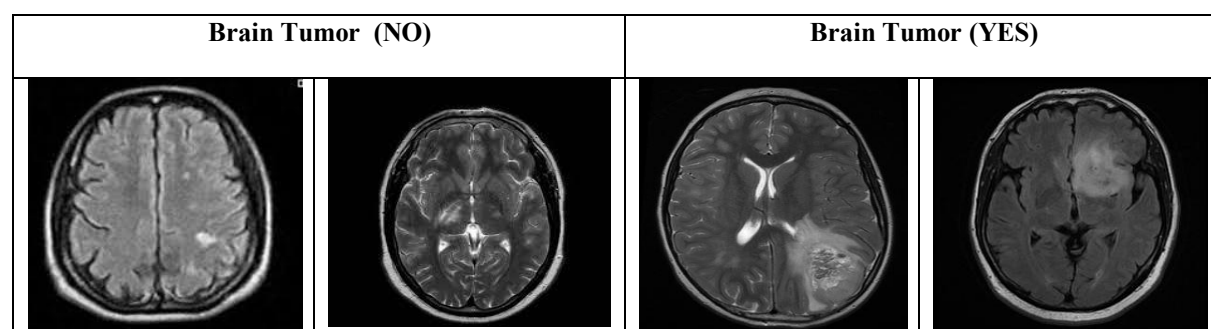


Figure 1. Brain MRI images.

2.2. Deep Learning Architectures

Deep learning is based on the concept of artificial neural networks and computational systems that mimic the functions of the human brain. Deep learning is based machine learning methods. Deep learning uses many layers for feature extraction and conversion. Each layer takes the output of the previous layer as input [10]. There are many deep learning architectures.

2.2.1. Alexnet

Alexnet is a convolutional neural network (CNN) architecture proposed by Alex Krizhevsky [11]. Basically it is similar to the LeNet model. The main reason for this similarity is that there are convolution and pooling layers

that follow each other. Approximately 60 million parameters are calculated in this architecture. Alexnet architecture is shown in Figure 2.

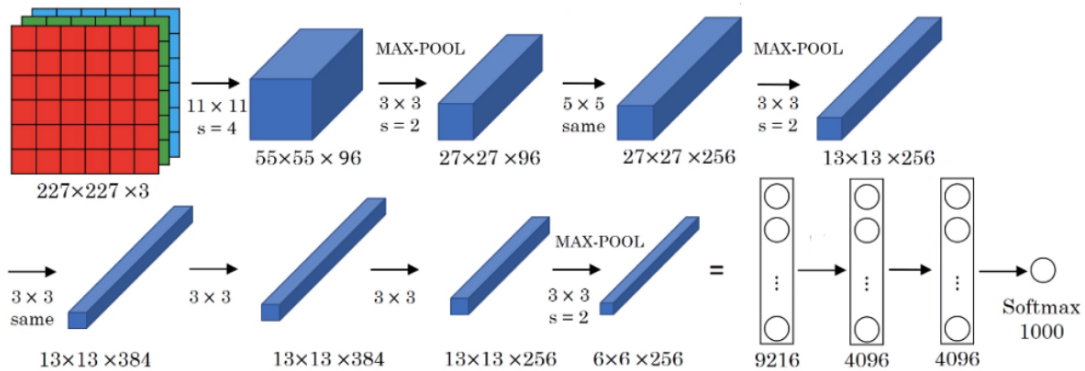


Figure 2. Alexnet architecture.

2.2.2. Resnet50

Residual network (ResNet) architecture was proposed by He Kaiming in 2015. ResNet consists of adding residual values and residual blocks to the architectural model. ResNet architecture kept the performance of the model while increasing depth. In addition, the number of parameters, which is an important factor in computational complexity, was reduced in this model. [12]. ResNet50 architecture is shown in Figure 3.

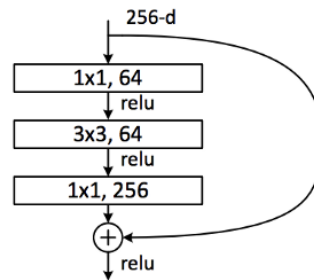


Figure 3. ResNet50 architecture.

2.2.3. GoogleNet

GoogleNet architecture was proposed by Christian Szegedy in 2015. GoogleNet is a deep learning architecture with hyperparameters optimized [13]. This model consists of 22 layers. Approximately 5 million parameters are calculated in this architecture. GoogleNet architecture is shown in Figure 4.

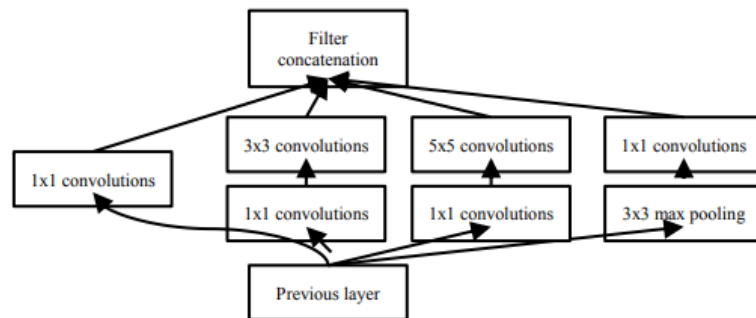


Figure 4. GoogleNet architecture.

3. Experimental Results

Deep learning architectures were used for the classification of brain tumor images. There are certain criteria that express the performance of the models in deep learning [14, 15]. All these performance metrics were calculated using Confusion Matrix [16]. A simple example of a Confusion matrix is given in Table 1. PC used in the present work has Core i7-10510U CPU, 1.80 GHz processor, 8 GB RAM, and 2 TB HDD.

Table 1. Confusion matrix

	Prediction No	Prediction Yes
Actual No	TN	FP
Actual Yes	FN	TP

The performance metrics of deep learning networks are given as Accuracy in Equation 1, Sensitivity in Equation 2, Specificity in Equation 3, Precision in Equation 4, Recall in Equation 5, and F-measure in Equation 6.

$$Accuracy = \frac{TP+TN}{TP+TN+FP+FN} \tag{1}$$

$$Sensitivity = \frac{TP}{TP+FN} \tag{2}$$

$$Specificity = \frac{TN}{TN+FP} \tag{3}$$

$$Precision = \frac{TP}{TP+FP} \tag{4}$$

$$Negative\ Predictive\ Value(NPV) = TN / (TN + FN) \tag{5}$$

$$F1 - score = \frac{2 \times Precision \times Recall}{Precision + Recall} \tag{6}$$

Accuracy and Loss plots obtained with AlexNet architecture are demonstrated in Figure 5. The confusion matrix and performance parameters of the AlexNet architecture are shown in Table 2 and Table 3, respectively.

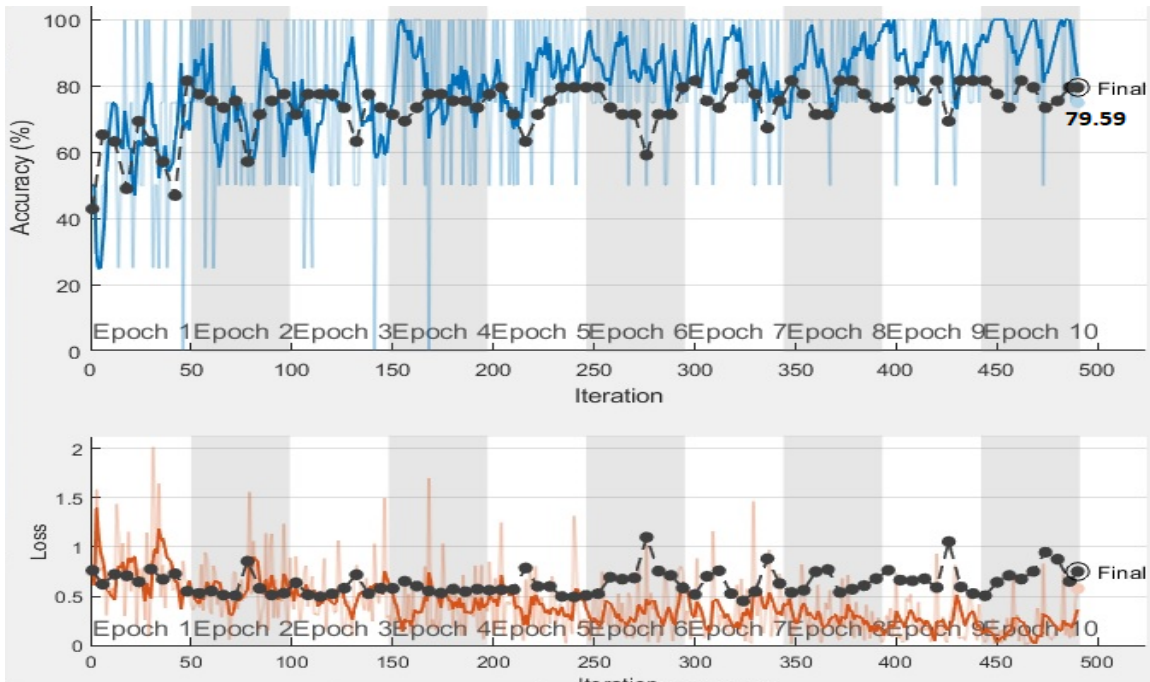


Figure 5. The accuracy and loss curve of AlexNet.

Table 2. Confusion matrix of AlexNet

	No	Yes
No	14	4
Yes	6	25

Table 3. Performance parameters of the AlexNet architecture

Accuracy	Sensitivity	Specificity	Precision	NPV	F1-Score
0.7959	0.70	0.8621	0.7778	0.8065	0.7368

Alexnet architecture has been tested with test data containing 49 images. 39 of these data were classified correctly. The remaining test data were classified incorrectly.

Accuracy and Loss plots obtained with ResNet architecture are demonstrated in Figure 6. The confusion matrix and performance parameters of the ResNet architecture are shown in Table 4 and Table 5, respectively.

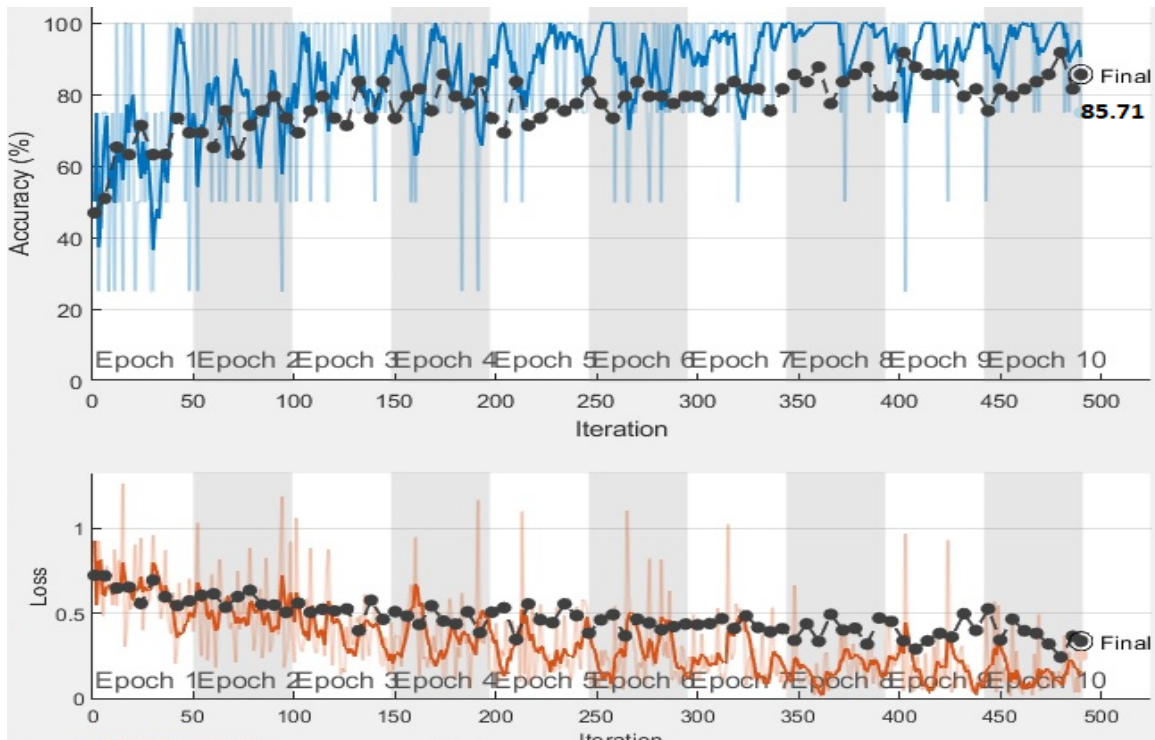


Figure 6. The accuracy and loss curve of ResNet.

Table 4. Confusion matrix of ResNet

	No	Yes
No	14	4
Yes	3	28

Table 5. Performance parameters of the ResNet architecture

Accuracy	Sensitivity	Specificity	Precision	NPV	F1-Score
0.8571	0.8235	0.8750	0.7778	0.9032	0.80

ResNet50 architecture has been tested with test data containing 49 images. 42 of these data were classified correctly. The remaining test data were classified incorrectly.

Accuracy and Loss plots obtained with GoogleNet architecture are demonstrated in Figure 7. The confusion matrix and performance parameters of the GoogleNet architecture are shown in Table 6 and Table 7, respectively

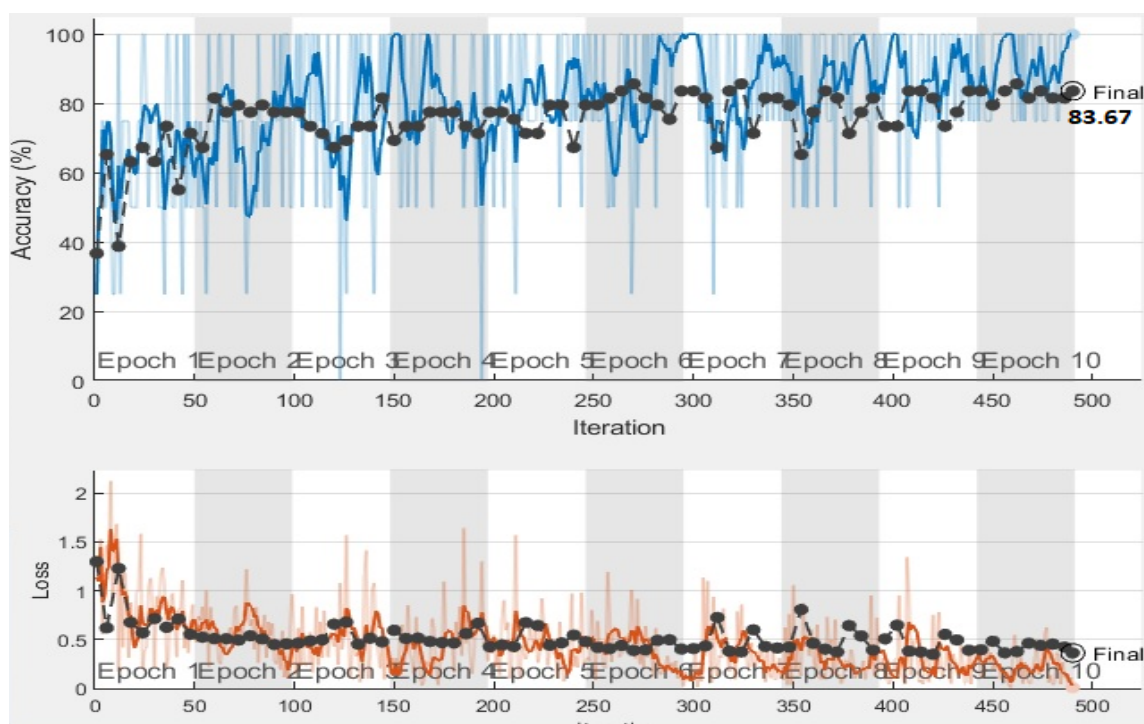


Figure 7. The accuracy and loss curve of GoogleNet.

Table 6. Confusion matrix of GoogleNet

	No	Yes
No	15	3
Yes	5	26

Table 7. Performance parameters of the GoogleNet architecture

Accuracy	Sensitivity	Specificity	Precision	NPV	F1-Score
0.8367	0.7500	0.8966	0.8333	0.8387	0.7895

GoogleNet architecture has been tested with test data containing 49 images. 41 of these data were classified correctly. The remaining test data were classified incorrectly.

4. Conclusions

In this paper, it was aimed to develop a method to diagnose a disease that changes human life completely negatively. The sooner the disease is diagnosed, the sooner the treatment process begins. In this study, deep learning methods were used to detect brain tumor from MRI images. The purpose of this classification process is to assist the doctor. Among the deep learning architectures, Alexnet, Resnet50, and Googlenet architectures were used during the experiments. The Resnet50 architecture achieved the highest accuracy rate during the experiments. The accuracy rate of the Resnet50 architecture is 85.71 percent. Googlenet architecture has the second highest accuracy rate after Resnet50 architecture. The architecture with the lowest accuracy is Alexnet. The scientific world continues to work on both diagnosing and treating brain tumors. In the future, architectures that will give higher accuracy can be developed for brain tumor diagnosis. We will try to develop a new method based on convolutional neural network in the near future. With this model, we will try to achieve higher accuracy than any known deep learning method.

References

- [1] Wu, X., Zhu, X., Wu, G. Q., Ding, W. (2013). Data mining with big data. IEEE transactions on knowledge and data engineering, 26(1), 97-107.

- [2] Amin, J., Sharif, M., Yasmin, M., Fernandes, S. L. (2018). Big data analysis for brain tumor detection: Deep convolutional neural networks. *Future Generation Computer Systems*, 87, 290-297.
- [3] URL-1, <https://www.acibadem.com.tr/ilgi-alani/beyin-tumoreri/>, Last Accessed Date: 27.01.2021
- [4] Çinar, A., Yildirim, M. (2020). Detection of tumors on brain MRI images using the hybrid convolutional neural network architecture. *Medical hypotheses*, 139, 109684.
- [5] URL-1, <https://www.kaggle.com/navoneel/brain-mri-images-for-brain-tumor-detection>, Last Accessed Date: 27.01.2021
- [6] Dong, H., Yang, G., Liu, F., Mo, Y., Guo, Y. (2017). Automatic brain tumor detection and segmentation using u-net based fully convolutional networks. In *annual conference on medical image understanding and analysis* (pp. 506-517). Springer, Cham.
- [7] Amin, J., Sharif, M., Yasmin, M., Fernandes, S. L. (2017). A distinctive approach in brain tumor detection and classification using MRI. *Pattern Recognition Letters*.
- [8] Wu, M. N., Lin, C. C., Chang, C. C. (2007). Brain tumor detection using color-based k-means clustering segmentation. In *Third International Conference on Intelligent Information Hiding and Multimedia Signal Processing (IIH-MSP 2007)* (Vol. 2, pp. 245-250). IEEE.
- [9] Chandra, G. R., Rao, K. R. H. (2016). Tumor detection in brain using genetic algorithm. *Procedia Computer Science*, 79, 449-457.
- [10] Şeker, A., Diri, B., Balık, H. H. (2017). Derin öğrenme yöntemleri ve uygulamaları hakkında bir inceleme. *Gazi Mühendislik Bilimleri Dergisi (GMBD)*, 3(3), 47-64.
- [11] Krizhevsky, A., Sutskever, I., Hinton, G. E. (2012). Imagenet classification with deep convolutional neural networks. *Advances in neural information processing systems*, 25, 1097-1105.
- [12] He, K., Zhang, X., Ren, S., Sun, J. (2016). Deep residual learning for image recognition. In *Proceedings of the IEEE conference on computer vision and pattern recognition* (pp. 770-778).
- [13] Szegedy, C., Liu, W., Jia, Y., Sermanet, P., Reed, S., Anguelov, D., Rabinovich, A. (2015). Going deeper with convolutions. In *Proceedings of the IEEE conference on computer vision and pattern recognition* (pp. 1-9).
- [14] Yildirim, M., Cinar, A. (2020). A deep learning based hybrid approach for COVID-19 disease detections. *Traitement du Signal*, 37(3), 461-468.
- [15] Ozturk, T., Talo, M., Yildirim, E. A., Baloglu, U. B., Yildirim, O., Acharya, U. R. (2020). Automated detection of COVID-19 cases using deep neural networks with X-ray images. *Computers in biology and medicine*, 121, 103792.
- [16] Townsend, J. T. (1971). Theoretical analysis of an alphabetic confusion matrix. *Perception & Psychophysics*, 9(1), 40-50.

Performance of Chaotic Mapping Multi-Objective Optimization Algorithms

Eyup EROZ^{1*}, Erkan TANYILDIZI²

¹ Software Engineering, Technology Faculty, Firat University, Elazig, Turkey

² Software Engineering, Technology Faculty, Firat University, Elazig, Turkey

*¹ eeroz@firat.edu.tr, ² etanyildizi@firat.edu.tr

(Geliş/Received: 07/02/2021;

Kabul/Accepted: 19/02/2021)

Abstract: Multi-objective optimization is defined as the process of producing suitable solutions to problems with multiple objectives. The randomly generated string of numbers is of great importance in achieving solutions close to the global optimum in intuitive multi-objective optimization. Collecting the randomly generated string of numbers in a certain area increases the risk of moving away from the global optimum. Chaotic maps are used to reduce this risk as it is not periodic as the variety of numbers produced in chaotic maps is high. For this reason, chaotic maps are used in the random number generation part of optimization algorithms. Chaos-based algorithms have become an important field of study because they are flexible and can escape from local minimums. In this study, the effects of chaotic maps on the new and successful Multi-objective Gold Sine Algorithm (MOGoldSA) were compared with the Multi-Objective Ant Lion Optimization (MOALO) algorithm.

Key words: Chaotic Map, Multi-Objective Optimization, Chaos-Based Algorithms, Metaheuristic Methods

Kaotik Haritalı Çok Amaçlı Optimizasyon Algoritmalarının Performansı

Öz: Çok amaçlı optimizasyon birden fazla amacı olan problemlere uygun çözümler üretme işlemidir. Sezgisel çok amaçlı optimizasyonda global optimuma yakın çözümler elde etmede rastgele üretilen sayı dizisi büyük öneme sahiptir. Rasgele üretilen sayı dizisinin belli bir alanda toplanması, global optimumdan uzaklaşma riskini arttırmaktadır. Bu riski azaltmak için kaotik haritalar kullanılmıştır. Kaotik haritalarda üretilen sayıların çeşitliliği yüksek olduğu için periyodik değildir. Kaotik haritalarda üretilen sayıların çeşitliliği yüksek olduğu için periyodik değildir. Bu nedenle optimizasyon algoritmalarının rasgele sayı üretim kısmında kaotik haritalar kullanılmıştır. Kaos temelli algoritmalar esnek ve lokal minimumdan kaçabilme özelliklerine sahip oldukları için önemli bir çalışma alanı haline gelmiştir. Bu çalışmada kaotik haritaların yeni ve başarılı Çok Amaçlı Altın Sinüs Algoritması (MOGoldSA) üzerinde etkileri, literatürde yer edinmiş Çok Amaçlı Karınca Aslanı Optimizasyonu (MOALO) algoritması ile karşılaştırılarak incelenmiştir.

Anahtar kelimeler: Kaotik Harita, Çok Amaçlı Optimizasyon, Kaos Temelli Algoritmalar, Metasezgisel Yöntemler

1. Introduction

Metaheuristic optimization algorithms are a very popular field that is easy to transform, has high solution capacity, and has wide usage. Metaheuristic optimization algorithms have been developed inspired by nature. They solve problems based on all physical or biological events that exist in nature [1]. Metaheuristic optimization is the process of generating suitable solutions for optimization problems by starting from a randomly generated number string. Heuristic optimization, starting from a random string of numbers during the optimal solution to the problem or achieve convergence iterations are targeted. Therefore, the most important criteria is to determine the random string of numbers to reach the optimum solution. Generating the same values in random number strings affects the performance of the algorithm. The main goal of heuristic optimization is to reach a global optimum. Accordingly, chaotic maps are used in random number generation to increase the performance of heuristic optimization algorithms [2].

Chaos theory is the study of chaotic dynamic systems sensitive to initial conditions. In the chaos theory, the theorem that the smallest changes that may occur in the initial conditions will have a large effect on the results. The "butterfly effect" is the most popular example of chaos theory. In this direction, it has been predicted that heuristic optimization algorithms can be used to generate random number generation with chaotic maps and to produce appropriate solutions to problems [3].

* Corresponding author: eeroz@firat.edu.tr. ORCID Number of authors: ¹ 0000-0003-2670-0606, ² 0000-0003-2973-9389

2. Chaotic Multi-Objective Gold Sine Algorithm

MOGoldSA is the applicable version of Gold-SA, a single-objective optimization algorithm, for multi-objective problems. Gold-SA is a math-based metaheuristic single-objective optimization algorithm developed from the sine function. Sinus function is a periodic function that repeats values at regular intervals. The duration of the sine function is 2π and all unit circles with sine values can be scanned as shown in Figure 1 [12].

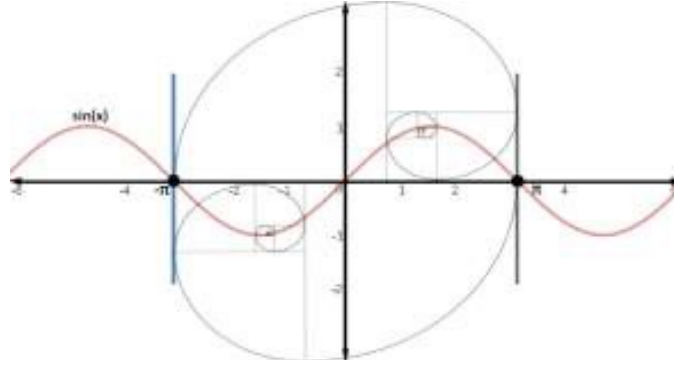


Figure 1. GoldSA scanning process [12]

Equation 1 is used for GoldSA to give the best result:

$$V(i, j) = V(i, j) * |\sin r_1| - p * \sin r_1 * |x_1 * D(j) - x_2 * V(i, j)| \quad (1)$$

Where, $V(i, j)$ is the value of the current solution in size. $D(j)$ determined target value is a random number in the range r_1 , $[0, 2\pi]$ and the interval p $[0, \pi]$. x_1 ve x_2 are coefficients obtained by the golden division method. These coefficients narrow the search area and allow the current value to approach the target value.

MOGoldSA was developed based on the hypothesis that Gold-SA can show the same success on multi-objective optimization problems, based on its features such as wide scanning of the search space, producing near-optimum results and fast operation while producing solutions to problems. All parameters of MOGoldSA except archive size are the same as Gold-SA [13].

In the MOGoldSA, p parameter is randomly determined in the range of $[0, \pi]$ for each search agent. These randomly generated values prevent a large search of the search space. To eliminate this problem, Mirjalili and Amir H. Gandomi [14] achieved successful results by normalizing the chaotic maps with Equation 2 and Equation 3. In this study, it is aimed to scan as much of the search space as possible in order to find better solutions to multi-objective optimization problems by using the r_1 , pattern shown in Equation 1, which is adaptively decreasing by integrating with normalized chaotic maps.

$$V(t) = Max - \frac{t}{T}(Max - Min) \quad (2)$$

$$Normalize(K_i(t); [a, b] \text{ dan } [0, V(t)] \text{ 'ye}): K_i^{norm}(t) = \frac{(K_i(t)-a) \times (V(t)-0)}{(b-a)} + 0 = \frac{(K_i(t)-a) \times (V(t))}{(b-a)} \quad (3)$$

Where, K : Chaotic map, i : Index of the chaotic map, t : Current iteration, T : Maximum number of iterations, $[Max - Min]$: Represents the adaptive range. $[a, b]$: Shows the range of chaotic maps. $V(t)$ is reduced by each iteration, while at each iteration $[a, b]$ matches $[0, V(t)]$. This situation refers to the adaptive normalization process.

As a result, the value of the coefficient p is updated using Equation 4.

$$p(t) = K_i^{norm}(t) + c - t \times ((c)/T) \quad (4)$$

Adding chaotic maps to the randomly generated sequence contributes to the random behavior of both adaptive p and chaotic maps at the same time. Chaotic maps provide to have a wide spectrum by generating different random

sequences each time. By changing the value of p abruptly and helping to get rid of the local minimum, it provides better convergence speed. Adaptive normalization, on the other hand, slows down the transition of the chaos-based MOGoldSA from the exploration phase to the exploitation phase.

3. Chaotic Multi-objective Ant Lion Optimizer

ALO algorithm was developed to imitate the hunting mechanisms of ant lions. The general steps of the algorithm are as follows [15]:

- a. Ants cluster is started with random values and are the main search agents in ALO.
- b. The fitness value of each ant is calculated.
- c. The ants make random walks around the ant lions and move on the search area.
- d. Antlion population is never evaluated.
- e. There is an antlion assigned to each ant.
- f. There is an elite antlion that affects the movement of ants.
- g. If any antlion gets better than elite, it will be replaced by elite.
- h. Steps b to g are repeatedly executed until an end criterion is met.
- i. The position and fitness value of the elite antlion is returned as the best estimate for the global optimum.

The main task of the ants is to explore the search area. They move in random walks in the search area. Ant lions maintain the best position achieved by the ants and are directed towards promising locations for ant search. To solve optimization problems, ALO simulates the random roaming of ants, clinging to an ant lion pit, building a pit, sliding towards ant lions, hunting and rebuilding the pit, and elite ant lion selection. The mathematical model established for each of the steps specified is presented in the next paragraphs.

The formula for the random walk of ants in the ALO algorithm is given in Equation 5:

$$X(t) = [0, \text{cumsum}(2r(t_1) - 1), \text{cumsum}(2r(t_2) - 1), \dots, \text{cumsum}(2r(t_n) -)] \quad (5)$$

Where, cumsum calculates the cumulative sum, n is the maximum number of iterations, t represents the random walk step

To keep the random walk within the search area and prevent the ants from overflowing, random walks are normalized using Equation 6 below:

$$X_i^t = \frac{(x_i^t - a_i) \times (d_i^t - c_i^t)}{(b_i - a_i)} + c_i^t \quad (6)$$

Where, c_i^t t . minimum variable i in iteration, d_i^t t . maximum variable i in iteration, a_i i . is the random walking minimum of the variable and b_i i . is the random walking maximum of the variable

ALO simulates the ants squeezing into the ant lion's pit by random walks and this process is given in Equation 7 and Equation 8.

$$c_i^t = \text{Antlion}_j^t + c^t \quad (7)$$

$$d_i^t = \text{Antlion}_j^t + d^t \quad (8)$$

Where, c^t the minimum of all variables in t . and d^t . Shows the vector containing the maximum of all variables in t . iteration. c_i^t , i . the minimum of all variables for ant, d_i^t , shows the maximum of all variables for the ant. Antlion_j^t , shows the position of selected j . ant lions in t . iteration.

Large ant lions create larger pits to increase their survival time. To simulate this process, ALO uses the roulette wheel operator who selects ant lions based on their suitability values. The roulette wheel helps ant lions striving to attract more ants. Using the formulas in Equation 9 and Equation 10, the limits of random walks should be reduced adaptively to simulate sliding ants from ant lions:

$$c^t = \frac{c^t}{l} \quad (9)$$

$$d^t = \frac{d^t}{I} \quad (10)$$

Where, I is ratio, c^t is the minimum of all variables in t . iteration, d^t , Shows the vector containing the maximum of all variables in t . iteration

The final step in ALO is to catch the ants and rebuild the pit. It is simulated as in Equation 11:

$$Antlion_j^t = Ant_i^t \text{ if } f(Ant_i^t) < (Antlion_j^t) \quad (11)$$

Where, t current number of iterations, $Antlion_j^t$, shows the position of selected j . ant lions in t . iteration, Ant_i^t i . indicates the ant's position in t . iteration.

The last operator in ALO is the elite, where the most suitable ant lion is stored during optimization. Elite is the only ant lion that can infect all ants. This means that random walks to ant lions are drawn towards a chosen ant lion or elite ant lion. The formula is given in Equation 12 to consider both cases.

$$Ant_i^t = \frac{R_A^t + R_E^t}{2} \quad (12)$$

Where, R_A^t is the random walk around the antlion selected using a roulette wheel and R_E^t is the random walk around the elite antlion.

The ALO algorithm created with the specified mathematical methods has been developed for multi-objective problems and the MOALO algorithm has been brought to the literature [16]. The optimum solutions found by using archive method were stored in MOALO, which tries to produce optimal solutions by using the Pareto method. The convergence of the MOALO algorithm is inherited from the ALO algorithm. If a solution is chosen from the archive, the ALO algorithm can improve its quality. However, a limit must be found for the archive, and solutions must be selected from the archive to improve distribution. In this approach, the perimeter of each solution is analyzed by considering a predefined radius. The number of solutions in the environment counts and is considered the measure of dispersion. Improving the distribution of solutions in the archive is carried out in two stages.

Equation 11 and Equation 13 must be substituted for the nature of multi-objective objects to require ALO to solve multi-objective problems.

$$Antlion_j^t = Ant_i^t \text{ if } f(Ant_i^t) < f(Antlion_j^t) \quad (13)$$

Where, t current number of iterations, $Antlion_j^t$, shows the position of selected j . ant lions in t . iteration, Ant_i^t i . indicates the ant's position in t . iteration.

The rest of the operators in MOALO are the same as in ALO. MOALO produces effective solutions to many constrained and unconstrained optimization problems in the literature. In order to increase this performance, it is aimed to produce more effective solutions by using chaotic maps during the generation of random number strings. Thus, Chaotic Ant Lion Optimizer (CMOALO) was developed.

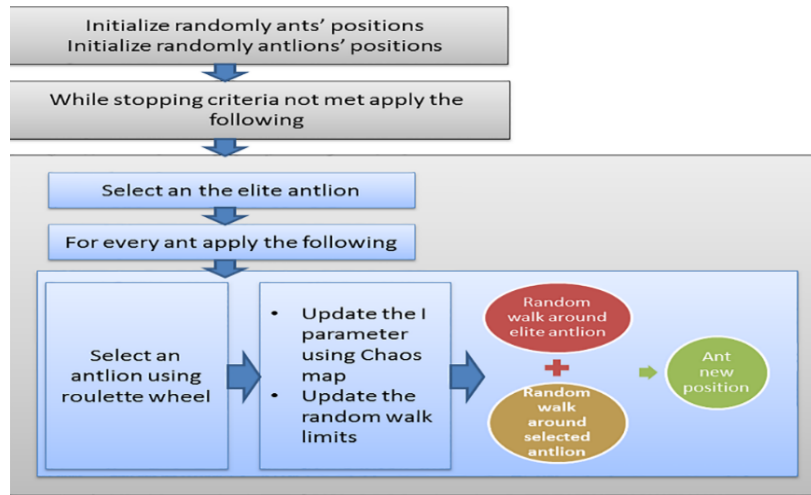


Figure 2. CMOALO [15]

4. Chaos Maps

Chaos literally means great disorder or confusion. Chaotic systems are dynamic systems that depend on initial conditions. Chaos theory studies the behavior of unpredictable systems. In order for a system to be chaotic, it must not be sensitive to initial conditions, topologically complex, periodic, ergodic and stochastic. Due to the dynamic properties of chaos variables, chaos search has the ability to escape from local optima according to random search. It has therefore been applied for optimization. Chaotic map is a map that exhibits a kind of chaotic behavior [17, 18]. In this study, 5 chaotic maps (Logical, Singer, Sinusoidal, Piecewise and Tent) were used for the comparison of multi-objective optimization algorithms. The mathematical expressions of the maps are as follows:

Table 1. Chaotic Maps

	Chaotic Maps	Function
C1	Piecewise	$x_{i+1} = \begin{cases} \frac{x_i}{P} & 0 \leq x_i < P \\ \frac{x_i - P}{0.5 - P} & P \leq x_i < 0.5, \\ \frac{1 - P - x_i}{0.5 - P} & 0.5 \leq x_i < 1 - P, 1 - P \leq x_i < 1 \\ \frac{1 - x_i}{P} & \end{cases} \quad (14)$
C2	Singer	$x_{i+1} = \mu(7.86x_i - 23.31x_i^2 + 28.75x_i^3 - 13.302875x_i^4), \mu = 2.3 \quad (15)$
C3	Sinusoidal	$x_{i+1} = ax_i^2 \sin(\pi x_i), a = 2.3 \quad (16)$
C4	Tent	$x_{i+1} = \begin{cases} \frac{x_i}{0.7} x_i < 0.7 \\ \frac{10}{3}(1 - x_i)x_i \geq 0.7 \end{cases} \quad (17)$
C5	Logical	$x_{i+1} = ax_i(1 - x_i), a = 4 \quad (18)$

5. Experimental Results

In this study, comparisons were made over 13 different comparison functions (constrained and unconstrained). In our studies using 11 different chaotic maps on MOGoldSA, 5 most effective chaotic maps were used [19]. Using these chaotic maps on the MOALO, two multi-objective optimization algorithms that produce successful results are compared. In the study, each algorithm was run 20,000 iterations and 100 optimum solutions were obtained. The mathematical expressions of some of the functions used are shown in Table 2.

Table 2. Mathematical model of some comparison functions used

F	Variable Limit	Objective Functions
FON	$x_i \in [-4,4]$ $i = 1, \dots, n$ $n = 10$	$f_1(x) = 1 - \exp\left(-\sum_1^3 \left(x_i - \frac{1}{\sqrt{3}}\right)^2\right)$
KUR	$x_i \in [-5,5]$ $i = 1, \dots, n$ $n = 3$	$f_1(x) = \sum_{i=1}^{n-1} \left(-10 \exp\left(-0.2 \sqrt{x_i^2 + \sqrt{x_{i+1}^2}}\right)\right)$ $f_2(x) = \sum_{i=1}^n (x_i ^{0.8} + 5 \sin x_i^2)$
CNEX	$x_1 \in [0,11]$ $x_2 \in [0,5]$	$f_1(x) = x_1$ $f_2(x) = (1 + x_2)/x_1$ $g_1(x) = 9x_1 + x_2 \geq 6$ $g_2(x) = -x_2 + 9x_1 \geq 1$
SRN	$x_1 \in [-20,20]$ $x_2 \in [-20,20]$	$f_1(x) = 2 + (x_1 - 2)^2 + (x_2 - 2)^2$ $f_2(x) = 9x_1 - (x_2 - 1)$ $g_1(x) = x_1^2 + x_2^2 \leq 225$ $g_2(x) = x_1 - 3x_2 + 10 \leq 0$

The criteria used to evaluate the success of the developed algorithms are called performance criteria. In our study, the performance criteria that have been included in the literature and frequently used in the comparison of multi-objective optimization algorithms were used. These; General Distance (GD) and Reversal General Distance (RGD)

General Distance (GD):

GD was proposed by Veldhuizen in 1998 and the solutions obtained are calculated by measuring the distances between the Pareto-optimal fronts. Whether a solution belongs to the optimal solution set is calculated by the distance of the obtained solution to the pareto optimal set. This criterion called General Distance is calculated with Equation 19. [20,21]:

$$GD = \frac{(\sum_{i=1}^{|Q|} d_i^p)^{1/p}}{|Q|} \quad (19)$$

Where, d_i parameters expression in Equation 19 is the Euclidean distance and it is calculated as shown in Equation 20.

$$d_i = \min_{k=1}^P |\sqrt{\sum_{m=1}^M (f_m^i - f_m^k)^2}| \quad (20)$$

Where, f_m^k , P 'nin k . of the element m . objective function value.

Reverse General Distance (RGD):

It is an improved version of the GD criterion. Unlike the GD criterion, Pareto optimally calculates the distance of the points on the front to the obtained solution set. The mathematical expression of the RGD criterion is included in Equation 21

$$RGD = \frac{(\sum_{i=1}^{|P|} d_i^q)^{1/q}}{|P|} \quad (21)$$

The biggest advantage of RGD is that it can measure both convergence and diversity of solutions simultaneously. Similar to GD, RGD is that as the number of targets increases, it becomes exponentially costly. [21].

Table 3 shows the statistical results of MOGoldSA according to GD criteria. According to these results, the Singer map was the most successful chaotic map with a success rate of 6/13, while the Logical map was 4/13, Piecewise map 2/13, Tent and Sinusoidal maps 1/13.

Table 3. CMOGoldSA: Statistical results according to GD criterion

		BEAM	BNH2	CNEX	CTP8	FON1	KUR1	SRN1	VIE1	ZDT1	ZDT2	ZDT3	ZDT4	ZDT6
Singer	Best	0,0196	5,3389	0,1011	0,1158	0,0088	14,8731	3,6958	0,0942	0,0134	0,0161	0,0174	0,4558	0,0098
	Mean	0,0249	8,5491	0,2333	0,2248	0,0134	15,0780	8,1060	0,2083	1,7700	3,0605	1,4542	0,8867	0,3403
	Worst	0,0380	8,6710	0,5421	0,8421	0,0253	15,4752	21,9288	0,5057	2,7173	4,1907	2,9696	0,9127	1,0561
	Std	0,0040	0,6067	0,0912	0,1309	0,0033	0,1854	4,9218	0,0990	1,0313	1,5669	1,0643	0,0851	0,3768
Sinusoidal	Best	0,0177	8,6188	0,1379	0,1293	0,0090	14,8748	3,1611	0,0991	0,0127	0,0145	0,0189	0,7854	0,0081
	Mean	0,0243	8,6602	0,2782	0,2446	0,0133	15,0907	7,7150	0,1825	1,3320	3,6167	1,3280	0,9084	0,3382
	Worst	0,0331	8,6705	0,8724	0,4753	0,0262	15,5087	14,2698	0,3196	2,8237	4,4080	2,7000	0,9127	1,0071
	Std	0,0039	0,0115	0,1753	0,0927	0,0039	0,2083	3,3208	0,0640	1,2426	0,9187	0,9787	0,0232	0,3959
Tent	Best	0,0164	8,5120	0,1278	0,1283	0,0120	14,8614	3,7117	0,0945	0,0137	0,0124	0,0140	0,5226	0,0089
	Mean	0,0242	8,6513	0,2172	0,2302	0,0149	15,1675	7,6690	0,2207	1,5216	3,2706	1,3654	0,8915	0,4319
	Worst	0,0318	8,6695	0,3728	0,5669	0,0235	15,5589	16,7396	0,4826	2,8675	4,2219	2,4975	0,9127	0,9719
	Std	0,0046	0,0324	0,0653	0,0995	0,0030	0,2229	2,9734	0,0877	1,1665	1,4843	0,8870	0,0766	0,3830
Piecewise	Best	0,0169	8,6199	0,1466	0,1159	0,0102	14,8678	3,1961	0,1070	0,0123	0,0127	0,0166	0,8137	0,0081
	Mean	0,0255	8,6613	0,2410	0,2168	0,0152	15,1163	6,8933	0,2253	1,1708	3,0995	1,2688	0,9065	0,2760
	Worst	0,0396	8,6695	0,5943	0,3378	0,0292	15,5114	13,2787	0,5596	2,7529	4,2769	2,8002	0,9127	0,9722
	Std	0,0049	0,0106	0,1060	0,0614	0,0051	0,2205	2,7146	0,0960	1,2342	1,4680	1,0747	0,0219	0,3754
Logical	Best	0,0160	8,5558	0,1332	0,1182	0,0089	14,8609	3,0946	0,1003	0,0124	0,0105	0,0196	0,7978	0,0097
	Mean	0,0241	8,6567	0,2316	0,2185	0,0135	15,0573	6,8826	0,1826	1,7028	3,0435	1,3600	0,9082	0,2024
	Worst	0,0356	8,6698	0,6840	0,4373	0,0251	15,4999	15,1967	0,3269	3,0148	4,2225	2,5894	0,9127	0,9188
	Std	0,0042	0,0223	0,1051	0,0853	0,0033	0,1863	3,3612	0,0595	1,2194	1,5496	0,9605	0,0210	0,3109

The statistical results of the CMOALO algorithm according to the GD criteria are given in Table 4. Considering these results, the Tent map was the most successful chaotic map at the rate of 5/13, while the Logical map was 4/13, Singer and Sinusoidal map 2/13, and Tent map 1/13.

Table 4. CMOALO: Statistical results according to GD criterion

		BEAM	BNH2	CNEX	CTP8	FON1	KUR1	SRN1	VIE1	ZDT1	ZDT2	ZDT3	ZDT4	ZDT6
Singer	Best	0,0186	8,6630	0,0418	0,0455	0,0078	15,5486	1,7511	0,0666	0,0786	0,3093	0,0167	3,7666	0,0082
	Mean	0,0256	8,6664	0,0588	0,0582	0,0100	15,6041	2,1612	0,1000	0,2097	0,6869	0,0408	12,6633	0,0118
	Worst	0,0500	8,6694	0,0863	0,0899	0,0132	15,6291	3,4782	0,1764	0,3758	0,7310	0,0852	23,8325	0,0180
	Std	0,0074	0,0016	0,0160	0,0115	0,0014	0,0176	0,4171	0,0295	0,0804	0,1084	0,0170	5,8379	0,0026
Sinusoidal	Best	0,0162	8,6608	0,0420	0,0441	0,0085	15,5569	1,6699	0,0595	0,1145	0,5204	0,0241	1,5464	0,0082
	Mean	0,0270	8,6661	0,0597	0,0549	0,0099	15,6068	2,0984	0,0986	0,2270	0,7083	0,0456	12,0797	0,0106
	Worst	0,0548	8,6687	0,1558	0,0898	0,0125	15,6274	2,6700	0,1597	0,4048	0,7309	0,0940	34,3103	0,0162
	Std	0,0092	0,0017	0,0245	0,0112	0,0011	0,0144	0,3281	0,0311	0,0792	0,0578	0,0182	8,4790	0,0020
Tent	Best	0,0154	8,6578	0,0383	0,0405	0,0078	15,1948	1,7320	0,0620	0,1498	0,6685	0,0617	14,3162	0,0081
	Mean	0,0279	8,6664	0,0709	0,0902	0,0092	15,5432	2,2705	0,1103	0,3525	0,7267	0,1945	28,6343	0,0659
	Worst	0,1306	8,6694	0,2982	0,1859	0,0109	15,6171	3,6464	0,1689	0,4774	0,7337	0,3455	44,9801	0,2662
	Std	0,0211	0,0022	0,0460	0,0418	0,0008	0,0773	0,4291	0,0303	0,0823	0,0156	0,0645	8,3718	0,0748
Piecewise	Best	0,0162	8,6608	0,0444	0,0404	0,0085	15,5569	1,7920	0,0675	0,0976	0,1794	0,0206	2,5639	0,0089
	Mean	0,0270	8,6661	0,0672	0,0627	0,0099	15,6068	2,1759	0,0940	0,1957	0,6797	0,0474	13,3858	0,0117
	Worst	0,0548	8,6687	0,1146	0,1159	0,0125	15,6274	3,3305	0,1703	0,3145	0,7310	0,1109	30,4019	0,0168
	Std	0,0092	0,0017	0,0201	0,0185	0,0011	0,0144	0,4162	0,0272	0,0625	0,1333	0,0236	6,7338	0,0019
Logical	Best	0,0154	8,6597	0,0374	0,0394	0,0088	15,5582	1,6751	0,0713	0,0996	0,4693	0,0162	1,4243	0,0087
	Mean	0,0217	8,6666	0,0564	0,0604	0,0101	15,6036	2,0199	0,1015	0,2240	0,7033	0,0335	10,8912	0,0114
	Worst	0,0316	8,6691	0,0891	0,1100	0,0127	15,6296	2,6162	0,1530	0,3779	0,7309	0,0517	33,4715	0,0184
	Std	0,0049	0,0020	0,0138	0,0172	0,0010	0,0156	0,2617	0,0254	0,0738	0,0751	0,0097	7,6318	0,0022

The statistical results of the CMOGoldSA algorithm according to the RGD criteria are shown in Table 5. According to the results, the Sinusoidal map produced successful results in 7 of 13 functions and became the most successful chaotic map, while the Logical map succeeded 6/13, Singer, Tent and Piecewise maps achieved a success rate of 3/13. Also, the Sinusoidal map reached optimum results in ZDT2 and ZDT4 functions, Logical ZDT3 and ZDT4 functions, Piecewise ZDT2, Tent and Singer in ZDT4 functions.

Table 5. CMOGoldSA: Statistical results according to RGD criterion

		BEAM	BNH2	CNEX	CTP8	FON1	KUR1	SRN1	VIE1	ZDT1	ZDT2	ZDT3	ZDT4	ZDT6
Singer	Best	0,0010	5,7684	0,0022	0,0022	0,0009	15,3118	0,7678	0,0036	0,0009	0,0003	0,0009	0,0000	0,0002
	Mean	0,0012	8,2012	0,0091	0,0078	0,0011	15,7382	1,9500	0,0126	2,1017	3,1650	1,5488	0,0010	0,9466
	Worst	0,0015	8,5275	0,0601	0,0224	0,0014	16,0898	3,6985	0,0458	3,2244	4,3519	3,1861	0,0078	3,9783
	Std	0,0001	0,4677	0,0108	0,0056	0,0001	0,2057	0,8097	0,0090	1,2969	1,6264	1,3829	0,0018	1,1435
Sinusoidal	Best	0,0011	8,0936	0,0021	0,0017	0,0009	15,2473	0,5931	0,0034	0,0007	0,0000	0,0008	0,0000	0,0002
	Mean	0,0013	8,3032	0,0061	0,0078	0,0011	15,7588	1,8752	0,0102	1,4344	3,6564	1,4461	0,0001	0,9473
	Worst	0,0015	8,5889	0,0153	0,0253	0,0013	16,0273	5,7892	0,0300	3,3335	4,3234	3,0472	0,0025	3,0880
	Std	0,0001	0,1155	0,0037	0,0057	0,0001	0,2047	1,1901	0,0056	1,4656	1,0193	1,3846	0,0005	1,1456
Tent	Best	0,0009	7,9854	0,0023	0,0023	0,0009	15,2952	0,6781	0,0038	0,0008	0,0003	0,0006	0,0000	0,0002
	Mean	0,0012	8,3069	0,0075	0,0086	0,0011	15,8170	1,4388	0,0133	1,7489	3,2868	1,3595	0,0004	1,1408
	Worst	0,0014	8,5607	0,0554	0,0483	0,0014	16,0341	3,1036	0,0486	3,2696	4,3369	3,0960	0,0045	2,8227
	Std	0,0001	0,1173	0,0094	0,0107	0,0001	0,1761	0,6103	0,0098	1,4429	1,5090	1,3883	0,0011	1,0680
Piecewise	Best	0,0010	8,0970	0,0019	0,0027	0,0010	15,2508	0,4966	0,0052	0,0009	0,0000	0,0006	0,0000	0,0002
	Mean	0,0013	8,2607	0,0090	0,0095	0,0011	15,7468	1,6787	0,0115	1,3031	3,1907	1,4583	0,0003	0,8479
	Worst	0,0015	8,4658	0,0348	0,0538	0,0013	16,0427	5,0288	0,0252	3,3105	4,4828	3,2030	0,0033	3,0393
	Std	0,0001	0,0882	0,0084	0,0099	0,0001	0,2242	0,9679	0,0057	1,5127	1,6375	1,3919	0,0009	1,1469
Logical	Best	0,0010	8,1310	0,0025	0,0017	0,0009	15,2696	0,5750	0,0048	0,0007	0,0003	0,0000	0,0000	0,0001
	Mean	0,0012	8,3086	0,0139	0,0064	0,0011	15,7545	1,6344	0,0172	1,9242	3,0808	1,4622	0,0003	0,6460
	Worst	0,0014	8,5161	0,0904	0,0289	0,0016	16,0259	3,3369	0,0415	3,3962	4,1574	3,3535	0,0040	3,4738
	Std	0,0001	0,0920	0,0202	0,0049	0,0001	0,2072	0,7028	0,0099	1,3986	1,5776	1,4046	0,0009	1,0787

The statistical results of the CMOALO algorithm are given in Table 6. According to the results, the Piecewise map produced very successful results at the rate of 8/13. The Logical map is followed by 4/13 and the Tent map with 2/13. In addition, Piecewise and Logical maps have achieved optimum results in ZDT2 function.

Table 6. CMOALO: Statistical results according to RGD criterion

		BEAM	BNH2	CNEX	CTP8	FON1	KUR1	SRN1	VIE1	ZDT1	ZDT2	ZDT3	ZDT4	ZDT6
Singer	Best	0,0186	8,6630	0,0418	0,0455	0,0078	15,5486	1,7511	0,0666	0,0786	0,3093	0,0167	3,7666	0,0082
	Mean	0,0256	8,6664	0,0588	0,0582	0,0100	15,6041	2,1612	0,1000	0,2097	0,6869	0,0408	12,6633	0,0118
	Worst	0,0500	8,6694	0,0863	0,0899	0,0132	15,6291	3,4782	0,1764	0,3758	0,7310	0,0852	23,8325	0,0180
	Std	0,0074	0,0016	0,0160	0,0115	0,0014	0,0176	0,4171	0,0295	0,0804	0,1084	0,0170	5,8379	0,0026
Sinusoidal	Best	0,0162	8,6608	0,0420	0,0441	0,0085	15,5569	1,6699	0,0595	0,1145	0,5204	0,0241	1,5464	0,0082
	Mean	0,0270	8,6661	0,0597	0,0549	0,0099	15,6068	2,0984	0,0986	0,2270	0,7083	0,0456	12,0797	0,0106
	Worst	0,0548	8,6687	0,1558	0,0898	0,0125	15,6274	2,6700	0,1597	0,4048	0,7309	0,0940	34,3103	0,0162
	Std	0,0092	0,0017	0,0245	0,0112	0,0011	0,0144	0,3281	0,0311	0,0792	0,0578	0,0182	8,4790	0,0020
Tent	Best	0,0154	8,6578	0,0383	0,0405	0,0078	15,1948	1,7320	0,0620	0,1498	0,6685	0,0617	14,3162	0,0081
	Mean	0,0279	8,6664	0,0709	0,0902	0,0092	15,5432	2,2705	0,1103	0,3525	0,7267	0,1945	28,6343	0,0659
	Worst	0,1306	8,6694	0,2982	0,1859	0,0109	15,6171	3,6464	0,1689	0,4774	0,7337	0,3455	44,9801	0,2662
	Std	0,0211	0,0022	0,0460	0,0418	0,0008	0,0773	0,4291	0,0303	0,0823	0,0156	0,0645	8,3718	0,0748
Piecewise	Best	0,0011	8,1834	0,0025	0,0020	0,0021	15,8882	0,2966	0,0025	0,0006	0,0000	0,0007	3,3302	0,0276
	Mean	0,0013	8,3683	0,0044	0,0048	0,0029	16,0165	0,4103	0,0043	0,0010	0,0001	0,0014	14,6304	0,1274
	Worst	0,0016	8,5468	0,0067	0,0063	0,0037	16,1998	0,6741	0,0101	0,0022	0,0003	0,0024	33,4134	0,3635
	Std	0,0002	0,0943	0,0011	0,0012	0,0004	0,0739	0,0858	0,0018	0,0004	0,0001	0,0004	7,2690	0,0924
Logical	Best	0,0011	8,2153	0,0021	0,0021	0,0023	15,8881	0,3007	0,0028	0,0005	0,0000	0,0009	1,3971	0,0169
	Mean	0,0013	8,3646	0,0048	0,0045	0,0029	16,0029	0,4283	0,0043	0,0012	0,0001	0,0014	11,9345	0,0994
	Worst	0,0016	8,5110	0,0063	0,0070	0,0036	16,1689	0,5515	0,0062	0,0033	0,0005	0,0036	35,7860	0,2220
	Std	0,0002	0,0886	0,0010	0,0012	0,0004	0,0704	0,0803	0,0010	0,0009	0,0002	0,0006	8,0832	0,0530

The success of CMOGoldSA and CMOALO algorithms, which are two successful multi-objective optimization algorithms in the literature, with chaotic maps were compared. According to the statistical results in Table 3 and Table 4, CMOALO 7/13 and CMOGoldSA were successful in Singer and Logical maps, while CMOGoldSA was 8/13 in Tent map, 7/13 CMOGoldSA in Sinusoidal map, and 9/13 in Piecewise map. It has been observed that the CMOALO optimization algorithm produces successful results. According to the GD criterion, it was observed that CMOGoldSA produced more successful results in Tent and Sinusoidal maps.

If two multi-objective optimization algorithms are compared according to the statistics given in Table 5 and Table 6; According to Sinusoidal and Piecewise maps, the CMOGoldSA algorithm produced a successful result

at the rate of 9/13, 8/13 in the Singer and Logical map, and 7/13 in the Tent map. In general, the CMOGoldSA optimization algorithm produced more successful results in all chaotic maps according to RGD criteria.

6. Conclusion

Chaotic maps are used to improve the performance of the multi-objective gold sine algorithm (MOGoldSA). Chaotic maps help MOGoldSA reach the large search area and gradually move into the exploitation phase. Based on these performance data, it was seen that better results were obtained in generating suitable solutions to the problem as a result of the small interventions made on random number strings used in the beginning in multi-objective optimization. The chaotic maps used in the study have generally produced successful results in producing solutions suitable for the constrained and unconstrained engineering problems and produced more successful results than the CMOALO algorithm, which has an important place in the literature.

References

- [1] Mirjalili S, Lewis A. The Whale Optimization Algorithm, *ADV ENG SOFTW* 2016; 95: 51-67
- [2] Tanyıldızı E, Cigal T. Kaotik Haritalı Balina Optimizasyon Algoritmaları, *FÜMD* 2017; 29(1): 307 – 317.
- [3] Tanyıldızı E, Demir G. Nümerik Optimizasyon için Kaotik Altın Sinüs Algoritması, *FUMBD* 2019; 31(1): 91 – 97.
- [4] S. M. P. J. S. S., “Multi-objective ant lion optimizer: a multi-objective optimization algorithm for solving engineering problems,” *Appl Intell*, DOI 10.1007/s10489-016-0825-8, 2016.
- [5] Wei G. Shoubin W. Chaos Ant Colony Optimization and Application. Fourth International Conference on Internet Computing for Science and Engineering;2009; Harbin, China.
- [6] Ayan K. and Kilic U. Solution of multi-objective optimal power flow with chaotic artificial bee colony algorithm, *INT REV ELECTR ENG-I*; 2011; England, 6(3):1365–1371.
- [7] Ying S, Yuelin G,Xudong S. Chaotic Multi-Objective Particle Swarm Optimization Algorithm Incorporating Clone Immunity. *Mathematics* 2019, 7, 146;
- [8] Dunia S. Ramzy A. A Chaotic Crow Search Algorithm for High-Dimensional Optimization Problems. *Basrah Journal for Engineering Sciences* January 2018; 17(1):15-25
- [9] Danqing G, Junping W, Jun H. Renmin H and Maoqiang S. Chaotic-NSGA-II: An effective algorithm to solve multi-objective optimization problems. *ICISS*; 2010; Guilin, China.
- [10] Zhang H. Zhou J. Zhang Y. Fang N. and Zhang R. Short term hydrothermal scheduling using multi-objective differential evolution with three chaotic sequences, *INT J ELEC POWER*; 2013;England; 47: 85–99.
- [11] Pei Y. and Hao J, "Non-dominated sorting and crowding distance based multi-objective chaotic evolution", *ICSI* 2017; Japan, pp. 15-22,
- [12] Tanyıldızı E, Demir G. Golden Sine Algorithm: A Novel Math-Inspired Algorithm, *ADV ELECTR COMPUT EN* 2017.
- [13] Eröz E. Yeni Çok Amaçlı Optimizasyon Algoritması: MOGoldSA, Fırat Üniversitesi Teknoloji Fakültesi Yazılım Mühendisliği Yüksek Lisans Tezi, 2020
- [14] Mirjalili S, Gandomi AH. Chaotic gravitational constants for the gravitational search algorithm. *APPL SOFT COMPUT* 2017. 53: 407-419.
- [15] Zawbaa HM, Emary E, Grosan C (2016) Feature Selection via Chaotic Antlion Optimization. *PLoS ONE* 11(3): e0150652. doi:10.1371/journal.pone.0150652
- [16] P. J. S. S. Mirjalili, “Multi-objective ant lion optimizer: a multi-objective optimization algorithm for solving engineering problems,” *Springer Science+Business Media*, 10.1007/s10489-016-0825-8, 2016.
- [17] Vohra R, Patel B. An Efficient Chaos-Based Optimization Algorithm Approach for Cryptography. *Communication Network Security*. 2012;1(4):75–79.
- [18] Ren B, Zhong W. Multi-objective optimization using chaos based PSO. *Information Technology*. 2011;10(10):1908–1916.
- [19] Eröz, E., Tanyıldızı, E., (2020). Kaotik Haritalı Çok Amaçlı Altın Sinüs Algoritmasının Performans Analizi. *Fırat Üniversitesi Mühendislik Bilimleri Dergisi*, 32(2),391-402.
- [20] Deb K. Multi-objective optimization using evolutionary algorithms. New York: John Wiley&Sons, 2001.
- [21] Van Veldhuizen, D. A. and Lamont, G. B. Multiobjective evolutionary algorithm research: A history and analysis. Technical Report TR-98-03, Department of Electrical and Computer Engineering, Graduate School of Engineering, Air Force Institute of Technology, WrightPatterson AFB, Ohio, 1998

One-dimensional Center Symmetric Local Binary Pattern Based Epilepsy Detection Method

Serkan METİN*

Department Of Management Information Systems, Faculty of Social Sciences and Humanities, Malatya Turgut Özal
University, Malatya, Turkey
serkan.metin@ozal.edu.tr

(Geliş/Received: 10/02/2021;

Kabul/Accepted: 15/02/2021)

Abstract: The diagnosis of epilepsy from the EEG signals is determined by the visual/manual evaluation performed by the neurologist. This evaluation process is laborious and evaluation results vary according to the experience level of neurologists. Therefore, automated systems that will be created using advanced signal processing techniques are important for diagnosis. In this study, a new feature extraction method is proposed using multiple kernel based one-dimensional center symmetric local binary pattern (1D-CSLBP) to identify epileptic seizures. To strengthen this method, levels have been created and multi-level feature extraction has been carried out. Discrete wavelet transform (DWT) was used to generate the levels and feature extraction was performed using the low pass filter coefficient (L bands) obtained at each level. Neighborhood component analysis (NCA) was used to select the most distinctive features. The obtained features are classified using the nearest neighbors (kNN) algorithm. A high performance method was obtained by using multiple kernel NCA and NCA. The 1D-CSLBP and NCA-based method has reached 100.0% accuracy in A-E, A-D-E, D-E, C-E situations.

Keywords: Feature extraction, local feature generation, feature selection, classification.

Tek Boyutlu Merkez Simetrik Yerel İkili Desen Tabanlı Epilepsi Tespit Yöntemi

Öz: EEG sinyallerinden epilepsi tanısı, nörolog tarafından yapılan görsel / manuel değerlendirme ile belirlenir. Bu değerlendirme süreci zahmetlidir ve değerlendirme sonuçları nörologların deneyim düzeyine göre değişir. Bu nedenle gelişmiş sinyal işleme teknikleri kullanılarak oluşturulacak otomatik sistemler tanı için önemlidir. Bu çalışmada, epileptik nöbetleri tanımlamak için çoklu çekirdek tabanlı tek boyutlu merkez simetrik yerel ikili model (1D-CSLBP) kullanılarak yeni bir özellik çıkarma yöntemi önerilmiştir. Bu yöntemi güçlendirmek için seviyeler oluşturulmuş ve çok seviyeli özellik çıkarımı gerçekleştirilmiştir. Seviyeleri oluşturmak için ayrık dalgacık dönüşümü (DWT) kullanılmış ve her seviyede elde edilen düşük geçişli filtre katsayısı (L bantları) kullanılarak özellik çıkarımı gerçekleştirilmiştir. Mahalle bileşen analizi (NCA), en ayırt edici özellikleri seçmek için kullanıldı. Elde edilen özellikler en yakın komşular (kNN) algoritması kullanılarak sınıflandırıldı. Çoklu çekirdek NCA ve NCA kullanılarak yüksek performanslı bir yöntem elde edildi. 1D-CSLBP ve NCA tabanlı yöntem, A-E, A-D-E, D-E, C-E durumlarında% 100.0 doğruluğa ulaşmıştır.

Anahtar kelimeler: Özellik çıkarma, yerel özellik üretimi, öznelik seçimi, sınıflandırma.

1. Introduction

The human brain has a complex structure consisting of billions of neurons and connecting with electrical signals [1-2]. The disease caused by recurrent attacks resulting from abnormal electrical discharges of these neurons is called epilepsy [3,4]. Epilepsy can affect individuals of all ages [5]. According to world health organization [6], It is considered one of the most common brain diseases among neurological disorders [7] [8] and affects approximately 1% of the population worldwide [9,10,11,12]. The number of epilepsy is more pronounced in developing countries [13].

Epileptic seizures are caused by temporary electrical disturbances in the brain [14]. Seizures usually begin with sudden attacks [15]. Diagnosis and monitoring of seizures is done with an electroencephalogram (EEG) signals and EEG signals defined as letter of brain [3]. We can extract more information as to brain using EEG signals [16, 17]. EEG [18] are collected through sensors attached to the scalp or electrodes. EEG signals are often used for the diagnosis of brain-based diseases [1,19-20]. EEG is considered as the most important diagnostic tool for epilepsy [6, 21, 22].

Generally, EEG signals are acquired between two seizures (interictal period) and rarely during one seizure (ictal period) [3]. Epilepsy patients have abnormalities in EEG signals [5,8]. The main feature of epileptic seizures in the EEG signal is the presence of spikes [10].

Epilepsy is usually diagnosed by a neurologist through visual evaluation of EEG signals [23, 24, 25]. Diagnosing epilepsy based on visual inspection of EEG signals is a laborious and lengthy process [3,5,26, 27,28].

* Corresponding author: serkan.metin@ozal.edu.tr. ORCID Number of authors: 0000-0003-1765-7474

In addition, results of visual analysis performed by different neurologists vary according to the level of experience of physicians [6,20,22,29]. Therefore, methods based on advanced signal processing techniques are important for fast, reliable and automated diagnosis of epilepsy from EEG signals [2,21]. Automatic detection of epileptic seizures can assist neurologists in evaluating long-term EEG recordings [25].

1.2. Literature review

With the development of information technologies, many artificial intelligence, machine learning techniques [8] and advanced digital signal processing methods have been applied [30] to efficiently detect epileptic seizures automatically [5,16,29]. Some of the automated EEG classification

Li et al. [7] presented a new automated seizure detection method based on multiscale radial fundamental function (MRBF) networks and Fisher vector (FV) coding. Jiang et al. [31] used a method for automatic seizure detection that uses features based on symplectic geometry decomposition. Mohammadpoory et al. [32] to be Support Vector Machine (SVM), K-Nearest Neighbor (KNN), Decision Tree (DT) and Naive Bayes (NB) as a classifier with the method based on weighted visibility graph entropy (WVGE) to describe seizure from EEG signals. He used four popular classifiers. Mahmoodiana et al. [33] used an approach based on cross-bispectrum properties to detect epileptic seizures. Yavuz et al. [34] used mel frequency cepstral coefficients (MFCCs) and neural network-based classification method to detect real-time seizures from EEG signals.

Sharma et al. [35] proposed a new semi-precise programming (SDP) formulation without any parameterization to design optimal orthogonal wavelet filter banks (OWFB) for automatic detection of epileptic seizure. Akyol [36] used the stacking unit-based DNN method to address the dual detection problem for epilepsy detection. Yuan et al. [37] used a method based on a weighted over learning machine (ELM) for seizure detection.

Zhou et al. [38] used singular spectrum analysis (SSA), support vector machine (SVM), extreme learning machine (ELM), and artificial neural network (ANN) to classify EEG signals. Yuan et al. [39] proposed a multi-image deep learning model to capture brain abnormality from multichannel epileptic EEG signals for seizure detection. Hossain et al. [40] used a deep CNN model for the task of seizure detection in the EEG epilepsy dataset. Liu et al. [41] used incremental entropy (IncrEn) and boost vector machines (SVMs) for automatic seizure detection in EEG signals. Harender and Sharma [42], Discrete wavelet transform (DWT) and Mean Absolute Value (MA), Standard Deviation (SD) and Mean power (AP), k-Nearest Neighbor (k-NN) classifier for detecting epileptic seizures from EEG signal used. Zhou et al. [43], the convolutional neural network (CNN) method was used to detect epileptic episodes. Li et al. [44] proposed a method for epileptic seizure detection using the CE-stSENet.

1.3. Dataset

The Bonn University Hospital is the commonly used database in the literature [3]. This dataset is named BONN EEG dataset and it was created by Andrzejak et al. [45]. It includes five categories from A to E, each containing 100 single-channel EEG segments with a length of 23.6 seconds duration from five healthy epilepsy patients. A class EEG signals were collected from healthy volunteers with eyes open; B class was collected from healthy volunteers with their eyes closed; C and D classes include seizure-free intervals, and subset E contains EEG signals obtained during active seizure [20].

2. Proposed Method

The main purpose of this study is to obtain high results in the Bonn EEG data set using a new feature extractor. For this purpose, a new feature extraction method using a multi-core one-dimensional central symmetric binary pattern (1D-CSLBP) is proposed. To strengthen this method, levels have been created and multi-level feature extraction has been carried out. Discrete wavelet transform (DWT) was used to generate the levels and feature extraction was performed using the low pass filter coefficient (L bands) obtained at each level. Neighborhood component analysis (NCA) was used to select the most prominent features. The properties obtained are classified using the k nearest neighbor (kNN) algorithm. The block diagram of the proposed method is given in Figure 1.

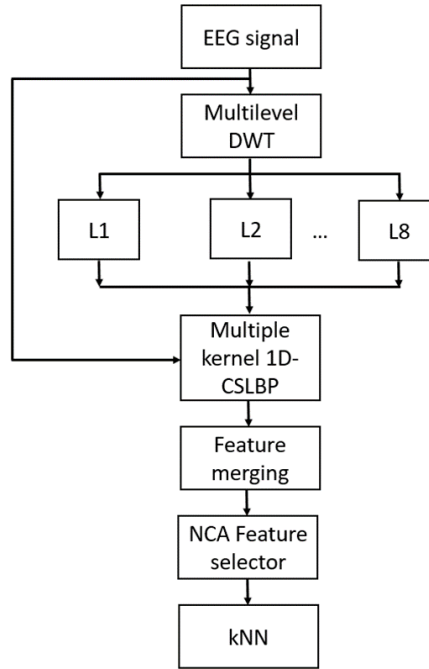


Figure 1. Flowchart of the presented 1D-CSLBP based EEG classification model.

As can be seen Figure 1, the main phases of the proposed method can be listed as follows. (i) 1D-CSLBP and DWT based multi-level feature extraction method, NCA based feature selection and classification. These phases are explained in detail in subsections.

2.1. Feature extraction

Feature generation phase is one of the most important phases of machine learning methods. The stronger and more distinctive the extracted feature, the higher the classification performance is obtained. Feature extraction methods are divided into two: handcrafted feature extraction and deep feature extraction. Manual feature extraction methods, on the other hand, are categorized into two categories: statistics-based and histogram-based (features obtained using descriptors). In this article, a new histogram-based feature extractor is proposed for the extraction of distinctive features, and this feature extractor is called multi-core 1D-CSLBP. Multi-core 1D-CSLBP is used as the key feature extractor of the proposed method. 8-level DWT is used to generate multi-level features. The steps of the recommended feature extraction method are given as follows.

Step 1: By using multilevel DWT, low pass DWT frequency bands are obtained. Here, daubechies 4 (db4) is used as the main wavelet function as DWT filter.

$$[L_1, H_1] = DWT(S) \quad (1)$$

$$[L_i, H_i] = DWT(L_{i-1}), i = \{2, 3, \dots, 8\} \quad (2)$$

In Eqs. 1 and 2, $DWT(\cdot)$ is DWT function, L_i, H_i i th level low-pass and high-pass filter coefficients and S is the used EEG signal. Eqs. 1 and 2 eight L bands are obtained. The length of each EEG signal used in the Bonn dataset was calculated to be 4097. The number of levels are calculated using $\left\lceil \log_2\left(\frac{4097}{9}\right) \right\rceil = 8$ equation. Herein, 4097 and 9 are defined length of the EEG and length of the used overlapping block respectively.

Step 2: Extract features from S and L vectors using 1DCSLBP.

$$O^1 = 1DCSLBP(S) \quad (3)$$

$$O^k = 1DCSLBP(L_{k-1}), k = \{2, 3, \dots, 9\} \quad (4)$$

Herein, $1DCSLBP(.)$ is used to define 1D-CSLBP. Steps of the 1D-CSLBP are given below.

Step 2.1: Divide the used signal into 9- sized overlapping blocks.



Figure 2. Graphical demonstration of the used nine sized overlapping window.

Step 2.2. Extract bits using signum (basic comparison function) and ternary functions.

$$bitS(i) = \begin{cases} 0, & s(i) < s(10-i) \\ 1, & s(i) \geq s(10-i) \end{cases}, i = \{1,2,3,4\} \quad (5)$$

$$bitU(i) = \begin{cases} 0, & s(i) - s(10-i) \leq d \\ 1, & s(i) - s(10-i) > d \end{cases} \quad (6)$$

$$bitL(i) = \begin{cases} 0, & s(i) - s(10-i) \geq -d \\ 1, & s(i) - s(10-i) < -d \end{cases} \quad (7)$$

Herein, $bitS$ is bits calculated using the signum function, $bitUY$ is upper ternary bits, $bitL$ is lower ternary bits. d is threshold value and it is calculated using Eq. 8.

$$d = \frac{std(S)}{2} \quad (8)$$

where $std(.)$ is standard deviation function.

Step 2.3. Calculate three feature signal using the generated bits.

$$OS^1(k) = \sum_{j=1}^4 bitS(j) * 2^{j-1}, k = \{1,2, \dots, U-8\} \quad (9)$$

$$OS^2(k) = \sum_{j=1}^4 bitU(j) * 2^{j-1} \quad (10)$$

$$OS^3(k) = \sum_{j=1}^4 bitL(j) * 2^{j-1} \quad (11)$$

Herein, OS^1, OS^2 and OS^3 are feature vector.

Step 2.4. Extract histograms

Step 2.5. Obtain 48 features by merging the extracted histograms.

Steps 2.1-2.5 are defined the 1DCSLBP feature extraction.

Step 3: Apply 1DCSLBP to generate (X) .

$$X((k-1) * 48 + j) = O^k(j), k = \{1,2, \dots, 9\}, j = \{1,2, \dots, 48\} \quad (12)$$

By applying Eq. 12, 432 size feature is extracted.

2.2. Feature selection

At this stage, the most significant 48 of the 432 features extracted using the NCA method (48 features were selected because multi-core 1D-CSLBP extracted 48 features). NCA is a method similar to the kNN algorithm and the main purpose of this method is to generate weights for each feature. All weights produced using NCA are positive. In this method, initial weights are assigned first. These weights are optimized using stochastic gradient descent (SGD) and a distance-based fitness function. NCA is a simple but effective method. For this reason, the NCA method is one of the methods frequently used in the literature. By using NCA, weights of all features are calculated and ordered indexes of the features are obtained by ordering these weights in descending order. Using these indices, the most significant properties are selected. Feature selection is the 4th step of the proposed method, and this step is as follows.

Step 4: Select the most valuable 48 features deploying NCA.

2.3. Classification

The last step of the proposed method is the classification stage. kNN classifier was used in the classification stage. The properties of the classifier used are as follows.

k: 1,

Distance: Manhattan uzaklığı,

Voting: None

Step 5: Classify 48 features employing kNN.

3. Experimental Results

The Bonn EEG dataset was used to test the performance of the proposed method on EEG signals. The main purposes of using the Bonn EEG dataset are as follows.

- The Bonn dataset is a frequently used dataset in the literature. Therefore, many comparison results can be obtained.

- Using the Bonn dataset, different situations are created and the performances of these situations are tested.

The situations used for tests in this article are as follows.

Table 1. The defined cases using Bonn EEG dataset.

Case	Classes
Case 1	AB-CD-E
Case 2	ABCD-E
Case 3	A-E
Case 4	A-D-E
Case 5	D-E
Case 6	C-E

Performance metrics used to test the situations shown in Table 1 are accuracy, recall, precision and F1-score. The performance metrics obtained according to the situations are given in the table below.

Table 2. Results (%) of the presented model.

Case	Accuracy	Recall	Precision	F1
Case 1	98.60	98.33	98.67	98.50
Case 2	99.60	99.0	99.75	99.37
Case 3	100.0	100.0	100.0	100.0
Case 4	100.0	100.0	100.0	100.0
Case 5	100.0	100.0	100.0	100.0
Case 6	100.0	100.0	100.0	100.0

According to the results in Table 2, the proposed 1D-CSLBP and NCA based method, 3-6. In cases it has reached 100.0% accuracy. A comparison table is given to show the performance of the proposed method and the comparative results are listed in Table 3.

Table 3. Comparatively results (%).

Case	Method	Accuracy (%)
Case 1	Orhan et al. [46]	95.60
	Hassan et al. [47]	97.60
	Our model	98.60
Case 2	Orhan et al. [46]	99.60
	Hassan et al. [47]	99.20
	Our model	99.60
Case 3	Acharya et al. [48]	98.50
	Hassan et al. [47]	100.0

	Our model	100.0
Case 4	Hassan et al. [47]	96.67
	Hassan et al. [47]	98.67
	Our model	100.0
Case 5	Kaya et al. [49]	95.50
	Siuly et al. [50]	93.60
	Our model	100.0
Case 6	Hassan et al. [47]	99.0
	Our model	100.0

As shown in Table 3, the proposed method has the best performance among all methods.

The advantages of the proposed method can be listed as follows.

- By using less number of features, high accuracy is obtained.
- The proposed method is simple and can be easily coded.
- A high performance method has been obtained by using multi-core 1D-CSLBP and NCA. The obtained method has reached high accuracy rates by using a simple classifier such as kNN.
- No optimization algorithm has been used to increase the performance of the method. This situation shows that the method is a cognitive method.

3. Conclusions

This research presents a new 1D-CSLBP and NCA based EEG classification model to detect epileptic seizures automatically. To generate low, medium and high level features, a multilevel feature extraction model is presented by employing 1D-CSLBP and DWT together. NCA is employed to choose the most discriminative features and 48 the most significant features are selected. Six cases are defined to evaluate the presented model. 100.0% accuracies were reached for Cases 4-6. 98.60% and 99.60% accuracies were attained for Cases 1-2. The calculated results, comparisons and findings obviously denoted the success of the presented 1D-CSLBP and NCA based model.

References

- [1] Al Ghayab, H.R., Li, Y., Siuly, S., Abdulla, S. (2019). A feature extraction technique based on tunable Q-factor wavelet transform for brain signal classification. *Journal of Neuroscience Methods*, 312, pp.43–52.
- [2] Kumar, S.P., Sriraam, N., Benakop, P.G. (2008). Automated Detection of Epileptic Seizures Using Wavelet Entropy Feature with Recurrent Neural Network Classifier. *TENCON 2008 - 2008 IEEE Region 10 Conference*, pp.1-5
- [3] Tzimourta, K.D., Tzallas, A.T., Giannakeas, N., Astrakas, L.G., Tsalikakis, D.G., Angelidis, P., Tsipouras, M.G. (2019). A robust methodology for classification of epileptic seizures in EEG signals. *Health and Technology*, 9, pp.135–142.
- [4] Raghu, S., Sriraam, N., Temel, Y., Rao, S.V., Hegde, A.S., Kubben, P.L. (2019). Performance evaluation of DWT based sigmoid entropy in time and frequency domains for automated detection of epileptic seizures using SVM classifier. *Computers in Biology and Medicine*, 110, pp.127–143.
- [5] Gu, X., Zhang, C., Ni, T. (2020). A Hierarchical Discriminative Sparse Representation Classifier for EEG Signal Detection. *IEEE/ACM Transactions on Computational Biology and Bioinformatics*, pp.1-11.
- [6] Ahammed, K., Ahmed, M.U. (2020). Epileptic Seizure Detection Based on Complexity Feature of EEG, *Journal of Biomedical Analytics*, 3(1), pp. 1-11.
- [7] Li, Y., Cui, W.G., Huang, H., Guo, Y.Z., Li, K., Tan T. (2019). Epileptic seizure detection in EEG signals using sparse multiscale radial basis function networks and the Fisher vector approach. *Knowledge-Based Systems*, 164, pp.96–106.
- [8] Tuncer, T., Dogan, S., Ertam, F., Subasi, A. (2020). A novel ensemble local graph structure based feature extraction network for EEG signal analysis. *Biomedical Signal Processing and Control*, 61, pp. 1-15.
- [9] Slimen, I.B., Seddik, H. (2020). Automatic Recognition of Epileptiform EEG Abnormalities Using Machine Learning Approaches. *5th International Conference on Advanced Technologies For Signal and Image Processing*, pp.1-4.
- [10] Pachori, R.B., Patidar, S. (2014). Epileptic seizure classification in EEG signals using second-order difference plot of intrinsic mode functions. *Computer Methods and Programs in Biomedicine*, 113, pp.494–502.
- [11] Juarez-Guerra, E., Alarcon-Aquino, V., Gomez-Gil, P. (2015). Epilepsy Seizure Detection in EEG Signals Using Wavelet Transforms and Neural Networks. *New Trends in Networking, Computing, E-learning, Systems Sciences, and Engineering*, 312, pp.261-269
- [12] Li, S., Zhou, W., Yuan, Q., Geng, S., Cai, D. (2013). Feature extraction and recognition of ictal EEG using EMD and SVM, *Computers in Biology and Medicine*, 43, pp.807–816

- [13] Ramanna, S., Tirunagari, S., Windridge, D. (2020). Epileptic seizure detection using constrained singular spectrum analysis and 1D-local binary patterns. *Health and Technology*, pp.1-11
- [14] Chandaka, S., Chatterjee, A., Munshi, S. (2009). Cross-correlation aided support vector machine classifier for classification of EEG signals. *Expert Systems with Applications*, 36, pp.1329–1336.
- [15] Shoeibi, A., Ghassemi, N., Alizadehsani, R., Rouhani, M., Hosseini-Nejad, H., Khosravi, A., Panahiazar, M., Nahavandi, S. (2020). A comprehensive comparison of handcrafted features and convolutional autoencoders for epileptic seizures detection in EEG signals. *Expert Systems With Applications*, pp.1-17
- [16] Ren, W., Han, M., Wang, J., Wang, D., Li, T. (2016). Efficient Feature Extraction Framework for EEG Signals Classification. *7th International Conference on Intelligent Control and Information Processing*, pp.167-172.
- [17] Guha, A., Ghosh, S., Roy, A., Chatterjee, S. (2020). Epileptic Seizure Recognition Using Deep Neural Network. *Advances in Intelligent Systems and Computing*, 937, pp.21-28.
- [18] Ibrahim, S., Djemal, R., Alsuwailem, A. (2018). Electroencephalography (EEG) signal processing for epilepsy and autism spectrum disorder diagnosis. *Biocybernetics and Biomedical Engineering*, 38, pp.16-26.
- [19] Liu, Y., Lin, Y., Jia, Z., Ma, Y., Wang, J. (2020). Representation based on ordinal patterns for seizure detection in EEG signals. *Computers in Biology and Medicine*, 126, pp.1-13.
- [20] Ren, W., Han, M. (2019). Classification of EEG Signals Using Hybrid Feature Extraction and Ensemble Extreme Learning Machine. *Neural Processing Letters*, 50, pp.1281–1301.
- [21] Tiwari, A.K., Pachori, R.B., Kanhangad, V., Panigrahi, B.K. (2017). Automated Diagnosis of Epilepsy Using Key-Point-Based Local Binary Pattern of EEG Signals. *IEEE Journal Of Biomedical And Health Informatics*, 21(4), pp.888-896.
- [22] Zhang, T., Chen, W., Li, M. (2018). Generalized Stockwell transform and SVD-based epileptic seizure detection in EEG using random forest. *Biocybernetics and Biomedical Engineering*, 38, pp.519 – 534.
- [23] Ibrahim, S., AlSharabi, K., Djemal, R., Alsuwailem A. (2016). An Adaptive Learning Approach for EEG-Based Computer Aided Diagnosis of Epilepsy, *International Seminar on Intelligent Technology and Its Application*, pp.55-60.
- [24] Zazzaro, G., Cuomo, S., Martone, A., Montaquila, R.V., Toraldo, G., Pavone L. (2019). EEG signal analysis for epileptic seizures detection by applying Data Mining techniques. *Internet of Things*, pp.1-14
- [25] Mahmoodian, N., Boese, A., Friebe, M., HDWTadnia, J. (2019). Epileptic seizure detection using cross-bispectrum of electroencephalogram signal. *Seizure: European Journal of Epilepsy*, 66, pp.4–11.
- [26] Das, P., Manikandan, M.S., Ramkumar, B. (2018). Detection of Epileptic Seizure Event in EEG Signals Using Variational Mode Decomposition and Mode Spectral Entropy. *IEEE 13th International Conference on Industrial and Information Systems (ICIIS)*, pp.42-47
- [27] Raghu, S., Sriraam, N., Hegde, A.S., Kubben, P.L. (2019). A novel approach for classification of epileptic seizures using matrix determinant. *Expert Systems With Applications*, 127, pp. 323-341
- [28] Jana, G.C., Sharma, R., Agrawal, A. (2020). A 1D-CNN-Spectrogram Based Approach for Seizure Detection from EEG Signal. *Procedia Computer Science*, 167, pp.403–412
- [29] Li, Y., Liu, Y., Cui, W.G., Guo, Y.Z., Huang, H., Hu, ZY. (2020). Epileptic Seizure Detection in EEG Signals Using a Unified Temporal-Spectral Squeeze-and-Excitation Network. *IEEE Transactions On Neural Systems And Rehabilitation Engineering*, 28(4), pp.782-794.
- [30] Thara, D.K., Premasudha, B.g., Nayak, R.S., Murthy, T.V., Prabhu, G.A., Hanoon, N. (2020). Electroencephalogram for epileptic seizure detection using stacked bidirectional LSTM_GAP neural network. *Evolutionary Intelligence*, pp.1-11
- [31] Jiang, Y., Chen, W., Li, M. (2020). Symplectic geometry decomposition-based features for automatic epileptic seizure detection. *Computers in Biology and Medicine*, 116, pp.1-12.
- [32] Mohammadpoory, Z., Nasrolahzadeh, M., HDWTadnia, J. (2017). Epileptic seizure detection in EEGs signals based on the weighted visibility graph entropy. *Seizure*, 50, pp.202–208.
- [33] Mahmoodian, N., Boese, A., Friebe, M., HDWTadnia, J. (2019). Epileptic seizure detection using cross-bispectrum of electroencephalogram signal. *Seizure: European Journal of Epilepsy*, 66, pp.4–11.
- [34] Yavuz, E., Kasapbaşı, M.C., Eyüpoğlu, C., Yazıcı, R.(2018). An epileptic seizure detection system based on cepstral analysis and generalized regression neural network. *Biocybernetics and Biomedical Engineering*, 38, pp.201-216.
- [35] Sharma, M., Bhurane, A.A., Acharya, U.R. (2018). MMSFL-OWFB: A novel class of orthogonal wavelet filters for epileptic seizure detection. *Knowledge-Based Systems*, 160, pp.265–277.
- [36] Akyol, K. (2020). Stacking ensemble based deep neural networks modeling for effective epileptic seizure detection. *Expert Systems With Applications*, 148, pp.1-9.
- [37] Yuan, Q., Zhou, W., Zhang, L., Zhang, F., Xu, F., Leng, Y., Wei, D., Chen, M. (2017). Epileptic seizure detection based on imbalanced classification and wavelet packet transform. *Seizure*, 50, pp.99–108.
- [38] Zhou, X., Ling, B.W.K., Li, C., Zhao, K. (2020). Epileptic seizure detection via logarithmic normalized functional values of singular values. *Biomedical Signal Processing and Control*, 62, pp.1-12.
- [39] Yuan, Y., Xun, G., Jia, K., Zhang, A. (2017). A Multi-view Deep Learning Method for Epileptic Seizure Detection using Short-time Fourier Transform. *Session 8: Automated Diagnosis and Prediction I ACM-BCB'17*, pp.213-222.
- [40] Hossain, M.S., Amin, S.U., Alsulaman, M., Muhammad, G.(2019). Applying Deep Learning for Epilepsy Seizure Detection and Brain Mapping Visualization. *ACM Trans. Multimedia Comput. Commun. Appl.*, 15(10), pp. 1-10.
- [41] Liu, X., Jiang, A., Xu, N. (2017). Automated Epileptic Seizure Detection in EEGs Using Increment Entropy, *2017 IEEE 30th Canadian Conference on Electrical and Computer Engineering (CCECE)*, pp.1-4.

- [42] Harender, Sharma, R.K. (2017). DWT based Epileptic Seizure Detection from EEG signal using k-NN classifier. International Conference on Trends in Electronics and Informatics, pp.762-765.
- [43] Zhou, M., Tian, C., Cao, R., Wang, B., Niu, Y., Hu, T., Guo, H., Xiang, J. (2018). Epileptic Seizure Detection Based on EEG Signals and CNN. *Frontiers Neuroinform.* 12(95), pp.1-33.
- [44] Li, Y., Liu, Y., Cui, WG., Guo, YZ., Huang, H., Hu, ZY. (2020). Epileptic Seizure Detection in EEG Signals Using a Unified Temporal-Spectral Squeeze-and-Excitation Network. *IEEE Transactions On Neural Systems And Rehabilitation Engineering*, 28(4), pp.782-794.
- [45] Lu, D., Triesch, J. (2019) Residual Deep Convolutional Neural Network for EEG Signal Classification in Epilepsy. eprint arXiv:1903.08100, pp.1-11.
- [46] Orhan, U., Hekim, M., Ozer, M. (2011). Eeg signals classification using the k-means clustering and a multilayer perceptron neural network model. *Expert Syst. Appl.*, 38(10), pp.13475–13481.
- [47] Hassan, A.R., Subasi, A., Zhang, Y. (2020). Epilepsy seizure detection using complete ensemble empirical mode decomposition with adaptive noise. *Knowledge-Based Systems*, pp.1-12.
- [48] Acharya, U.R., Sree, S.V., Ang, P.C.A., Yanti, R., Suri, J.S. (2012). Application of nonlinear and wavelet based features for the automated identification of epileptic eeg signals. *Int. J. Neural Syst.* 22(02), pp.1-14.
- [49] Kaya, Y., Uyar, M., Tekin, R., Yıldırım, S. (2014). 1d-local binary pattern based feature extraction for classification of epileptic eeg signals, *Appl. Math. Comput.* 243, pp.209–219.
- [50] Siuly, S., Li, Y., Wen, P. (2011). Clustering technique-based least square support vector machine for eeg signal classification. *Comput. Methods Programs Biomed.*, 104(3), pp.358–372.

Novel Fuzzy Kernels Based Local Binary Pattern And Local Graph Structure Methods

Serkan METİN^{1*}, Şengül DOĞAN²

¹ Department Of Management Information Systems, Faculty of Social Sciences and Humanities, Malatya Turgut Özal University, Malatya, Turkey

² Department of Digital Forensics Engineering, Technology Faculty, Firat University, Elazığ, Turkey

*¹ serkan.metin@ozal.edu.tr, ² sdogan@firat.edu.tr

(Geliş/Received: 11/02/2021;

Kabul/Accepted: 15/02/2021)

Abstract: Local descriptors are the most effective textural image recognition methods. Local descriptors generally consist of two phases. These are binary feature coding and histogram extraction phases, and they often use the signum function for the binary feature extraction. In this article, new fuzzy-based mathematical kernels are proposed for binary feature encoding in local descriptors. Fuzzy kernels consist of membership degree calculation and coding these membership degrees. In order to calculate membership degrees, four fuzzy sets are utilized. The proposed fuzzy kernels are considered as binary feature-extraction functions, and a novel textural image recognition architecture is created using these fuzzy kernels. These architecture phases are; (1) binary feature coding with fuzzy kernels, (2) calculating lower and upper images, (3) histogram extraction, (4) feature reduction with maximum pooling, (5) classification. In the classification phase, a quadratic kernel-based support vector machine (SVM) classifier is utilized. The presented fuzzy kernels are implemented on the Local Binary Pattern (LBP) and Local Graph Structure (LGS). 16 novel methods are presented using fuzzy kernels for each descriptor. In this article, LBP and LGS are used, and 32 novel fuzzy-based methods are proposed to improve recognition capability. 3 facial images and 3 textural image datasets are used to evaluate the methods' performance. The experimental results clearly illustrate that the fuzzy kernels based LBP and LGS methods have high facial and textural image recognition capability.

Keywords: Fuzzy coding, local binary pattern, local graph structure, texture recognition, face recognition, biometrics.

Yeni Bulanık Çekirdeklere Dayalı Yerel İkili Desen ve Yerel Grafik Yapısı Yöntemleri

Öz: Yerel tanımlayıcılar, en etkili dokusal görüntü tanıma yöntemleridir. Yerel tanımlayıcılar genellikle iki aşamadan oluşur. Bunlar ikili özellik kodlama ve histogram çıkarma aşamalarıdır ve genellikle ikili özellik çıkarımı için işaret işlevini kullanırlar. Bu makalede, yerel tanımlayıcılarda ikili özellik kodlaması için yeni bulanık tabanlı matematiksel çekirdekler önerilmiştir. Bulanık çekirdekler, üyelik derecesi hesaplaması ve bu üyelik derecelerinin kodlanmasından oluşur. Üyelik derecelerini hesaplamak için dört bulanık küme kullanılır. Önerilen bulanık çekirdekler, ikili özellik çıkarma işlevleri olarak kabul edilir ve bu bulanık çekirdekler kullanılarak yeni bir dokusal görüntü tanıma mimarisi oluşturulur. Bu mimari aşamalar; (1) bulanık çekirdekli ikili özellik kodlaması, (2) alt ve üst görüntülerin hesaplanması, (3) histogram çıkarma, (4) maksimum havuzlama ile özellik azaltma, (5) sınıflandırma. Sınıflandırma aşamasında, ikinci dereceden çekirdek tabanlı bir destek vektör makinesi (SVM) sınıflandırıcısı kullanılır. Sunulan bulanık çekirdekler, Yerel İkili Model (LBP) ve Yerel Grafik Yapısı (LGS) üzerinde uygulanmaktadır. Her tanımlayıcı için bulanık çekirdekler kullanılarak 16 yeni yöntem sunulmaktadır. Bu makalede, LBP ve LGS kullanılmış ve tanıma yeteneğini geliştirmek için 32 yeni bulanık tabanlı yöntem önerilmiştir. Yöntemlerin performansını değerlendirmek için 3 yüz görüntüsü ve 3 dokusal görüntü veri kümesi kullanılır. Deneysel sonuçlar, bulanık çekirdeklere dayalı LBP ve LGS yöntemlerinin yüksek yüz ve dokusal görüntü tanıma kapasitesine sahip olduğunu açıkça göstermektedir.

Anahtar kelimeler: Bulanık kodlama, yerel ikili desen, yerel grafik yapısı, doku tanıma, yüz tanıma, biyometri.

1. Introduction

Texture image recognition is used in many areas such as the face, iris, facial expression, perceptual hashing, wood, palm, etc. [1-3]. These methods generally consist of pre-processing, feature extraction, and classification stages, and local descriptors are commonly used in the feature extraction phase [4]. The first known local descriptors are LBP. LBP uses 3 x 3 non-overlapping blocks and signum function to extract textural features [5, 6]. LBP generally consists of two main stages, and these are binary feature coding and histogram extraction. This histogram is utilized as a feature of the image. LBP is often used in the literature because it provides many advantages in textural image analysis. The advantages of LBP are as follows [7-9].

- 1- LBP can be easily programmed.

* Corresponding author: serkan.metin@ozal.edu.tr. ORCID Number of authors: ¹ 0000-0003-1765-7474, ² 0000-0001-9677-5684

- 2- LBP is well discriminator.
- 3- LBP has a short execution time.
- 4- LBP can be easily applied in real-time applications.

These advantages indicate that LBP is an effective textural image operator. Therefore, many LBP-like local patterns have been proposed in the literature. When 8-bit features are extracted by using LBP, 4-bit features are extracted by using Center Symmetric Local Binary Pattern (CSLBP), and 9 bits are extracted by using Local Quadruple Pattern (LQPAT) [10, 11]. Therefore, feature sets of 16, 256, and 512 dimensions are obtained using these textural operators. Recognition and classification operations are performed by using the acquired features. These methods consist of binary pattern coding and histogram extraction sections as LBP. In addition, there are graph-based micropatterns in the literature. The first known method is LGS (Local Graph Structure) method. Several methods such as SLGS (Symmetric LGS), ELGS (Extended LGS), VLGS (Vertical LGS), VSLGS (Vertical Symmetric LGS) were presented after the high performance achieved by the LGS method [12-14]. The majority of the LGS and LBP-based methods use the signum function, and they only aim to improve the recognition performance by changing pattern shapes [15].

In this article, fuzzy-based binary feature extraction functions are proposed to improve the performance of local descriptors. These are called fuzzy kernels in this article, and the technical contribution of the proposed method is as follows.

- 4 novel binary feature extraction functions are presented using 4 fuzzy sets.
- A novel textural image recognition architecture is proposed in this article. 16 different feature extraction methods were obtained for each descriptor using this architecture.
- In this article, fuzzy kernels are applied to the LBP and LGS. The main purpose of using LBP and LGS is to be widely used in the literature. The effect of fuzzy on LBP and LGS are analyzed in detail.
- 6 databases were used to test the proposed methods' performance, and these databases consist of textural and facial images. The performances of the proposed methods are tested in both facial and textural image recognition using these databases.

2. Related Works

Related work has been mentioned in this part of the article. These are the local descriptors previously proposed in the literature. These are LBP and LGS. These methods are mentioned respectively. In the proposed method, the mathematical structure of these descriptors is changed [12-14].

2.1. Local Binary Pattern

LBP is the first local descriptor, and it was presented in 1996. This method consists of two main phases, and these are binary feature coding and histogram extraction. LBP uses 3 x 3 size blocks to extract textural features of the images. This is the main descriptor, and it has several variations in the literature. The LBP is summarized graphically in Fig. 1 [5].

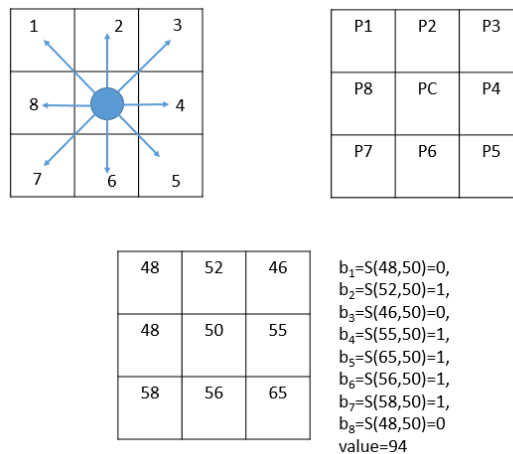


Figure 1. Graphical outline of LBP.

As shown in Fig. 1, LBP uses the signum function to extract binary features. The mathematical definition of the signum function is given in Eq. 1.

$$S(a, b) = \begin{cases} 0, & a - b < 0 \\ 1, & a - b \geq 0 \end{cases} \quad (1)$$

Also, a mathematical description of the LBP is given in Eq. 2-6.

$$LBP_{i,j}^1 = S(p_{i,j}, p_{i+1,j+1}) \times 128 + S(p_{i,j+1}, p_{i+1,j+1}) \times 64 \quad (2)$$

$$LBP_{i,j}^2 = S(p_{i,j+2}, p_{i+1,j+1}) \times 32 + S(p_{i+1,j+2}, p_{i+1,j+1}) \times 16 \quad (3)$$

$$LBP_{i,j}^3 = S(p_{i+2,j+2}, p_{i+1,j+1}) \times 8 + S(p_{i+2,j+1}, p_{i+1,j+1}) \times 4 \quad (4)$$

$$LBP_{i,j}^4 = S(p_{i+2,j}, p_{i+1,j+1}) \times 2 + S(p_{i+1,j}, p_{i+1,j+1}) \quad (5)$$

$$LBP_{i,j} = LBP_{i,j}^1 + LBP_{i,j}^2 + LBP_{i,j}^3 + LBP_{i,j}^4 \quad (6)$$

where, p is the pixel of the image, S is signum function, $BP_{i,j}^k, k = \{1,2,3,4\}$ 2-bit values of the LBP and $LBP_{i,j}$ defines LBP value of the 3 x 3 size of block [16, 17].

2.2. Local Graph Structure

LGS is a graph-based descriptor. It is similar to LBP. The main purpose of the LGS is to extract dominant feature using graphs. This operator uses 3 x 4 size of block and signum function like LBP to extract feature. In Fig. 2, LGS is summarized as graphically [13, 18].

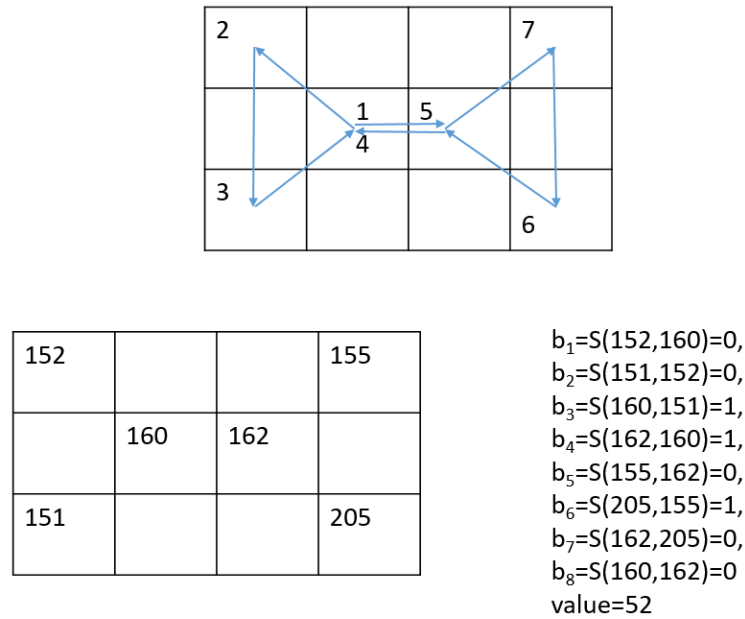


Figure 2. Graphical outline of LGS.

Mathematical definition of LGS is given in Eq. 7-11.

$$LGS_{i,j}^1 = S(p_{i,j}, p_{i+1,j+1}) \times 128 + S(p_{i,j+1}, p_{i,j+2}) \times 64 \quad (7)$$

$$LGS_{i,j}^2 = S(p_{i,j}, p_{i,j+2}) \times 32 + S(p_{i+1,j+2}, p_{i+1,j+1}) \times 16 \quad (8)$$

$$LGS_{i,j}^3 = S(p_{i,j+3}, p_{i+1,j+2}) \times 8 + S(p_{i+2,j+3}, p_{i,j+3}) \times 4 \quad (9)$$

$$LGS_{i,j}^4 = S(p_{i+1,j+2}, p_{i+2,j+3}) \times 2 + S(p_{i+1,j+1}, p_{i+1,j+2}) \quad (10)$$

$$LGS_{i,j} = LGS_{i,j}^1 + LGS_{i,j}^2 + LGS_{i,j}^3 + LGS_{i,j}^4 \quad (11)$$

Where $LGS_{i,j}^k, k = \{1,2,3,4\}$ 2-bit values of the LGS and $LGS_{i,j}$ defines LGS value of the 3×4 size of block [12, 19].

3. The Fuzzy-Based Binary Feature Extraction Functions

4 fuzzy functions are used in this article to extract binary features. These functions consist of two phases. These are;

1. Calculation membership degree,
2. Coding.

The presented fuzzy functions are explained below.

3.1. Triangle Function

One of the basic fuzzy sets is the triangle and is widely used in the literature. This set is given below.

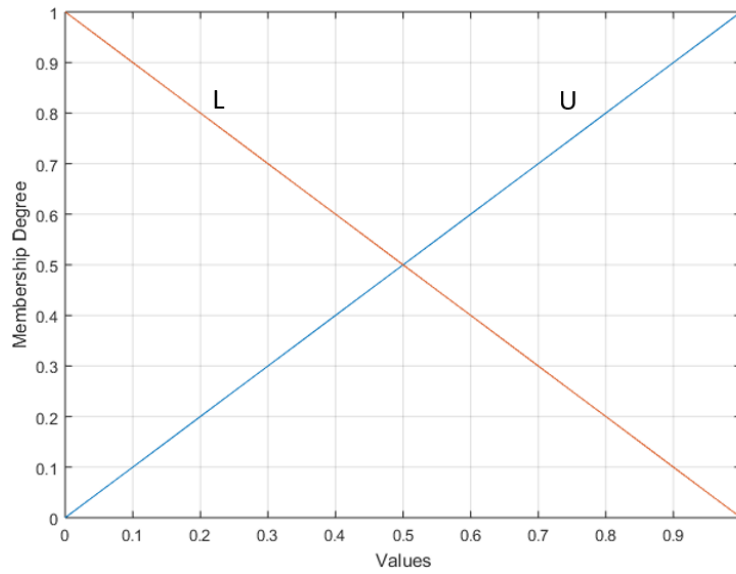


Figure 3. The used triangle fuzzy set.

The used triangle fuzzy set is shown in Fig. 3. The function obtained by using this set is called as $\text{tri}(\cdot)$ in this article, and the mathematical definition of the $\text{tri}(\cdot)$ is given in Eq. 12-13.

$$L = \begin{cases} 0, & x > 0.5 \\ 1, & x \leq 0.5 \end{cases} \quad (12)$$

$$U = \begin{cases} 1, & x \geq 0.5 \\ 0, & x < 0.5 \end{cases} \quad (13)$$

3.2. Trapezoid Function

Trapezoid function one of the widely used fuzzy sets. Therefore, this set is used in this article. A function is created by using these sets, and it is called as $\text{trap}(\cdot)$ in this article. The fuzzy set used to create this function is shown in Fig. 4.

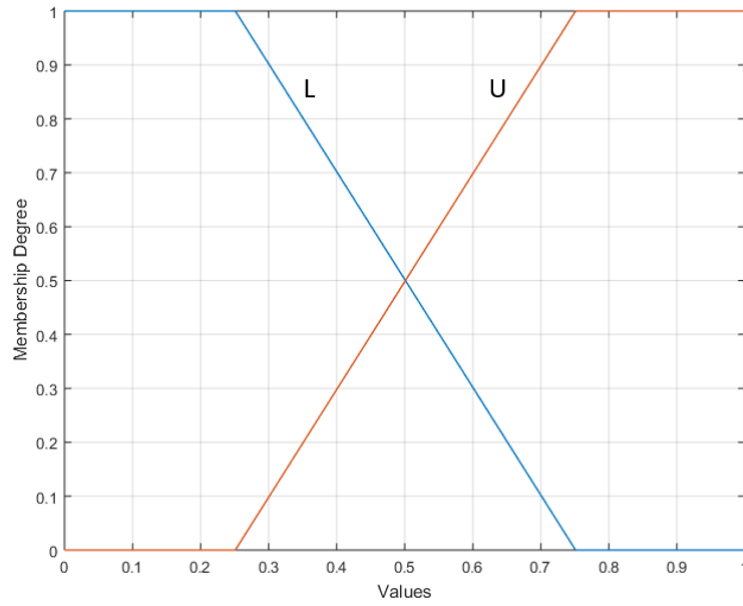


Fig. 4. The used trapezoid fuzzy set.

The mathematical definition of the trap(.) function is given in Eq. 14-15.

$$L = \begin{cases} 1, & x \leq 0.25 \text{ and } 0.5 < x \leq 0.75 \\ 0, & 0.25 < x \leq 0.5 \end{cases} \quad (14)$$

$$U = \begin{cases} 1, & x \geq 0.5 \\ 0, & x < 0.5 \end{cases} \quad (15)$$

3.3. Stair Function

In this section, a novel fuzzy set is obtained by modifying the trapezoid fuzzy set, and this function is called a stair. The trapezoid fuzzy set used by stair function is shown in Fig. 5.

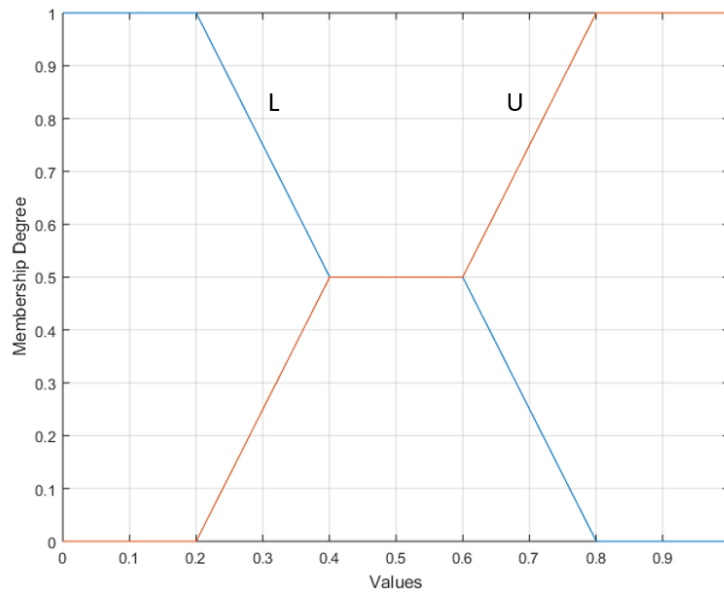


Figure 5. The used stair fuzzy set.

The mathematical definition of the stair(.) function is given Eq. 16-17.

$$L = \begin{cases} 1, & x \leq 0.6 \\ 0, & x > 0.6 \end{cases} \quad (16)$$

$$U = \begin{cases} 1, & x \geq 0.4 \\ 0, & x < 0.4 \end{cases} \quad (17)$$

3.4. Butterfly Function

Here, this function is called a butterfly because it looks like a butterfly shape. This fuzzy set is a modified version of the trapezoid fuzzy set. This function is called as but(.), and the graphical outline of this set is shown in Fig. 6.

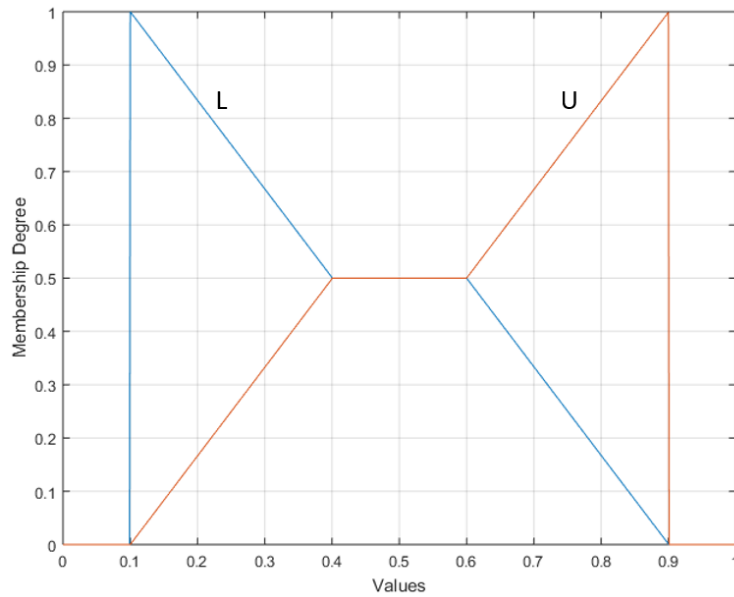


Figure 6. The fuzzy set of butterfly function.

The mathematical definition of the but(.) is given in Eq. 18-19.

$$L = \begin{cases} 1, & 0.1 < x \leq 0.6 \\ 0, & x \leq 0.1 \text{ and } x \geq 0.9 \end{cases} \quad (18)$$

$$U = \begin{cases} 1, & 0.4 < x \leq 0.9 \\ 0, & x < 0.4 \text{ and } x > 0.9 \end{cases} \quad (19)$$

4. The Proposed Fuzzy-Based Descriptors

In this paper, 4 novel fuzzy kernels are presented to increase the recognition rate. The proposed kernels are applied to descriptors that are widely used in the literature and have multiple variations. There are LBP and LGS. Also, a novel textural image recognition architecture for LBP and LGS is proposed in this article, and 32 novel methods are presented using this architecture. This architecture consists of lower and upper image calculation using fuzzy kernels, histogram extraction, using maximum pooling for feature reduction and classification. The general block diagram of the presented architecture is shown in Fig. 7 [20].

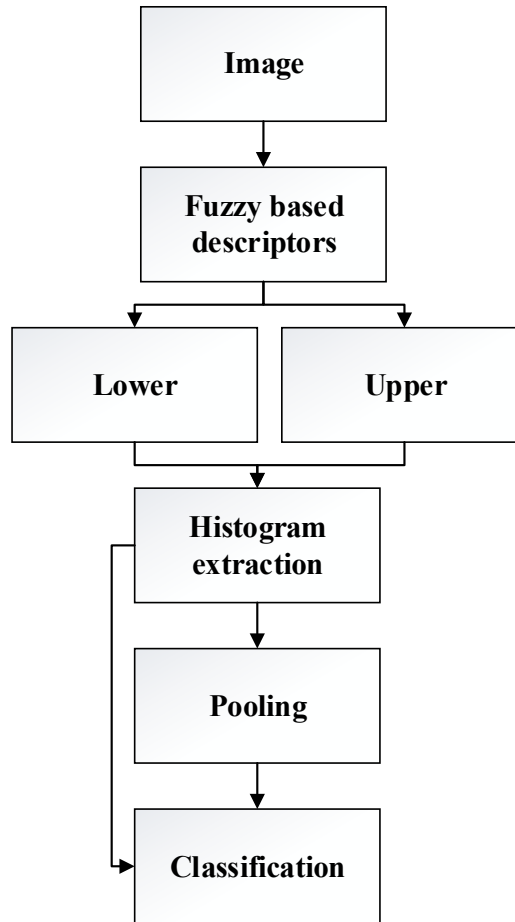


Figure 7. Block diagram of the proposed fuzzy architecture.

The steps of the presented architecture are given below.

Step 1: Load image.

Step 2: Choose LBP or LGS pattern.

Step 3: Calculate differences of neighborhood pixels.

Step 4: Select one of the fuzzy function to extract binary features of the image.

Step 5: Extract histograms.

Step 6: Reduce feature using pooling. This step is used for the pooled method.

The pseudocode of the used maximum pooling is given Algorithm 1.

Algorithm 1. Maximum pooling

Input: The feature vector is f with the size of 512.

Output: Pooled feature vector is pf with the size of 256.

```

1: counter=1;
2: for  $i=1$  to 512 steps by 2 do
3:    $block_1 = f_i$ 
4:    $block_2 = f_{i+1}$ 
5:    $pf_{counter} = \max(block)$ 
6:    $counter = counter + 1$ 
7: endfor
    
```

Step 7: Classify these features.

The methods given above are outlined in the sub-sections of this chapter, and abbreviation of the methods and images are listed in Table 1.

Table 1. Abbreviation of the methods and images.

No	Name	Abbreviation	Dimension
1	Lower image	L	M x N
2	Upper image	U	M x N
3	Fuzzy LBP	FLBP	512
4	Fuzzy LBP of L	FLBPL	256
5	Fuzzy LBP of U	FLBPU	256
6	Pooled fuzzy LBP	PFLBP	256
7	Fuzzy LGS	FLGS	512
8	Fuzzy LGS of L	FLGSL	256
9	Fuzzy LGS of U	FLGSU	256
10	Pooled fuzzy LGS	PFLGS	256

In Table 1, M and N are the width and height of the cover image.

4.1. Fuzzy LBP

LBP is the most frequently used and most variant local descriptor in the literature. The general steps of the proposed fuzzy LBP methods are as follows.

Step 1: Load image.

Step 2: Divide the image into 3 x 3 size blocks.

Step 3: Calculate differences array using Eq. 20.

$$\begin{aligned}
 f_1 &= I_{i,j} - I_{i+1,j+1}, f_2 = I_{i,j+1} - I_{i+1,j+1}, \\
 f_3 &= I_{i,j+2} - I_{i+1,j+1}, f_4 = I_{i+1,j} - I_{i+1,j+1} \\
 f_5 &= I_{i+1,j+2} - I_{i+1,j+1}, f_6 = I_{i+2,j} - I_{i+1,j+1}, \\
 f_7 &= I_{i+2,j+1} - I_{i+1,j+1}, f_8 = I_{i+2,j+2} - I_{i+1,j+1}
 \end{aligned} \tag{20}$$

f vector defines differences of neighborhood pixels.

Step 4: Normalize these differences.

$$x = \frac{f - f_{min}}{f_{max} - f_{min}} \tag{21}$$

where x vector defines normalized differences.

Step 5: Calculate the lower and upper values of this block. These are $tri(\cdot)$, $tra(\cdot)$, $stair(\cdot)$ and $but(\cdot)$

$$[L, U] = \text{fuzzy function}(x) \tag{22}$$

Where $\text{fuzzy function}(x)$ defines $tri(x)$, $trap(x)$, $stair(x)$ or $but(x)$.

Step 6: Extract histogram of L and U.

Step 7: In FLBP (Fuzzy LBP), combine histograms of the L and U, use histogram of L for FLBPL, use histogram of U FLBPU, and finally use maximum pooling for PFLBPB (Pooled FLBP).

4.2. Fuzzy LGS

LGS is the first well-known graph-based texture operator in the literature and uses the signum function for binary feature extraction. New fuzzy LGSs are proposed using fuzzy functions in this article. The proposed fuzzy LGS steps are as follows.

Step 1: Load image.

Step 2: Divide the image into 3 x 4 size overlapping blocks.

Step 3: Calculate differences vector using Eq. 23.

$$\begin{aligned}
f_1 &= I_{i+1,j+1} - I_{i,j}, f_2 = I_{i,j} - I_{i+2,j}, \\
f_3 &= I_{i+2,j} - I_{i+1,j+1}, f_4 = I_{i+1,j+1} - I_{i+1,j+2} \\
f_5 &= I_{i+1,j+2} - I_{i,j+3}, f_6 = I_{i,j+3} - I_{i+2,j+3}, \\
f_7 &= I_{i+2,j+3} - I_{i+1,j+2}, f_8 = I_{i+1,j+2} - I_{i+1,j+1}
\end{aligned} \tag{23}$$

Step 4: Normalize differences using Eq. 14.

Step 5: Calculate L and H images using Eq. 15.

Step 6: Extract histogram of the L and U.

Step 7: Use the selected feature.

5. Experimental Results and Discussions

In this article, six databases were used to test the performance of fuzzy coding-based methods. Three of these databases are face datasets, and the other three are texture datasets. The properties of the used datasets are given in Table 2 [21-24].

Table 2. The attributes of the facial and textural databases for performance evaluation.

No	Database Name	Classes	Samples	Total	Resolution	Format	Type
1	AT&T	30	10	300	92 x 112	JPEG	Face
2	Face94	30	10	300	180 x 200	JPEG	Face
3	AR	31	10	310	768 x 576	RAW	Face
4	Outex TC 00000	24	20	480	128 x 128	RAS	Texture
5	Outex TC 00001	24	88	2112	64 x 64	RAS	Texture
6	Outex TC 00013	68	20	1360	128 x 128	BMP	Texture

Performance analyzes were carried out using the above 6 different databases. Accuracy (Acc) was used to obtain the experimental results. The mathematical definition of Acc is given in Eq. 24 [25].

$$Acc (\%) = \frac{\text{Number of true predicted samples}}{\text{Number of total samples}} \times 100 \tag{24}$$

In the final phase, the quadratic kernel Support Vector Machine (SVM) [26, 27] was used to classify the methods. The attributes of the SVM are listed in Table 3.

Table 3. Attributes of the SVM

Cross-validation folds	10
Kernel function	Quadratic
Kernel scale	Automatic
Box constraint level	1
PCA	Disable
Multiclass method	One vs All
Standardize data	True

5.1. Experiments of LBP and Fuzzy coding based LBPs

In this article, 16 novel fuzzy LBP methods are proposed using 4 fuzzy kernels. In this section, the fuzzy LBP method was evaluated, and the experiments of the LBP were discussed. These experiments are listed in Table 4.

Table 4. Performance analysis of LBP methods

		FLBP	FLBPL	FLBPU	PFLBP	LBP
Triangle	1	92.3	86.7	90.7	90.0	75.3
	2	99.3	99.0	99.3	99.3	98.3
	3	91.3	89.7	91.0	93.2	92.9
	4	99.8	99.8	99.8	99.8	99.7
	5	98.7	98.5	98.7	98.6	98.4
	6	79.3	77.4	78.7	82.3	78.2
Trapezoid	1	92.3	90.0	93.7	94.3	75.3
	2	99.3	99.3	99.0	99.7	98.3
	3	91.3	97.1	91.0	95.5	92.9
	4	99.8	99.4	99.8	99.4	99.7
	5	98.7	95.9	98.7	98.1	98.4
	6	79.3	74.3	78.7	80.2	78.2
Stair	1	92.3	84.0	89.0	93.0	75.3
	2	99.3	97.7	96.3	98.0	98.3
	3	91.3	94.8	91.3	96.8	92.9
	4	99.8	99.8	99.8	99.8	99.7
	5	98.7	97.9	98.2	98.7	98.4
	6	79.3	76.4	75.9	81.0	78.2
Butterfly	1	93.3	90.3	88.0	92.7	75.3
	2	98.0	98.0	98.0	98.0	98.3
	3	94.8	94.2	91.0	94.2	92.9
	4	100	100	99.8	100	99.7
	5	99.5	99.0	99.2	99.2	98.4
	6	81.8	79.3	78.6	82.1	78.2

In Table 4, the best values are shown in bold font. If FLBP, FLBPL, FLBPU, and PFLBP are evaluated, the best 11 values in FLBP, 4 best values in FLBPL, 5 best values in FLBPU, 14 best values in PFLBP, and 2 best values in LBP are obtained. It has been observed that the proposed methods have a positive effect on the face and textural image recognition phase. The Fig.8. show the comparison of fuzzy kernels graphically.

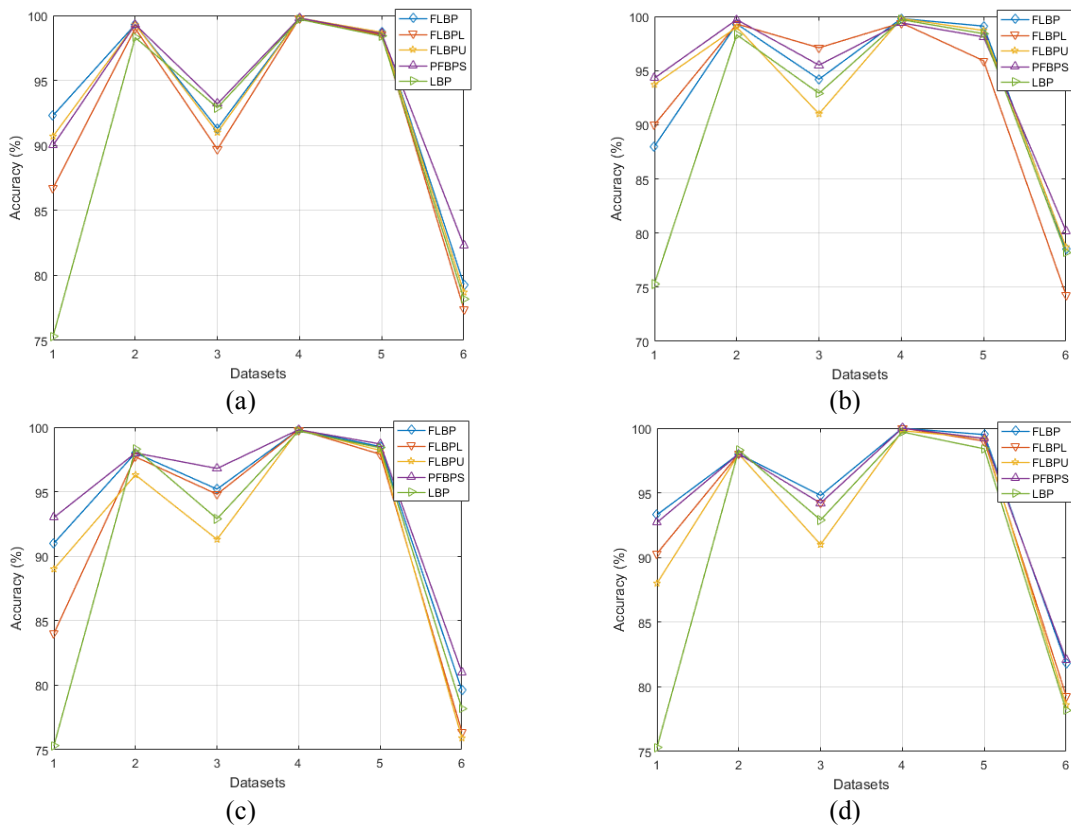


Figure 8. Performance comparison of the fuzzy functions based LBPs and LBP (a) triangle function based LBPs and LBP (b) trapezoid function based LBPs and LBP (c) stair function based LBPs and LBP (d) butterfly function LBPs and LBP.

As shown in Fig. 8, it is generally observed that the butterfly kernel-based FLBP method is more successful than the other methods. In addition, boxplot analyzes of triangle, trapezoid, stair, and butterfly functions were performed. The results are shown in Fig. 9.

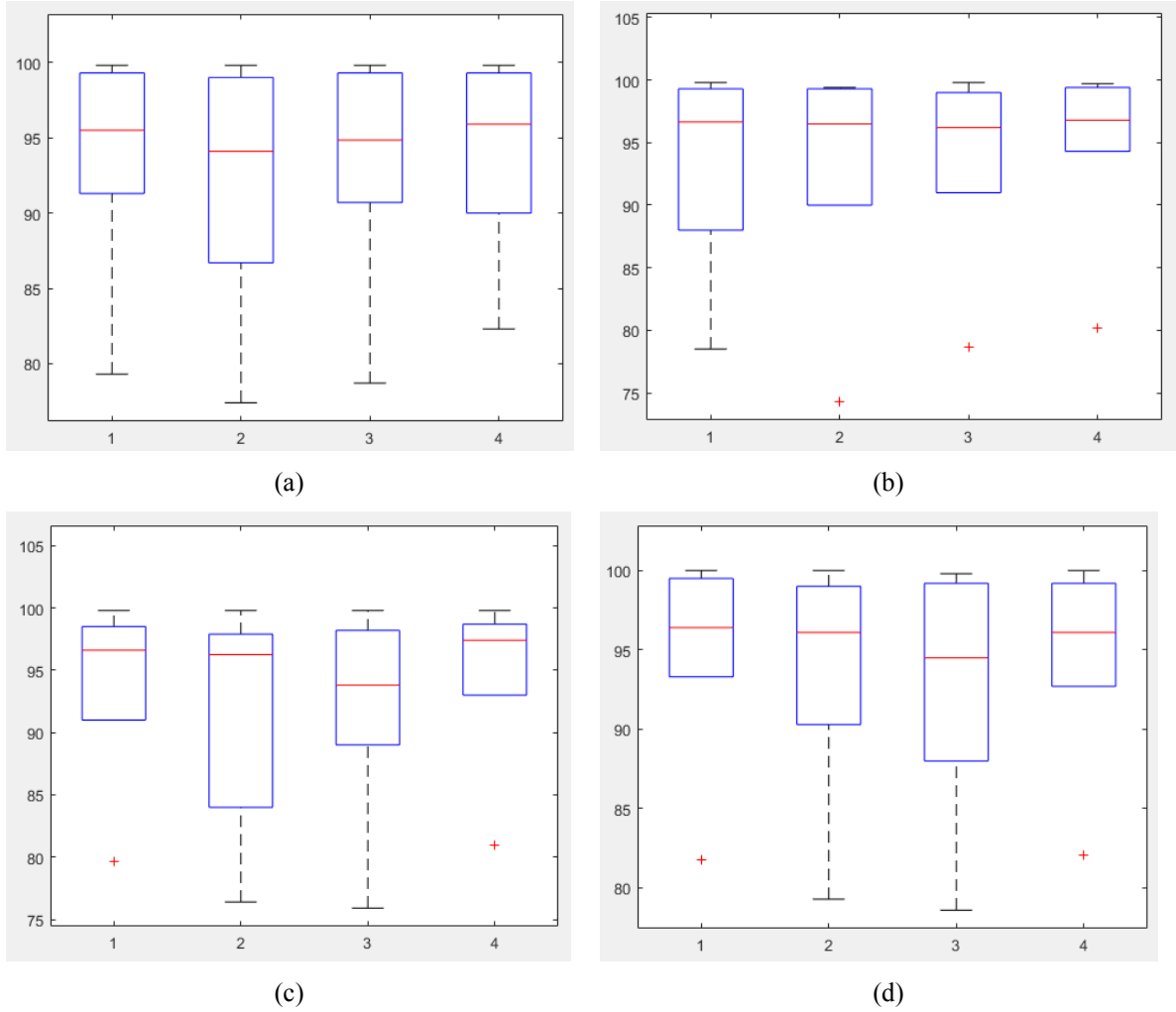


Figure 9. Boxplot analysis of fuzzy coding based LBPs (a) Triangle function based LBPs (b) Trapezoid function LGSs (c) Stair function based LGSs (d) Butterfly function based LGSs.

The performance of the 4 fuzzy functions used is evaluated. The average performance of fuzzy coding based LBP methods for the 6 databases used is given in Table 5.

Table 5. The average accuracy of the fuzzy function for LBP.

Triangle	Trapezoid	Stair	Butterfly
93.05	93.45	92.93	93.71

The average performance of the Signum kernel LBP method for 6 databases is calculated as 90.47%. As a result, all fuzzy kernels have a positive effect on the recognition of the LBP.

5.2. Experiments of LGS and Fuzzy coding based LGSs

LGS is the first known, frequently used, and most variant graph-based descriptor in the literature. Experimental results of proposed fuzzy-based LGS methods are given in this section.

Table 6. Performance analysis of LGS methods

		FLGS	FLGSL	FLGSU	PFLGS	LGS
Triangle	1	95.7	94.3	92.0	93.7	92.3
	2	100.0	100.0	100.0	100.0	99.0
	3	97.4	96.8	97.1	97.1	96.8
	4	100.0	100.0	99.6	99.6	99.7
	5	98.9	98.6	98.4	98.8	98.0
	6	79.8	79.7	78.5	80.3	79.6
Trapezoid	1	95.0	83.0	81.3	93.0	92.3
	2	100.0	99.7	99.7	100.0	99.0
	3	97.4	95.8	94.2	98.1	96.8
	4	100.0	99.8	99.6	100.0	99.7
	5	98.8	98.2	95.5	98.1	98.0
	6	77.8	80.1	70.4	76.3	79.6
Stair	1	89.3	90.7	91.0	87.7	92.3
	2	100.0	100.0	100.0	100.0	99.0
	3	97.1	94.5	94.5	97.4	96.8
	4	100.0	99.8	100.0	100.0	99.7
	5	98.5	98.5	97.7	98.7	98.4
	6	78.1	76.3	76.8	82.6	79.6
Butterfly	1	96.3	93.3	91.3	95.3	92.3
	2	100.0	100.0	100.0	100.0	99.0
	3	97.4	95.8	94.8	97.7	96.8
	4	100.0	100.0	100.0	100.0	99.7
	5	99.0	98.2	98.5	99.1	98.0
	6	79.9	79.0	77.1	78.5	79.6

In Table 6, the best values are shown in bold font. If FLGS, FLGSL, FLGSU, and PFLGS are evaluated, the best 15 values in FLGS, 6 best values in FLGSL, 6 best values in FLGSU, and 13 best values in PFLGS are obtained. Performance comparisons of the fuzzy kernel-based LGS methods and LGS are shown in Fig. 10. According to the results of databases, the best score is achieved for the butterfly kernel-based FLGS method.

In addition, boxplot analyzes of triangle, trapezoid, stairs, and butterfly functions were performed, and the results of these are shown in Fig. 11.

The performance of the 4 fuzzy functions is evaluated. The average performance of fuzzy kernel-based LGS methods for the 6 databases is listed in Table 7.

Table 7. The average accuracy of the fuzzy function for LGS methods.

Triangle	Trapezoid	Stair	Butterfly
94.85	92.99	93.72	94.63

The average performance of Signum kernel LGS method for 6 databases is calculated as 94.23%. It has been observed that the triangle and butterfly function has a positive effect on LGS.

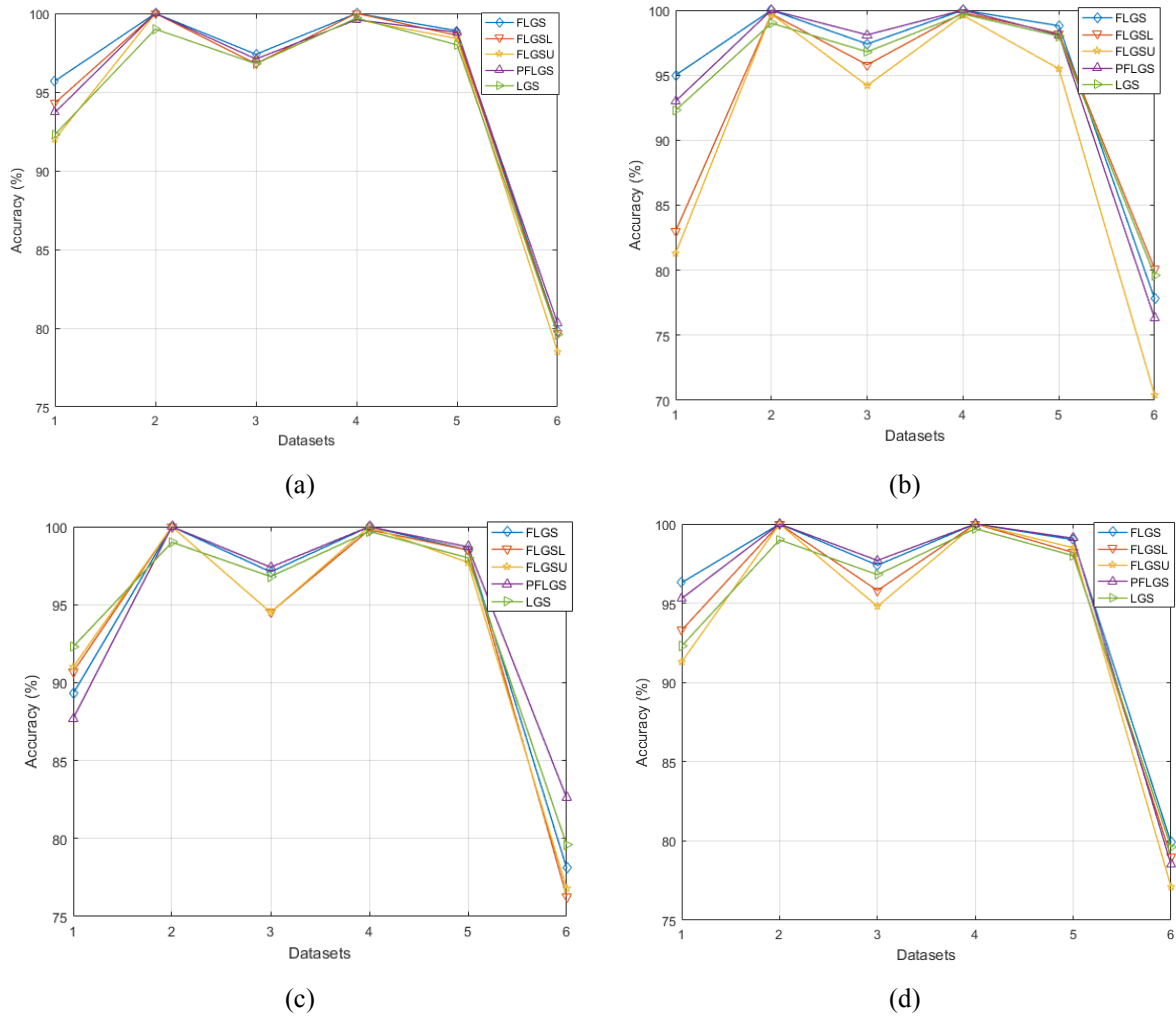


Figure 10. Performance comparison of the fuzzy functions based LGSs and LGS (a) triangle function based LGSs and LGS (b) trapezoid function based LGSs and LGS (c) stair function based LGSs and LGS (d) butterfly function LGSs and LGS.

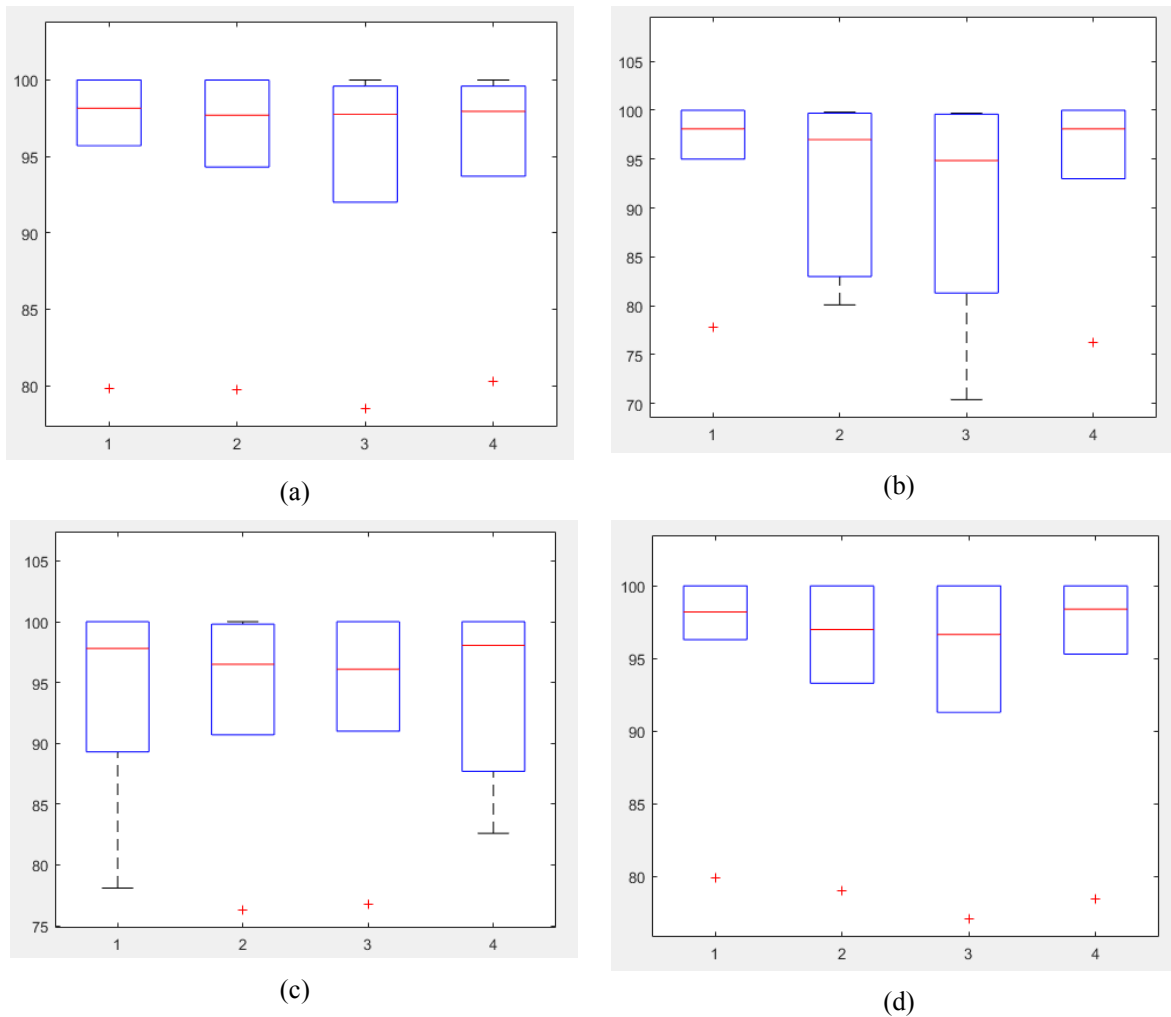


Figure 11. Boxplot analysis of fuzzy kernel-based LGS methods (a) Triangle function based LGSs (b) Trapezoid function LGSs (c) Stair function based LGSs (d) Butterfly function based LGSs.

6. Conclusions and recommendations

In this study, a new fuzzy-based texture image recognition architecture is presented. In this architecture, binary feature extraction is performed using fuzzy-based functions instead of signum function. Fuzzy-based functions are design using fuzzy sets and rules. Triangle and trapezoid fuzzy sets are widely used in the literature. Stair and butterfly fuzzy sets are presented as modifications of the trapezoid fuzzy set in this study. Fuzzy kernels are proposed using these fuzzy sets. The proposed fuzzy kernels are applied to LBP and LGS methods, and 16 new descriptors are defined for each method. The performance of the proposed methods is tested using 3 face databases (AT & T, Face94, AR) and 3 texture databases (Outex TC 00000, Outex TC 00001, Outex TC 00013). The average accuracy rate is calculated as 90.47 with signum kernel-based LBP. In fuzzy kernel-based LBP, the average accuracy rates for the triangle, trapezoid, stair, butterfly are assessed as 93.05, 93.45, 92.93, 93.71, respectively, for all databases used in the study. The average accuracy rate is 94.23 with signum kernel-based LGS. In fuzzy kernel-based LGS, the average accuracy rates are 94.85, 92.99, 93.72, 94.63, respectively. Also, the best methods are butterfly kernel FLBP and FLGS methods. When the results are evaluated, all fuzzy kernels are observed to improve the recognition rate of LBP. The recognition rates of the triangle and butterfly fuzzy kernels increase in LGS. At the same time, experimental results and discussions clearly show that fuzzy coding has a positive effect on both methods. It is shown in this article that new fuzzy coding methods can be developed using different fuzzy kernels in future studies, and these methods can be applied to other local descriptors in the literature.

References

- [1] Li J, Sang N, Gao C. LEDTD: Local edge direction and texture descriptor for face recognition. *Signal Processing: Image Communication*. 2016;41:40-5.
- [2] Nguyen K, Fookes C, Jillela R, Sridharan S, Ross A. Long range iris recognition: A survey. *Pattern Recognition*. 2017;72:123-43.
- [3] Lekdioui K, Messoussi R, Ruichek Y, Chaabi Y, Touahni R. Facial decomposition for expression recognition using texture/shape descriptors and SVM classifier. *Signal Processing: Image Communication*. 2017;58:300-12.
- [4] Qin C, Chen X, Luo X, Zhang X, Sun X. Perceptual image hashing via dual-cross pattern encoding and salient structure detection. *Information Sciences*. 2018;423:284-302.
- [5] Ojala T, Pietikainen M, Maenpaa T. Multiresolution gray-scale and rotation invariant texture classification with local binary patterns. *IEEE Transactions on pattern analysis and machine intelligence*. 2002;24:971-87.
- [6] Ojala T, Pietikainen M, Harwood D. A comparative study of texture measures with classification based on featured distributions. *Pattern recognition*. 1996;29:51-9.
- [7] Ojala T, Valkealahti K, Oja E, Pietikainen M. Texture discrimination with multidimensional distributions of signed gray-level differences. *Pattern Recognition*. 2001;34:727-39.
- [8] Zhou H, Wang R, Wang C. A novel extended local-binary-pattern operator for texture analysis. *Information Sciences*. 2008;178:4314-25.
- [9] Fathi A, Naghsh-Nilchi AR. Noise tolerant local binary pattern operator for efficient texture analysis. *Pattern Recognition Letters*. 2012;33:1093-100.
- [10] Pei H, Yanqing S, Chaowei T, Siman Z. Center-symmetric local binary pattern based on weighted neighbor contribution. *Optik*. 2016;127:11599-606.
- [11] Chakraborty S, Singh SK, Chakraborty P. Local quadruple pattern: A novel descriptor for facial image recognition and retrieval. *Computers & Electrical Engineering*. 2017;62:92-104.
- [12] Bashier HK, Hoe LS, Hui LT, Azli MF, Han PY, Kwee WK, et al. Texture classification via extended local graph structure. *Optik*. 2016;127:638-43.
- [13] Abdullah MFA, Sayeed MS, Muthu KS, Bashier HK, Azman A, Ibrahim SZ. Face recognition with symmetric local graph structure (slgs). *Expert Systems with Applications*. 2014;41:6131-7.
- [14] Rakshit RD, Nath SC, Kisku DR. Face identification using some novel local descriptors under the influence of facial complexities. *Expert Systems with Applications*. 2018;92:82-94.
- [15] Abusham EE, Bashir HK. Face recognition using local graph structure (LGS). *International Conference on Human-Computer Interaction: Springer*; 2011. p. 169-75.
- [16] Ahonen T, Hadid A, Pietikainen M. Face recognition with local binary patterns. *European conference on computer vision: Springer*; 2004. p. 469-81.
- [17] Tuncer T, Dogan S. Pyramid and multi kernel based local binary pattern for texture recognition. *Journal of Ambient Intelligence and Humanized Computing*. 2020;11:1241-52.
- [18] Tuncer T, Dogan S, Ertam F, Subasi A. A novel ensemble local graph structure based feature extraction network for EEG signal analysis. *Biomedical Signal Processing and Control*. 2020;61:102006.
- [19] Dong S, Yang J, Chen Y, Wang C, Zhang X, Park DS. Finger Vein Recognition Based on Multi-Orientation Weighted Symmetric Local Graph Structure. *Ksii Transactions on Internet & Information Systems*. 2015;9.
- [20] Vipparthi SK, Nagar SK. Local extreme complete trio pattern for multimedia image retrieval system. *International Journal of Automation and Computing*. 2016;13:457-67.
- [21] Samaria FS, Harter AC. Parameterisation of a stochastic model for human face identification. *Proceedings of 1994 IEEE workshop on applications of computer vision: IEEE*; 1994. p. 138-42.
- [22] Libor Spacek's Facial Image Database, Face94 Database, <http://cswww.essex.ac.uk/mv/allfaces/faces94.html> (accessed June 1, 2018).
- [23] Martinez AM, Kak AC. Pca versus lda. *IEEE transactions on pattern analysis and machine intelligence*. 2001;23:228-33.
- [24] Ojala T, Maenpaa T, Pietikainen M, Viertola J, Kyllonen J, Huovinen S. Outex-new framework for empirical evaluation of texture analysis algorithms. *Object recognition supported by user interaction for service robots: IEEE*; 2002. p. 701-6.
- [25] Tuncer T, Dogan S, Plawiak P, Acharya UR. Automated arrhythmia detection using novel hexadecimal local pattern and multilevel wavelet transform with ECG signals. *Knowledge-Based Systems*. 2019;186:104923.
- [26] Vapnik V. The support vector method of function estimation. *Nonlinear Modeling: Springer*; 1998. p. 55-85.
- [27] Vapnik V. The nature of statistical learning theory: Springer science & business media; 2013.

Industrial Automation and Edge Computing: SCADA, PLC, PAC, IO-LINK

Fatih TOPALOĞLU^{1*}

¹ Department of Computer Engineering, Faculty of Engineering and Natural Sciences, Malatya Turgut Özal University, Malatya, Turkey

*¹ fatih.topaloglu@ozal.edu.tr

(Geliş/Received: 21/01/2021;

Kabul/Accepted: 01/02/2021)

Abstract: Increasing interest in Industry 4.0 applications has brought with it many new technologies and strategies for processing all kinds of production-related data, which are at the center of this trend. Although many of these technologies are not very new, they have not yet reached sufficient recognition in the industry. The term edge computing is among the concepts that need to be clarified in this context. Edge computing draws local intelligence and data processing capability to the parts of the communication network close to the end devices such as pumps, motors, sensors, relays that produce data, and performs the analysis of the data without the need to transfer it somewhere. However, this process also has difficulties. Edge computing architectures in industrial applications need to address bandwidth, management complexity, latency, and network security risks. With this study, four important architectural solutions that help to optimize resource usage on the edge computing platform for industrial applications are proposed and analyzed.

Key words: Edge computing, industrial automation, SCADA, PLC, PAC, IO-LINK.

Endüstriyel Otomasyon ve Uç Bilişim: SCADA, PLC, PAC, IO-LINK

Öz: Endüstri 4.0 uygulamalarına artan ilgi, bu trendin merkezinde yer alan üretim ile ilgili her türlü veriyi işlemeye yönelik birçok yeni teknoloji ve stratejiyi de beraberinde getirmiştir. Bu teknolojilerin birçoğu pek yeni olmasa da, sektörde yeterli bilinirliğe henüz erişememiştir. Uç bilişim terimi de bu bağlamda netleştirilmesi gereken konseptler arasında yer alır. Uç bilişim, yerel zeka ve veri işleme kabiliyetini haberleşme ağının veri üreten pompa, motor, sensör, röle gibi uç cihazlara yakın kısımlarına çekerek verinin bir yere aktarılmasına gerek kalmadan analizini gerçekleştirir. Ancak bu sürecin de zorlukları bulunur. Endüstriyel uygulamalarda uç bilişim mimarilerin bant genişliği, yönetim karmaşası, gecikme süresi ve ağ güvenliği risklerine çözüm getirmesi gerekir. Yapılan çalışma ile endüstriyel uygulamalar için uç bilişim platformunda kaynak kullanımını optimize etmeye yardımcı olan dört önemli mimari çözüm için önerilmiş ve analiz edilmiştir.

Anahtar kelimeler: Uç bilişim, endüstriyel otomasyon, SCADA, PLC, PAC, IO-LINK.

1. Introduction

Edge computing technology offers important opportunities to system integrators and business owners to increase productivity in production in the age of Industry 4.0 or to ensure the most efficient use of data in industrial systems. With its computing ability in edge computing, it can perform near real-time insight and predictive analysis. While modern industry practices break down molds, they can also face many challenging and daunting demands. This is where the starting point for developing solutions for edge computing in industrial applications emerges.

While the previous studies covered the general features of edge computing for the sectors, the requirements of the industrial automation field in particular were taken as basis in the study. For this purpose, four important automation architectures, Supervisory Control and Data Acquisition (SCADA), Programmable Logic Controller (PLC), Programmable Automation Controller (PAC) and IO-LINK, have been proposed and analyzed.

Edge computing provides crucial transformations for industrial applications. Today, businesses are developing edge computing and cloud computing to store, analyze and process data faster for specific workloads such as latency-sensitive applications. In this study, an important set of criteria for edge informatics applications in industrial automation systems was defined by making a comprehensive literature review of online and printed copies of relevant journals and printed books.

For the purpose of the document, the remainder of the article continues as follows. The proposed architectures for the solution, considering the development of the industrial automation system, were firstly SCADA architecture, Secondly PLC architecture, Thirdly PAC architecture, fourthly data processing features of

* Corresponding author: fatih.topaloglu@ozal.edu.tr. ORCID Number of authors: ¹ 0000-0002-2089-5214

IO-LINK architectures at the end, and finally, important requirements and solutions in the discussion and suggestions. recommendations have been put forward.

2. Edge Computing Architectures in Industrial Automation

With the advancement of technology, the automation sector gains more value and tries to produce more innovations in order to keep up with technology. Industrial automation systems are also the basis of these production stages. Automation systems can also be referred to as a device or software set that allows the user to communicate with the machine and production facilities.

Edge computing brings significant advantages to industrial automation systems as it significantly optimizes resource usage. First of all, the processors used in the relevant devices provide more efficient hardware security with a relatively low power requirement. In this way, it quickly captures flow-related data in order to detect possible product defects.

2.1. SCADA

SCADA systems are used in critical infrastructure and industrial sectors [1]. SCADA system is a combination of data acquisition and telemetry (wireless data transfer). Their primary functions are data collection, data processing for use by the operator, and control of remote devices by the operator [2].

The data collected from the end devices actuators, drive motors, valves, lamps, speed measuring devices, proximity detectors, temperature, force and moment electronic sensors are converted to electrical signals and transferred to the SCADA system. The commands given from the SCADA system are converted to electrical signals in this layer, allowing the desired movements to occur in the real world.

In order for the SCADA system to undertake the monitoring and control functions, the input and output information of the process is defined in a database. When each information corresponding to the process variables in the database needs to be processed, the transaction blocks to be used are performed in the database definition phase. SCADA data to be processed in edge computing are quality data, production efficiency data, production cost data, maintenance data and statistical data.

SCADA systems have an alarm structure developed to continuously monitor process variables and warn the operator in case these variables reach undesired values. In addition, they report the production results made in different shifts in the factory, certain variables of the process, the results of the events on request or as events occur or periodically. Thus, production prescriptions are put into practice. Recipes can be associated with graphics, allowing the operator to easily access and modify recipes if necessary.

The SCADA system, the Remote Terminal Unit (RTU), which forms the data collection and control terminal units, the communication system that allows data or information to be sent mutually to another region in a region, the facilities spread over a wide geographic area are monitored and managed remotely with a computer-based structure. It consists of Master Terminal Unit (MTU) units. Efficient communication is required for efficient flow messages between MTU and PLCs / RTUs [3].

In a SCADA system, remote terminal units, main terminal units, communication networks, data collection units, sensors and sensors, software, central control room, control panels, scada system terminals, computer screens, printers, uninterruptible power supplies can be included. Figure 1. shows a typical SCADA system.

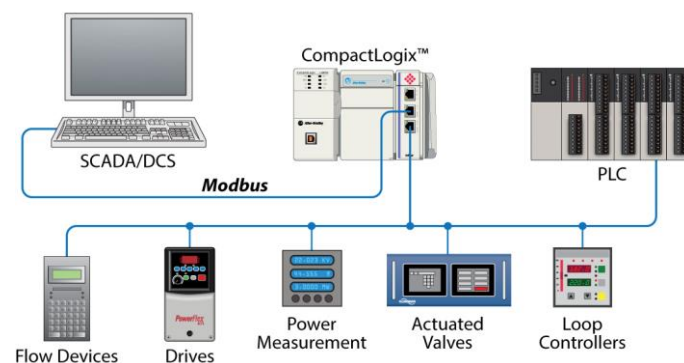


Figure 1. SCADA system

All kinds of information collected from control devices in the SCADA system are kept in a variable in the database called Tagname. This information should be processed and adapted to the needs and demands of the business. SCADA software helps employees to process and view data in the decision process. The software determines what to monitor, when to monitor, acceptable parameter ranges, response type, etc. determines [4].

2.2. PLC

PLCs are microprocessor-based devices used in the control of processes such as production departments in factories or control of machines. PLCs were first used by the automotive industry in the late 1960s [5–9]. This supervisory system scans the input information at speeds invisible to the naked eye, and works in a way to respond in close to real time with the corresponding exit information.

The most important feature of PLC is that the program commands are processed in real time, and it enables the realization of functions by sending it to the modules connected with the outside world such as input / output and communication in the shortest time possible. PLC can be more easily connected to sensors and actuators [10]. Thus, they can be used as a solution in industrial applications where timing is critical.

For this purpose, functions such as logic, sequencing, counting, data processing, comparison and arithmetic operations, PLC system, which evaluates inputs and assigns outputs with programming support, provides communication between processor - memory modules and power supply, and the brain of programmable controllers is the central processing unit, which is used to store the control program in the microcontroller. The memory unit consists of the input unit that enables it to be used by accepting the signal it receives from the controlled machines, the processor or an external switch or sensor, and the output unit where the controller provides output signals to control the process at the output. Figure 2. shows a typical PLC system.

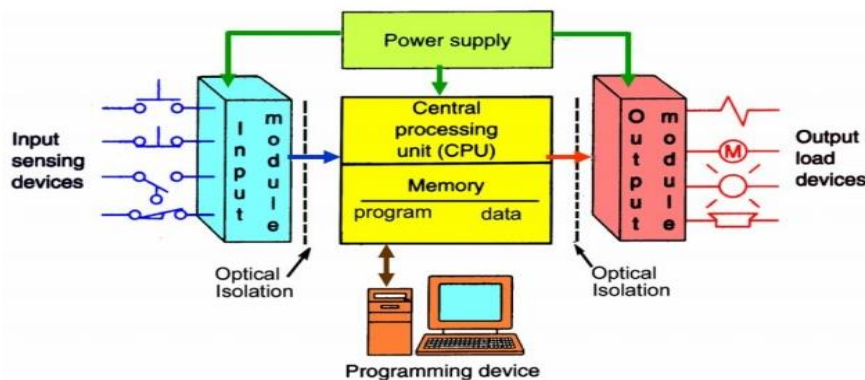


Figure 2. PLC system

Data management, including data collection, review and processing with PLC, has improved in recent years. PLCs can be used as data collectors about the process they control. This data is then compared with reference data in the controller's memory and transferred to another device for reporting.

The PLC system determines the physical events, changes and movements occurring in the field with various measuring devices and evaluates the received information according to the written user program. It also reflects the results resulting from logical operations to the field through the elements it commands.

Since PLCs replace relay-based logic circuits, a programming language consisting of open and closed key symbols called ladder logic is often used when programming PLCs. This programming language is designed to be programmed with schematic or ladder diagrams instead of common computer languages [6,11-14].

2.3. PAC

A typical control system has an interface created by signals from sensors or actuators. Since very extensive applications have been developed in modern industry, creating this interface is quite laborious and the controller requires many requirements. This is where the starting point for the development of PACs emerges.

Since PLCs and PC-based controllers are insufficient in modern industry applications where the features listed at the beginning are required; PACs have emerged as open, multi-functional and integrated control systems are needed. PACs expand the capabilities of PLCs, integrate with PC-based control devices and gather two separate branches together. Recent examples of the industrial use of the PAC framework are given in [15], where a coal preparation plant is automatically controlled using the PAC, and [16] where tide simulations are performed using the PAC framework.

PACs use modern data networks to interact with distributed I / O, drivers, other PAC devices, and corporate elements. They store data in a way superior to PLCs. PACs, which have a better computing power compared to PLCs, are also ahead with their control power. Combining all these features, PACs have revolutionized the field of automation. Figure 3. shows a typical PAC system.

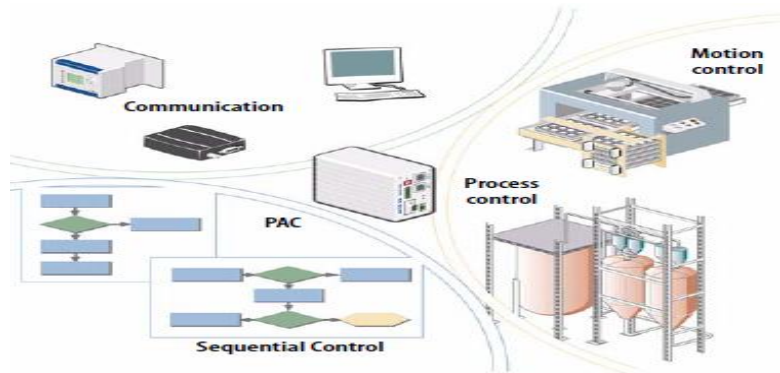


Figure 3. PAC system

In terms of edge information security, PACs use a single platform, it is a reliable platform because it is the Real Time Operating System (RTOS). Therefore, drives, motions, logic circuits and process control are carried out on a single platform. On the contrary, PAC has provided a better solution for this issue, since more than one platform is needed in PLCs. PACs have many functions in these modern industry applications, system studies, performance, status, etc. It monitors centrally, which results in an improved communication structure, machine performance and time savings.

PACs have a much more advanced role thanks to their ability to monitor remotely, data collection, data processing, and organize simple interfaces with Human Machine Interface (HMI) using their large network capacity, memory and processing power. For example, a typical PAC has three basic networks (Ethernet, TCP / IP and web services such as http or SNMP), expandable flash memory, and multitasking functionality.

Among the basic features of PAC components that will provide data processing at the edge, having a more open architecture, better and easier communication and control capabilities, multi-language support, multitasking applications, modular design, more analog I / O (Input / Output) options, Integration with many databases such as SQL and easy programming with USB port.

2.4. IO- LINK

IO-Link ensures the availability of the data requested by the industry operating with the internet in the Industry 4.0 process. All information about this sector is based on the internet. Usually these sources of information are sensors. Thanks to IO-Link, sensors will be solved in transactions such as passage information and status tracking. In the industry sector where the internet is important, standards and continuity are important. IO-Link steps in on this issue and tries to strengthen the communication of sensors that will ensure this continuity.

IO-Link; It is a point-to-point distributed serial communication protocol that is used to communicate with sensors and actuators, and has been found in search of an easier and global solution. The IO-Link technology, developed to communicate with the lowest level of controller automation, has an efficient point-to-point link. It is only designed for the further development of the connection technology between sensors and actuators. Performance characteristics for wireless sensor / actuator communication systems are typically defined by sequential response times of 10 ms or less, and up to 100 sensors and actuators in a production cell spanning several meters [17-19].

The IO-Link Wireless system can be classified as narrowband communication systems [19,20]. Transmits between IO-Link and devices at a speed of 230 kBaud in 400 micro seconds. Large data packages can also be selected if desired. Processed data, manufacturer ID data, system parameters and configuration data, control data can be sent via IO-Link if required. With complex sensors, data can be transmitted in real time. Thus, a very effective and economical automation solution is provided and the cabling process becomes much simpler. Figure 4. shows a typical IO-Link system.

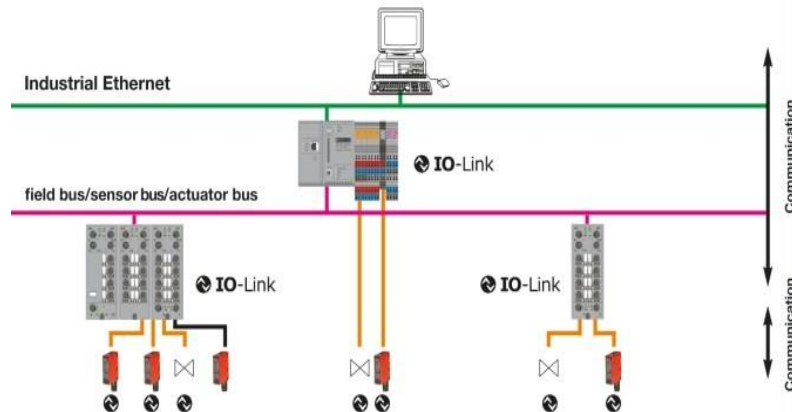


Figure 4. IO Link system

One of the strong advantages of IO-Link is data availability with far-reaching implications. Access and management of sensor data keeps system components running smoothly, streamlines device replacement and optimizes machine maintenance; thus, costs are reduced and the risk of downtime is reduced.

In edge computing applications, in addition to the remote adjustment of IO-Link's sensors, the data storage feature provides automatic reloading of data when changing the device. Users can transfer the existing sensor parameter values to the changed sensor in order to make the device change quickly.

3. Discussion and Suggestions

It is necessary to transfer data to the management in the field by exchanging data with SCADA Application Enterprise Resource Planning (ERP) software and reflecting the writings made by the management to the field. This can be achieved if the databases to be used with the programs are standard and accessible such as SQL or MySQL.

To develop application software using SCADA systems, communication protocols must be defined and the database structure must be defined. Communication protocols provide communication between units that need to communicate with each other in order for SCADA to be the information backbone of the enterprise.

In order for the SCADA system to undertake the monitoring and control functions, the input and output information of the process is defined in a database. Each information corresponding to the process variables in the database is defined as a label, gate or point. The alarms related to the levels where these process variables should be found and the transaction blocks to be used when these variables need to be processed are performed in the database definition phase.

In whatever form, a SCADA software must support the PLC system in order to be applied to the system. If an automation system is to be newly installed and the SCADA system is included in the planning, the selection of SCADA software is easier. However, if SCADA will be installed on an existing automation system, it should be examined whether it supports these PLCs while selecting the driver software of the installed PLC devices.

Generally, SCADA systems are selected in accordance with the operating system platform used in the information processing and automation systems of the enterprises. In addition to Microsoft's operating systems as a stable and common operating system, some businesses may prefer open source (Linux) operating systems in terms of cost. SCADA systems running on almost zero-cost Linux are also available for such open source platforms. However, this requires PLC driver software.

Data acquisition and control speed of communication channels significantly affects the SCADA system. Consequently, the user interface and application software in the control center are also affected. The application of the SCADA System with the highest level of success depends on the communication system.

The most important part of the SCADA system that affects the speed performance is the communication network. All operations involving data transfer and updating between units that are connected to each other at various automation levels of the controlled systems are carried out over communication networks. Therefore, communication is of great importance in SCADA applications.

Digital controllers with relay and hardware program work in real time. In other words, the change in the input information is immediately reflected on the output. This is called parallel signal processing. Memory programmed command orders in PLC are evaluated depending on time. In other words, a change in input is not reflected on the output immediately. This form of signal processing is called serial signal processing, and this is a disadvantage for the PLC.

Control devices are the input, output, communication module etc. of many modules. It is formed by combining. Of course, in such a modular system, there is a complete harmony between all modules when the device is enlarged.

These modules, which were initially independent from each other, are interconnected with a "BUS" system. The CPU creates a closed unit over this "BUS" system and organizes the transport of all data and orders. There are also compact devices created for minor control problems (eg LOGO). These are generally in a closed unit with a fixed number of inputs and outputs. These are generally in a closed unit with a fixed number of inputs and outputs.

In the PLC, the information from the field is the transformation of the actions that occur in the environment into electrical signals. This information can be analog or digital. If the incoming information is analog, query can be made for a certain range of the incoming value, if it is digital, it can be queried according to the presence or absence of the signal. These sensing events are carried out with entry cards, and intervention events with exit cards.

The system to be controlled by PLC may vary in size. Only one machine can be controlled or a complete control of a factory can be performed. The only difference is the capacity of the controller used.

As the systems used develop, PACs also develop in terms of their expandable structures. This expansion is provided by the PLC-type suspension module or by networkable devices such as distributed I / O blocks.

The modularity inherent in PAC in data processing at the edge also offers the possibility of distributing intelligence into a system using network communication or removable memory cards. This is possible because the development environment of the PAC uses logic I / O maps to separate hardware details from the program. Therefore, program modifications are not required for adding, removing, modifying or replacing a device connected to the PAC.

The flexible and modular designs of the PACs enable the creation of independent automation cells that can be added to larger networks for edge computing. This offers infinite modular design capability and increased flexibility and scalability while simplifying maintenance and reducing downtime.

The use of portable storage devices increases the availability of PACs compared to PLC and PC-based controllers in remote control applications where network access is not possible. For example, large data sets can be maintained with local SQL databases on flash cards so that they can be disassembled and replaced at regular intervals.

In edge computing, IO-Link can be integrated into all standard open communication systems and automation systems and can be operated comfortably from the control. It is advantageous to use IO-Link technology for sensors with simple structures such as scanners, reflective sensors or fiber optics.

Even a sensor that does not know the IO-Link language can be connected to the IO module. However, the difficult part is that it needs to use an extra interface. With its developed versions, it has provided an external data management feature and thus has given itself another momentum. With its data management feature, the possibility of changing the sensor is provided without the need to make parameter settings again.

When processing data at the edge, IO-Link allows users to view errors and the status of the device. Thus, users can see the sensor's performance as well as its performance and evaluate the machine's efficiency.

Safety is very important for edge computing devices used in industrial automation applications. Security solutions in electronic markets today are very expensive. However, low-cost solutions are essential for these systems to become widespread across all industrial applications [21].

4. Conclusion

Edge computing is a type of edge computing method used extensively in smart application applications. Depending on the type of industrial applications, data takes place in the edge information system as time sensitive. At this point, SCADA, PLC, PAC, and IO Link architectures are important issues in the industrial automation industry, and the future of the industry lies in the hands of these technologies. With this study, the architectures proposed for edge information applications in industrial automation systems are analyzed and solutions are offered for the determined requirements.

With the models suggested in the article, you can manage workloads across all devices in industrial applications, regardless of number and cloud, deploy applications reliably and seamlessly in all edge locations, maintain openness and flexibility to adapt to evolving needs, and operate more securely and with confidence It will help to perform such operations.

Edge computing architectures proposed and analyzed for industrial applications will increase functionality in businesses by processing large amounts of data and reveal the potentials of this data, while also offering new business opportunities. This will produce faster, more reliable and more consistent results for operators and customers. In the process of Industry 4.0, the analytical features of these architectures will greatly strengthen innovation.

References

- [1] Stouffer K, Falco J, Scarfone K. Guide to Industrial Control Systems (ICS) Security, National Institute of Standards and Technology, Gaithersburg, MD, USA: NIST Pubs, 2011.
- [2] Gaushell DJ, Darlington HT. Supervisory Control and Data Acquisition. Proc. IEEE, 1987; 75(12): 1645–1658.
- [3] Oliveira RM, Facina MSP, Ribeiro MV, Vieira AB. Performance Evaluation of In-home Broadband PLC Systems Using a Cooperative MAC Protocol. Computer Networks 2016; 95: 62–76.
- [4] Li H. Wide Area Voltage Monitoring and Optimization. Ph. D, dissertation, Dept. Elec. Eng., Washington State University, Pullman, USA: Pubs, 2013.
- [5] Bartelt TLM. Industrial Electronics: Devices, Systems and Applications. Albany, New York, USA: Delmar Publishers, 1997.
- [6] Herman SL, Sparkman BL. Electricity and Controls for HVAC/R. 6th ed. Clifton Park, New York, USA: Delmar Cengage Learning, 2010.
- [7] Kilian CT. Modern Control Technology: Components and Systems. 2nd ed. Novato, CA : Delmar Thomson Learning, 2000.
- [8] Parr EA. 16-Programmable Controllers. In: Laughton MA, Warne DJ, editors. Electrical Engineer's Reference Book. 16th ed. Nestfield, London, UK: Newnes, 2003.
- [9] Edan Y, Pliskin N. Transfer of software engineering tools from information systems to production systems. Comput Ind Eng 2001; 39(1–2): 19–34.
- [10] Kiran AR, Sundeep BV, Vardhan CS and Mathews N. The principle of programmable logic controller and its role in automation Int. J. Eng. trends Technol. 2013; 4(3): 500–502.
- [11] Rehg JA, Sartori GJ. Programmable Logic Controllers. 2nd ed. Saaddle River, New Jersey, USA: Pearson, 2009.
- [12] Petruzella FD. Programmable Logic Controller. 4th ed. New York, USA: Mc Graw-Hill, 2011.
- [13] Michel G. Programmable logic controllers-Architecture and applications. 1st ed. New Jersey, USA: Wiley, 1990.
- [14] Rullán A. Programmable logic controllers versus personal computers for process control. Comput Ind Eng 1997; 33(1–2): 421–4.
- [15] Zhang L. Applications of PAC in control system at Xeiqiao new coal prepartaion plant. Coal Preperation Technology 2013; 3: 80-81.
- [16] Zhang XD. Tide Simulation System Based on PAC. Modern Electronic Technique 2008; 21(11): 113-116.
- [17] Koerber HJ, Wattar H, Scholl G. Modular Wireless RealTime Sensor/Actuator Network for Factory Automation Applications, IEEE Transactions on Industrial Informatics 2007; 3: 111–119.
- [18] Frotzscher A, Wetzker U, Bauer M, Rentschler M, Beyer M, Elspass S, Klessig H. Requirements and current solutions of wireless communication in industrial automation, in: 2014 IEEE International Conference on Communications Workshops (ICC), June 2014; Sydney, Australian: pp. 67–72.
- [19] Krush D, Cammin C, Heynicke R, Scholl G. Standardisierung eines schnellen drahtlosen Sensor/Aktor-Netzwerkes fuer die Fertigungsautomatisierung, Technisches Messen 2016; 83 (4), 201–207.
- [20] Heynicke R, Krush D, Scholl G, Kaercher B, Ritter J, Gaggero P, Rentschler M. IO-Link Wireless Enhanced Sensors and Actuators for Industry 4.0 Networks, in: Proceedings – AMA Conferences 2017 with SENSOR and IRS2; June 2017; Wunstorf, Germany: AMA Service GmbH, pp. 134–138.
- [21] Al - Saffar H, Erçelebi E. Development of smart security system for remote control using small computer. Turkish Journal of Science & Technology 2017; 12(2): 107-112.

COPYRIGHT RELEASE FORM

TURKISH JOURNAL OF SCIENCE AND TECHNOLOGY (TJST) Published by Firat University

Firat University, Fen Bilimleri Enstitüsü Müdürlüğü
Turkish Journal of Science & Technology Editörlüğü
Elazığ-TURKEY,
Manuscript title:

Full names of all authors (in order to appear on manuscript):

Name, address etc. of corresponding author:

ID Number: Telephone:

E-mail: Mobile phone:

The author(s) warrant(s) that:

- a) the manuscript submitted is his/her/their own original work;
- b) all authors participated in the work in a substantive way and are prepared to take public responsibility for the work;
- c) all authors have seen and approved the manuscript as submitted;
- d) the manuscript has not been published and is not being submitted or considered for publication elsewhere;
- e) the text, illustrations, and any other materials included in the manuscript do not infringe upon any existing copyright or other rights of anyone. Notwithstanding the above, the Contributor(s) or, if applicable the Contributor's Employer, retain(s) all proprietary rights other than copyright, such as

- a) patent rights;
- b) to use, free of charge, all parts of this article for the author's future works in books, lectures, classroom teaching or oral presentations;
- c) the right to reproduce the article for their own purposes provided the copies are not offered for sale.

However, reproduction, posting, transmission or other distribution or use of the article or any material contained therein, in any medium as permitted hereunder, requires a citation to the Journal and appropriate credit to Firat University as publisher, suitable in form and content as follows:

Title of article, author(s), journal title and volume/issue, Copyright© year.

All materials related to manuscripts, accepted or rejected, including photographs, original figures etc., will be kept by Turkish Journal of Science and Technology editority for one year following the editor's decision. These materials will then be destroyed. I/We indemnify Firat University and the Editors of the Journals, and hold them harmless from any loss, expense or damage occasioned by a claim or suit by a third party for copyright infringement, or any suit arising out of any breach of the foregoing warranties as a result of publication of my/our article. I/We also warrant that the article contains no libelous or unlawful statements and does not contain material or instructions that might cause harm or injury.

This copyright form must be signed by all authors. Separate copies of the form (completed in full) may be submitted by authors located at different institutions; however, all signatures must be original.

ID number: ID number:

Full name (block letters) Full name (block letters)

Signature Date Signature Date

ID number: ID number:

Full name (block letters) Full name (block letters)

Signature Date Signature Date

ID number: ID number:

Turkish authors must supply their ID card number; foreign authors must supply their passport number (if possible)